学位論文（要約）

Search for supersymmetry in the final state with multiple jets, missing transverse momentum and one isolated lepton, using 20.3 fb^{-1} of data recorded by the ATLAS detector at $\sqrt{s} = 8$ TeV

(ATLAS検出器を用いた重心系エネルギー8 TeVにおける1本のレプトンを終状態に持つ超対称性事象の探索)

平成25年12月博士(理学)
申請

東京大学大学院理学系研究科
物理学専攻

佐々木雄一

Abstract

Supersymmetry is one of the most attracting theories beyond the Standard Model. In the context of R-parity conserving supersymmetry model, the supersymmetric particles are produced in pairs and the lightest supersymmetric particle (LSP) is stable. Large gluino and squark production cross-sections are expected at the proton-proton collisions. Once gluinos and squarks are produced, they decay through a cascade of multiple stages to the final states with the LSP. The LSP is only weakly interacting and escapes detection, resulting in large missing transverse momentum $E_{\mathrm{T}}^{\mathrm{miss}}$. The decay also accompanies many hadronic jets and several leptons, which often give a distinct signature from the Standard Model processes.

This thesis presents a general search for supersymmetry in final states with jets, missing transverse momentum and one isolated electron or muon, using $20.3\,\mathrm{fb}^{-1}$ of proton-proton collision data at $\sqrt{s} = 8$ TeV recorded by the ATLAS detector at the LHC in 2012.

One of the notorious backgrounds in proton-proton colliders is QCD multi-jet, which has an overwhelming cross-section, can be suppressed by requiring an isolated electron or muon. Therefore, leptonic analysis is an ideal way to search for new physics with small cross-sections at the LHC. Based on a topology selection of one lepton, large $E_{\mathrm{T}}^{\mathrm{miss}}$ and multiple jets, three signal regions are introduced to cover general supersymmetric event topologies.

Since no excess over the Standard Model expectation is found in the Signal Regions, the results are interpreted as mass limits in several models. In a minimal supergravity model, a gluino mass up to 1200 GeV is excluded, and a squark mass is excluded up to 1500 GeV. The result is also interpreted in a simplified model and an upper limit on the cross-section times branching fraction is set on the gluino pair-production cross-section $\sigma(\tilde{g}\text{-}\tilde{g})$ and branching fraction $\mathrm{Br}(\tilde{g} \to qqW^{(*)}\tilde{\chi}_1^0)$, which is

$$\sigma(\tilde{g}\text{-}\tilde{g}) \times \mathrm{Br}(\tilde{g} \to qqW^{(*)}\tilde{\chi}_1^0)^2 < 20\,\mathrm{fb}$$

This limit is a good approximation independent of the gluino decay pattern except for some extreme mass spectra.

Contents

1 The Standard Model and Supersymmetry

1.1 Introduction

The Standard Model (SM) is a quite successful model to describe the phenomena below the electroweak energy scale of $O(100)$ GeV with great accuracy. On the other hand, once we consider higher energy up to the Grand Unified Theory (GUT, $\Lambda_{\mathrm{GUT}}{\sim}10^{16}$ GeV) or The Planck scale ($M_{\mathrm{pl}}{=}1.22\times10^{19}$ GeV), there arise some problems the SM cannot explain.

One natural question is "why the electroweak energy scale and the GUT or Planck scales are so separated by a significant order?", which is called "hierarchy problem". The hierarchy problem gives rise to a problem on the Higgs mass, whose bare mass receives large radiative corrections of an order of the fundamental scale. To yield the physical Higgs mass at the electroweak scale, a large degree of cancellation between bare mass and quantum corrections is needed (naturalness problem). The long-sought Higgs boson, the final missing ingredient in the Standard Model, was discovered at the LHC in 2012 [1]. The mass of the Higgs boson was measured to be ∼126 GeV, which is an interesting challenge to naturalness and the discovery of supersymmetric particles at the LHC. The WMAP [2] experiment made a valuable measurement of the fraction of ingredients of the universe. The results suggest that more than 85 % of the total matter in the universe is made of "Dark Matter" (DM), for which the Standard Model does not have an appropriate candidate. Gravity is also a problem which is not described within the framework of the SM. Supersymmetry is one of the solutions aiming to solve the problems mentioned above. The brilliant solution of supersymmetry will be discussed in Section 1.4 after introducing the SM in the next Section.

1.2 The Standard Model

The Standard Model consists of two theories: electroweak theory and Quantum ChromoDynamics (QCD). Electroweak theory is particularly interesting because it introduces the Higgs mechanism, which also plays an important role in supersymmetry theories. We start from introducing elementary particles and forces in the Standard Model, then describe electroweak theory. QCD theory is explained later mainly from the experimental aspect.

1.2.1 Elementary particles in the Standard Model

In the framework of the Standard Model, matter consists of quarks and leptons, which are collectively-referred to as fermions. There are six types of quarks (up, down, charm, strange, top and bottom) and six leptons (electron, muon, tau and their paired neutrinos). As shown in Fig. 1, they are classified into three groups, called generations. An anti-particle accompanies for each fermion with the same mass but the opposite quantum numbers, such as charge. All fermions have spin $\frac{1}{2}$.

There are the particles which intermediates forces between fermions, which are called gauge bosons. A photon conveys the electromagnetic force, $W^{\pm}$ and Z^0 bosons intermediate the weak force and a gluon conveys the strong force. All these bosons have spin 1. The remaining force, gravity, is not included in the framework of the Standard Model.

1.2.2 Electroweak theory

Detailed description of electroweak theory and the Higgs mechanism are documented in Appendix A, so only a simple overview and several important notations are introduced here.

The weak force couples through weak isospin, which obeys SU(2) symmetry (to avoid confusion, we add a subscript L in the following). The left-handed fermions are put into $\mathrm{SU}(2)_L$ doublets, such as

$\begin{pmatrix} u_L \\ d_L \end{pmatrix}$ and $\begin{pmatrix} \nu_L \\ e_L \end{pmatrix}$. Here the subscript means that the fermions are left-handed. The doublets are denoted by capital letters, such as L for leptons and Q for quarks. A right-handed fermion forms $SU(2)_L$ singlet and represented by a small letter with subscript R, for example, e_R (electron), u_R (up quark). Then we introduce U(1) symmetry, which is proportional to Hypercharge Y. Gauge theory give birth to electromagnetic and the weak interactions at the same time from $U(1)_Y \times SU(2)_L$ symmetry. In the framework of gauge theory, the gauge bosons are prohibited to have explicit mass terms, which is opposed to experimental results. This problem is solved by the Higgs mechanism. The Higgs mechanism introduces a $SU(2)_L$ complex scalar doublet ϕ with an unstable potential. As a result of Spontaneous Symmetry Breaking (SSB), a new stable vacuum is chosen where the massive bosons arise. The expectation value of the Higgs field after SSB $\langle\phi\rangle$ is called Vacuum Expectation Value or VEV. Fermion masses are also explained in gauge theory through Yukawa coupling constant y.

Figure 1: Particles in the Standard Model.

1.2.3 QCD

Quantum Chromo Dynamics (QCD) describes the strong interactions of quarks and gluinos. The theory has "Chromo" in its name because the theory is based on $SU(3)_C$ symmetry and fundamental representation **3** seems to behave like three colors. A quark (anti-quark) obeys **3** ($\bar{\mathbf{3}}$) representation. A **8** representation generated in $\mathbf{3} \otimes \bar{\mathbf{3}} = \mathbf{8} \oplus \mathbf{1}$ is assigned to a gluon. Another difficulty of QCD is that the strength of its coupling constant α_S is too strong to perform perturbative calculations. As a result, first or second order perturbation doesn't give sufficient accuracy, which weakens the prediction power.

A complete overview of QCD goes far beyond the scope of this thesis, therefore, only important conclusions necessary in the analysis are summarized.

Asymptotic freedom :

In renormalization group theory, the running of coupling constant is evaluated by β-function. In the lowest non-trivial order, β-function for SU(3) theory with the number of generation n_{gen} is

given as

$$\beta_1(\alpha) = \frac{\alpha^2}{2\pi}\left(-11 + \frac{n_{\text{gen}}}{3}\right), \tag{1}$$

where α represents the coupling constant, $\alpha = \frac{g^2}{4\pi}$. For QCD, n_{gen} is 3, which results in a negative value for the β-function. A negative β-function means that the coupling constant becomes weaker at higher energy. This feature makes perturbative calculations possible in hard collisions at the LHC energy scale, while the calculations of low energy phenomenon around $\Lambda_{\text{QCD}} \sim O(1)\,\text{GeV}$ become difficult, because the coupling constant diverges near Λ_{QCD}, which breaks the perturbation. This behavior is problematic for jet shower simulation since jet shower is made up of many productions of light hadrons at the energy scale of $O(1)\,\text{GeV}$. To cope with the problem, Monte Carlo generators stop jet evolution at some energy scale and the existing quarks are forced to be changed into hadrons. This technical trick is called "Hadronization".

Even at high energy, the coupling constant α_S depends strongly on the energy scale compared with weak or electromagnetic coupling constants. As a result, the choice of the energy scale at which α_S is evaluated becomes important. In Monte Carlo simulation, the energy scale, called renormalization scale, is determined by an empirical formula. Therefore impact of the choice is evaluated by varying the energy scale and taken into the uncertainty.

Confinement :

QCD predicts a very strong forces between two colored particles. Contrary to electromagnetic forces, it becomes stronger when they are separated farther. As a result of this behavior, there exists a distance at which the potential energy exceeds quark masses, and beyond the distance, creation of a new particle pair is favored in the light of the total energy. The distance is smaller than the diameter of proton, so it is impossible to see an isolated colored particle, which is often said as colored particles are "confined".

As a result, a few number of quarks and gluinos produced in a collision consequently pair-create a lot of particles as they get separated, forming a shower-shape jet. This process is called "fragmentation".

1.3 Problems of the Standard Model

Although the Standard Model describes a wide range of phenomena, there exist several exceptions which cannot be explained in the Standard Model. The followings are such interesting phenomena. They're important because they might lead to the theories beyond the Standard Model.

1.3.1 Grand unification

In the grand unification theory, electromagnetic, weak and strong forces are thought to stem out from one force at the GUT scale. If it is correct, the coupling constants for these three forces should be the same strength at the GUT scale. In renormalization theory, the energy dependence of coupling constant α_i is evaluated by

$$\frac{1}{\alpha_i(Q)^2} - \frac{1}{\alpha_i(Q_0)^2} = -\frac{b_i}{2\pi}\ln\left(\frac{Q}{Q_0}\right), \tag{2}$$

where Q_0 is the energy scale at which the coupling constant α_i is measured (usually m_Z is chosen) and Q is the energy scale at which α_i is evaluated. In the Standard Model, b_i is

$$b_i^{\text{SM}} = \begin{pmatrix} b_1 \\ b_2 \\ b_3 \end{pmatrix} = \begin{pmatrix} 0 \\ -\frac{22}{3} \\ -11 \end{pmatrix} + n_{\text{gen}}\begin{pmatrix} \frac{4}{3} \\ \frac{4}{3} \\ \frac{4}{3} \end{pmatrix} + n_{\text{Higgs}}\begin{pmatrix} \frac{1}{10} \\ \frac{1}{6} \\ 0 \end{pmatrix}, \tag{3}$$

where n_{gen} is the number of generations and n_{Higgs} is the number of Higgs doublets, which are 3 and 1, respectively. Parameters in the parentheses are the function of number of particles appearing in loop calculations. The running of coupling constants are evaluated as plotted in Fig. 2 (left). The three lines do not intersect at one point.

On the other hand, in Minimal Supersymmetric Standard Model (MSSM), which will be introduced later, the coefficients b_i are modified because of newly introduced particles. b_i, then, becomes,

$$b_i^{\text{MSSM}} = \begin{pmatrix} b_1 \\ b_2 \\ b_3 \end{pmatrix} = \begin{pmatrix} 0 \\ -6 \\ -9 \end{pmatrix} + n_{\text{gen}} \begin{pmatrix} 2 \\ 2 \\ 2 \end{pmatrix} + n_{\text{Higgs}} \begin{pmatrix} \frac{3}{10} \\ \frac{1}{2} \\ 0 \end{pmatrix}. \tag{4}$$

Note that the number of Higgs fields n_{Higgs} is 2 in MSSM. If supersymmetry exists at the mass scale of around $O(1)$ TeV, the three coupling constants cross around $Q = O(10^{16})$ GeV and the grand unification occurs as shown in Fig. 2 (right).

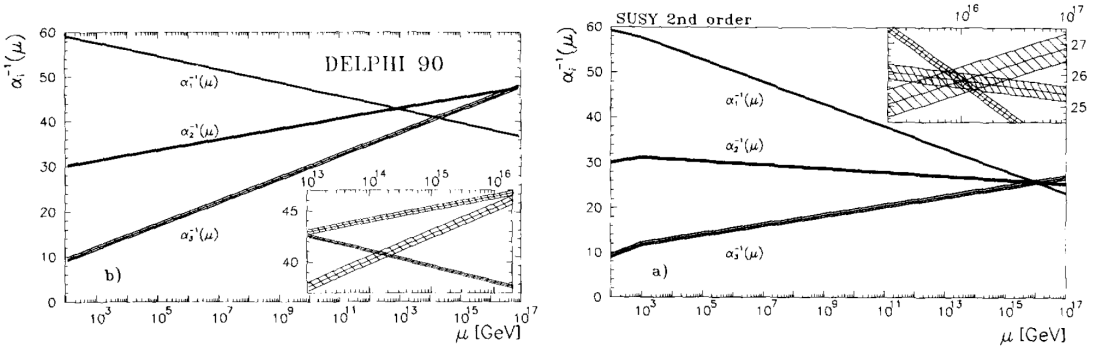

Figure 2: First order evolution of the tree coupling constants in the Standard Model using M_Z and $\alpha_S(M_Z)$ from DELPHI data (left) and the second order evolution of the tree coupling constants in MSSM assuming SUSY mass scale M_{SUSY} of around 1 TeV (right) [3].

1.3.2 Hierarchy problem

Masses of the SM particles are all below the electromagnetic scale, i.e. $O(100)$ GeV, while the Planck scale is $M_{\text{Pl}} \sim 10^{16}$ GeV, where gravity finally becomes as strong as the other three forces. The unnatural splitting between these energy scales are called "hierarchy problem".

Another problem, which is also called "hierarchy problem", occurs for the Higgs mass. In the leading order, the Higgs mass is $O(100)$ GeV (see Appendix A.3), however, once we include higher order corrections, the one-loop diagram containing a Dirac fermion f with mass m_f, shown in Fig. 3 (left) also contributes. If the Higgs field couples to f through a term $-\lambda_f H \bar{f} f$, then the Feynman diagram in Fig. 3 (left) yields a correction of

$$\Delta m_H^2 = -\frac{|\lambda_f|^2}{8\pi^2} \Lambda_{\text{UV}}^2 + ..., \tag{5}$$

where Δ_{UV} is ultraviolet energy cutoff used to regulate the loop integral, or it can be interpreted as the energy scale to which the SM is valid. If there is no new physics beyond the SM up to the Planck scale, then the Higgs mass diverges quadratically.

Let's assume a heavy complex scalar particle S with mass m_S that couples to the Higgs through a term $-\lambda_S |H|^2 |S|^2$, the Feynman diagram in Fig. 3 (right) gives a correction of

$$\Delta m_H^2 = \frac{\lambda_S}{16\pi^2} [\Lambda_{\text{UV}}^2 - 2m_S^2 \ln(\Lambda_{\text{UV}}/m_S) + ...]. \tag{6}$$

As shown later, two scalar particles are newly introduced for each of the SM fermion in the supersymmetry framework. If these scalar particles have coupling constants satisfying $\lambda_S = |\lambda_f|^2$, the first terms of Eq. 5 and Eq. 6 cancel each other and the problematic quadrature divergence does not occur any more. This cancellation mechanism is the primary motivation of introducing supersymmetry.

1.3.3 Dark matter

WMAP [2] measured the contents of the universe in a great accuracy:

$$\begin{aligned} \Omega_{\mathrm{b}} h^2 &= 0.0227 \pm 0.0006, \\ \Omega_{\mathrm{cdm}} h^2 &= 0.110 \pm 0.006, \\ \Omega_{\Lambda} &= 0.74 \pm 0.03, \end{aligned} \tag{7}$$

where h is a dimensionless parameter defined from the Hubble constant H_0,

$$H_0 = 100\, h\, \mathrm{km\, s^{-1}\, Mpc^{-1}}. \tag{8}$$

All the values on the right-hand-side in Eq. 7 are the fractions with respect to the critical density of the universe ρ_c, which is

$$\rho_c c^2 = 5.4 \pm 0.5\, \mathrm{GeV \cdot m^{-3}}. \tag{9}$$

$\Omega_{\mathrm{b}} h^2$ is the fraction of Baryonic matter, $\Omega_{\mathrm{cdm}} h^2$ is the fraction of cold Dark Matter and Ω_{Λ} represents the dark energy. The coldness (or slowness) of dark matter is important for formation of complex structure in the universe, such as galaxy. Assuming a hot dark matter with a relativistic speed, the structure gets smoothed and no star is formed. The dark matter should have the following properties:

- To explain the contents of current universe, dark matter should be stable over the lifetime of the universe.
- The charge of dark matter should be zero, therefore electromagnetic force cannot or only weakly interact with dark matter.
- To be a cold dark matter, it should be heavy. A quantitative limit comes from a comparison with the mass and the energy scale at which dark matter decoupled from heat-equilibrium in the early universe.

There's no particle which satisfies above conditions in the framework of the Standard Model.

Weakly Interacting Massive Particles (WIMPs) is one of the candidates. WIMPs have masses roughly between 10 GeV and a few TeV, and an interaction cross-sections of the weak force. As shown later, the lightest supersymmetry particle (LSP) cannot decay further in R-parity conserving supersymmetry models and becomes a good dark matter candidate satisfying above requirements.

Figure 3: Example diagrams showing 1-loop radiative corrections which contribute to m_h. The loop of a Dirac fermion f (left) with a coupling constant λ_f and the one of a scalar particle S (right) with a coupling constant λ_S.

1.4 Supersymmetry

As discussed in the previous section, the Standard Model contains some problems and there must be a new physics beyond the SM. Pursuing the theory of everything, many theorists have proposed solutions in the last several decades. Supersymmetry introduces "superpartners" of the SM particles which have different spin by $\frac{1}{2}$. Since fermions and bosons have spin $\frac{1}{2}$ and spin 0, respectively, supersymmetry is often referred to as symmetry between fermion and boson.

There exist several supersymmetry models with different particle contents. We focus on the simplest model, Minimal Supersymmetric Standard Model (MSSM), which contains the minimal extension of the Standard Model particles.

1.4.1 SUSY breaking

Although the basic concept of supersymmetry is simple, recalling the fact that the superpartner with *exact* the same mass has not yet been observed, supersymmetry must be "broken" in a sense that supersymmetric particles are much heavier than the SM partners. We see how the SUSY breaking is introduced in the MSSM framework below[1].

We start from introducing the most general form of SUSY breaking Lagrangian [4], which is

$$\begin{aligned}\mathcal{L}_{\text{soft}}^{\text{MSSM}} &= \tfrac{1}{2}\left(M_3\tilde{g}\tilde{g} + M_2\tilde{W}\tilde{W} + M_1\tilde{B}\tilde{B} + \text{c.c.}\right) \\ &\quad -\left(\tilde{\bar{u}}\mathbf{a}_u\tilde{Q}H_u - \tilde{\bar{d}}\mathbf{a}_d\tilde{Q}H_d - \tilde{\bar{e}}\mathbf{a}_e\tilde{L}H_d + \text{c.c.}\right) \\ &\quad -\tilde{Q}^\dagger\mathbf{m}_{\tilde{Q}}^2\tilde{Q} - \tilde{L}^\dagger\mathbf{m}_{\tilde{L}}^2\tilde{L} - \tilde{\bar{u}}\mathbf{m}_{\tilde{\bar{u}}}^2\tilde{\bar{u}}^\dagger - \tilde{\bar{d}}\mathbf{m}_{\tilde{\bar{d}}}^2\tilde{\bar{d}}^\dagger - \tilde{\bar{e}}\mathbf{m}_{\tilde{\bar{e}}}^2\tilde{\bar{e}}^\dagger \\ &\quad -m_{H_u}^2H_u^*H_u - m_{H_d}^2H_d^*H_d - (bH_uH_d + \text{c.c.})\end{aligned} \tag{10}$$

The terms in the Lagrangian are chosen so that the resultant SUSY breaking does not introduce the quadrature divergence again. The first line gives masses to the superpartners of gauge bosons. M_3, M_2 and M_1 correspond to the masses of gluino $\tilde{g}$, wino $\tilde{W}$ and bino $\tilde{B}$, respectively. The second line contains (scalar)^3 type interactions (trilinear coupling). $\tilde{\bar{u}}, \tilde{\bar{d}}, \tilde{\bar{e}}$ are the vector of right-handed up-type squarks, down-type squarks and sleptons. Each component of the vector represents a particle in three generations. $\tilde{Q}, \tilde{L}$ are similar vectors but of left-handed particles, each of which is a weak isospin doublet as in Eq. 108. H_u, H_d are the Higgs potentials which couple to up-type and down-type fermions. Finally, $\mathbf{a}_u, \mathbf{a}_d, \mathbf{a}_e$ are complex 3×3 matrices in family space with dimension of mass. These terms resemble the fermion mass term in Eq.108 and actually the terms are in one-to-one correspondence with the Yukawa couplings,

$$\mathbf{a}_u = A_{u0}\mathbf{y}_u, \quad \mathbf{a}_d = A_{d0}\mathbf{y}_d, \quad \mathbf{a}_e = A_{e0}\mathbf{y}_e, \tag{11}$$

where, $\mathbf{y}_X$ is called Yukawa matrix in which the Yukawa couplings are contained as the components. The third line consists of squark and slepton mass terms. Each of $\mathbf{m}_{\tilde{Q}}^2, \mathbf{m}_{\tilde{L}}^2, \mathbf{m}_{\tilde{\bar{u}}}^2, \mathbf{m}_{\tilde{\bar{d}}}^2, \mathbf{m}_{\tilde{\bar{e}}}^2$ is a 3×3 matrix in family space that can have complex entries. However, from the experimental limits on the flavor-changing neutral current and CP-violation, the squark and slepton mass matrices are required to be flavor-blinded, which is realized when the mass matrices are proportional to the identity matrix $\mathbf{1}$ before renormalization group evolution:

$$\begin{aligned}&\mathbf{m}_{\tilde{Q}}^2 = m_{\tilde{Q}}^2\mathbf{1}, \quad \mathbf{m}_{\tilde{\bar{u}}}^2 = m_{\tilde{\bar{u}}}^2\mathbf{1}, \quad \mathbf{m}_{\tilde{\bar{d}}}^2 = m_{\tilde{\bar{d}}}^2\mathbf{1}, \\ &\mathbf{m}_{\tilde{L}}^2 = m_{\tilde{L}}^2\mathbf{1}, \quad \mathbf{m}_{\tilde{\bar{e}}}^2 = m_{\tilde{\bar{e}}}^2\mathbf{1}.\end{aligned} \tag{12}$$

Finally, in the last line of Eq. 10 we have supersymmetry breaking contributions to the Higgs potential. $m_{H_u}^2, m_{H_d}^2$ are the contributions to the up-type and down-type Higgs masses.

[1] The discussion is closely related to the content of the next section, so one should refer the Section 1.4.2 when an undefined particle or parameter appears in the text.

The original SUSY breaking Lagrangian contains many free parameters, especially as the components of matrices. However, introducing the assumptions such as Eq. 11 and Eq. 12, 124 parameters in the original Lagrangian are reduced to a few parameters.

1.4.2 Particles in MSSM

Next, we look into the particles introduced in MSSM and their properties. Figure 4 illustrates the correspondence between the SM particles and their superpartners in MSSM.

Figure 4: Illustrations of the SM particles and their corresponding superpartners in the framework of MSSM.

Higgs and Higgsino :

In the MSSM framework, two Higgs doublets with weak hypercharges of $Y = +1/2$ and $Y = -1/2$ are introduced. The former one, denoted as H_u, gives masses to up-type fermions, while the latter one, H_d, couples to down-type fermions. Each of them is composed of neutral and charged components,

$$H_u = \begin{pmatrix} H_u^+ \\ H_u^0 \end{pmatrix}, \quad H_d = \begin{pmatrix} H_d^0 \\ H_d^- \end{pmatrix}. \tag{13}$$

Inserting the components into the SUSY Lagrangian, we obtain a potential related to the Higgs boson

$$\begin{aligned} V = & \quad (|\mu|^2 + m_{H_u}^2)(|H_u^0|^2 + |H_u^+|^2) + (|\mu|^2 + m_{H_d}^2)(|H_d^0|^2 + |H_d^+|^2) && (14) \\ + & \quad |b(H_u^+ H_d^- - H_u^0 H_d^0 + c.c.| && (15) \\ + & \quad \frac{1}{8}(g^2 + g'^2))(|H_u^0|^2 + |H_u^+|^2 - |H_d^0|^2 - |H_d^0|^2 - |H_d^-|^2)^2 && (16) \\ + & \quad \frac{1}{2} g^2 |H_u^+ H_d^{0*} + H_u^0 H_d^{-*}|^2, && (17) \end{aligned}$$

where g, g' are the gauge coupling constants and the terms proportional to μ come from the Higgs interaction terms in the SUSY Lagrangian. We perform the same calculation of SSB as in the Higgs mechanism in the Standard Model, i.e. find the minimum of potential V and expand the potential about the minimum. Using $SU(2)_L$ and $U(1)_Y$ symmetries, we can set $H_u^+ = H_d^- = 0$. Also, the vacuum expectation values of the two remaining Higgs fields, $\langle H_u^0 \rangle$ and $\langle H_d^0 \rangle$, can be set to real and positive. We require that the VEVs are compatible with the observed phenomenology of electroweak symmetry breaking. Let us write

$$v_u = \langle H_u^0 \rangle, \quad v_d = \langle H_d^0 \rangle. \tag{18}$$

Then, the quadrature sum of these two terms corresponds to v in the Standard Model,

$$v^2 = v_u^2 + v_d^2. \tag{19}$$

The ratio of the VEVs is written as

$$\tan\beta = \frac{v_u}{v_d}. \tag{20}$$

The original Higgs doublets have eight freedom in total. Three of them are eaten by three electroweak bosons and five freedoms remain as physical Higgs fields. They consist of two CP-even natural scalar bosons h^0 and H^0, one CP-odd natural scalar boson A^0 and a charge +1 scalar boson H^+ and its conjugate charge -1 scalar boson H^-. The mass of each Higgs field is given as

$$m_{A^0}^2 = 2|\mu|^2 + m_{H_u}^2 + m_{H_d}^2, \tag{21}$$

$$m_{h^0,H^0}^2 = \frac{1}{2}\left(m_{A^0}^2 + m_Z^2 \mp \sqrt{\left(m_{A^0}^2 - m_Z^2\right)^2 + 4m_Z^2 m_{A^0}^2 \sin^2(2\beta)} \right), \tag{22}$$

$$m_{H^\pm}^2 = m_{A^0}^2 + m_W^2. \tag{23}$$

$|\mu|$ is obtained by the following relation:

$$m_Z^2 = \frac{|m_{H_d}^2 - m_{H_u}^2|}{\sqrt{1 - \sin^2(2\beta)}} - m_{H_u}^2 - m_{H_d}^2 - 2|\mu|^2. \tag{24}$$

Note that these Higgs masses are obtained at tree-level calculations. The radiative correction to the Higgs mass will be discussed in Section 1.4.5.

The superpartners of the Higgs bosons are called Higgsinos. The superpartners for the neutral components are denoted as $\tilde{H}_u$ and $\tilde{H}_d$, and those of the charged components are $\tilde{H}^+$ and $\tilde{H}^-$, respectively. The mass of Higgsinos is given by μ.

Gluino :

The superpartners of gluon is called gluino $\tilde{g}$. The mass of gluinos is represented as M_3 as shown in Eq 10.

Wino and Bino :

The superpartners of electroweak gauge bosons are called wino $\tilde{W}$ and bino $\tilde{B}$ (they are collectively-referred to as electroweak gauginos). The masses of winos and bino are given by M_2 and M_1, respectively.

The higgsinos and electroweak gauginos mix with each other because of the effects of electroweak symmetry breaking. Neutral higgsinos and neutral gauginos combine to form four mass eigenstates

called *neutralinos*. In the gauge-eigenstates basis $\Psi^0 = \left(\tilde{B}, \tilde{W}^0, \tilde{H}_d^0, \tilde{H}_u^0\right)$, the neutralino mass part of the Lagrangian is

$$\mathcal{L}_{\text{neutralino mass}} = \frac{1}{2}(\Psi^0)^T \mathbf{M}_{\tilde{N}} \Psi^0 + c.c., \tag{25}$$

where

$$\mathbf{M}_{\tilde{N}} = \begin{pmatrix} M_1 & 0 & -c_\beta s_W m_Z & s_\beta s_W m_Z \\ 0 & M_2 & c_\beta c_W m_Z & -s_\beta c_W m_Z \\ -c_\beta s_W m_Z & -c_\beta c_W m_Z & 0 & -\mu \\ s_\beta s_W m_Z & -s_\beta c_W m_Z & -\mu & 0 \end{pmatrix}. \tag{26}$$

Here we introduced abbreviations: $s_W = \sin\theta_W, c_W = \cos\theta_W$, $s_\beta = \sin\beta$ and $c_\beta = \cos\beta$.

The charged Higgsinos and winos mix in a similar way to form two mass eigenstates with charge ± 1, which are called *charginos*. In the gauge-eigenstate basis $\Psi^\pm = (\tilde{W}^\pm, \tilde{H}^\pm_{u/d})$, the chargino mass terms in the Lagrangian are

$$\mathcal{L}_{\text{chargino mass}} = -\frac{1}{2}(\Psi^\pm)^T \mathbf{M}_{\tilde{N}} \Psi^\pm + c.c. \tag{27}$$

with

$$\mathbf{M}_{\tilde{N}} = \begin{pmatrix} M_2 & \sqrt{2} s_\beta m_W \\ \sqrt{2} s_\beta m_W & \mu \end{pmatrix}. \tag{28}$$

We denote the neutralino and chargino mass eigenstates as $\tilde{\chi}_i^0$ $(i = 1, 2, 3, 4)$ and $\tilde{\chi}_i^\pm$ $(i = 1, 2)$. The labels are assigned so that $m_{\tilde{\chi}_1^0} < m_{\tilde{\chi}_2^0} < m_{\tilde{\chi}_3^0} < m_{\tilde{\chi}_4^0}$ and $m_{\tilde{\chi}_1^\pm} < m_{\tilde{\chi}_2^\pm}$.

Squark and Slepton :

Squarks $\tilde{q}$ are the superpartners of quarks. They have the same quantum numbers of the corresponding quarks except for spin and mass. They behave in the same way as their partners under gauge interactions. The superpartners of left-handed and right-handed quarks are written as $\tilde{q}_L$ and $\tilde{q}_R$. However, since sparticles do not have helicities, the handedness does not refer to its helicity but just specifies its quantum numbers. So, for example, only a left-handed squark $\tilde{q}_L$ couples to W bosons while a right-handed squark $\tilde{q}_R$ doesn't. With this notation, gauge interactions are consistent with their SM partners.

Similarly, sleptons $\tilde{l}$ are the superpartners of leptons. These superparticles also have the same quantum numbers as their SM partners except for spin and mass.

The masses of the first and second generation squarks and sleptons are calculated as follow assuming they have the same mass m_0 at the GUT scale,

$$\begin{array}{llllll} m^2_{\tilde{d}_L} & = m_0^2 & +K_3 & +K_2 & +\frac{1}{36}K_1 & +\Delta_{\tilde{d}_L}, \\ m^2_{\tilde{u}_L} & = m_0^2 & +K_3 & +K_2 & +\frac{1}{36}K_1 & +\Delta_{\tilde{u}_L}, \\ m^2_{\tilde{u}_R} & = m_0^2 & +K_3 & & +\frac{4}{9}K_1 & +\Delta_{\tilde{u}_R}, \\ m^2_{\tilde{d}_R} & = m_0^2 & +K_3 & & +\frac{1}{9}K_1 & +\Delta_{\tilde{d}_R}, \\ m^2_{\tilde{e}_L} & = m_0^2 & + & +K_2 & +\frac{1}{4}K_1 & +\Delta_{\tilde{e}_L}, \\ m^2_{\tilde{\nu}_e} & = m_0^2 & + & +K_2 & +\frac{1}{4}K_1 & +\Delta_{\tilde{\nu}}, \\ m^2_{\tilde{e}_R} & = m_0^2 & + & & +K_1 & +\Delta_{\tilde{e}_R}, \end{array} \tag{29}$$

K_3, K_2 and K_1 represent the contributions obtained during the renormalization group evolution, which are related to $\mathrm{SU}(3)_C$, $\mathrm{SU}(2)_L$ and $\mathrm{U}(1)_Y$ forces, respectively. Since left-handed squarks, $\tilde{d}_L, \tilde{u}_L$, feel all three forces, all the term contributes to their masses. Right-handed squarks, $\tilde{u}_R, \tilde{d}_R$, do not couple to $\mathrm{SU}(2)_L$ force, therefore K_2 term doesn't contribute. Left-handed sleptons, $\tilde{u}_R, \tilde{d}_R$,

do not interact with $SU(3)_C$ as they don't have color charges. Right-handed slepton, $\tilde{e}_R$, is the lightest among these particles since it feels only $U(1)_Y$ force through hypercharge Y.

The last term Δ_X represents a small contribution from the electroweak symmetry breaking [4]. We focus on the heavy particles for which this contribution is negligible.

Assuming the coupling constant unification occurs at $Q_0 = 2 \times 10^{16}$ GeV and fermion masses are unified at that energy scale, the following values are obtained at the electroweak scale:

$$K_1 \sim 0.15 m_{1/2}^2, \quad K_2 \sim 0.5 m_{1/2}^2, \quad K_3 \sim (4.5 - 6.5) m_{1/2}^2, \tag{30}$$

where $m_{1/2}$ is the unified mass of gauginos at the GUT scale.

Due to strong Yukawa couplings, masses of third generation squarks and sleptons take different forms. Here we take stop $\tilde{t}$ for example but the same discussion hold for sbottom and stau as well. Left- and right-handed stops are mixed by the interactions with the Higgs potential and the soft breaking term. We consider the terms which contributes to the following mass Lagrangian:

$$\mathcal{L}_{\text{stop masses}} = -\left(\tilde{t}_L^* \;\; \tilde{t}_R^*\right) \mathbf{m}_{\tilde{t}}^2 \begin{pmatrix} \tilde{t}_L \\ \tilde{t}_R \end{pmatrix}. \tag{31}$$

First, a contribution of the form $y_t^2 H_u^{0*} \tilde{t}_L^* \tilde{t}_L$ and $y_t^2 H_u^{0*} \tilde{t}_R^* \tilde{t}_R$ (the diagrams are shown in Fig. 5) contribute to the diagonal terms. At the VEV, $y_t H_u$ is equal to top mass, therefore this contribution gives a mass term proportional to the top mass m_t. Second, the diagram shown in Fig. 6 contributes to the off-diagonal term. This interaction is represented as $-\mu^* y_t (v \cos\beta) \tilde{t}_R^* \tilde{t}_L + c.c.$. The final contribution comes from the soft breaking term which is represented as $a_t (v \sin\beta) \tilde{t}_L \tilde{t}_R^* + c.c.$. This term contributes to the off-diagonal term as it mixes left- and right-handed stops.

Adding up these terms, we obtain the mass matrix of stops $\mathbf{m}_{\tilde{t}}^2$,

$$\mathbf{m}_{\tilde{t}}^2 = \begin{pmatrix} m_{Q_3}^2 + m_t^2 + \Delta_{\tilde{u}_L} & v(a_t^* \sin\beta - \mu y_t \cos\beta) \\ v(a_t^* \sin\beta - \mu y_t \cos\beta) & m_{\tilde{u}_3}^2 + m_t^2 + \Delta_{\tilde{u}_R} \end{pmatrix}. \tag{32}$$

In a similar way, one can obtain the mass matrix of sbottom in the gauge-eigenstate basis of $(\tilde{b}_L, \tilde{b}_R)$ with the right-handed squark mass of

$$\mathbf{m}_{\tilde{b}}^2 = \begin{pmatrix} m_{Q_3}^2 + \Delta_{\tilde{d}_L} & v(a_b^* \cos\beta - \mu y_b \sin\beta) \\ v(a_b^* \cos\beta - \mu^* y_b \sin\beta) & m_{\tilde{d}_3}^2 + \Delta_{\tilde{d}_R} \end{pmatrix}, \tag{33}$$

and the stau mass matrix in the gauge-eigenstate basis of $(\tilde{\tau}_L, \tilde{\tau}_R)$ is

$$\mathbf{m}_{\tilde{\tau}}^2 = \begin{pmatrix} m_{L_3}^2 + \Delta_{\tilde{e}_L} & v(a_\tau^* \cos\beta - \mu y_\tau \sin\beta) \\ v(a_\tau^* \cos\beta - \mu^* y_\tau \sin\beta) & m_{\tilde{e}_3}^2 + \Delta_{\tilde{e}_R} \end{pmatrix}. \tag{34}$$

The mass eigenstates are denoted as $\tilde{t}_1, \tilde{t}_2$, $\tilde{b}_1, \tilde{b}_2$, and $\tilde{\tau}_1, \tilde{\tau}_2$. The subscripts are defined so that $m_{\tilde{X}_1} < m_{\tilde{X}_2}$. The masses of third generation fermions at the electroweak scale, m_{Q_3}, $m_{\tilde{u}_3}$, $m_{\tilde{d}_3}$, m_{L_3}, and $m_{\tilde{e}_3}$, are summarized in Eq. (6.5.41)-(6.5.45) in Ref. [4].

1.4.3 R-parity

In MSSM, one needs to introduce a new symmetry in order to forbid the term which induces the baryon and lepton number violations. It is called R-parity P_R and written as

$$P_R = (-1)^{3(B-L)+2s}, \tag{35}$$

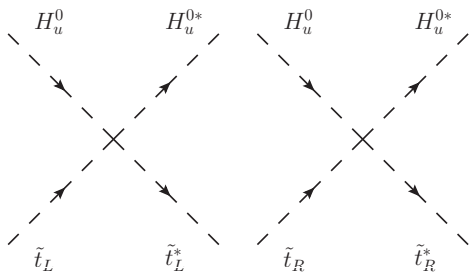

Figure 5: Interactions with the form of (scalar)^4. The coupling constant is proportional to y_t^2.

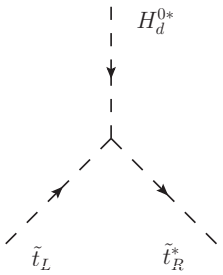

Figure 6: Interaction with the form of (scalar)^3. The coupling constant is proportional to $\mu^* y_t$.

where B and L are the baryon and lepton numbers, and s denotes the spin. P_R takes $+1$ for the SM particles and -1 for the SUSY partners. Models that violate R-parity are also possible if the resultant violations are well below experimental limits, but in this thesis only the R-parity conserving models are considered. As a result of R-parity conservation, SUSY particles must be produced in pairs and they decay to stable Lightest SUSY Particles (LSP).

1.4.4 Minimal supergravity model

The original 124 free parameters in the SUSY breaking Lagrangian are reduced down to a few parameters by the assumptions from experimental requirements such as Eq. 11 and Eq. 12. The number of parameters can be further reduced by introducing SUSY-breaking models.

The breaking is assumed to originate in the hidden sector, which is the collection of unobserved hypothetical particles that do not directly interact via the Standard Model gauge bosons, and the breaking effect is transferred to the MSSM sector by a specific mechanism. In Minimal Supergravity model (MSUGRA) or Constrained Supersymmetry model (CMSSM), gravity is thought to be the messenger that mediates the breaking. The parameters in MSUGRA/CMSSM model is reduced to 4 and one sign, which makes the model highly predictive.

m_0: All masses of squarks and sleptons are assumed to be universal at the GUT scale, which is represented by m_0.

$m_{1/2}$: All masses of gauginos are assumed to be universal at the GUT scale, which is represented by $m_{1/2}$. The following relationship holds for gaugino masses,

$$\frac{M_1}{\frac{5}{3}g'^2} = \frac{M_2}{g^2} = \frac{M_3}{g_S^2} = m_{1/2}. \tag{36}$$

At the electroweak scale, they are

$$\begin{aligned} M_1 &\sim 0.4 m_{1/2}, \\ M_2 &\sim 0.8 m_{1/2}, \\ M_3 &\sim 2.4 m_{1/2}. \end{aligned} \tag{37}$$

A_0**:** All trilinear couplings (Eq. 11) are common in this model.

$\tan\beta$**:** The ratio of VEVs of two Higgs bosons as defined in Eq. 20.

$sign(\mu)$**:** The sign of μ. The absolute value is determined through Eq. 24.

In most of the parameter space, there are two possible LSP candidates: $\tilde{\chi}_1^0$ and $\tilde{\tau}_1^{\pm}$. However, $\tilde{\tau}_1^{\pm}$ is usually forbidden as LSP should be neutral to be a dark matter candidate.

1.4.5 Discovery of the Higgs boson

The primary motivation of supersymmetry is to solve the quadrature divergence of the Higgs mass. This, in turn, sets limits on SUSY parameters [5]. Considering the recent results of the Higgs decay branches [6], the light neutral Higgs h^0 seems to have quite the same properties of the SM Higgs boson, which happens when h^0 is much lighter than the other Higgs particles. This configuration is referred to as "decoupling limit". In this limit, the Higgs mass with one-loop order correction is written as

$$m_h^2 \sim m_Z^2 \cos^2 2\beta + \frac{3}{(4\pi)^2}\frac{m_t^4}{v^2}\left[\ln\frac{m_{\tilde{t}}^2}{m_t^2} + \frac{X_t^2}{m_{\tilde{t}}^2}\left(1 - \frac{X_t^2}{12 m_{\tilde{t}}^2}\right)\right], \tag{38}$$

where $X_t = A_t - \mu\cot\beta$, which is the off-diagonal term of stop mass matrix in Eq. 32. Figure 7 shows the contours of m_h as a function of stop mass $m_{\tilde{t}}$ and the stop mixing parameter X_t for $\tan\beta = 20$. The red/blue bands show the Higgs mass range m_h = 124-126 GeV obtained by two different programs. The dotted lines show the degree of fine-tuning Δ, which is defined as the maximum sensitivity to fundamental parameters p_i,

$$\Delta \equiv \max_i \left|\frac{\partial \ln m_h^2}{\partial p_i}\right|. \tag{39}$$

The smallest fine-tuning is obtained when $|X_t| = \sqrt{6} m_{\tilde{t}}$, which is referred to as "maximal mixing". The parameters of MSUGRA/CMSSM sample used in the analysis are chosen so that this maximal mixing is realized. In this configuration, one of the stop masses becomes 20-30% lighter than the masses without mixing. As a result, stops are more likely to appear in decay chains, which increase the complexity of events.

The Higgs mass is also affected by a gluino mass through 2-loop order corrections [7, 8], which sets an limit on a gluino mass M_3:

$$M_3 \lesssim 900 \text{ GeV } \sin\beta \left(\frac{\log(\Lambda/\text{TeV})}{3}\right)^{-1} \left(\frac{m_h}{120 \text{ GeV}}\right) \left(\frac{\Delta^{-1}}{20\,\%}\right)^{-\frac{1}{2}}, \tag{40}$$

where Λ denotes the SUSY breaking scale. Allowing 10% fine-tuning, one finds the gluino mass should be below about 1.3 TeV. Although the limit varies depending on the fine-tuning condition, we safely expect that the gluino mass lies at $O(1)$ TeV and inside the LHC energy scale.

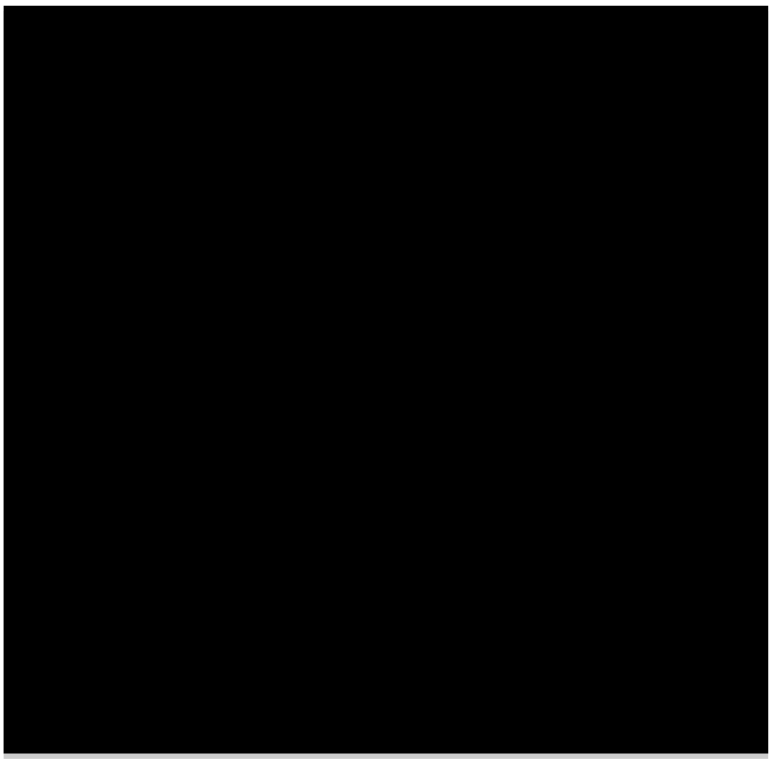

Figure 7: Contours of m_h in MSSM as a function of a common stop mass $m_{\tilde{t}}$ and the stop maxing parameter X_t for $\tan\beta = 20$. The red/blue bands show the Higgs mass range m_h = 124-126 GeV obtained by two different programs. The dotted lines show the degree of "fine-tuning". This plot is cited from Ref. [5].

2 LHC and ATLAS detector

2.1 Large Hadron Collider

The Large Hadron Collider (LHC) [9] was constructed to collide two proton beams with an unprecedented center-of-mass energy of 14 TeV and a luminosity of $10^{34}\,\mathrm{cm}^{-2}\,\mathrm{s}^{-1}$ aiming at an investigation of electroweak symmetry breaking and searches for the Higgs boson as well as physics beyond the Standard Model. During the data taking period in 2012, the accelerator was operating at a center-of-mass energy of 8 TeV with a peak luminosity of $7.73 \times 10^{33}\,\mathrm{cm}^{-2}\,\mathrm{s}^{-1}$. Figure 8 shows the peak luminosity recorded by ATLAS in 2012.

The beam circulating in the LHC ring is clustered to small chunks, called bunch, with a few cm in length and the transverse size of $O(10)\,\mu$m, containing approximately 1×10^{11} protons per bunch. The bunches make collisions at the center of the detectors every 50 ns, which is twice lower rate than the original design. This is due to the beam instability observed during the run and will be cured in the next data taking phase, giving the designed collision rate of 25 ns or 40 MHz. Table 1 summarizes the proton beam parameters of the LHC.

	Designed Parameters	Current Parameters
Proton Energy [GeV]	7000	4000
Number of Protons in a bunch	1.15×10^{11}	1×10^{11}
Number of Bunches in the ring	2808	1380
Peak luminosity [$\mathrm{cm}^{-2}\,\mathrm{sec}^{-1}$]	1.0×10^{34}	7.73×10^{33}
Bunch spacing [ns]	25	50

Table 1: Designed LHC beam parameters and the ones in 2012 data taking period.

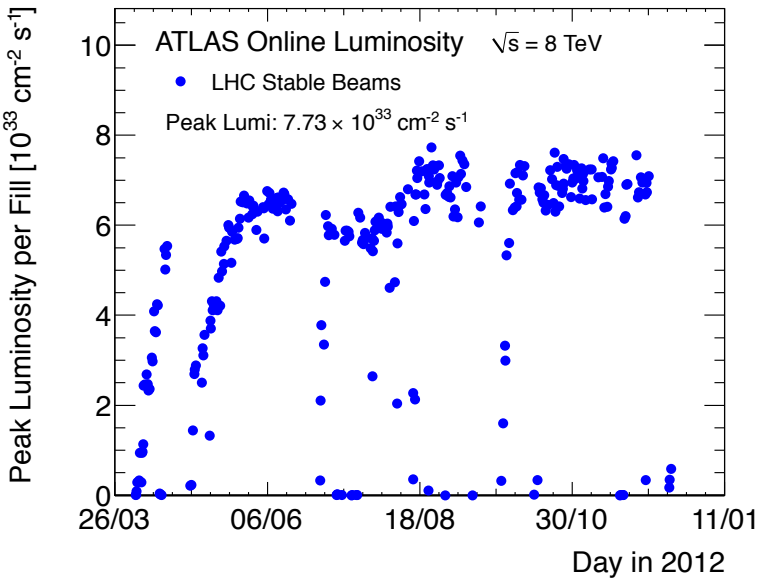

Figure 8: Peak luminosity recorded by the ATLAS detector per day in 2012.

The LHC is installed in the tunnel where LEP machine was originally placed. Total length of the tunnel is 26.7 km and the whole part lies about 100 m below the ground surface. The LHC uses super-

conducting magnets to bend 4 TeV beams. The original proton is produced from hydrogen gas by stripping the electron, then the proton is accelerated by LINAC2 to 50 MeV. The proton is fed to Proton Synchrotron Booster (BOOSTER) to obtain 1.4 GeV, and passed to the following accelerator, called Proton Synchrotron (PS), which accelerates the proton to 450 GeV, and finally, the 450 GeV proton is injected to the LHC. The LHC accelerates the proton to the target energy of the experiment.

There are four big experiments running in the LHC. ATLAS and CMS [10] are general-purpose detectors designed for studying Higgs boson and the physics beyond standard Model. LHCb [11] experiment studies B-physics, and ALICE [12] is dedicated to heavy ion collisions. Figure 9 shows the schematic overview of the LHC and four experiments.

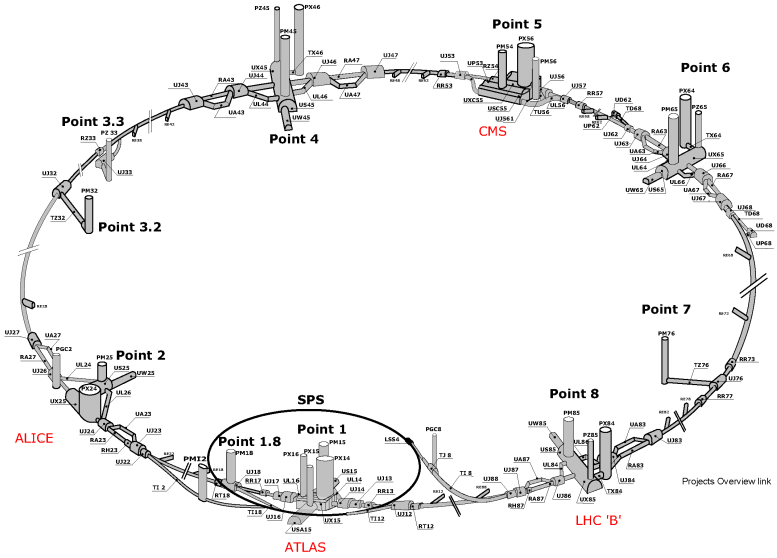

Figure 9: A schematic overview of LHC.

2.2 ATLAS detector

The ATLAS[2] experiment [13, 14, 15] is a general-purpose detector placed at the LHC. It is designed to study various types of physics signatures, which allows to discover the Higgs boson, extra dimensions and also supersymmetry. As opposed to CMS detector, which is also targeting new physics, the ALTAS detector is designed as huge as possible so as to measure the tracks precisely by making the most of the detector length or to minimize the escaping shower energy from the calorimeter. As a result, the ATLAS detector is 44 m along the beam axis and 22 m in diameter.

2.2.1 Coordinate system

The x-axis is defined as the direction of the center of LHC ring, and the y-axis points to the opposite direction from the center of the earth. A right-handed coordinate system is used in the ATLAS, therefore the z-axis points along the beam axis. A-side is defined as the part of ATLAS detector with positive z, and C-side is the opposite. Azimuthal angle ϕ and polar angle θ are defined in a usual way of the right-handed coordinate, so ϕ is the angle around the beam axis, starting from the direction of x-axis, and θ is the polar angle from z-axis.

Pseudo-rapidity η is defined using θ

$$\eta = -\ln\tan\left(\frac{\theta}{2}\right). \tag{41}$$

Pseudo-rapidity η is an approximation of the following rapidity y at the mass-less limit

$$y = \frac{1}{2}\ln\left(\frac{E + p_z}{E - p_z}\right), \tag{42}$$

where E is the energy of a given particle and p_z is the transverse momentum. Here, "transverse" is defined with respect to z-axis. The distance of given two objects ΔR is often used, which is defined as the square-sum of η and ϕ distances,

$$\Delta R = \sqrt{\Delta\eta^2 + \Delta\phi^2}. \tag{43}$$

2.2.2 Magnet system

The ATLAS magnet system consists of four super-conducting magnets. One solenoid magnet is immersed inside the detector and two toroidal magnets placed at the end-cap of A and C-sides. The last big toroidal magnet is placed outermost of the detector around the barrel.

The solenoid magnet is aligned to the beam axis and provides a 2 Tesla axial magnetic field. The magnetic field bends the tracks of charged particles in the inner detector, which allows to measure the momentum from the sagitta of tracks. A 5.8 m length solenoid is placed just inside of LAr calorimeter, which measures the energy of electron, photon and jets, so the material thickness is minimized as much as possible. A single layer coil made of Al-stabilized NbTi conductor is placed in the inner wall of the LAr calorimeter. The inner and outer diameters of the solenoid magnet is 2.46 m and 2.56 m, which corresponds to ~0.66 radiation length at normal incidence. The return flux of the magnet is guided by the hadronic calorimeter to minimize the leakage to the muon spectrometer.

One barrel toroidal and two end-cap toroidal magnets produce toroidal magnetic field of approximately 0.5 Tesla and 1 Tesla for the muon spectrometers in the barrel and in the end-cap regions, respectively. Figure 10 shows the schematic view of all the magnetic systems. The barrel toroid consists of eight coils encased in individual racetrack-shaped, stainless-steel vacuum vessels. The overall size of the

[2] ATLAS is an acronym of A Toroidal LHC ApparatuS

barrel toroid system is 25.3 m in length along the beam axis, with the inner and outer diameters of 9.4 m and 20.1 m. Each end-cap toroid consists of a single cold mass build up from eight flat, square coil units and eight keystone wedges, bolted together into a rigid structure. Both of the end-cap and barrel toroids are build up with the same materials and coil structures: pure Al-stabilized Nb/Ti/Cu conductor with a pancake-shape in section.

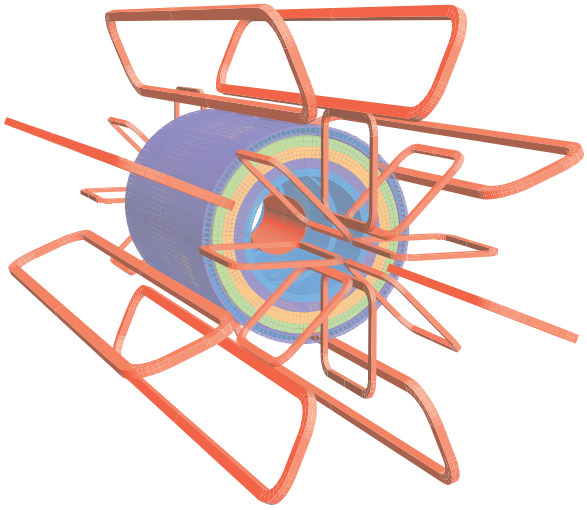

Figure 10: Schematic overview of the magnet system of ATLAS.

2.2.3 Tracking system

In the ATLAS detector, "tracking system" usually means the inner detectors (ID) without including outermost muon spectrometer (MS). The inner detectors consist of three different detectors as shown in Fig.11:

Pixel detector : The pixel detector locates the innermost layer, only 5 cm away from the beam. It consists of 1744 silicon pixel modules and each has pixel sensors of $50 \times 400\,\mu$m along ϕ and z-axis. The intrinsic resolution in the barrel is $10\,\mu$m $(r-\phi)$ and $115\,\mu$m (z), and, in the end-cap disks, it is $10\,\mu$m $(r-\phi)$ and $115\,\mu$m (r).

Silicon micro-strip detector (SCT): Silicon micro-strip detector is often called as SCT, which is the abbreviation of Semiconductor Tracker. One SCT module consists of one pairs of 6.4 cm-length layers on which single-sided silicon micro-strip sensors are placed. Each micro-strip sensor layer has strip sensors with a mean pitch of $80\,\mu$m. Two strip layers are glued slightly off-aligned by ± 20 m radian around the geometrical center as shown in Fig. 12, which gives the detector a sensitivity to the z-position of hits.

Transition Radiation Tracker (TRT) : TRT locates the outside of SCT system, which consists of 4 mm diameter straw tubes. The straw tube is filled with Xe gas (70 %) and some CO_2, O_2 gas (27 % and 3 %, respectively) as quencher gas. Each straw tube has a thin wire at the center and a high voltage is applied between the wire and tube. The gaps of the straw tubes are stuffed with fibers made of polypropylene or polyethylene.

TRT detects the passage of a charged particles in two ways. One is by detecting the ionization of gas, and one is by detecting the transition radiation which is produced when a charged particle

passes the polymer fibers. Since transition radiation is emitted only from electrons and drops large energy when absorbed by gas, TRT is able to discriminate electrons from the other charged particles by setting an appropriate energy threshold.

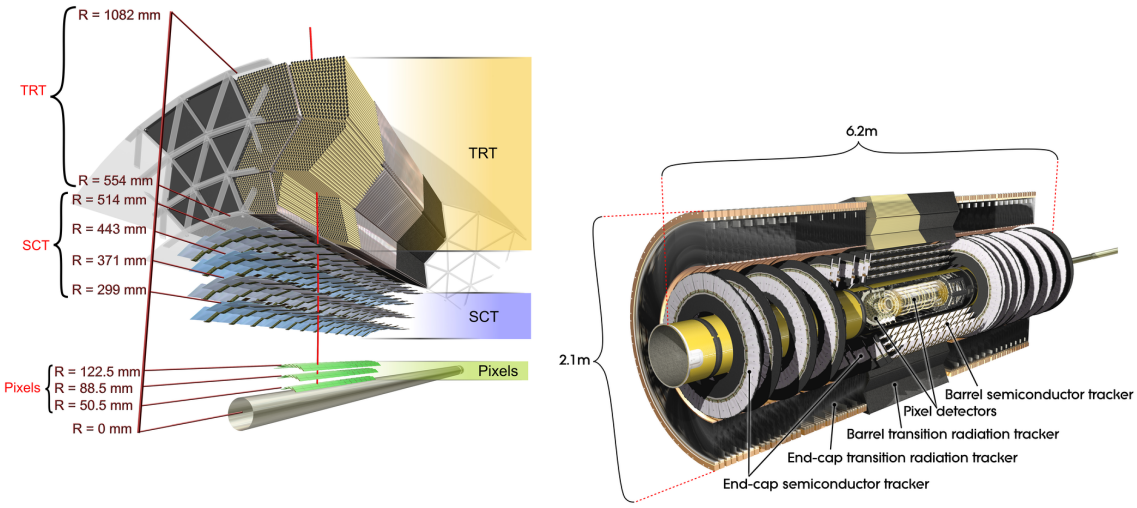

Figure 11: Schematic overviews of tracking system. Left plot shows the cross-section and right plot gives the bird-eye view.

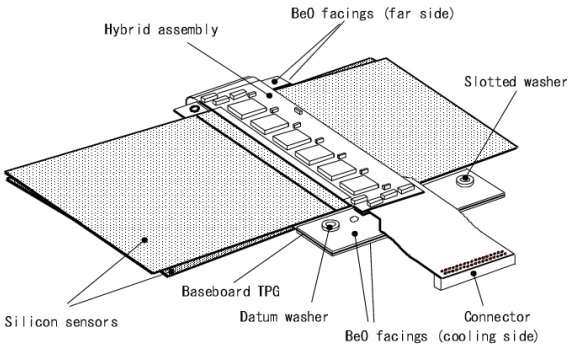

Figure 12: Illustration of SCT.

2.2.4 Calorimeter system

The ATLAS calorimeters cover the range of $|\eta| < 4.9$. Fine granularity electromagnetic (EM) calorimeters are used for the precise measurement of electrons and photons. Hadron calorimeters are made with rather coarser granularity but are sufficient for their primary purpose, jet reconstruction. Figure 13 shows the ATLAS calorimeter system and more details of Tile calorimeter are documented in Appendix I.

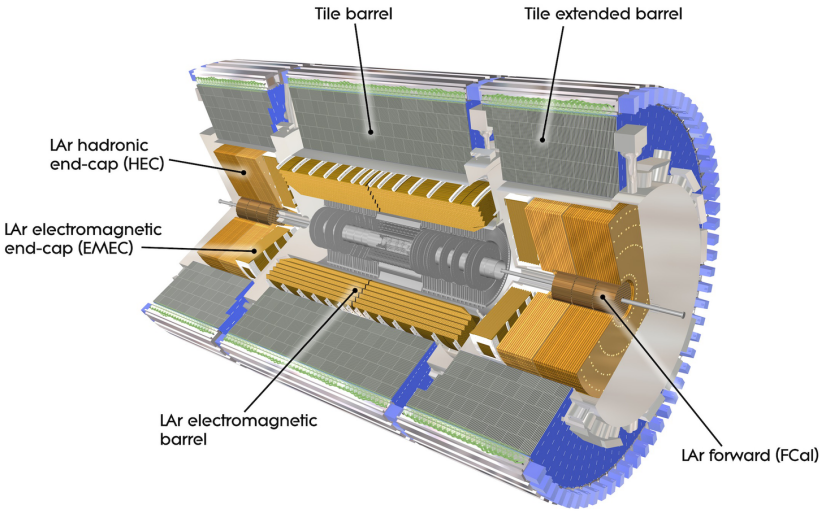

Figure 13: Schematic overview of ATLAS Calorimeter system.

EM calorimeter EM calorimeter is divided into barrel part ($|\eta| < 1.475$) and two end-cap parts ($1.375 < |\eta| < 3.2$). EM calorimeter is Lead-LAr detector with accordion-shaped kapton electrodes and lead absorber plates over its full coverage. Figure 14 shows a sketch of EM calorimeter in the barrel region. EM calorimeter is constructed from three layers in radial direction. Additional pre-sampler detector is placed in $|\eta| < 1.8$, which consists of an active LAr layer of 1.1 cm (0.5 cm) thick in the barrel (end-cap) region. It is used to correct the energy loss in upstream material.

Tile calorimeter Tile calorimeter is placed outside of EM calorimeter in the barrel region. The central barrel part covers $|\eta| < 1.0$ and two extended barrels cover $0.8 < |\eta| < 1.7$. Tile calorimeter collects shower energy using 14 mm thick steel plates as absorber and 3 mm thick scintillating tiles as active material. It is longitudinally segmented in three layers approximately 1.5, 4.1 and 1.8 interaction length thick for the barrel and 1.5, 2.6 and 3.3 interaction length for the extended barrel. Two sides of the scintillating tiles are read out by wavelength shifting fibers into two separate photo-multiplier tubes.

LAr hadronic end-cap calorimeter Hadronic end-cap calorimeter (HEC) consists of two independent wheels in each end-cap behind the end-cap EM calorimeter. To reduce the drop in material density in the transition part between the end-cap and the forward calorimeter around $|\eta| = 3.1$, HEC extends out to $|\eta| = 3.2$. Also HEC covers up to $|\eta| < 1.5$ in the barrel region and slightly overlaps with the barrel tile calorimeter which covers $|\eta| < 1.7$. Each wheel has four layers. The innermost layer is built from 25 mm parallel copper plates, while the outer layers use 50 mm copper plates, interleaved with 8.5 mm LAr gaps as the active medium.

LAr forward calorimeter Forward calorimeter (FCal) is integrated into the end-cap cryostat covering the range of $3.1 < |\eta| < 4.9$. FCal is approximately 10 interaction lengths deep and consists of three modules in each end-cap. The first module is made of copper optimized for electromagnetic measurements. The other two are made of tungsten for hadronic interaction measurements. Liquid argon is used as the sensitive medium. In order to reduce the amount of neutrons reflected into the inner detector cavity, the front face of the FCal is recessed by about 1.2 m with respect to the EM calorimeter front face.

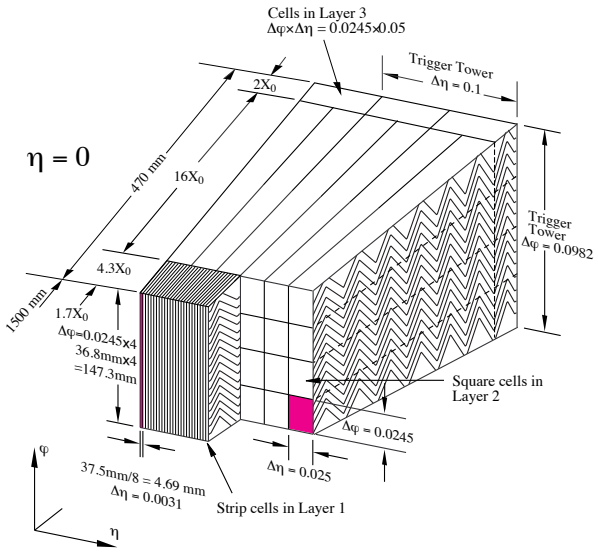

Figure 14: Expanded view of EM calorimeter. The magenta square shows the minimum unit size of EM calorimeter.

2.2.5 Muon system

The ATLAS muon system measures muon momentum using the magnetic deflection of muon tracks in the super-conducting air-core toroid magnets. Over the range of $|\eta| < 1.4$, magnetic field is provided by the barrel toroid. For $1.6 < |\eta| < 2.7$, muon tracks are bent by the two end-cap magnets inserted into both ends of the barrel toroid. Between these regions, $1.4 < |\eta| < 1.6$, the magnetic field is provided by a combination of barrel and end-cap magnets. Four types of muon chambers are used for the measurement of muon hit positions. Figure 15 shows the layout of the muon system.

Monitored Drift Tubes (MDT) measure the track properties precisely in the range of $|\eta| < 2.7$ ($|\eta| < 2.0$ for the innermost plane). These chambers consist of three or four layers of drift tubes, which achieve an average resolution of 80 μm per tube or about 3 μm per chamber. In the center of the detector ($|\eta| \sim 0$), a gap in chamber coverage is left open for service. Cathode Strip Chambers (CSC), which are multi-wire proportional chambers with cathodes segmented into strips, are used in the innermost plane of $2.0 < |\eta| < 2.7$ for additional precise track measurement. The resolution of chamber is 40 μm in the bending plane and about 5 mm in the transverse plane.

The muon trigger system consists of Resistive Plate Chambers (RPC) and Thin Gap Chambers (TGC) covering $|\eta| < 1.05$ and $1.05 < |\eta| < 2.4$, respectively. RPC consist of three concentric cylindrical layers around the beam axis, referred to as trigger stations. Each station further consists of two independent detector layers, each measuring η and ϕ. TGC are multi-wire proportional chambers with the wire-to-wire distance of 1.8 mm. TGC are also used to determine azimuthal positions to complement the measurement of MDT in the bending direction.

2.2.6 Trigger system

The ATLAS experiment is designed to receive data at 40 MHz but the data acquisition system can only commit data to permanent storage at the rate of a few hundred Hz. To select "interesting" events from the large number of incoming events, trigger system are made up of three layers, Level1 (L1), Level2 (L2) and event filter (EF). L1 trigger searches for high transverse momentum muons, electrons, photons, jets, τ-leptons decaying into hadrons, large missing and total transverse energy. In each event, L1 trigger

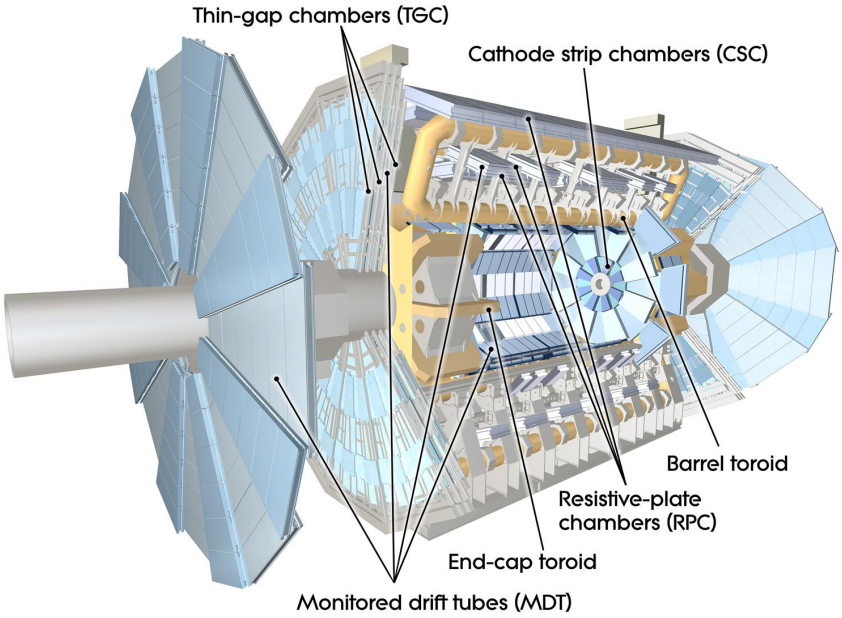

Figure 15: Overview of Muon Spectrometer system.

defines one or more Regions-of-Interest (RoI) which is the geometrical coordinate in η and ϕ where an interesting feature is found. The maximum acceptable L1 rate is 75 kHz and the L1 decision must reach the front-end electronics within 2.5 μs after the bunch-crossing to tell the front-end electronics whether the event stored in the buffer should be read or discarded. L2 trigger is seeded by the RoI information provided by L1 trigger. Taking longer time to process data, L2 trigger analyses the events in more detail for further reduction of trigger rate. L2 trigger is designed to reduce the trigger rate to approximately 3.5 kHz within an event processing time of about 40 ms in average. EF trigger reduces the event rate to roughly 200 Hz, reconstructing the objects with almost the same definitions as the offline analyses and determine the event to be stored.

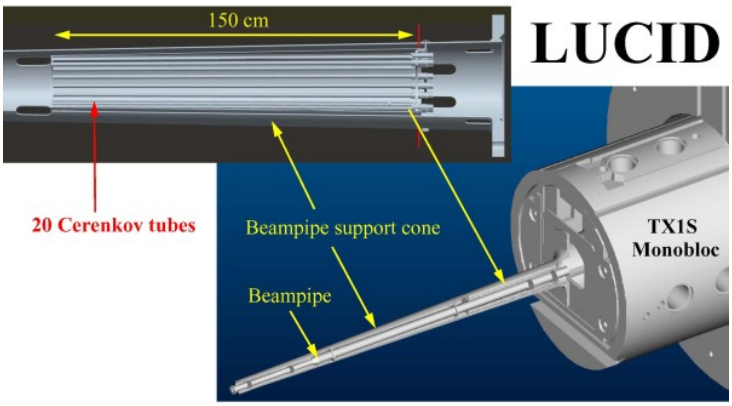

Figure 16: Cut-away view of LUCID detector.

2.2.7 Luminosity detectors

There prepared several methods and detectors to measure the luminosity in ATLAS. LUCID (Luminosity measurement using a Cerenkov Integrating Detectors) is one of such detectors. LUCID are located on each side of the interaction point (IP) at a distance of 17 m, covering the pseudo-rapidity range of $5.6 < |\eta| < 6.0$. LUCID are made of aluminum tubes filled with C_4F_{10} gas and surrounds the beam-pipe as shown in Fig. 16 (top left). By counting the Cerenkov photons radiated by the high energy charged particles along the beam axis, which are produced by inelastic collisions of protons, it measures the integrated luminosity and provide online monitoring of the instantaneous luminosity and beam conditions. Four Beam Current Transformers (BCT) placed per LHC ring [16] directly measure the beam current. Four BDT consists of two DC current transformers (DCCT) and two fast beam current transformers (FBCT). FBCT has a higher time resolution enough to measure the charge in each bunch separately, while CDDT can measure only the averaged beam current. The luminosity is estimated using the beam profile information, which will be discussed in Section 4.1.1.

3 Object reconstruction and definition

Leptonic supersymmetry search employs many types of objects, such as jets, electrons, muons and missing transverse momentum, whose definitions are discussed in this section. The object definitions used in the analysis are all following the ATLAS-default recommendations.

3.1 Track

Tracks are primarily used to determine the point of proton-proton collision, which is called Primary Vertex (PV). One bunch crossing usually contains one hard and several pile-up collisions, which accompanies many outgoing objects. The primary vertex candidate with the largest track p_{T} sum is chosen as the Primary Vertex of hard collision. A distance from the Primary Vertex is a good quantity to classify an object to hard collision products or not. Heavy flavor hadrons with long life time often make vertices away from a Primary Vertex, which are called Secondary Vertex. Secondary Vertex is identified in track reconstruction procedure and used to tag b-jets. Reconstructed tracks are also used in the following object definitions of electron, muon and jets. Tracks with p_{T}>0.4 GeV and $|\eta| < 2.5$ are reconstructed as baseline tracks.

3.2 Jet

Particle in a jet create showers in the calorimeter, which are called "clusters". Jet reconstruction procedure starts from finding clusters, then determines the cluster types by their shape information and apply appropriate energy calibrations. The clusters are summed up to form jets and, finally, calibrated again so that the jet energy matches to that of the original parton.

3.2.1 Clustering

Clusters are reconstructed by Topo-cluster algorithm [17]. Clustering starts with finding one "seed cell" which is defined as a cell with at least four times higher energy than noise level σ_{Noise}. Here σ_{Noise} is defined as root-mean-square of the noise distribution. The adjacent cells with energy E_{cell} are added up to the seed cell if $E_{\mathrm{cell}} > \sigma_{\mathrm{Noise}}$ is satisfied, forming a cluster. This process is repeated to sum up all the cells until there are no more adjacent cells with $E_{\mathrm{cell}} > 2\sigma_{\mathrm{Noise}}$. Finally, one layer of the neighborhood cells are included to the cluster to sum up the shower leakage. No energy threshold is considered in the last step. Center of cluster is calculated by the weighted average of cells.

3.2.2 Classification

The raw cluster energy is called EM-scale energy, which is calibrated to gives a good estimation for electromagnetic shower. For hadronic shower, EM-scale energy is not correct due to the missing energy carried out by neutrons and neutrinos. Hadronic clusters need to be calibrated to compensate the missing energy. Clusters are classified to EM-like, Hadron-like or unknown, based on the following variables:

F_{EM} : Fraction of the energy deposit in EM calorimeter over the total energy, i.e. $F = E_{\mathrm{EM}}/E_{\mathrm{total}}$.

λ : Cluster barycenter depth in the calorimeter.

ρ : Average cell density weighted by cell energy.

Cluster energies are then multiplied by a calibration constant estimated using Monte Carlo. Calibration constants includes the following corrections to compensate instrumental effects:

Out-Of-Cluster correction : Some fraction of the shower energy escapes from the active region at its tail. This correction is applied to recover the lost energy.

Dead material correction : This correction compensates the energy deposit outside of the active regions of LAr and Tile calorimeters. Also the lost energy in upstream materials, such as the inner detector, magnetic coils and cryostat walls are recovered.

3.2.3 Jet finding

Calibrated clusters are then summed up to form jets [18] using anti-k_T algorithm [19] with a distance parameter $R = 0.4$. Anti-k_T algorithm is infrared safe to all orders in perturbative QCD [20] and also robust against pile-up as it starts summing constituents up from higher momentum. In the algorithm, two types of distances are defined:

$$d_{ij} = \min(k_{ti}^{2p}, k_{tj}^{2p}) \cdot \frac{(y_i - y_j)^2 + (\phi_i - \phi_j)^2}{R^2}, \quad (44)$$

$$d_{iB} = k_{ti}^{2p}, \quad (45)$$

where p is the parameter which governs the relative power of energy versus geometrical scales. $p = -1$ is chosen in anti-k_T algorithm, thus it has a prefix of "anti-". i, j runs over all cluster objects. The pair of clusters which has the minimum d_{ij} are summed up to make a new object. After including the new object into the list of clusters and removing the original two objects, all d_{ij} and d_{iB} are recalculated. This procedure continues until one of d_{iB} becomes the smallest than the others. Then object i is removed from the object list, classified as a jet. This process continues until all clusters are removed from the list.

3.2.4 Calibration

A method called Jet Energy Scale (JES) calibration [21] is applied to jets. Calibration constants are determined as a function of p_{T} and η using Monte Carlo so that p_{T} of reconstructed jet matches to the corresponding true parton p_{T}.

As a confirmation of the calibration, differences between data and Monte Carlo simulation are assessed using *in-situ* techniques exploiting the transverse momentum balance between a jet and a well measured reference object. First, the p_{T} balance between a central and a forward jet in the events having only two jets is selected to check the equality of jet response in large η region. After removing η dependence, p_{T} of a photon or Z boson decaying to electrons or muons is used as a reference to check the calibration within $|\eta| < 1.2$. Finally, the events in which low-p_{T} jets are recoiled against a high p_{T} jet are used to check the jet response in TeV regime. In this measurement, the low-p_{T} jets are limited within $|\eta| < 2.8$ while the leading jet is required to be within $|\eta| < 1.2$.

The residual of Jet Energy Scale calibration evaluated by the combination of these *in-situ* techniques is shown in Fig. 17, together with statistical and systematic uncertainties. All the measurements show consistent results and the maximum discrepancy is 3% in p_{T}>1 TeV. The total uncertainty is 3% at the maximum. Including additional uncertainties due to pile-up and flavor response, a fractional uncertainty <2.5% is obtained for central jets with $p_{\mathrm{T}} > 100$ GeV as shown in Fig. 18 (left). The plot on the right shows the η dependence of JES uncertainty for jet with $p_{\mathrm{T}} = 40$ GeV.

3.2.5 Pileup suppression

Low p_{T} particles from multiple soft collisions (pile-up) increase the calorimeter activity and shift jet energies. To remove the energy shift, a pile-up correction has been developed based on the idea that noise (pile-up) has a lower energy density than signal jets [22]. "Median p_{T} density" ρ, is defined as

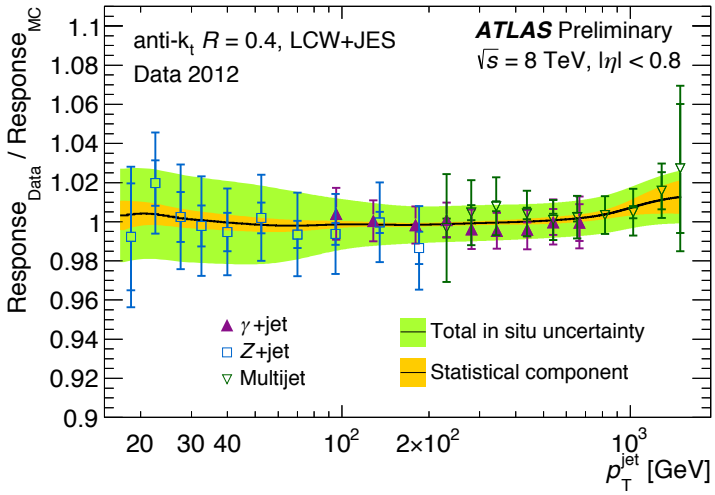

Figure 17: Residual of JES calibration obtained from the combination of the *in-situ* techniques with statistical and systematic uncertainties. This plot is cited from Ref. [21].

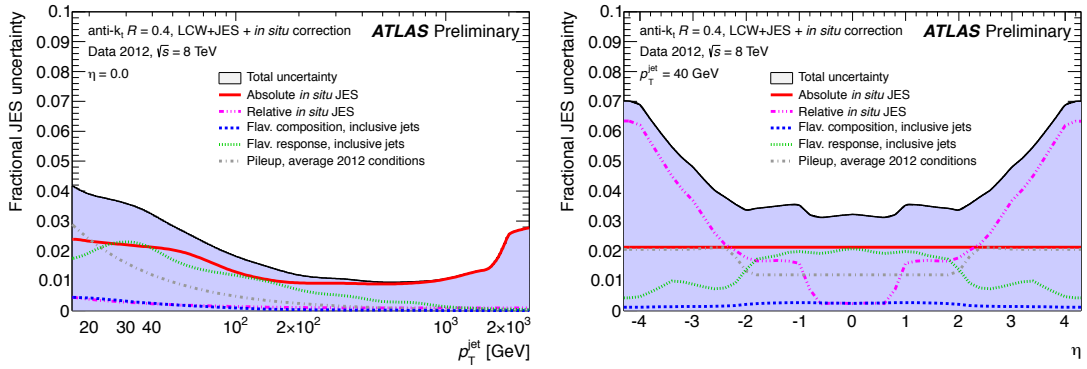

Figure 18: JES and additional uncertainties due to pile-up, flavor response and composition for central jets (left) and for jets with p_{T}=40 GeV (right). These plots are cited from Ref. [21].

the median of $p_T^{\mathrm{jet}}/A^{\mathrm{jet}}$ of all the jets. Here, A^{jet} is the geometrical area of a jet which is determined jet by jet by adding up all the clusters involved. The number of pile-up jets is much larger than jets from a hard collision, therefore the median is mainly determined by pile-up jets without a significant bias. Figure 19 (left) illustrates that ρ increases with the number of primary vertex per bunch crossing N_{PV}. ρ provides a direct estimate of the global pile-up activity in any given event, while A^{jet} provides an estimate of a jet's sensitivity to pileup. By multiplying these two quantities, an estimate of the effects of pile-up is obtained. Subtracting this estimate from the original jet p_{T} permits to reduce the dependence on pile-up:

$$p_T^{\mathrm{jet,corr}} = p_T^{\mathrm{jet}} - \rho \times A^{\mathrm{jet}}. \tag{46}$$

Figure 19 (right) shows the root-mean-square of $(p_{\mathrm{T}}^{\mathrm{jet,corr}} - p_{\mathrm{T}}^{\mathrm{true}})$ as a function of the average number of pileup interactions per bunch crossing $\langle\mu\rangle$. The impact of pile-up on jet p_{T} is evident from the linear rise observed in the uncorrected points. Compared to the previous offset correction method [23] based on $\langle\mu\rangle$ and N_{PV} used in 2011, the jet area method further mitigates the degradation in jet p_{T} resolution.

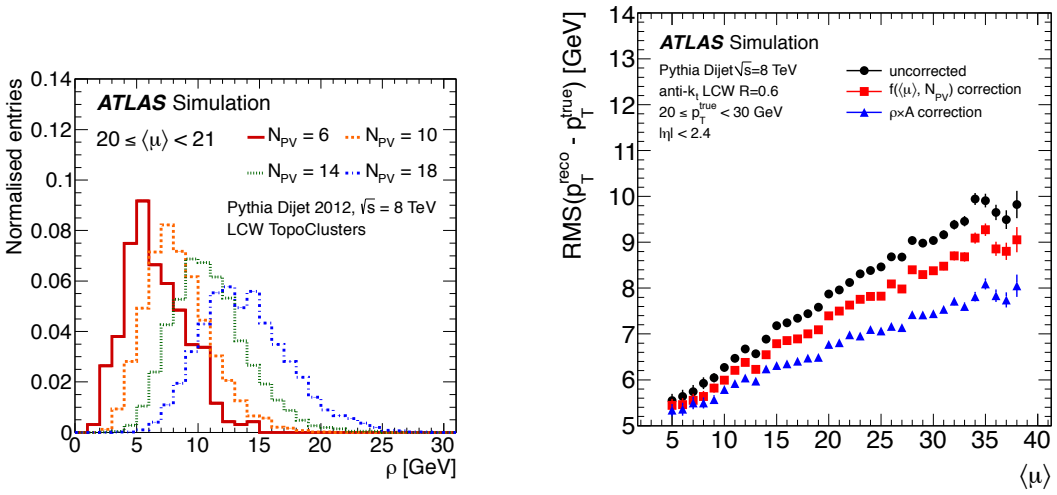

Figure 19: (Left) ρ distribution for four representative values of the reconstructed Primary Vertex multiplicity N_{PV}. (Right) Root-mean-square width of the distributions of $(p_{\mathrm{T}}^{\mathrm{reco}} - p_{\mathrm{T}}^{\mathrm{true}})$ for anti-k_T (R=0.6) jets. These plots are cited from Ref. [22].

3.2.6 *b*-tagging

Several tagging algorithms have been invented for better *b*-tagging efficiency. A method based on neural-network, `MV1`, which combines the inputs from `IP3D`, `SV1` and `JetFitter`, is used to improve purity and efficiency.

`IP3D` [24] is the tagging algorithm using the likelihood technique in which input variables are compared with pre-defined distributions for both *b*- and light-jet hypotheses, obtained from Monte Carlo simulation. The signed transverse impact parameter significance and the longitudinal impact parameter significance, along with their correlation, are used as the input parameters.

`SV1` [24] is also an algorithm based on the likelihood technique, but using reconstructed Secondary Vertex information. It uses ΔR between a jet and a *b*-hadron, and the number of two-track vertices. Also, the combined two-dimensional information of the Secondary Vertex mass and the energy fraction of the Secondary Vertex with respect to the total tracks are employed.

These methods have a drawback of giving a bad tagging efficiency in case a long-lived hadron is emitted from the decay as these methods assume only one Secondary Vertex. `JetFitter` [25] takes the decay of long-lived hadrons into consideration under the assumption that the long-lived hadron decays occur on the flight axis of the initial *b*-hadron. The separation between *b*-, *c*- and light-jets is performed based on the likelihood method.

`MV1` algorithm combines the results from these methods using a neural-network. As the tagging efficiency is not critical in our analysis, we use a moderate working point at which 60% of *b*-jets are tagged. At this working point, light-jet rejection factor of 577, *c*-jet rejection factor of 8 and tau-jet rejection factor of 23 are obtained, respectively[3]. The discrepancy of the tagging efficiency between data and Monte Carlo is corrected by applying a scale factor.

[3]The rejection factor is defined as the number of jets out of which one jet is mis-tagged as a *b*-jet.

3.2.7 Object definition

Jet candidates defined in the previous section may contain "fake" jets. Here we apply further cleanings to define sets of genuine jets that are used in the analysis. Fake jets, such as cosmic muons, noise in the detector electronics and the particles not originating from the proton collision, are eliminated as follow.

- Pulse shapes of calorimeters are monitored for all jets. If the shape differs from the usual one, the jet may be a noise and is judged as a fake jet.
- The baseline voltage of LAr electronics takes some time to settle to the usual level after incoming of a jet. Instability of baseline voltage makes negative energy cells and if the total negative energy is sizable, the jet is tagged as a fake jet.
- The energy fraction of a radial layer in the total jet energy should be smaller than a specific threshold. If one layer has a significant fraction of the energy, it may be a fake jet produced by a scrapping particle, flying into the detector parallel to the beam axis.

Next, electron showers, which are also reconstructed as jets, are removed. Jet within $\Delta R < 0.2$ from preselected electrons (defined in Table 4 for Hard electron and Table 5 for Soft electron) are removed.

Finally, we define four types of jets: signal jets, b-jets, $E_{\mathrm{T}}^{\mathrm{miss}}$ jets and overlap removal jets. Signal jets are the ones on which our kinematic selections are applied. b-tagging is checked for signal jets with 60% efficiency working point to define b-jets. $E_{\mathrm{T}}^{\mathrm{miss}}$ jets are the collection of jets with $|\eta| < 2.5$ and p_{T}>20 GeV, which are defined to calculate $E_{\mathrm{T}}^{\mathrm{miss}}$ [4]. Overlap removal jets are defined to be used in the lepton isolation check, which will be discussed in Section 3.3.4. Table 2 summarizes their definitions.

Cut	Value/description			
Jet Type	overlap removal	$E_{\mathrm{T}}^{\mathrm{miss}}$	signal	b-jet
Acceptance	$p_{\mathrm{T}} > 20$ GeV		$p_{\mathrm{T}} > 30$ GeV	
	No limit on $\|\eta\|$	$\|\eta\| < 2.5$		
Overlap	$\Delta R(\mathrm{jet}, e) > 0.2$			
Other	–		`MV1` with 60% efficiency working point	

Table 2: Summary of the jet selection criteria.

3.3 Electron

Electron reconstruction [26] starts from clustering electromagnetic calorimeter cells and then the cluster is matched to an inner detector track. As jets contain many tracks and calorimeter activities, raw electron candidates contain many "fake" electrons from jets, which are rejected by requiring additional quality selections such as Bremsstrahlung radiations in TRT and the absence of hadronic activity. Then we define several sets of electrons which are used in the following analysis.

3.3.1 Cluster reconstruction

Electron reconstruction begins with forming a seed cluster. A method called sliding window algorithm [17] with a window size of 3×5 in $\eta \times \phi$ middle layer cell units (0.025×0.025), finds a seed cluster with energy above 2.5 GeV.

[4] Note that clusters between $2.5 < |\eta| < 4.9$ are included in $E_{\mathrm{T}}^{\mathrm{miss}}$ calculation as Soft term, which will be mentioned in Section 3.5.

3.3.2 Track-to-cluster matching

Reconstructed tracks are matched to seed clusters by extrapolating to the second layer of calorimeter. The impact point are then compared to the corresponding seed cluster position. If several tracks match to the same cluster, the tracks that have SCT hits are preferred and the one with the smallest ΔR to the seed cluster survives. After track-to-cluster matching, cluster energy is recomputed with 3×7 (5×5) sliding window in the barrel (end-cap). Finally, four-momentum is computed using the track and cluster information. Energy information is taken from the cluster and the direction is taken from the track when there are more than 3 hits in TRT and silicon tracker, otherwise the cluster η and ϕ are used.

3.3.3 Further improvements

Reconstructed electrons are then checked if they pass a set of identification selections to obtain a maximum rejection of fake electrons. Three identification criteria are defined: `Loose++`, `Medium++` and `Tight++`, as listed in Table 3. All electrons are required to pass `Medium++` condition in both Soft and Hard lepton analyses.

`Medium++` electron, for example, requires the absence of hadron activities at the tail of showers. Also it checks whether Bremsstrahlung radiations occurred in TRT, which gives an useful information to discriminate electrons from other heavier particles, such as pion. `Tight++` selection further requires a consistency between the track momentum and cluster energy, which reduces an accidental match of tracks and clusters.

3.3.4 Hard electron definition

If one finds an electron nearby a jet, the electron is likely to be the decay product of a hadron in the jet. Such "fake leptons" should be rejected to reduce the QCD multi-jet background. Therefore, if an electron is close to the overlap removal jet (defined in Section 3.2.7) within $\Delta R < 0.4$, the electron is vetoed.

Then the following types of electrons are defined: $E_{\mathrm{T}}^{\mathrm{miss}}$ electron, preselected electron, crack electron, loose electron and signal electron. $E_{\mathrm{T}}^{\mathrm{miss}}$ electrons are used in $E_{\mathrm{T}}^{\mathrm{miss}}$ calculation in Section 3.5. The electrons with p_{T}>10 GeV and $|\eta| < 2.47$ are taken into $E_{\mathrm{T}}^{\mathrm{miss}}$ calculation. Preselected electrons are used for vetoing the events with a second lepton. As will be discussed in Section 5, a second lepton increases full-leptonic decay of $t\bar{t}$ background and leads to a sensitivity loss. To veto such events, preselected electrons are defined as loose as possible. Crack electrons are defined as the electrons falling into the crack region of the calorimeter ($1.37 < |\eta| < 1.52$), where the barrel and endcap calorimeters intersect. A large correction is needed for an electron to compensate the energy loss in the crack region, which introduces a huge uncertainty on the reconstructed energy. As crack electrons worsen $E_{\mathrm{T}}^{\mathrm{miss}}$ resolution and increases backgrounds in our signal region, we veto the events with at least one crack electron. Loose electrons are defined to make a fake-enriched region to estimate the QCD multi-jet background (detail will be discussed in Section 6.1). In the electron channel, the leading lepton should pass signal electron selection. Signal electron selection is designed to reduce the QCD multi-jet background by requiring `Tight++` quality selection. In addition, the following track isolation is required:

$$\texttt{ptcone20}/p_{\mathrm{T}} < 0.10, \tag{47}$$

where `ptcone20` is the sum of track momentum within $\Delta R < 0.2$ from the electron track (the electron track itself is not included). Fake electrons stemmed from jets may accompany many charged hadron tracks, therefore, this condition greatly reduce fake electrons. To further reduce the fake electrons from heavy flavor hadrons, the radial distance between the track and Primary Vertex d_0^{PV} is required to be smaller than 1 mm. Also the distance along the beam axis z_0^{PV} should be smaller than 2 mm, which

Type	Description
`Loose++`	
Hadronic leakage	Ratio of E_T in the first sampling of the hadronic calorimeter to E_T of the EM cluster.
Middle layer of EM calorimeter	Ratio in η of cell energies in 3×7 versus 7×7 cells. Ratio in ϕ of cell energies in 3×3 versus 3×7 cells. Lateral width of the shower. Lateral shower width, $\sqrt{(\sum E_i \eta_i^2)/(\sum E_i) - ((\sum E_i \eta_i)/(\sum E_i))^2}$, where W_i is the energy and η_i is the pseudo-rapidity of cell i and the sum is calculated within a window of 3×5 cells.
Strip layer of EM calorimeter	Shower width, $\sqrt{(\sum E_i (i - i_{\max})^2)/(\sum E_i)}$, where i runs over all strips in a window of $\Delta\eta \times \Delta\phi \sim 0.0625 \times 0.2$, corresponding typically to 20 strips in η, and $i_{\max}$ is the index of the highest-energy strip.
	The ratio of the difference between the largest and second largest energy deposits in the cluster over the sum of these energies.
Track-cluster matching	$\Delta\eta$ between the cluster position in the strip layer and the extrapolated track.
Track quality	The number of hits in the pixel detector. The number of total hits in the pixel and SCT detectors.
`Medium++` (in addition to `Loose++` conditions)	
Third layer of EM calorimeter	Ratio of the energy in the third layer to the total energy.
Track quality	The number of hits in Blayer (discriminates against photon conversions). Transverse impact parameter.
TRT	Ratio of the number of high-threshold hits to the total number of hits in the TRT.
`Tight++` (in addition to `Medium++` conditions)	
Track-cluster matching	$\Delta\phi$ between the cluster position in the middle layer and the extrapolated track. Ratio of the cluster energy to the extrapolated track.
TRT	Total number of hits in the TRT.
Conversions	Veto electron candidates matched to reconstructed photon conversions.

Table 3: Summary of the electron selection criteria.

Cut	Value/description				
Electron Type	Preselected	$E_{\mathrm{T}}^{\mathrm{miss}}$	Crack	Loose	Signal
Acceptance	$p_{\mathrm{T}} > 10$ GeV			$p_{\mathrm{T}} > 25$ GeV	
	$\lvert\eta\rvert < 2.47$		$1.37 < \lvert\eta\rvert < 1.52$	$\lvert\eta\rvert < 2.47$	
Quality	Medium++				Tight++
Overlap Removal	$\Delta R(e, \mathrm{jet}) > 0.4$		–	$\Delta R(e, \mathrm{jet}) > 0.4$	
Isolation	–				ptcone20/$p_{\mathrm{T}} < 0.10$
Impact Parameter	–				d_0^{PV} ≤1 mm
	–				$\lvert z_0^{\mathrm{PV}}\rvert$ ≤2 mm

Table 4: Summary of the hard electron selection criteria.

Cut	Value/description				
Electron Type	Preselected	$E_{\mathrm{T}}^{\mathrm{miss}}$	Crack	Loose	Signal
Acceptance	$p_{\mathrm{T}} > 7$ GeV			10 GeV $< p_{\mathrm{T}} <$ 25 GeV	
	$\lvert\eta\rvert < 2.47$		$1.37 < \lvert\eta\rvert < 1.52$	$\lvert\eta\rvert < 2.47$	
Quality	Medium++				
Overlap Removal	$\Delta R(e, \mathrm{jet}) > 0.4$		–	$\Delta R(e, \mathrm{jet}) > 0.4$	
Isolation	–				ptcone30/$p_{\mathrm{T}} < 0.16$
Impact Parameter	–				$\lvert d_0^{\mathrm{PV}}/\sigma(d_0^{\mathrm{PV}})\rvert$ ≤5
	–				$\lvert z_0^{\mathrm{PV}} \sin\theta\rvert < 0.4$ mm

Table 5: Summary of the soft electron selection criteria.

ensures that the electron comes from a hard collision, not from pile-up. Table 4 gives the summary of these electron definitions.

3.3.5 Soft electron definition

In the soft lepton analysis, electrons from p_{T}>10 GeV are used to define signal and loose electrons, while the other electrons start from p_{T}>7 GeV. In addition, the following items are modified for signal electron to obtain better efficiency and background rejection.

- Medium++ criteria,
- ptcone30/$p_{\mathrm{T}}^{\ell} < 0.16$,
- $\lvert z_0^{\mathrm{PV}} \sin\theta\rvert < 0.4$ mm,
- $\lvert d_0^{\mathrm{PV}} \sin\theta/\sigma(d_0^{\mathrm{PV}})\rvert < 5$.

Here, z_0 is the track distance from the primary vertex along the beam axis, and θ is the polar angle of the track direction. $\sigma(d_0^{\mathrm{PV}})$ is the uncertainty of d_0^{PV}. ptcone30 is defined as the sum of track momentum in $\Delta R < 0.3$ from the electron. Table 5 summarizes soft electron definitions.

3.3.6 Performance

The overall electron efficiency consists of a reconstruction (Section 3.3.1-3.3.2) efficiency and an identification (Section 3.3.3) efficiency.

Figure 20 (left) shows the electron reconstruction efficiency as a function of transverse energy E_T, measured with tag-and-probe method [27] using 2012 dataset. The efficiency in 2012 is higher than 97% for $E_T > 10$ GeV and is well reproduced by Monte Carlo simulation within the uncertainty. The right plot of Fig. 20 (right) shows the electron identification efficiencies as a function of E_T. For `Medium++` and `Tight++` lepton selections, a 2% level discrepancy is observed. Therefore, the efficiency is corrected in the analysis but the uncertainty associating with the correction is well below 2%, thus negligible.

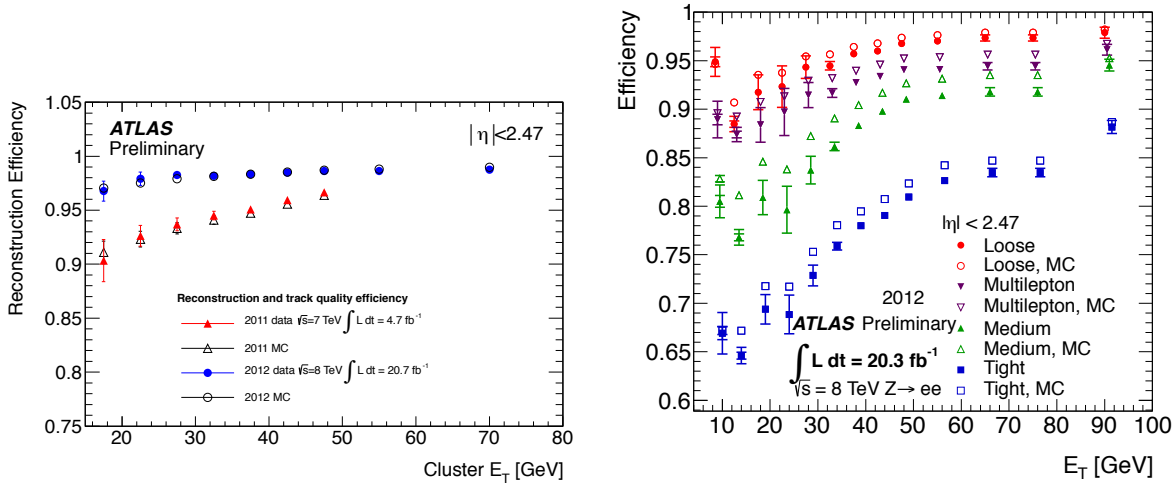

Figure 20: (Left) Efficiency of electron reconstruction is shown as a function of transverse energy E_T for the electrons in the central part of the detector with $|\eta| < 2.47$ for data (filled markers) and MC (open markers) for 2011 (triangles) and 2012 (circles) datasets. The total (statistical and systematic) uncertainty is displayed as the error bars. (Right) Identification efficiency of electrons from $Z \to ee$ decay for `Loose`, Multi-lepton, `Medium` and `Tight` selections are shown as a function of E_T for $|\eta| < 2.47$. These plots are cited from Ref. [27].

3.4 Muon

Muon tracks are reconstructed separately by two detectors: Muon Spectrometer and Inner Detector. The information of these two tracks are then combined to improve quality using STACO [28] or Segment-tagged muon algorithms. Further improvements of purity is achieved by requiring good hits for trackers.

3.4.1 Standalone muons

The muons reconstructed by the outermost muon detector (called Muon Spectrometer or MS) are historically called standalone muon since Muon Spectrometer is designed to detect muons independently of the other parts of the detector. The standalone algorithm first builds track segments in each of the three muon stations and then links the segments to form tracks. In STACO algorithm, an algorithm called Muonboy [29] is used to form spectrometer tracks from these segments. Segment-tagged muon algorithm uses the raw segment information to identify muon tracks, combined with the inner tracker information.

3.4.2 Inner detector muons

Inner detector tracks reconstructed in Section 3.1 are used to define inner detector muons. These tracks contain the tracks from pile-up, electron and fake tracks. Therefore Muon Spectrometer information

should be combined to select pure muon tracks.

3.4.3 STACO muons

Match chi-square χ^2_{match} is defined as the difference between the standalone muon track and the inner detector track vectors weighted by their combined covariance matrix:

$$\chi^2_{\text{match}} = (\mathbf{T}_{\text{MS}} - \mathbf{T}_{\text{ID}})^{\text{T}} (\mathbf{C}_{\text{MS}} + \mathbf{C}_{\text{ID}})^{-1} (\mathbf{T}_{\text{MS}} - \mathbf{T}_{\text{ID}}) . \tag{48}$$

Here $\mathbf{T}$ denotes a vector of track parameters and $\mathbf{C}$ is the covariance matrix. The subscript ID refers to the inner detector and MS to the muon spectrometer. The pair having the best χ^2_{match} is chosen for the combination. Then the combined muon track vector is given by

$$\mathbf{T} = \left(\mathbf{C}_{\text{ID}}^{-1} + \mathbf{C}_{\text{MS}}^{-1}\right)^{-1} \left(\mathbf{C}_{\text{ID}}^{-1}\mathbf{T}_{\text{ID}} + \mathbf{C}_{\text{MS}}^{-1}\mathbf{T}_{\text{MS}}\right). \tag{49}$$

ID information dominates the measurement up to p_{T}=80 GeV in the barrel and p_{T}=20 GeV in the endcap. For higher p_{T} ($\lesssim$ 100 GeV), the ID and MS measurements have similar weight while the MS dominates in $p_{\text{T}} \gtrsim 100$ GeV.

3.4.4 Segment-tagged muons

Segment-tagged muon reconstruction starts from Inner Detector tracks, extrapolates them to the inner station of Muon Spectrometer, and tries to match them to the segments not yet associated to the muons reconstructed by STACO algorithm. Segment-tagged muon algorithm provides an efficiency improvement for low p_{T} muons.

3.4.5 Hard muon definition

Both STACO and Segment-tagged muons are combined to increase the reconstruction efficiency over a wide p_{T} range. To improve purity, the following hit qualities are required for the candidate muons.

- The number of hits in the pixel detector should be larger than 1. If, after the reconstruction, the pixel sensor which is passed by the track is found to be malfunctioning, the number of hits is increased by the number of such malfunctioning sensors to increase efficiency.
- Similarly, the number of SCT hits are requested to be greater than 6. Again, the number of malfunctioning SCT sensors are added up to the number.
- If more than 3 holes are found in Pixel and SCT detectors along the extrapolated track, the track quality is judged as bad.
- If the muon passes a working innermost pixel sensor, a hit should be recorded in that sensor.
- If $|\eta| < 1.9$, the number of TRT hits should be larger than 5 and the outlier tubes near the track should not exceed more than 10% of the total TRT hits.
- If $|\eta| \geq 1.9$ and the number of TRT hits is larger than 5, the outlier tubes near the track should not exceed more than 10% of the total TRT hits.

To reject fake muons from hadron decays, muons within $\Delta R < 0.4$ from an overlap removal jet (defined in Section 3.2.7) is vetoed.

Then the following muons are defined: $E_{\mathrm{T}}^{\mathrm{miss}}$ muon, loose muon, preselected muon and signal muon. The usages for these muons are the same as electrons in the previous section. The isolation condition of signal muon is different from that of electron, which is

$$\texttt{ptcone20} < 1.8 \text{ GeV}, \tag{50}$$

where `ptcone20` is the sum p_{T} of all tracks within $\Delta R < 0.2$. The definitions are summarized in Table 6.

3.4.6 Soft muon definition

Most of the definitions are the same as those of Hard Muon. Here we see only the differences. First, p_{T} thresholds are changed to 6 GeV for all muons. In addition, signal muon is requested to pass the following isolation conditions

- `ptcone30` < 1.2 GeV,
- $|z_0^{\mathrm{PV}} \sin\theta| < 0.4$ mm,
- $|d_0^{\mathrm{PV}}/\sigma(d_0^{\mathrm{PV}})| \leq 3$.

z_0^{PV} is the track distance from the primary vertex along the beam axis and θ is the polar angle of the track. d_0^{PV} is the radial distance between the track and the Primary Vertex. $\sigma(d_0^{\mathrm{PV}})$ is the uncertainty of d_0^{PV}. Table 7 gives the summary of soft muon definition.

3.4.7 Performance

Figures 21 show the muon efficiency as a function of p_{T} (left) and η (right). The muons reconstructed by both STACO and Segment-tagged algorithms are combined. The efficiency is larger than 98% for $p_{\mathrm{T}} > 20$ GeV, and the discrepancy between data and Monte Carlo is well below 1%. The discrepancy is corrected by introducing a correction factor, but the impact is negligible.

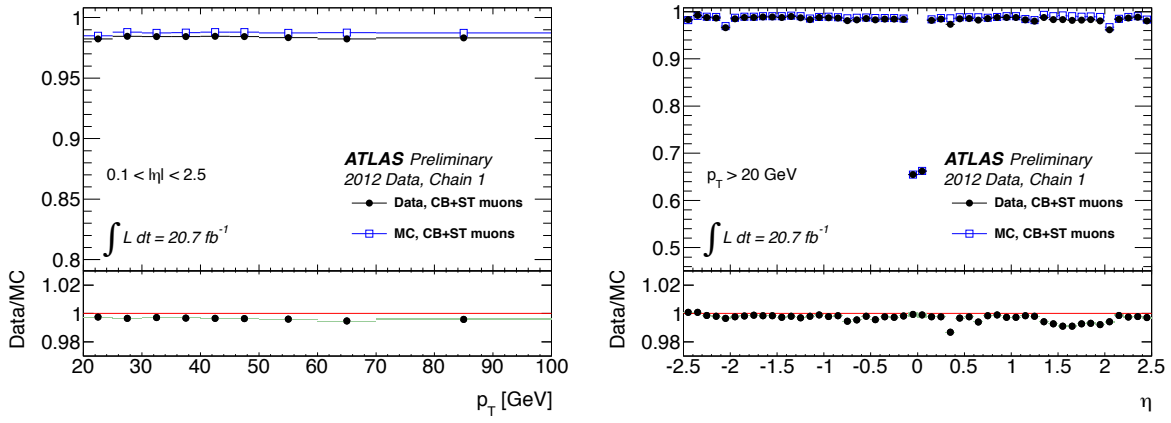

Figure 21: Reconstruction efficiency for STACO and Segment-tagged muons as a function of p_{T} (left) and $|\eta|$ (right). The bottom panel shows the ratio between data and Monte Carlo. These plots are cited from Ref. [30].

Cut	Value/description			
Muon Type	Preselected	$E_{\mathrm{T}}^{\mathrm{miss}}$	Loose	Signal
Acceptance	$p_{\mathrm{T}} > 10$ GeV		$p_{\mathrm{T}} > 25$ GeV	
	$\lvert\eta\rvert < 2.4$			
Overlap Removal	$\Delta R(\mu, \mathrm{jet}) > 0.4$			
Isolation	–			`ptcone20` < 1.8 GeV

Table 6: Summary of the hard muon selection criteria.

Cut	Value/description			
Muon Type	Preselected	$E_{\mathrm{T}}^{\mathrm{miss}}$	Loose	Signal
Acceptance	$p_{\mathrm{T}} > 6$ GeV			
	$\lvert\eta\rvert < 2.4$			
Overlap Removal	$\Delta R(\mu, \mathrm{jet}) > 0.4$			
Isolation	–			`ptcone30` < 1.2 GeV
Impact Parameter	–			$\lvert z_0^{\mathrm{PV}} \sin\theta\rvert < 0.4$ mm
	–			$\lvert d_0^{\mathrm{PV}}/\sigma(d_0^{\mathrm{PV}})\rvert \leq 3$

Table 7: Summary of the soft muon selection criteria.

3.5 Missing transverse momentum

$E_{\mathrm{T}}^{\mathrm{miss}}$ is defined as the missing momentum in the transverse plane calculated from all objects reconstructed in the previous sections. Namely, $E_{\mathrm{T}}^{\mathrm{miss}}$ is calculated as follow,

$$\begin{aligned} \mathbf{E}_T^{miss} = & - \sum_{\mathrm{Electron}} \mathbf{p}_T^{\mathrm{Electron}} \\ & - \sum_{\mathrm{Muon}} \mathbf{p}_T^{\mathrm{Muon}} \\ & - \sum_{\mathrm{Jet}} \mathbf{p}_T^{\mathrm{Jet}} \\ & - \sum_{\mathrm{Soft}} \mathbf{E}_T^{\mathrm{Soft}} \end{aligned} , \tag{51}$$

where,

Electron : $E_{\mathrm{T}}^{\mathrm{miss}}$ electrons defined in Table 4 (Hard Lepton) or Table 5 (Soft Lepton) are included.

Muon : $E_{\mathrm{T}}^{\mathrm{miss}}$ muons defined in Table 6 (Hard Lepton) or Table 7 (Soft Lepton) are used.

Jet : $E_{\mathrm{T}}^{\mathrm{miss}}$ jets defined in Table 2 are included. Hadronic τ-jets are also classified to this term. The jets with $p_{\mathrm{T}}^{\mathrm{jet}}$<20 GeV are included in the soft term.

Soft : Soft term consists of the Topo-Clusters and tracks within $|\eta| < 4.9$ not associated to any physics objects.

$E_{\mathrm{T}}^{\mathrm{miss}}$ (scalar) is defined as the norm of $\mathbf{E}_T^{miss}$,

$$E_{\mathrm{T}}^{\mathrm{miss}} = |\mathbf{E}_T^{miss}|. \tag{52}$$

3.5.1 Performance

Figure 22 shows the $E_{\mathrm{T}}^{\mathrm{miss}}$ distribution in $Z^0 \to \mu\mu$ events [31]. As $Z^0 \to \mu\mu$ events do not have an escaping neutrino in the final state, it provides a good environment to investigate $E_{\mathrm{T}}^{\mathrm{miss}}$ resolution, which is the most difficult quantity to be reproduced in Monte Carlo due to the detector response and the contribution from pile-up. As can be seen from the plot, the agreement between data and Monte Carlo is quite well.

The pile-up dependence of the $E_{\mathrm{T}}^{\mathrm{miss}}$ resolution is shown in Fig. 23. The black filled (hollow) points show the $E_{\mathrm{T}}^{\mathrm{miss}}$ resolution of data (Monte Carlo) as a function of the number of primary vertex per a bunch crossing N_{PV}. In high pile-up condition ($N_{\mathrm{PV}} \gtrsim 15$), the Monte Carlo has a slightly lower resolution by 1-2 GeV. However, since we require a large $E_{\mathrm{T}}^{\mathrm{miss}}$ (>150 GeV at least), the difference is small enough to be neglected.

3.6 Kinematic variables

In the analysis phase, interesting events are selected by putting thresholds on several kinematic selections, which are designed to pick up typical characteristics of the supersymmetry events. Based on the reconstructed objects in the previous sections, the following kinematic variables are defined:

p_{T}^{ℓ} : Transverse momentum of the leading lepton is represented as p_{T}^{ℓ}. In the electron (muon) channel, the signal lepton defined in Table 4 (Table 6) (Hard Lepton) or Table 5 (Table 7) (Soft Lepton) is used.

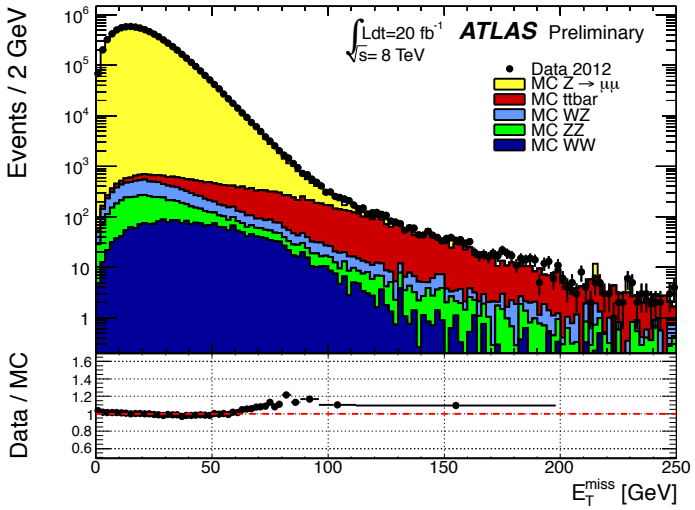

Figure 22: $E_{\mathrm{T}}^{\mathrm{miss}}$ distribution after requiring two muons. The black points show 2012 data, the other colored histograms show the various Standard Model processes. This plot is cited from Ref. [31].

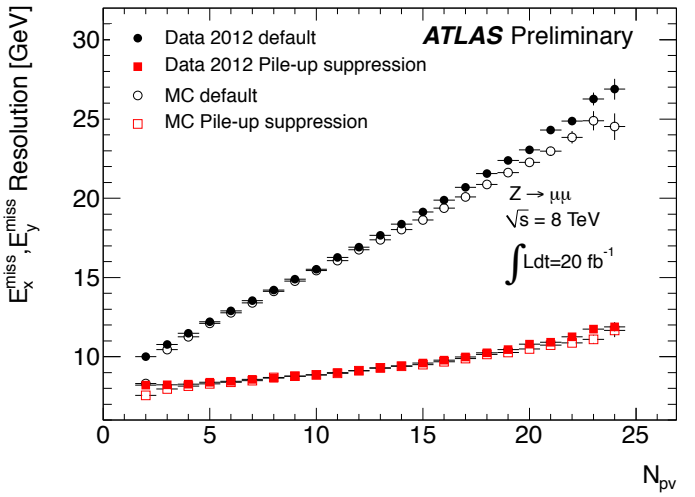

Figure 23: $E_{\mathrm{T}}^{\mathrm{miss}}$ resolution as a function of the number of primary vertex per a bunch crossing N_{PV}, measured in $Z^0 \to \mu\mu$ events. The black filled (hollow) circles show the data (Monte Carlo) with the default pile-up correction. The red filled (hollow) squares show the ones with STVF pile-up corrections (not used in the analysis) [31].

$p_{\mathrm{T}}^{\mathrm{jet}}$: Transverse momentum of a jet is represented as $p_{\mathrm{T}}^{\mathrm{jet}}$. Jets are sorted by their transverse momentum and indices are specified from the hardest jet, for example the transverse momentum of the leading and the next leading jets are expressed as $p_{\mathrm{T}}^{\mathrm{jet1}}$ and $p_{\mathrm{T}}^{\mathrm{jet2}}$. Signal jets defined in Table 2 are used.

$N_{\mathbf{jet}}^{\mathbf{X}}$: The number of jets with transverse momentum larger than X GeV is denoted as $N_{\mathrm{jet}}^{\mathrm{X}}$. The signal jets defined in Table 2 are used.

m_{T} : Transverse mass m_{T} is defined as

$$m_{\mathrm{T}} = \sqrt{2E_{\mathrm{T}}^{\mathrm{miss}} p_{\mathrm{T}}^{\ell} \left(1 - \cos\Delta\phi(E_{\mathrm{T}}^{\mathrm{miss}}, \mathrm{lep})\right)}, \tag{53}$$

where $\Delta\phi(E_{\mathrm{T}}^{\mathrm{miss}}, \mathrm{lep})$ is the opening angle of $E_{\mathrm{T}}^{\mathrm{miss}}$ and the lepton. m_{T} has a clear cut-off for the events with only one missing object. For example, $m_T \leq m_W$ holds for W+jets production and the cut-off is called Jacobian peak. No clear peak appears for the events with more than two missing objects, such as a supersymmetry event with two LSPs, therefore m_{T} is a good variable to suppress W+jets and semi-leptonic $t\bar{t}$ backgrounds.

m_{eff} : Effective mass m_{eff} is defined as

$$m_{\mathrm{eff}} = p_{\mathrm{T}}^{\ell} + E_{\mathrm{T}}^{\mathrm{miss}} + \sum_{\mathrm{jet}} p_{\mathrm{T}}^{\mathrm{jet}}, \tag{54}$$

where "jet" runs over all the signal jets with $p_{\mathrm{T}}^{\mathrm{jet}}$>30 GeV. m_{eff} is the sum of transverse momentum of all objects reconstructed in the detector and represents the energy scale of a collision. For supersymmetric particles, m_{eff} is known to be roughly proportional to the initial particle masses.

3.7 Event cleanings

The ATLAS detector is a complex of several sub-detectors, which then consist of multiple cells and electronics. A good working efficiency was achieved during 2012 data taking period, however, there exists some period in which one of the sub-detector was malfunctioning. The data in such period is removed by selecting only good "LumiBlocks", which is the smallest time chunk ($\sim O(1)$ minute) in data recording. Also a set of flags are defined to find event-by-event electronics failures. The events without any failure flag are used for the further analysis. In addition, the following items are checked to reject bad quality events:

- To make sure that a hard collision occurs in the bunch crossing, a Primary Vertex with at least 5 tracks is required. If no such Primary Vertex is found in the event, the event is rejected.
- If a crack electron (defined in Table 4, 5) is found in the event, the event is vetoed as it has a bad $E_{\mathrm{T}}^{\mathrm{miss}}$ quality.
- In addition to the detector problems, the cosmic muon makes unphysical $E_{\mathrm{T}}^{\mathrm{miss}}$ thus becomes a background of supersymmetry search. To remove such events, we veto the cosmic muon events based on the muon trajectory distance from the Primary Vertex. The cosmic muon is defined as the preselected muons with one of the following conditions,
  - $|z_0^{\mathrm{PV}}| > 1.0\,\mathrm{mm}$,
  - $d_0^{\mathrm{PV}} > 0.2\,\mathrm{mm}$.
- Finally, to veto the events with a possible fake $E_{\mathrm{T}}^{\mathrm{miss}}$ due to other detector problems, the following fake $E_{\mathrm{T}}^{\mathrm{miss}}$ veto is applied:

– If one of the jets passes the following criteria, then the event is judged as having a fake $E_{\mathrm{T}}^{\mathrm{miss}}$ thus vetoed:
  * $p_{\mathrm{T}}^{\mathrm{jet}}$>40 GeV,
  * $\mathrm{B}_{\mathrm{jet}}^{\mathrm{corr}} > 0.05$,
  * $\Delta\phi(E_{\mathrm{T}}^{\mathrm{miss}}, \mathrm{jet}) < 0.3$.

  $\mathrm{B}_{\mathrm{jet}}^{\mathrm{corr}}$ is a variable to estimate the possible energy loss due to a malfunctioning of the calorimeter cells in a jet. The estimation is based on the geometrical shape of jets and if a cell has significantly small energy for the position in the jet, then the difference between the measured and the expected cell energy is counted as missing energy. $\mathrm{B}_{\mathrm{jet}}^{\mathrm{corr}}$ is the fraction of the total missing energies with respect to the total jet energy.

– During 2012 data taking period, a specific region of Hadron Endcap calorimeter (-1.85<η<-1.55, -0.7363<ϕ<0.) is turned off due to a malfunction of the electronic circuit. Since the detector collects only a part of jet energies, jet reconstruction itself is not affected by this problem, but reconstructed energies are inevitably underestimated, which makes large fake $E_{\mathrm{T}}^{\mathrm{miss}}$. To remove such events, a fake $E_{\mathrm{T}}^{\mathrm{miss}}$ estimation algorithm has been invented. The method loops over the jets with $p_{\mathrm{T}}^{\mathrm{jet}}$>20 GeV which are pointing the problematic region. If such a jet exists in the event, the size of fake missing momentum $E_{\mathrm{T}}^{\mathrm{miss}}$(fake) is estimated by the following set of equations,

$$p_T^{\mathrm{corr}} = p_T \cdot \frac{1 - B_{\mathrm{cell}}^{\mathrm{corr}}}{1 - B_{\mathrm{jet}}^{\mathrm{corr}}}, \tag{55}$$

$$E_{\mathrm{T}}^{\mathrm{miss}}(\mathrm{fake}) = p_T^{\mathrm{corr}} - p_T, \tag{56}$$

  where p_T is the reconstructed transverse momentum of the jet, $B_{\mathrm{cell}}^{\mathrm{corr}}$ is the fraction of the energy which is assigned to the bad calorimeter cells estimated from the average of the neighboring cells. The correction based on $B_{\mathrm{cell}}^{\mathrm{corr}}$ is applied to all jets in default, however, it is designed to work well only for a small hole-like malfunction. Since the geometrical size of the LAr failure is too large to be corrected by $B_{\mathrm{cell}}^{\mathrm{corr}}$, the correction is replaced by the one based on $B_{\mathrm{jet}}^{\mathrm{corr}}$, which can be adopted to a large size of malfunction. p_T^{corr} is the corrected transverse momentum, and by subtracting the original jet p_{T}, $E_{\mathrm{T}}^{\mathrm{miss}}$(fake) is estimated.

  In principle, we can correct the fake $E_{\mathrm{T}}^{\mathrm{miss}}$ by adding $E_{\mathrm{T}}^{\mathrm{miss}}$(fake) to the original $E_{\mathrm{T}}^{\mathrm{miss}}$, but to be conservative, we rather veto the events. If $E_{\mathrm{T}}^{\mathrm{miss}}$(fake) passes both of the following conditions, $E_{\mathrm{T}}^{\mathrm{miss}}$(fake) is judged to have a non-negligible contribution, thus the event is vetoed.

$$E_{\mathrm{T}}^{\mathrm{miss}}(\mathrm{fake}) > 10\,\mathrm{GeV}, \tag{57}$$

$$E_{\mathrm{T}}^{\mathrm{miss}}(\mathrm{fake})/E_{\mathrm{T}}^{\mathrm{miss}} > 0.1. \tag{58}$$

3.8 Triggers

Three different triggers are employed to select hard electron, muon, and soft lepton events. Due to overwhelming QCD multi-jet backgrounds, a trigger which directly tags a soft lepton cannot be used, but alternatively we use a $E_{\mathrm{T}}^{\mathrm{miss}}$ trigger to select soft lepton events. Also for the hard lepton triggers, not only a lepton trigger but also additional conditions are required so as to reduce the trigger rate. It is important to check if the trigger efficiencies are sufficient enough for the kinematic selections required in the following analysis.

Electron trigger : Electron trigger fires when an electron is found in an event. But it is suffered from the mis-firings from fake electrons and the trigger rate is overwhelmed by them. We require large $E_{\mathrm{T}}^{\mathrm{miss}}$ at trigger level to reduce the background.

A trigger called `EF_e24vh_medium1_EFxe35_tclcw` tags the events which have

- at least one `medium++` quality electron with p_{T}^{ℓ}>25 GeV,
- $E_{\mathrm{T}}^{\mathrm{miss}}$ larger than 80 GeV.

`EF_e24vh_medium1_EFxe35_tclcw` has a few % efficiency loss for large lepton p_{T}. To compensate the efficiency loss, `EF_e60_medium1` is added in the trigger menu, which fires for the electron with p_{T}>60 GeV.

Figure 24 shows the electron trigger efficiency as a function of offline $E_{\mathrm{T}}^{\mathrm{miss}}$ (corresponding to $E_{\mathrm{T}}^{\mathrm{miss}}$ defined in Section 3.5). $E_{\mathrm{T}}^{\mathrm{miss}}$ used in the trigger decision is different from the offline $E_{\mathrm{T}}^{\mathrm{miss}}$: the trigger $E_{\mathrm{T}}^{\mathrm{miss}}$ is based on a different calibration scheme and muons are not added up when calculating momentum balance. As a result, a slight topology dependence is expected. The difference between $t\bar{t}$ (red) and W+jets (blue) gives the rough size of the topology dependence. To select a similar topology as our Signal Regions, the following kinematic selections are applied: m_{T}>60 GeV, $p_{\mathrm{T}}^{\mathrm{jet1}}$>80 GeV, $p_{\mathrm{T}}^{\mathrm{jet3}}$>40 GeV and exactly 1 electron. The efficiency calculation is performed based on a method in which the events are selected by an orthogonal trigger and the trial trigger is tested on those events to measure the efficiency.

$$\text{Trigger efficiency (trial trigger)} = \frac{\text{Number of events passing both the trial and orthogonal triggers}}{\text{Number of events passing the orthogonal trigger}} \tag{59}$$

For the orthogonal trigger, an isolated electron trigger is used here.

The trigger efficiency becomes fully efficient for $E_{\mathrm{T}}^{\mathrm{miss}}$>80 GeV and the difference between data and Monte Carlo ($t\bar{t}$, W+jets) is below 1%, thus negligible.

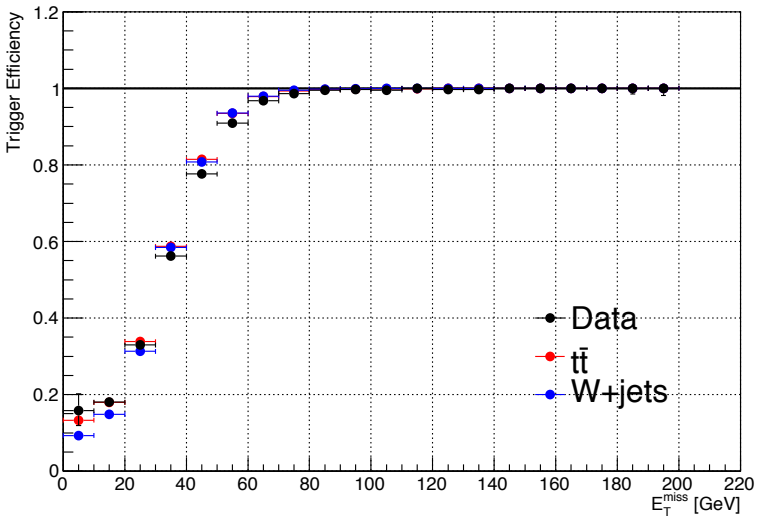

Figure 24: Trigger efficiency of `EF_e24vh_medium1_EFxe35_tclcw` as a function of $E_{\mathrm{T}}^{\mathrm{miss}}$.

Muon trigger : Muon trigger fires when a muon is found in an event. The muon trigger is also suffered from fake muons from QCD multi-jet background. To reduce fake trigger rate, we use a $E_{\mathrm{T}}^{\mathrm{miss}}$+muon+jet trigger: `EF_mu24_j65_a4tchad_EFxe40_tclcw`, which selects the events with

- at least one muon with p_{T}>25 GeV,
- $E_{\mathrm{T}}^{\mathrm{miss}}$ larger than 120 GeV,
- at least one jet with $p_{\mathrm{T}}^{\mathrm{jet}}$>80 GeV.

Figures 25 show the efficiency plots, which are measured in the same way as the Electron case with an isolated muon trigger being used for the orthogonal trigger. The left plot shows $E_{\mathrm{T}}^{\mathrm{miss}}$ dependence and the right plot shows jet p_{T} dependence. For the left plot, exactly 1 muon, m_{T}>60 GeV, $p_{\mathrm{T}}^{\mathrm{jet1}}$>80 GeV and $p_{\mathrm{T}}^{\mathrm{jet3}}$>40 GeV are required, while for the right plot, exactly 1 muon, m_{T}>60 GeV and $E_{\mathrm{T}}^{\mathrm{miss}}$>150 GeV are required. The trigger is fully efficient after requiring $E_{\mathrm{T}}^{\mathrm{miss}}$>120 GeV and $p_{\mathrm{T}}^{\mathrm{jet1}}$>100 GeV, where the difference between data and Monte Carlo is below 1%.

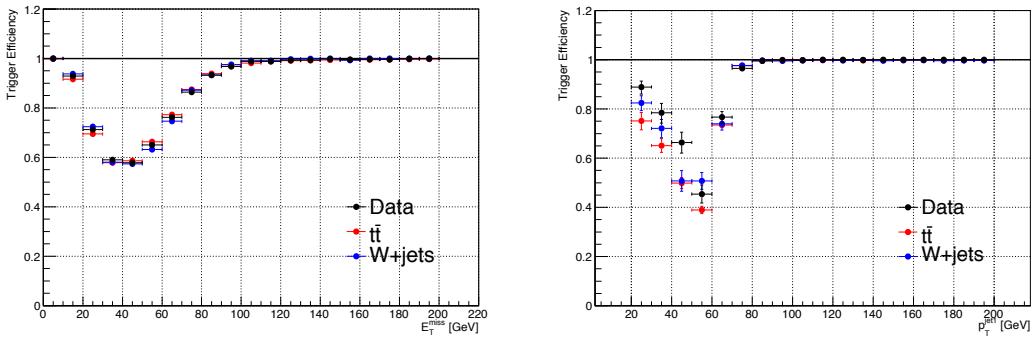

Figure 25: Trigger efficiencies of `EF_mu24vh_j65_a4tchad_EFxe40_tclcw` as functions of $E_{\mathrm{T}}^{\mathrm{miss}}$ (left) and $p_{\mathrm{T}}^{\mathrm{jet}}$ (right).

$E_{\mathrm{T}}^{\mathrm{miss}}$ **trigger :** Lepton p_{T} thresholds of the lepton triggers are too high to tag events in the soft lepton analysis. Instead, triggers based on $E_{\mathrm{T}}^{\mathrm{miss}}$ are used. Two different triggers are combined since the lowest un-prescaled triggers were changed during 2012 data taking period, which are summarized in Table. 8. Since `EF_xe80T_tclcw_loose` trigger does not use the first three bunches in a bunch train, the luminosity becomes slightly lower for the trigger. The loss is 10%, so a scaling factor of 0.9 is multiplied to the first 2.1 fb^{-1} of data, leading to an luminosity of 1.9 fb^{-1}. As a result, the integrated luminosity for the soft lepton analysis becomes 20.1 fb^{-1}.

For both of the triggers, the efficiencies reach to a plateau after requiring the following condition,

- $E_{\mathrm{T}}^{\mathrm{miss}}$ larger than 200 GeV.

Since no serious discrepancy is observed between data and Monte Carlo above this threshold and no significant topology dependence is found, no further corrections or the uncertainty is introduced for this trigger.

Figure 26 shows the trigger efficiency curve of `EF_xe80_tclcw_loose` with the following conditions: exactly 1 electron, m_{T}>60 GeV, $p_{\mathrm{T}}^{\mathrm{jet1}}$>80 GeV and $p_{\mathrm{T}}^{\mathrm{jet3}}$>40 GeV. An isolated electron trigger is used for the orthogonal trigger.

The triggers mentioned above are summarized in Table 9.

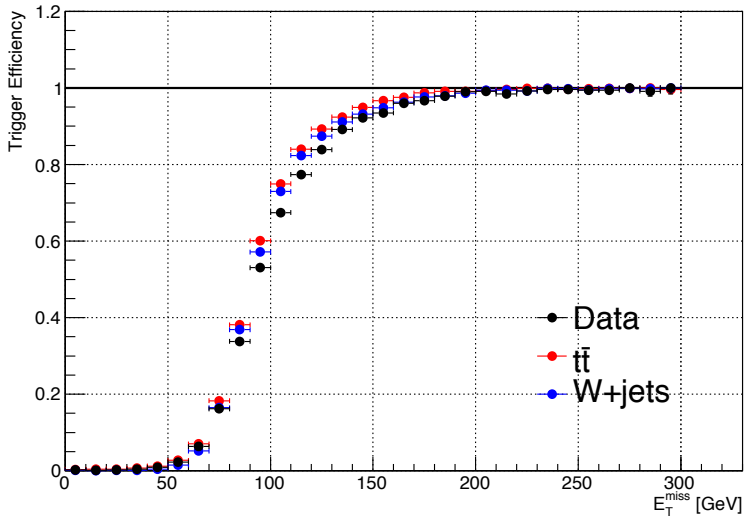

Figure 26: Trigger efficiencies of `EF_xe80_tclcw_loose` as a function of $E_{\mathrm{T}}^{\mathrm{miss}}$.

Trigger	delivered lumi.	rescaled lumi.
`EF_xe80T_tclcw_loose`	2.1 fb^{-1}	1.9 fb^{-1}
`EF_xe80_tclcw_loose`	18.2 fb^{-1}	18.2 fb^{-1}

Table 8: The lowest un-prescaled triggers and their delivered and rescaled luminosities.

Channel	Trigger	Luminosity	Comments
Electron	`EF_e24vh_medium1_EFxe35_tclcw` or `EF_e60_medium1`	20.3 fb^{-1}	Fully efficient with : Electron p_{T}>25 GeV $E_{\mathrm{T}}^{\mathrm{miss}}$>80 GeV
Muon	`EF_mu24_j65_a4tchad_EFxe40_tclcw`	20.3 fb^{-1}	Fully efficient with : Muon p_{T}>25 GeV $E_{\mathrm{T}}^{\mathrm{miss}}$>120 GeV at least 1jet with $p_{\mathrm{T}}^{\mathrm{jet}}$>80 GeV
Soft Lepton	`EF_xe80T_tclcw_loose` or `EF_xe80_tclcw_loose`	20.1 fb^{-1}	Fully efficient with : $E_{\mathrm{T}}^{\mathrm{miss}}$>200 GeV.

Table 9: Summary of the triggers. The "Comments" show the minimum offline selection needed in the analysis.

4 Data and Monte Carlo simulation

4.1 Data samples

This thesis uses the data recorded by the ATLAS detector in proton-proton collision at the center-of-mass energy of $\sqrt{s} = 8\,\text{TeV}$. These events were collected from April 5th to December 6th in 2012. The data taken in the period yields a total integrated luminosity of $21.3\,\text{fb}^{-1}$. To assure a good data quality, all detectors are required to be turned on and working without a fatal problem. The detector condition is recorded for each LumiBlock and the LumiBlocks flagged as problematic are eliminated, leaving an integrated luminosity of $\int L\,dt = 20.3 \pm 0.6\,(2.8\%)\,\text{fb}^{-1}$. Figure 27 shows the LHC delivered, ALTAS recorded, and good-for-physics integrated luminosities.

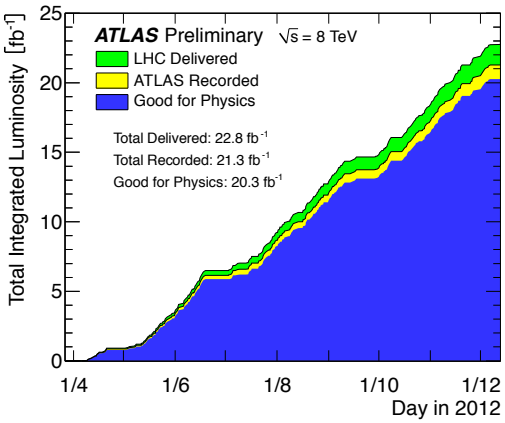

Figure 27: LHC delivered (green), ATLAS recorded (yellow), and good-for-physics (blue) luminosities. The x-axis shows the date in 2012.

4.1.1 Luminosity measurement

The ATLAS detector has several algorithms and sub-detectors [32] to monitor the luminosity. They mostly count the number of reference events μ_{vis} and calculate the luminosity using the cross-section of the event σ_{vis} as

$$\mathcal{L} = \frac{\mu_{\text{vis}} n_b f_r}{\sigma_{\text{vis}}}. \tag{60}$$

The unknown parameter σ_{vis} is calibrated beforehand by an absolute luminosity measurement, *van der Meer* (*vdM*) scan. *vdM* scan, or often referred to as *beam separation scan*, measures spacial proton density profile of bunches by shifting the impact offset between two colliding beams. Also the absolute number of protons in a bunch is measured by monitoring the beam current at the same time. With these information, the absolute luminosity is calculated as

$$\mathcal{L} = \frac{n_b f_r n_1 n_2}{2\pi \Sigma_x \Sigma_y}, \tag{61}$$

where n_1, n_2 are the number of protons contained in two colliding bunches and Σ_x, Σ_y are the root-mean-square of transverse proton distribution.

By equating Eq. 60 and Eq. 61, σ_{vis} is obtained as,

$$\sigma_{\text{vis}} = \mu_{\text{vis}} \frac{2\pi \Sigma_x \Sigma_y}{n_1 n_2}. \tag{62}$$

Here we have only measurable values in the equation and hence σ_{vis} is determined.

4.2 The Standard Model samples

Monte Carlo samples are produced by Monte Carlo generators and then processed with detector simulations using `GEANT4` [33]. Energy deposit of particles in the active detector material is converted into detector outputs, emulating the real detector. The generated events are processed through trigger simulation and reconstructed with the same software as real data.

Monte Carlo generators produce events in two steps [34]: Matrix-Element and Parton-Shower calculations. The former step evaluates Feynman-diagram at the Leading-Order (LO) or at the Next-to-Leading-Order (NLO) to determine the kinematics of the outgoing partons (quark and gluon). The strong coupling constant α_S used in Matrix-Element calculation strongly depends on the energy scale of the hard process, called "renormalization scale". In Monte Carlo generators, the energy scale is determined by an empirical formula depends on physics processes. The uncertainty of the arbitrariness is evaluated and included in the systematic uncertainty.

Though Matrix-Element calculation is precise, it has a drawback of the processing time, especially when the number of outgoing partons increases. In addition, the perturbation theory of QCD process becomes a bad approximation in low energy scale near $\Lambda_{\text{QCD}} \sim 1$ GeV. Therefore Matrix-Element calculation is used to evaluate only hard processes and the following evaluation is performed by Parton-Shower algorithm. Parton-Shower algorithm uses collinear approximation to evaluate the emission probability of additional partons. For example, the differential cross-section of a gluon emission from a quark $d\sigma(q \to q + g)$ is approximated as

$$d\sigma(q \to q + g) \sim \alpha_S \, \sigma_0 \, \frac{d\theta^2}{\theta^2} \, dz \, P_{ji}(z), \tag{63}$$

where σ_0 is the cross-section without the gluino emission, θ is the opening angle of the emission. $P_{ji}(z)$ is $i \to j$ splitting function, which describes the distribution of the fraction z of energy of i carried by j. In case of $q \to q + g$, the splitting function is

$$P_{qg}(z) = \frac{1}{2}\left[z^2 + (1 - z^2)\right]. \tag{64}$$

The partons emitted from Matrix-Element and Parton-Shower algorithms have an inevitable overlap. When two partons are overlapped, the parton from Matrix-Element is prioritized because Matrix-Element calculation is more accurate. This procedure is called matching. Two different methods are proposed to perform matching [35]: MLM and CKKW. MLM matching is based on geometrical separation of partons to remove the double count. On the other hand, CKKW matching decides the rejection based on k_T-measure [36, 37].

The momentum distribution of incoming partons in proton is given by Parton Distribution Function (PDF). PDF measured in the other colliders with lower center-of-mass energy is evolved by DGLAP equation [38, 39, 40] to the LHC energy. The energy scale at which PDF is evaluated is called "factorization scale". Factorization scale is determined event by event using an empirical formula. The arbitrariness is evaluated and taken into systematics (detail will be discussed in Section 7.2).

The outgoing partons are often off-shell[5], therefore they need to emit additional partons to back to their physical (on-shell) states. The emission is called *Final State Radiation* (FSR). The same radiation is emitted before the hard process, called *Initial State Radiation* (ISR). The entire process is kicked back by the sum momentum of ISR and FSR, therefore their contributions make a visible impact not only on

[5]The degree of offshellness is sometimes refereed to as "virtuality".

jets but also on the momentum of objects such as supersymmetry particles and electroweak bosons. Most part of ISR and FSR are simulated in Parton-Shower algorithm.

The cross-section of proton-proton collision (including both elastic and inelastic interactions) is $O(100)$ m barn at 8 TeV, so more than 1 proton pairs may interact in one bunch crossing, which are referred to as *pile-up*. Pile-up events are generated with `PYTHIA8` [41] with AM2 tune [42] and the LO PDF set `MSTW2008LO` [43, 44, 45]. The impact of pile-up is a small efficiency loss in lepton identification, energy shift in jets and resultant resolution deterioration in $E_{\mathrm{T}}^{\mathrm{miss}}$. To treat all these effects, the pile-up events are superimposed to the hard collision events before starting object reconstruction. The average number of interactions per bunch crossing $\langle\mu\rangle$ in Monte Carlo are controlled so that it reproduces the distribution of data.

4.2.1 Standard Model processes

The Standard Model processes are background candidates for supersymmetry searches. Especially, if a process accompanies a lepton, large $E_{\mathrm{T}}^{\mathrm{miss}}$ and high p_{T} jets, it contaminates to our signal region. Two major such backgrounds are W+jets and $t\bar{t}$ productions. Event topologies for these processes will be discussed in Section 5.1. The following processes also contribute to the background and are included in the background estimation, however the impact is small compared with $t\bar{t}$ and W+jets.

Single top : Decay of a top-quark accompanies a lepton, a neutrino and jets. However, since the production cross-section is small compared with $t\bar{t}$ production, Single Top production does not become a dominant background.

Dibosons : WW, WZ, ZZ productions are collectively-referred to as Diboson production and some fractions of them decay into leptonic final states. However, due to small cross-sections and soft event topologies, the processes does not play an important role in background estimation.

$t\bar{t}$+V : $t\bar{t}$ production accompanied by an electroweak boson W, Z is denoted as $t\bar{t}$+V. The cross-section for these productions is $O(10^{-3})$ times smaller than $t\bar{t}$ production, therefore negligible.

Z+jets : $Z \to ll$ decay becomes a background if one of the leptons is not identified. However, the production cross-section of this process is about 10 times smaller than W+jets and also $E_{\mathrm{T}}^{\mathrm{miss}}$ is so small because it doesn't have a neutrino in the final state. Therefore, the contribution of this process cannot be large.

Table 10 shows the Standard Model processes included in the analysis. Detail configurations of Monte Carlo generation are discussed below.

W/Z+jets :

W/Z+jets processes are generated with Sherpa [46] using NLO PDF sets CT10 [47]. Matrix-Element calculates up to 4 partons and additional partons are emulated by Parton-Shower algorithm implemented in Sherpa. To obtain correct production fractions of c- and b-quarks, these quarks are treated as massive particles in Matrix-Element calculation.

Reference cross-sections are calculated by DYNNLO [48, 49] implemented with LO MSTW2008 PDF sets [43, 44, 45]. In the cross-section calculation for Z+jets, $m_{ll} > 60$ GeV is applied to remove low mass Drell-Yan process. Inclusive cross-sections for $W^{\pm} \to l^{\pm}\nu$ and $Z^0 \to l^{\pm}l^{\mp}$ processes are 12.2 nb and 1.15 nb, respectively. Cross-section uncertainty of Z+jet is taken from the comparison of generator level cross-section (LO) and NNLO calculation using DYNNLO, which gives 12% difference. Similar uncertainty estimation is applied to W+jets and gives the same size.

$t\bar{t}$:

$t\bar{t}$ process is generated at NLO by Powheg [50] generator with LO PDF sets CTEQ6L1 [51]. Parton-Shower emulation is performed by Pythia6.4 [52]. All the partons except for the objects produced in hard process are collectively-referred to as underlying event. The latest underlying-event tune called *Perugia 2011C tune* [53] is used for this production.

Cross-section for $t\bar{t}$ production are evaluated at NNLO, which is $252.89^{+13.30}_{-14.52}$ pb for top quark mass of 172.5 GeV/c^2 [54]. The error cited here is the quadrature sum of the scale dependence and PDF uncertainties. Scale uncertainty is evaluated by varying renormalization and factorization scales by a factor of 2 or 1/2 independently. For PDF uncertainty, PDF4LHC prescription [55] is applied.

Single Top :

Single Top consists of three different production processes. For all of these processes, CTEQ6L1 [51] LO PDF set is used and Parton-Shower is simulated by Pythia6.4 [52] with *Perugia tune 2011C* [53]. The cross-section is calculated using NNLO PDF set MSTW2008 [43, 44, 45].

- ***t*-channel**
  AcerMC [56] is used to generate events. Cross-section is calculated at NNLL level [57], which is $87.76^{+3.44}_{-1.91}$ pb.
- ***s*-channel**
  Powheg [50] is used to generate events. Cross-section is calculated at NNLL level [58], which is 5.61 ± 0.22 pb.
- ***Wt*-channel**
  Powheg [50] is used for event generations. Cross-section is calculated at NNLL level [59], which is 22.37 ± 1.52 pb. Wt-channel production has an overlap with $t\bar{t}$ since they have the same final states $t + (W + b)$. The overlap is removed by Diagonal Removal (DR) method [60, 61] and an uncertainty is introduced to punish the arbitrariness of this choice (the size of uncertainty is evaluated in Section 7.2.3).

Dibosons :

Diboson production is generated by Sherpa [46] with LO PDF sets CT10 [47]. Matrix-Element calculates up to 3 partons. A lepton p_{T} cut of p_{T}^{ℓ}>5 GeV and an invariant mass cut of $m_{ll} > 0.1$ GeV are applied.

NLO cross-section is calculated by MCFM [62], giving 5.88 pb (for $WW \rightarrow llvv$), 10.33 pb (for $WZ \rightarrow lllv$) and 9.69 pb (for $ZZ \rightarrow llll$). Uncertainties are taken from the difference between the NLO and LO calculations, which gives about 50%. Other dibosons productions having hadronic final states are also included, whose cross-section is 33.8 pb in total at LO.

$t\bar{t}$**+***V* :

$t\bar{t}$+V production is generated by MadGraph [63] with Pythia for Parton-Shower emulation and CTEQ6L1 [51] LO PDF sets. Up to 2 partons are calculated with Matrix-Element.

NLO cross section calculations have been performed for $t\bar{t}$+W in Ref. [64] and for both $t\bar{t}$+W and $t\bar{t}$+Z in Ref. [65]. PDF uncertainty and renormalization/factorization scale uncertainties are reported in the references, which are 8% and 21%, respectively. However, to be conservative, the difference between NLO and LO cross-section is referred as the uncertainty (30%). The cross-sections are 0.232 pb (for $t\bar{t}$+W) and 0.2057 pb (for $t\bar{t}$+Z).

Process	Cross-section [pb] (the order of the perturbation)	Generator
W+jets ($W^{\pm} \to l^{\pm}\nu$)	$12.2 \times 10^3 \pm 12\%$ (NNLO)	Sherpa
Z+jets ($Z^{\pm} \to l^{\pm}l^{\mp}$)	$1.15 \times 10^3 \pm 12\%$ (NNLO)	Sherpa
$t\bar{t}$	$252.89^{+13.30}_{-14.52}$ (NNLO)	Powheg+Pythia
Single Top (t-channel)	$87.76^{+3.44}_{-1.91}$ (NNLL)	AcerMC+Pythia
Single Top (s-channel)	5.61 ± 0.22 (NNLL)	Powheg+Pythia
Single Top (Wt-channel)	22.37 ± 1.52 (NNLL)	Powheg+Pythia (DR)
Dibosons ($WW \to llvv$)	$5.88 \pm 50\%$ (NLO)	Sherpa
Dibosons ($WZ \to lllv$)	$10.33 \pm 50\%$ (NLO)	Sherpa
Dibosons ($ZZ \to llll$)	$9.69 \pm 50\%$ (NLO)	Sherpa
Dibosons (Others)	$33.8 \pm 50\%$ (LO)	Sherpa
$t\bar{t}$+W	$0.232 \pm 30\%$ (NLO)	MadGraph+Pythia
$t\bar{t}$+Z	$0.206 \pm 30\%$ (NLO)	MadGraph+Pythia

Table 10: Summary of the Monte Carlo generators and the cross-sections.

4.3 Signal samples

4.3.1 Signal models

The supersymmetry models and their configurations in event generations are summarized in this section. We consider the following models:

- MSUGRA/CMSSM models
- Simplified models

MSUGRA/CMSSM model is based on a physical scenario of gravity mediated SUSY breaking as discussed in Section 1.4.4, while Simplified model [66] is constructed without assuming any SUSY breaking model but sets sparticle masses by hand to produce various mass hierarchy just in case the SUSY breaking is occurred in an unexpected scenario.

4.3.2 MSUGRA/CMSSM model

MSUGRA/CMSSM model is defined by 5 parameters (details are in Section 1.4.4):

$$m_0,\ m_{1/2},\ \tan\beta,\ A_0,\ sign(\mu). \tag{65}$$

In sample production, m_0 and $m_{1/2}$ are scanned in the ranges of m_0=200-6000 GeV and $m_{1/2}$=400-1000 GeV. The grid points are generated every 50 GeV in both m_0 and $m_{1/2}$, with some additional points for the low mass regions and no points for the regions where no sensitivity is expected. In order to be compatible with the discovery of Higgs with m_h =126 GeV [67], A_0 and $\tan\beta$ are adopted to $A_0 = -2m_0$ and $\tan\beta = 30$ (see Section 1.4.5). The sign of μ is set to be positive. The generated points are displayed in Fig. 28. Top plot shows production cross-sections obtained with NLL-fast [68] and Prospino [69]. The relative uncertainty of the cross-section is shown in the bottom, which includes PDF, normalization and factorization scales and strong coupling uncertainties (see Section 7.3.1 for detail). SUSY-HIT [70] interfaced to SOFTSUSY [71] and SDECAY [72] is used to calculate the sparticle mass spectra and decay tables, and to guarantee consistent electroweak symmetry breaking. For each point 40 k events are generated with `HERWIG++` generator [73] with `UEEE3/CTEQ6L1` PDF sets [51]. Only the processes with colored sparticle production are generated. Note that MSUGRA/CMSSM samples treat all the particle

masses and their decays correctly, therefore the decay chains may include, for example, the decays via third generation squarks, second or third lightest neutralinos, and so on.

4.3.3 Simplified models

Simplified models starts from direct pair-production of gluinos or squarks. The gluino (squark) decays into two (one) quarks and a chargino, and the chargino subsequently decays to a W boson and a neutralino LSP. Figures 29 show the decay diagram of gluino-gluino (left) and squark-squark (right) simplified models. The masses of gluino (squark), chargino and LSP are free parameters, however, we reduce the parameters into two in order to visualize in two dimensional plane.

First way is to set chargino mass $m_{\tilde{\chi}_1^\pm}$ to the halfway of gluino mass $m_{\tilde{g}}$ (or squark mass $m_{\tilde{\mathrm{q}}}$) and LSP mass $m_{\tilde{\chi}_1^0}$:

$$m_{\tilde{\chi}_1^\pm} = \frac{m_{\tilde{\mathrm{g}}/\tilde{\mathrm{q}}} + m_{\tilde{\chi}_1^0}}{2}. \tag{66}$$

This grid is referred to as "Half-x" in the following. Gluino (or squark) mass and LSP mass are left as free parameters.

The other way is to fix LSP mass and vary chargino mass. The LSP mass is set to 60 GeV, which is slightly higher than the lowest model-independent limit obtained in DELPHI experiment[74], and the gluino (squark) and chargino masses are taken as free parameters. For better visualization and interpretation, the chargino mass is not used directly but the following x is defined instead

$$x = \frac{m_{\tilde{\chi}_1^\pm} - m_{\tilde{\chi}_1^0}}{m_{\tilde{g}/\tilde{q}} - m_{\tilde{\chi}_1^0}}. \tag{67}$$

This grid spanned by gluino (squark) mass and x is referred to as "Grid-x". Table 11 summaries the signal models.

In the case of squark production, only left-handed first- and second-generation squarks are considered. These simplified model grids are all generated using `MadGraph` [63] and `Pythia6` [52], and the NLO+NLL cross-sections are calculated using `NLL-fast` [68]. In total 60 k events are generated per point for Half-x grids, 30 k per point for Grid-x. In the case of gluino-gluino Half-x grid, the number of events generated per point increases up to 80 k near the diagonal, where $m_{\tilde{g}}$ is close to $m_{\tilde{\chi}_1^0}$.

Signal Model		Comments
MSUGRA/CMSSM		Minimum Supergravity model compatible with $m_h = 126$ GeV.
Simplified Model	$\tilde{g}$-$\tilde{g}$, Half-x $\tilde{\mathrm{q}}$-$\tilde{\mathrm{q}}$, Half-x	Pair produced gluinos (squarks) decays into LSP via a chargino. x is fixed at 1/2. $m_{\tilde{\chi}_1^0}$ is a free parameter.
	$\tilde{g}$-$\tilde{g}$, Grid-x $\tilde{\mathrm{q}}$-$\tilde{\mathrm{q}}$, Grid-x	Pair produced gluinos (squarks) decays into LSP via a chargino. $m_{\tilde{\chi}_1^0}$ is fixed at 60 GeV. x is a free parameter.

Table 11: Summary of the signal models.

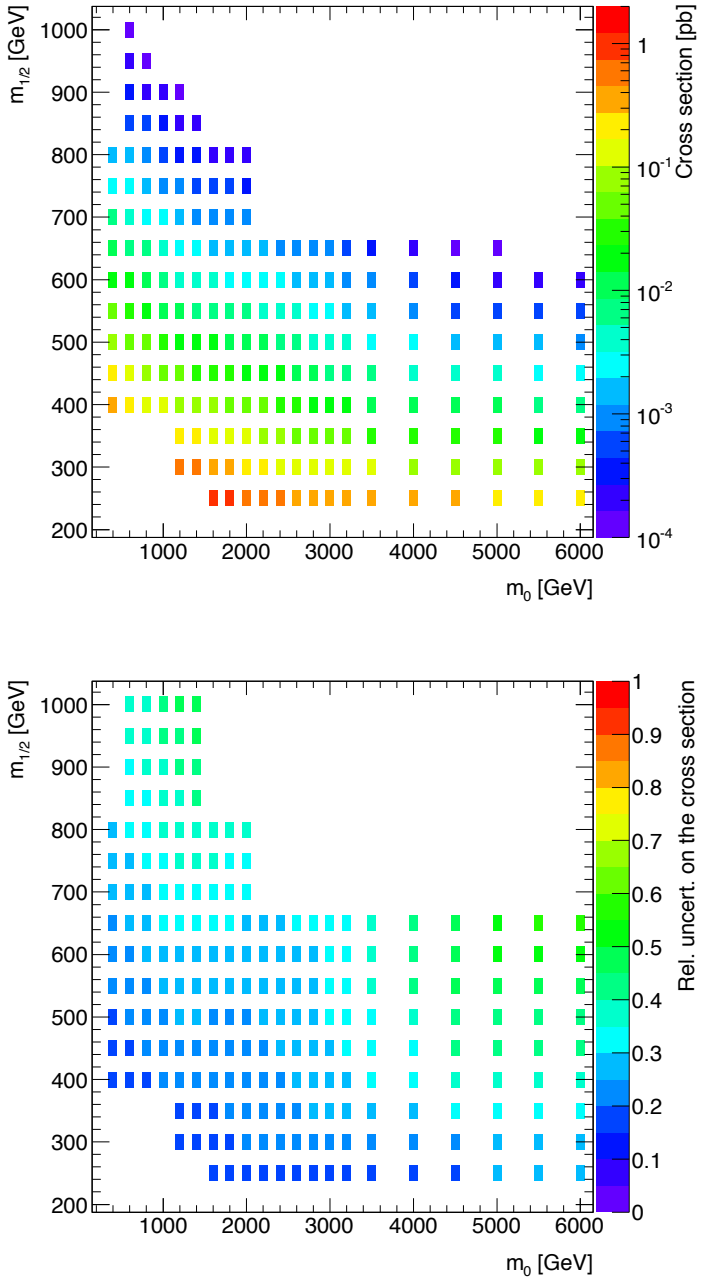

Figure 28: Cross-section (top) and its relative uncertainty (bottom) of MSUGRA/CMSSM model. $\tan\beta$ is 30, A_0 is $-2m_0$ and sign(μ) is positive.

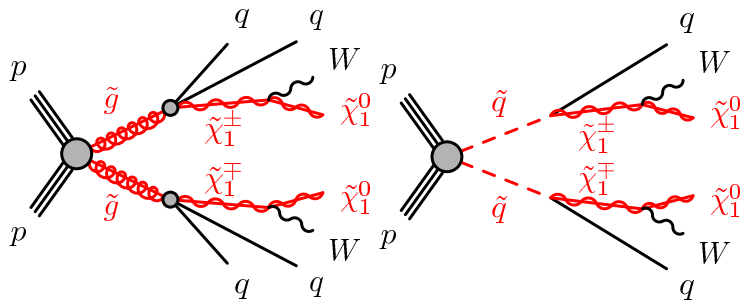

Figure 29: Representative diagrams of the Simplified models. On the left (right), the production of a gluino (squark) pair followed by chargino decay is shown.

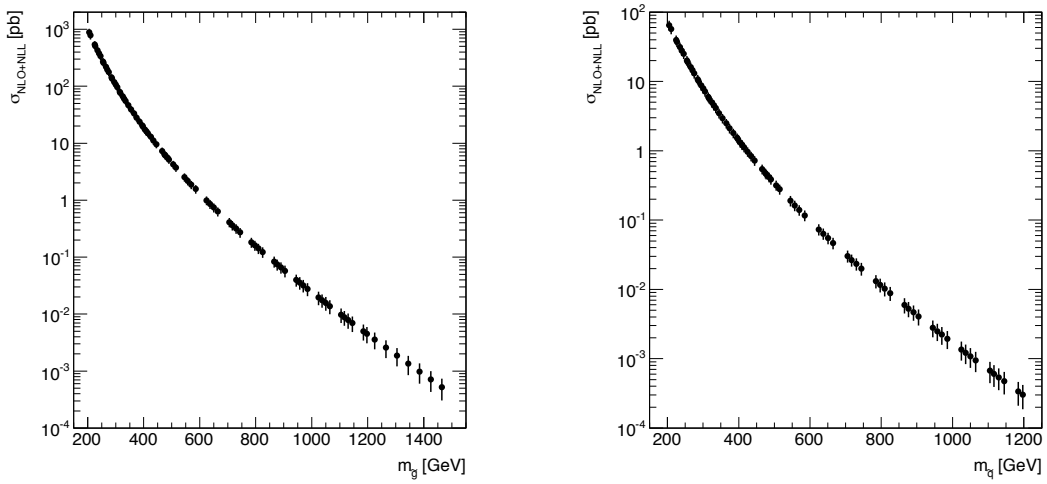

Figure 30: (Left) production cross sections are shown as a function of gluino masses for gluino pair production in the context of Simplified Model. The associated uncertainties are also shown as the error bars. (Right) the same plot for the squark pair-production.

5 Signal Region optimization

We optimize our Signal Regions so that a good signal and background separation is realized and the resultant sensitivity is maximized over a wide range of signals. First, we investigate event topologies of both background and signals. Important variables to be optimized are introduced in this part. The difficulty of the optimization is in the correlations between the variables. A complete optimization considering the correlation is performed as the next step, which will be discussed in Section 5.2 and also in Appendix B.

5.1 Event topology

Event topologies are determined by two parts: production and decay. We overview event topologies of supersymmetry signals and our major backgrounds, $t\bar{t}$ and W+jets, mainly in these two viewpoints. The distributions of kinematic variables are then reviewed.

5.1.1 Signals

Examples of signal production diagrams are shown in Fig. 31. All sparticles should be produced in pairs due to the R-parity conservation. We focus on gluino and squark productions in this thesis. A gluino decays into a quark and a squark if it is kinematically possible: $\tilde{g} \to q\tilde{\mathrm{q}}$. A squark then decays into a quark and an electroweak gaugino, $\tilde{\mathrm{q}} \to q\tilde{\chi}$. If the gluino decay $\tilde{g} \to q\tilde{\mathrm{q}}$ is not allowed, these successive decays occur via a off-shell squark: $\tilde{g} \to q\tilde{\mathrm{q}}^* \to qq\tilde{\chi}$. In the Simplified model assuming $\tilde{g}$-$\tilde{g}$ production, the squark mass is set heavier than the gluino mass, therefore a gluino always decays in three-body mode. The type of the electroweak gaugino $\tilde{\chi}$ produced in the squark decay is determined by the mass hierarchy of electroweak gauginos or the mixing of them. The lightest chargino $\tilde{\chi}_1^\pm$ and the second lightest neutralino $\tilde{\chi}_2^0$ play the role in the decay chain in most cases. A chargino $\tilde{\chi}_1^\pm$ then decays into a W boson and a LSP: $\tilde{\chi}_1^\pm \to W^\pm + \tilde{\chi}_1^0$. Similarly, a second lightest neutralino decays into a Z boson and a LSP: $\tilde{\chi}_2^0 \to Z^0 + \tilde{\chi}_1^0$. Simplified models literary simplify the decay chain and assumes only one-step decay via a chargino: $\tilde{q}\,(\tilde{g}) \to q(q)\,\tilde{\chi}_1^\pm \to q(q)\,W^\pm\,\tilde{\chi}_1^0$. W bosons in the decay chain may emit leptons, which we use to tag the events. Another possible lepton source is from a slepton decay, $\tilde{l^\pm} \to l^\pm + \tilde{\chi}_1^0$, however, this doesn't dominate in our parameter space and signal models. Figure 32 summarizes the decays we discussed here.

The production process of the Simplified models is limited to only $\tilde{\mathrm{q}}$-$\tilde{\mathrm{q}}$ or $\tilde{g}$-$\tilde{g}$, while the initial particles of MSUGRA/CMSSM model are the mixture of $\tilde{\mathrm{q}}$-$\tilde{\mathrm{q}}$ $\tilde{g}$-$\tilde{g}$ and $\tilde{\mathrm{q}}$-$\tilde{g}$. Fractions for these contributions are plotted in Fig. 33. Gluino mass becomes lighter than squark mass in large m_0 region, which explains the dominance of $\tilde{g}$-$\tilde{g}$ production in that region. On the other hand, low m_0 regime is dominated by $\tilde{\mathrm{q}}$-$\tilde{\mathrm{q}}$ or $\tilde{\mathrm{q}}$-$\tilde{g}$ productions with roughly equal contributions. As discussed in Section 1.4.5, one of the stops becomes much lighter than first or second generation squarks for the current configuration, thus the production or decay involving stops become dominant. The upshot is the increase in the number of jets, which pushes up the entire sensitivity.

5.1.2 W+jets

W+jets events are produced by a pair-annihilation of a quark and its anti-quark: $q + \bar{q} \to W^\pm$. The anti-quark is provided from sea-quarks or from the splitting of gluon as shown in Fig. 34. Additional jets may accompany as ISR. Since each vertex accompanies one α_S, the production cross-section fails constantly as the number of jets.

W boson immediately decays into two fermions. The fraction of leptonic decay $W^+ \to l^+\nu$ is 11% for each lepton flavor. Since only one invisible particle ν emits in the leptonic decay, the transverse mass m_T

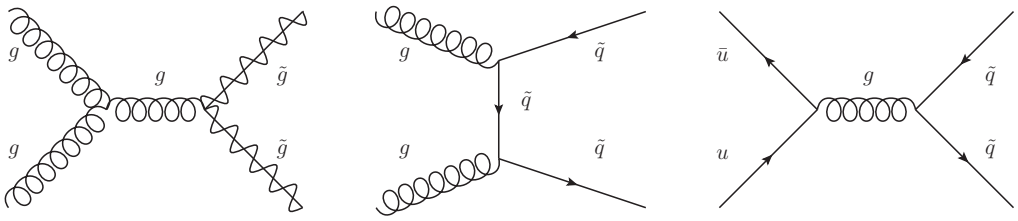

Figure 31: Feynman diagrams which contribute to gluino and squark productions.

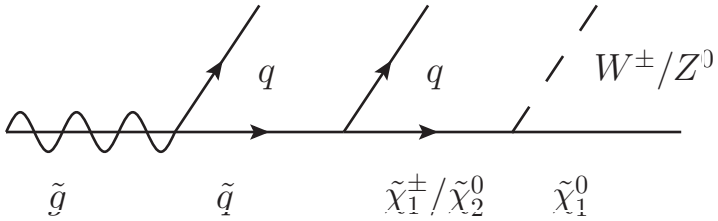

Figure 32: Schematic diagram of successive decays starting from a gluino. The squark may be virtual depending on the mass hierarchy. In the Simplified model assuming gluino pair-production, the squark mass is set heavier than the gluino, therefore a gluino is always decay in three-body mode. In MSUGRA/CMSSM model, another electroweak gaugino may appear in the decay chain, while in the Simplified model all the decays are assumed to happen in one-step via a chargino. As the "maximum mixing" configuration is applied for MSUGRA/CMSSM model, one of stops is much lighter than first or second generation squarks. Therefore, the squark appears in the decay chain is most likely a stop.

has a clear cut-off, called Jacobian peak. After requiring $m_{\mathrm{T}} > m_W = 80.4$ GeV, there remain only two possibilities for W+jets to pass the selection: (1) W boson is highly off-shell, (2) $E_{\mathrm{T}}^{\mathrm{miss}}$ is mis-measured due to its resolution. Signal regions are defined so that $m_{\mathrm{T}} \gg m_W$, where the first type of background dominates.

5.1.3 $t\bar{t}$

$t\bar{t}$ events are produced mainly from a gluon pair as shown in Fig. 35. Top decays via a W boson, $t \to b$+W, and a usual W boson decay follows both leptonically and hadronically. As a result, the final states are classified into three modes: full-hadronic decay ($t\bar{t} \to b\bar{b} + q\bar{q}q\bar{q}$ the branching fraction is 49%), semi-leptonic decay ($t\bar{t} \to b\bar{b} + q\bar{q}l\nu$: 41%), and full-leptonic decay ($t\bar{t} \to b\bar{b} + l\nu l\nu$: 10%). A semi-leptonic decay, $t\bar{t} \to b\bar{b} + q\bar{q}l\nu$, has one neutrino and one lepton in the final state, therefore the event topology is similar to that of W+jets except for the number of jets. For example, m_{T} selection of $m_{\mathrm{T}} > m_W$ effectively reduces this background. On the other hand, m_{T} distributes without a clear cut-off for full-leptonic decay $t\bar{t} \to b\bar{b} + l\nu l\nu$. Its decay topology resembles the decay of supersymmetric particles, which has two missing LSPs. Full-leptonic decays can be reduced by vetoing events with more than two leptons.

5.1.4 Kinematic variables for signal region optimization

A signal region is defined by a set of thresholds on kinematic variables. We look into these kinematic variables to find appropriate thresholds, comparing the shapes of signals and backgrounds. In the course

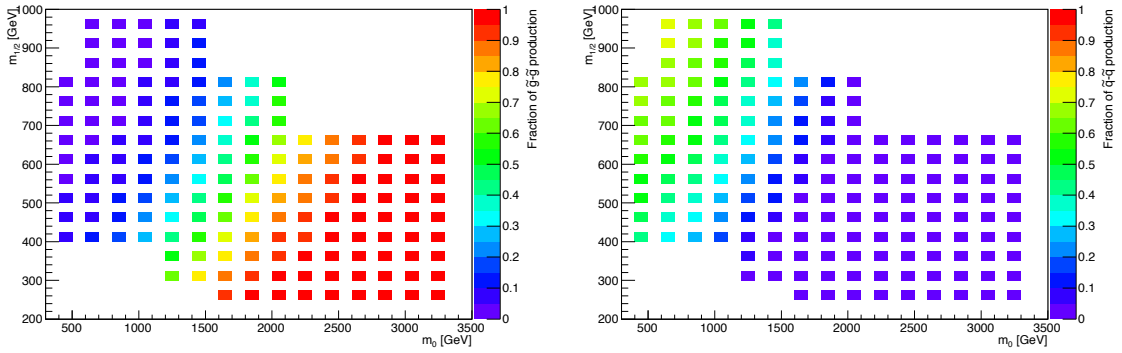

Figure 33: (Left) Fraction of $\tilde{g}$-$\tilde{g}$ contribution compared with the total colored particle production. (right), the same fraction of $\tilde{q}$-$\tilde{q}$ contribution. The fraction of $\tilde{q}$-$\tilde{g}$ production can be calculated by subtracting the fractions from 1.

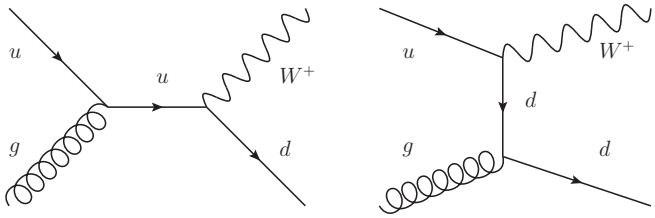

Figure 34: Feynman diagrams which contribute to W+jet productions.

of the discussion, we classify the signal models into three groups and define corresponding signal regions.

p_{T}^{ℓ} : Transverse momentum of lepton p_{T}^{ℓ} varies significantly for on-shell and off-shell W bosons. Figure 36 shows p_{T}^{ℓ} distributions for Half-x grid of the Simplified Model with $m_{\tilde{g}}$~600 GeV. ΔM is defined as the mass difference between chargino and LSP, i.e. $\Delta M \equiv m_{\tilde{\chi}_1^{\pm}} - m_{\tilde{\chi}_1^0}$. The lepton p_{T} distributes broadly around 40 GeV when ΔM is larger than the mass of W boson and on-shell decay $\chi_1^{\pm} \rightarrow W^{\pm} + \tilde{\chi}_1^0$ occurs. On the other hand, if ΔM is smaller than W boson mass, the decay occurs through a three body decay via a off-shell W boson, $\chi_1^{\pm} \rightarrow W^{\pm *} + \tilde{\chi}_1^0 \rightarrow l^{\pm}\nu + \tilde{\chi}_1^0$, and the lepton p_{T} becomes soft as it is emitted via a three body decay.

We introduce a dedicated signal region which is optimized for such *degenerate* signals by selecting a soft lepton. An upper threshold on lepton p_{T} ($25\,GeV$) is introduced so as to be orthogonal to the

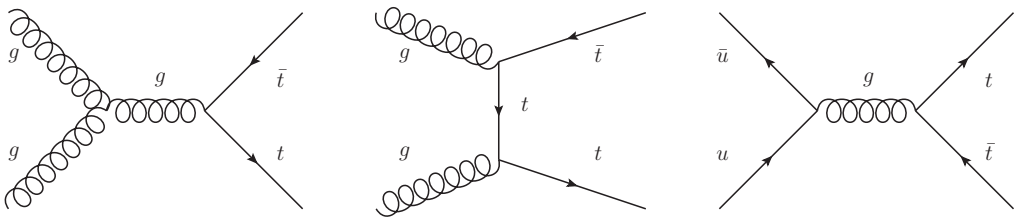

Figure 35: Feynman diagrams which contribute to $t\bar{t}$ productions.

Hard Lepton Signal Regions.

Leptons from QCD multi-jet events have a soft transverse momentum, therefore Soft lepton analysis suffers from QCD multi-jet contribution. In the course of optimization, a selection on the geometrical separation between lepton and jets, $\min_{\text{jet}} \Delta R(\text{lepton}, \text{jet}) > 1.0$, effectively removes the background (Fig. 37). We apply this selection in the Soft lepton analysis.

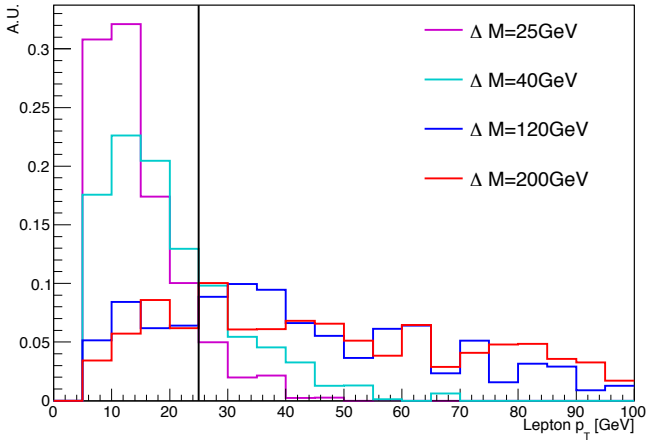

Figure 36: Lepton p_{T} distributions of several signal points taken from Half-x grid of the Simplified Model with $m_{\tilde{g}}$~600 GeV. ΔM is the mass difference between chargino and LSP, i.e. $\Delta M \equiv m_{\tilde{\chi}_1^{\pm}} - m_{\tilde{\chi}_1^0}$. $E_{\mathrm{T}}^{\mathrm{miss}}$> 200 GeV is applied.

$N_{\mathbf{jet}}$: The number of jets further divides the hard lepton signal region. Figure 38 (left) shows the number of jet distribution of $\tilde{g}$-$\tilde{g}$ and $\tilde{\mathrm{q}}$-$\tilde{\mathrm{q}}$ signals on top of the background distributions. A clear difference in the number of jets between the signals is observed, which is because each gluino decay has one additional quark than in a squark decay. We divide the hard lepton signal region into two, Tight SR with $N_{\mathrm{jet}}^{40} \geq 5$ and Loose SR with $N_{\mathrm{jet}}^{40} \geq 3$, focusing $\tilde{g}$-$\tilde{g}$ and $\tilde{\mathrm{q}}$-$\tilde{\mathrm{q}}$ productions, respectively.

We require the Soft Signal Region to cover not only the soft lepton topology, in which the mass difference between chargino and LSP is small, but also the case with small mass splitting between gluino (squark) and LSP. In such a case, the number of jets passing a specific p_{T} threshold becomes small as shown in Fig. 38 (right). Therefore, the threshold of the number of jets are set to 3 for jets with p_{T}>30 GeV.

m_{T} : Transverse mass m_{T} is a good variable to suppress W+jets and semi-leptonic $t\bar{t}$ backgrounds. Figure 39 show m_{T} distributions for Hard (left) and Soft (right) lepton analyses. Number of jet selections and $E_{\mathrm{T}}^{\mathrm{miss}}$ selections are applied as mentioned in the caption. A clear Jacobian peak is observed in both cases. m_{T} distributions in the soft lepton plots suggest to put thresholds as low as possible to keep reasonable signal yields, for example at 100 GeV. For the hard lepton case, the slopes of signals become similar as that of background at around $m_{\mathrm{T}} \sim 150$ GeV, therefore a threshold is optimized here.

$E_{\mathrm{T}}^{\mathrm{miss}}$: Missing transverse momentum distributions are shown in Fig 40. SUSY events have hard $E_{\mathrm{T}}^{\mathrm{miss}}$ distributions, while the background distributions decrease constantly. Optimization should be performed by considering not only the signal to background ratio but rather the "sensitivity" that

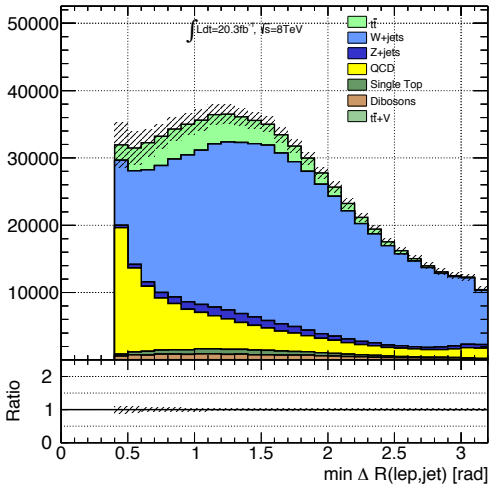

Figure 37: $\min_{\text{Jet}} \Delta R(\text{Leading Lepton, Jet})$ distribution after requiring 1 soft lepton and at least one jet with p_{T}>20 GeV.

affects to the final limits. We will optimize the thresholds in the next section with a more sophisticated method.

m_{eff} : Effective mass m_{eff} is known to be sensitive to heavy particle productions since it is roughly proportional to the masses of colored particles initially produced. Figure 41 shows the correlation of the initial particle masses and the means of their m_{eff} distributions. Black points represent signal points taken from Grid-x ($m_{\tilde{\chi}_1^0}$ is fixed at 60 GeV), which show a clear linear correlation. However, signal points of Half-x grids (varying $m_{\tilde{\chi}_1^0}$), which are shown in red, distribute broader and the correlation seems week. This feature suggests that m_{eff} has a good correlation with the initial particle mass for light LSP cases. m_{eff} becomes smaller than the original particles masses for heavy LSP case, because a significant fraction of the energy is consumed to create heavy LSPs. Since it is difficult to set an universal threshold on m_{eff}, we use m_{eff} as a final discriminating variable and perform a fit on the shape. For reference, m_{eff} distributions are shown in Fig. 42.

5.2 Signal Region Optimization

We introduced three signal regions, Tight, Loose and Soft, in the previous section. The thresholds on lepton p_{T}, the number of jets and m_{T} are readily determined, however, $E_{\text{T}}^{\text{miss}}$ and m_{eff} show no clear structure at which the thresholds should be optimized.

The kinematic variables have strong correlations. For example, N_{jet} have a positive correlation with m_{eff} because m_{eff} includes p_{T} sum of jets as its ingredients, thus the best optimized threshold of m_{eff} should change depending on the N_{jet} selection. An ideal way of optimization is to try all possible combinations of selections and find the best set. We perform a complete scan over thresholds, which is documented in Appendix B. The resultant Signal Regions are summarized in Table 12.

The expected exclusion regions are shown in Figs. 43 and 44. Tight, Loose and Soft SRs are combined and binning of m_{eff} is taken into the calculation. Black lines show a mean expected limit and yellow bands show $\pm 1\sigma$ uncertainties. The uncertainty includes both statistical errors and a systematic uncertainty of 30%. Profile-Likelihood method is used in the calculation. For reference, a separate limit obtained by each SR is superimposed in magenta (Tight SR), blue (Loose SR) and green (Soft SR) line.

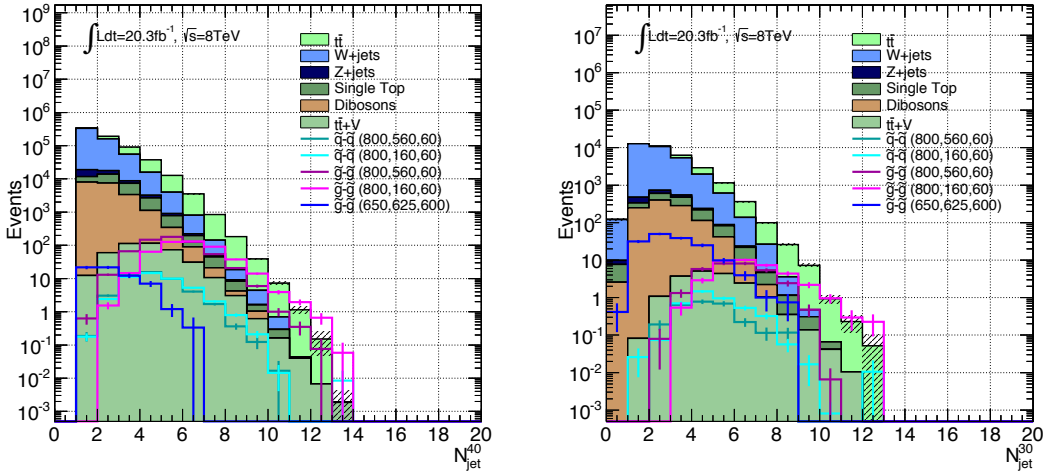

Figure 38: Number of jets distributions after requiring: (left) 1 hard lepton, one jet with p_{T}>80 GeV and $E_{\mathrm{T}}^{\mathrm{miss}}$>100 GeV; (right) soft 1 lepton and $E_{\mathrm{T}}^{\mathrm{miss}}$>200 GeV. For signal samples, q̃-q̃ productions with $(m_{\tilde{\mathrm{q}}}, m_{\tilde{\chi}_1^\pm}, m_{\tilde{\chi}_1^0})$ =(800,560,60) (dark cyan) and (800,160,60) (light cyan), and $\tilde{g}$-$\tilde{g}$ productions with $(m_{\tilde{g}}, m_{\tilde{\chi}_1^\pm}, m_{\tilde{\chi}_1^0})$ =(800,560,60) (dark magenta) and (800,160,60) (light magenta) are plotted. Blue line shows a degenerate point with $(m_{\tilde{g}}, m_{\tilde{\chi}_1^\pm}, m_{\tilde{\chi}_1^0})$ =(650,625,600).

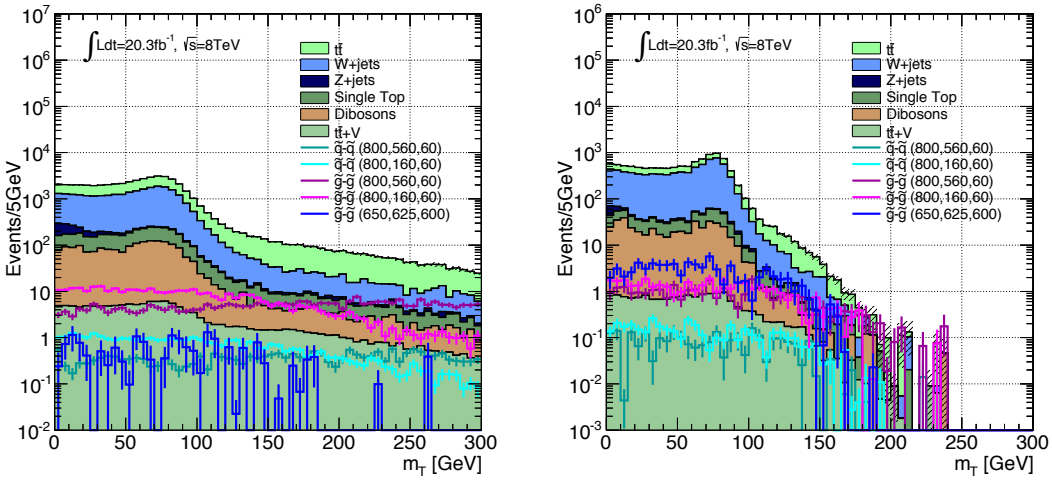

Figure 39: m_{T} distributions after requiring: (left) 1 hard lepton, $E_{\mathrm{T}}^{\mathrm{miss}}$>150 GeV and three jets with p_{T}>40 GeV, in which the leading jets should be harder than p_{T}>80 GeV; (right) soft 1 lepton, $E_{\mathrm{T}}^{\mathrm{miss}}$>200 GeV, and three jets with p_{T}>30 GeV. For signal samples, q̃-q̃ productions with $(m_{\tilde{\mathrm{q}}}, m_{\tilde{\chi}_1^\pm}, m_{\tilde{\chi}_1^0})$ =(800,560,60) (dark cyan) and (800,160,60) (light cyan), and $\tilde{g}$-$\tilde{g}$ productions with $(m_{\tilde{g}}, m_{\tilde{\chi}_1^\pm}, m_{\tilde{\chi}_1^0})$ =(800,560,60) (dark magenta) and (800,160,60) (light magenta) are plotted. Blue line shows a degenerate point with $(m_{\tilde{g}}, m_{\tilde{\chi}_1^\pm}, m_{\tilde{\chi}_1^0})$ =(650,625,600).

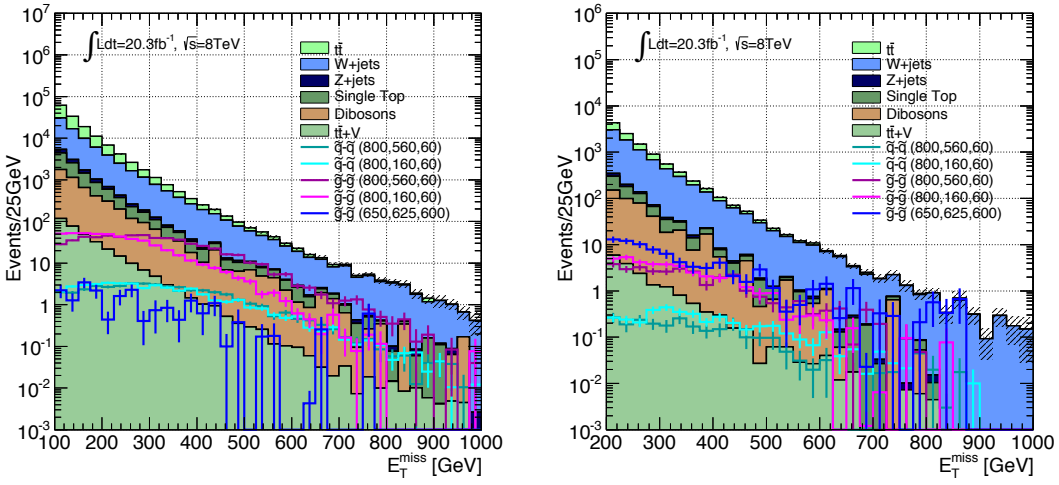

Figure 40: $E_{\mathrm{T}}^{\mathrm{miss}}$ distributions after requiring: (left) 1 hard lepton and three jets with p_{T}>40 GeV, in which the leading jets should be harder than p_{T}>80 GeV; (right) soft 1 lepton and three jets with p_{T}>30 GeV. For signal samples, $\tilde{\mathrm{q}}$-$\tilde{\mathrm{q}}$ productions with $(m_{\tilde{\mathrm{q}}}, m_{\tilde{\chi}_1^\pm}, m_{\tilde{\chi}_1^0})$ =(800,560,60) (dark cyan) and (800,160,60) (light cyan), and $\tilde{g}$-$\tilde{g}$ productions with $(m_{\tilde{g}}, m_{\tilde{\chi}_1^\pm}, m_{\tilde{\chi}_1^0})$ =(800,560,60) (dark magenta) and (800,160,60) (light magenta) are plotted. Blue line shows a degenerate point with $(m_{\tilde{g}}, m_{\tilde{\chi}_1^\pm}, m_{\tilde{\chi}_1^0})$ =(650,625,600).

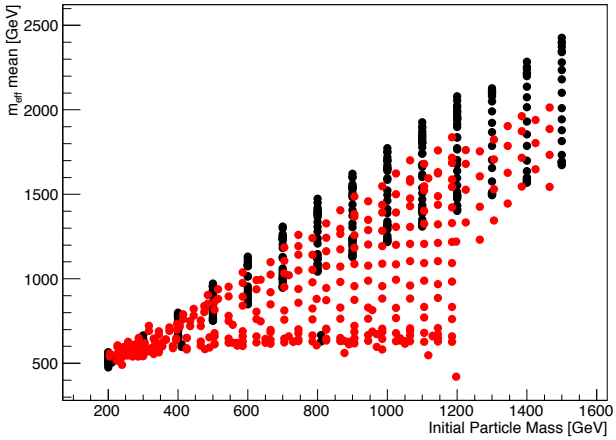

Figure 41: Signal points in the Simplified Models with $\tilde{g}$-$\tilde{g}$ and $\tilde{\mathrm{q}}$-$\tilde{\mathrm{q}}$ productions are shown. x-axis represents $m_{\tilde{g}}$ or $m_{\tilde{\mathrm{q}}}$ and y-axis shows the mean of the m_{eff} distribution. Black points show Grid-x ($m_{\tilde{\chi}_1^0}$=60 GeV) and red points show Half-x grid. See Section 4.3.3 for their definitions.

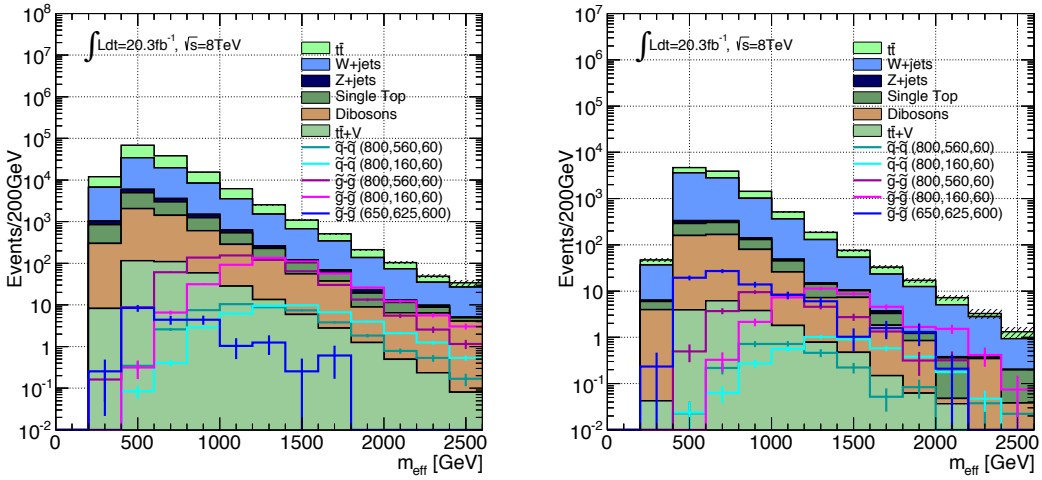

Figure 42: m_{eff} distributions after requiring: (left) 1 hard lepton and three jets with 40 GeV, in which the leading jets should be harder than 80 GeV; (right) soft 1 lepton and three jets with p_{T}>30 GeV. For signal samples, q̃-q̃ productions with $(m_{\tilde{q}}, m_{\tilde{\chi}_1^\pm}, m_{\tilde{\chi}_1^0})$ =(800,560,60) (dark cyan) and (800,160,60) (light cyan), and $\tilde{g}$-$\tilde{g}$ productions with $(m_{\tilde{g}}, m_{\tilde{\chi}_1^\pm}, m_{\tilde{\chi}_1^0})$ =(800,560,60) (dark magenta) and (800,160,60) (light magenta) are plotted. Blue line shows a degenerate point with $(m_{\tilde{g}}, m_{\tilde{\chi}_1^\pm}, m_{\tilde{\chi}_1^0})$ =(650,625,600).

Variable	Tight SR	Loose SR	Soft SR
Preselections			
Leading lepton p_{T}	>25 GeV		[10 GeV, 25 GeV] (Electron), [6 GeV, 25 GeV] (Muon)
Next leading lepton p_{T}	<10 GeV		<7 GeV (Electron), <6 GeV (Muon)
Signal Region specific selections			
Number of jets	N_{jet}^{40} ≥5	3≤ N_{jet}^{40} <5	N_{jet}^{30} ≥3
Leading jet p_{T}	>120 GeV	> 80 GeV	>100 GeV
m_{T}	>150 GeV	>120 GeV	>100 GeV
$E_{\text{T}}^{\text{miss}}$	>350 GeV	>250 GeV	>300 GeV
$m_{\text{eff}}^{\text{incl30}}$	Binned [800,1200,1600, 2000,2400] and >2400 GeV	Binned [450,700,950, 1200,1450] and >1450 GeV	Binned [450,700,950, 1200,1450] and >1450 GeV

Table 12: Optimized signal regions.

These lines clearly show where they have good sensitivities. $\tilde{q}$-$\tilde{q}$ production grid in Fig. 43 shows that Tight and Loose Signal Regions have similar sensitivity, cooperatively increasing the combined sensitivity. In the diagonal region of $\tilde{g}$-$\tilde{g}$ grid in Fig. 44, Soft Signal Region mainly drives the limit. The combined limits in the other regions are basically driven by the Tight Signal Region.

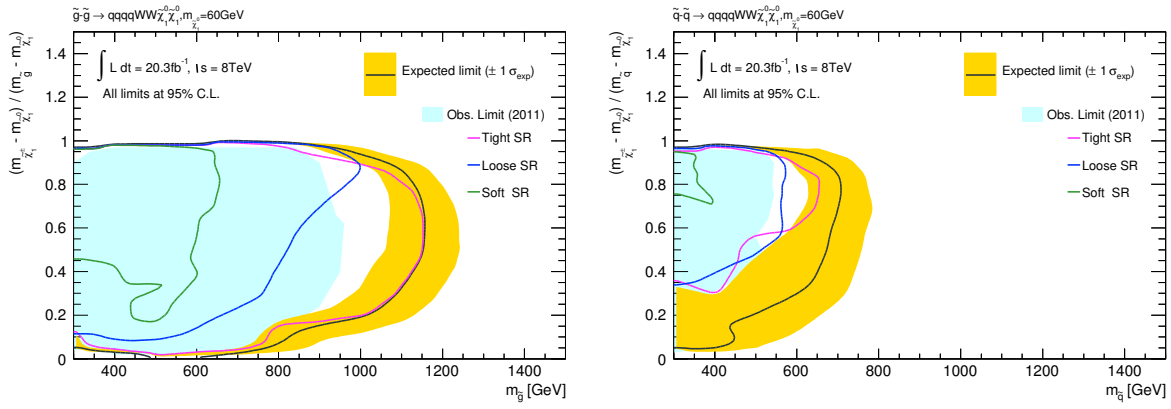

Figure 43: The expected limits are shown for Simplified Models (Grid-x) of $\tilde{g}$-$\tilde{g}$ (left) and $\tilde{q}$-$\tilde{q}$ (right) pair production. $m_{\tilde{\chi}_1^0}$ is fixed at 60 GeV and $x = (m_{\tilde{\chi}_1^\pm} - m_{\tilde{\chi}_1^0})/(m_{\tilde{g}/\tilde{q}} - m_{\tilde{\chi}_1^0})$ is taken as y-axes. The black line shows an expected limit and the yellow band corresponds to the uncertainty of the limit. The decomposed limits obtained by three separate Signal Regions are also shown in magenta (Tight SR), blue (Loose SR) and green (Soft SR) lines.

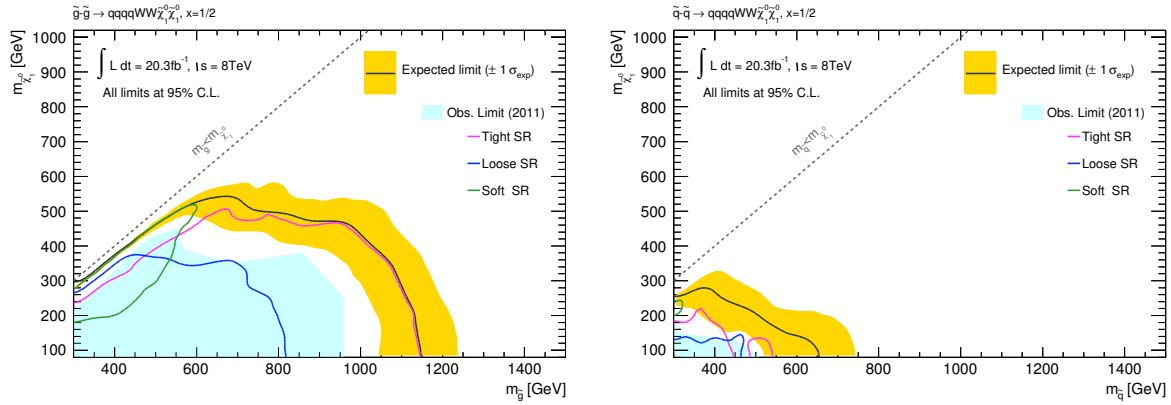

Figure 44: The expected limits are shown for Simplified Models (Half-x) of $\tilde{g}$-$\tilde{g}$ (left) and $\tilde{q}$-$\tilde{q}$ (right) pair production. $x = (m_{\tilde{\chi}_1^\pm} - m_{\tilde{\chi}_1^0})/(m_{\tilde{g}/\tilde{q}} - m_{\tilde{\chi}_1^0})$ is fixed at 1/2 and $m_{\tilde{\chi}_1^0}$ is taken as y-axes. The black line shows an expected limit and the yellow band corresponds to the uncertainty of the limit. The decomposed limits obtained by three separate Signal Regions are also shown in magenta (Tight SR), blue (Loose SR) and green (Soft SR) lines.

6 Background estimation

6.1 Multi-jet background

QCD multi-jet events are a notorious background in the LHC due to its large cross-section. A large part of QCD multi-jet events do not accompany leptons, hence the lepton requirement greatly reduces the background. However, a small fraction of QCD multi-jet events accompany a lepton due to the following reasons:

- π^0 decays into two photons. A e^+e^- pair is created when one of the photons hits the first layer of pixel tracker (photon conversion).
- Some fraction of heavy flavor hadrons decay into final states with leptons. Since most of such leptons are collinear to the jets, they are rejected by overlap removal (as discussed in Section 3.3.4). The remaining leptons that are emitted far from jets contaminate our signal region.
- $\pi^\pm$ track is mis-identified as a fake electron if the track accidentally matches to a calorimeter cluster produced by charge exchange π^0 production followed by its decay, $\pi^0 \to \gamma\gamma$.

Large cross-section of QCD multi-jets obviously exceeds our computing capacity for Monte Carlo simulation. Hence, we estimate QCD multi-jets background using data itself with a method called Matrix-Method. Matrix-Method estimates the shape and yield of QCD multi-jets from the difference between fake-enriched and fake-suppressed distributions. Details of Matrix-Method are documented in Appendix C. Missing transverse momentum of QCD multi-jet events mainly originates from $E_{\mathrm{T}}^{\mathrm{miss}}$ mis-measurement and typically quite small. Since we require at least $E_{\mathrm{T}}^{\mathrm{miss}}$>150 GeV for all regions, the QCD multi-jet component falls into one of the minor backgrounds.

6.2 W+jet and $t\bar{t}$ backgrounds

W+jets is a sub-dominant background as it satisfies the baseline topology of our analysis: $E_{\mathrm{T}}^{\mathrm{miss}}$, lepton and multiple jets. The cross-section of W+jets is also quite large compared with the other backgrounds (except for QCD multi-jets). $t\bar{t}$ has rather smaller cross-section, but the decay topology resembles supersymmetric events, which makes $t\bar{t}$ the most dominant background in many supersymmetry searches. These two backgrounds contribute more than 75% of the backgrounds in the Signal Regions. Thus a dedicated estimation is applied for these backgrounds.

6.2.1 Control Regions

Monte Carlo simulation is employed to estimate W+jets and $t\bar{t}$ backgrounds. But Monte Carlo simulation is not so accurate to calculate the processes with multi-jets. The number of jet distribution is not reproduced in most of the generators used in the ATLAS analyses. The discrepancy often amounts to O(10)% level, which is quite large compared with the other systematics. To reduce the uncertainty, W+jets and $t\bar{t}$ Monte Carlos are normalized to data in a dedicated "Control Region" (CR), in which the same jet selection is required as in the Signal Regions, and a normalization factor (or often called as scale factor) absorbs the data-MC discrepancy. In addition, the Control Region is set closer to the Signal Region in $E_{\mathrm{T}}^{\mathrm{miss}}$-$m_{\mathrm{T}}$ plane to avoid making a big extrapolation over $E_{\mathrm{T}}^{\mathrm{miss}}$ and m_{T}. Table 13 shows the kinematic selections of Control Regions corresponding to the Loose, Tight and Soft Signal Regions. The regions are illustrated on $E_{\mathrm{T}}^{\mathrm{miss}}$-$m_{\mathrm{T}}$ plane in Fig. 45.

One important issue on defining Control Region is signal contamination. Assuming the existence of supersymmetry signals, especially the ones with large cross-sections, the signal "contaminates" the Control Regions and the number of observed events is increased. Once signal contamination occurs, the

normalization factors of backgrounds are overestimated, which leads to a larger background estimation in the Signal Region, spoiling discovery sensitivity.

Figure 46 show the fraction of signal contamination in the Control Regions for Simplified models. Plots on the left column show $\tilde{g}$-$\tilde{g}$ production of Half-x grid, in which a chargino mass is set to a halfway of gluino and LSP masses, and the right plots show $\tilde{g}$-$\tilde{g}$ production of Grid-x with varying chargino mass (see Table 11 for summary). The results for Tight, Loose and Soft Control Regions are placed from top to bottom. W+jets and $t\bar{t}$ Control Regions, also electron and muon channels are all combined. The contour lines show contaminations of signals in the Control Regions, which are defined as

$$\text{Signal Contamination} = \frac{N_{\text{Sig}}}{N_{\text{Bkg}}}, \tag{68}$$

where N_{Sig} and N_{Bkg} are numbers of signal and backgrounds in the Control Region. The signal contamination around the expected sensitivity limits is estimated at about 20% in the worst case, Which is small enough for our analysis. In limit calculation, the normalization factors and signal yields are all fitted simultaneously, taking signal contamination into account. So the limit is always correct even with a heavy signal contamination. Only drawback is a loss of sensitivity.

Variable	Tight CR	Loose CR	Soft CR
Pre-selections Same as the SRs			
Specific selections			
Number of jets	$N_{\text{jet}}^{40} \geq 5$	$3 \leq N_{\text{jet}}^{40} < 5$	$N_{\text{jet}}^{30} \geq 3$
Leading jet p_{T}	>120 GeV	>80 GeV	>100 GeV
m_{T}	80-150 GeV	80-120 GeV	60-100 GeV
$E_{\text{T}}^{\text{miss}}$	250-350 GeV	150-250 GeV	200-300 GeV
$m_{\text{eff}}^{\text{incl30}}$	>800 GeV	>800 GeV	>500 GeV

Table 13: Kinematic selections defining the Control Regions.

6.2.2 Validation Regions

W+jets and $t\bar{t}$ samples are extrapolated to the Signal Regions along $E_{\text{T}}^{\text{miss}}$ and m_{T} as illustrated in Fig. 45. Two Validation Regions (VR) are defined to validate the extrapolation for each Signal Region. The Validation Regions are defined with the same lepton selections, jet requirements and m_{eff} selection as the Control Regions, but one of m_{T} and $E_{\text{T}}^{\text{miss}}$ is set to the same as the Signal Region. Figure 45 illustrates the Validation Regions on m_{T}-$E_{\text{T}}^{\text{miss}}$ plane. The Validation Region with higher $E_{\text{T}}^{\text{miss}}$ selection is denoted as VR ($E_{\text{T}}^{\text{miss}}$), while the one with higher m_{T} selection is written as VR (m_{T}). Tables 14 and 15 summarize the kinematic selections of the Validation Regions for m_{T} and $E_{\text{T}}^{\text{miss}}$, respectively.

Signal contamination is serious for the Validation Regions because they are set so close to the Signal Regions. However, if no significant discrepancy is observed both in the Signal and Validation Regions, the correctness of background estimation and the absence of signal are simultaneously concluded.

6.2.3 $t\bar{t}$ correction

Since supersymmetry searches look into extreme phase spaces such as many jets and large m_{eff}, where general-purpose event generators are not fully tuned, we introduce corrections before using them for

Variable	Tight VR (m_{T})	Loose VR (m_{T})	Soft VR (m_{T})
Preselections Same as the SRs			
Specific selections			
Number of jets	$N_{\mathrm{jet}}^{40} \geq 5$	$3 \leq N_{\mathrm{jet}}^{40} < 5$	$N_{\mathrm{jet}}^{30} \geq 3$
Leading jet p_{T}	>120 GeV	>80 GeV	>100 GeV
m_{T}	>150 GeV	>120 GeV	>100 GeV
$E_{\mathrm{T}}^{\mathrm{miss}}$	250-350 GeV	150-250 GeV	200-300 GeV
$m_{\mathrm{eff}}^{\mathrm{incl30}}$	>800 GeV	>800 GeV	>500 GeV

Table 14: Kinematic selections defining the Validation Regions to check the extrapolation on m_{T}.

Variable	Tight VR ($E_{\mathrm{T}}^{\mathrm{miss}}$)	Loose VR ($E_{\mathrm{T}}^{\mathrm{miss}}$)	Soft VR ($E_{\mathrm{T}}^{\mathrm{miss}}$)
Preselections Same as the SRs			
Specific selections			
Number of jets	$N_{\mathrm{jet}}^{40} \geq 5$	$3 \leq N_{\mathrm{jet}}^{40} < 5$	$N_{\mathrm{jet}}^{30} \geq 3$
Leading jet p_{T}	>120 GeV	>80 GeV	>100 GeV
m_{T}	80-150 GeV	80-120 GeV	60-100 GeV
$E_{\mathrm{T}}^{\mathrm{miss}}$	>350 GeV	>250 GeV	>300 GeV
$m_{\mathrm{eff}}^{\mathrm{incl30}}$	>800 GeV	>800 GeV	>500 GeV

Table 15: Kinematic selections defining the Validation Regions to check the extrapolation on $E_{\mathrm{T}}^{\mathrm{miss}}$.

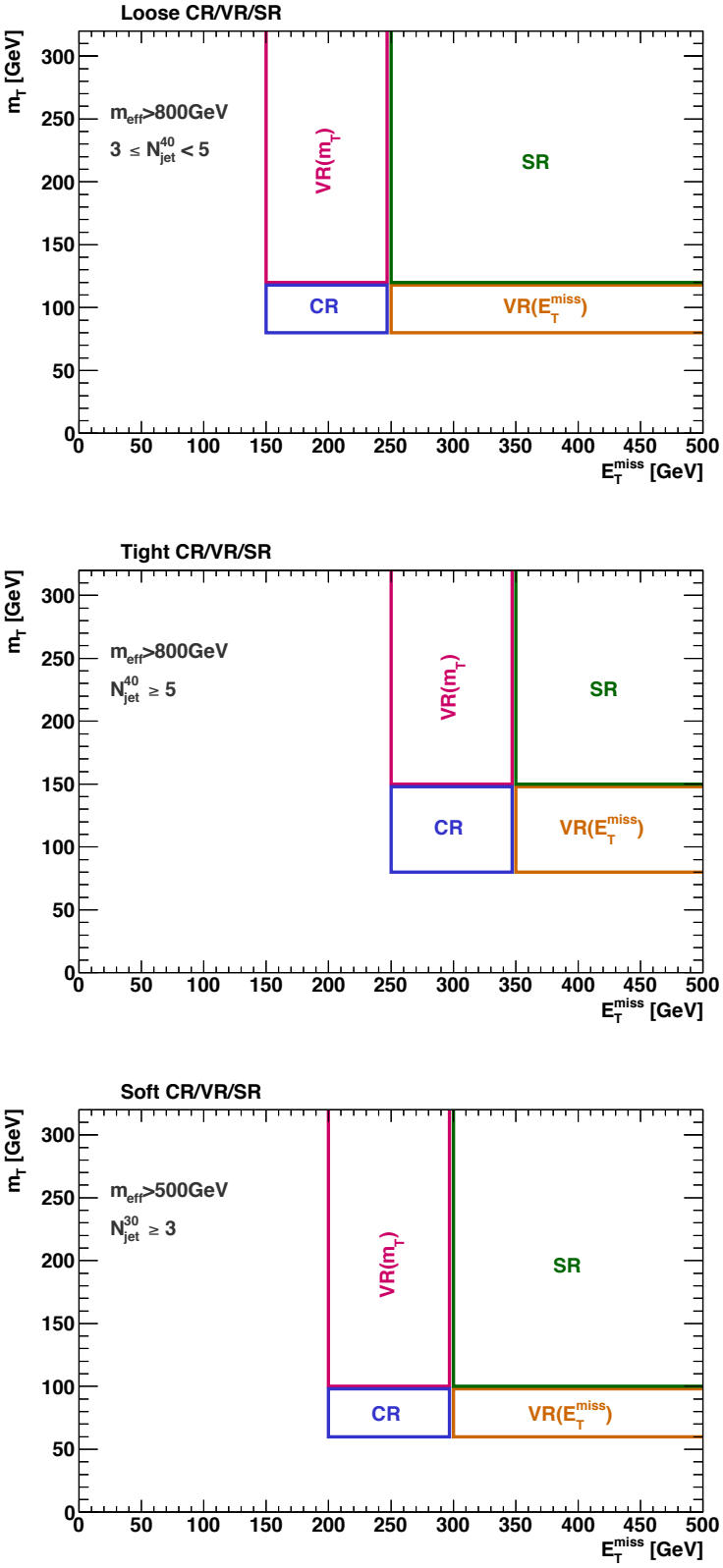

Figure 45: Control, Validation and Signal Region are shown on $E_{\mathrm{T}}^{\mathrm{miss}}$-$m_{\mathrm{T}}$ plane. Tight, Loose and Soft regions are placed from top to bottom.

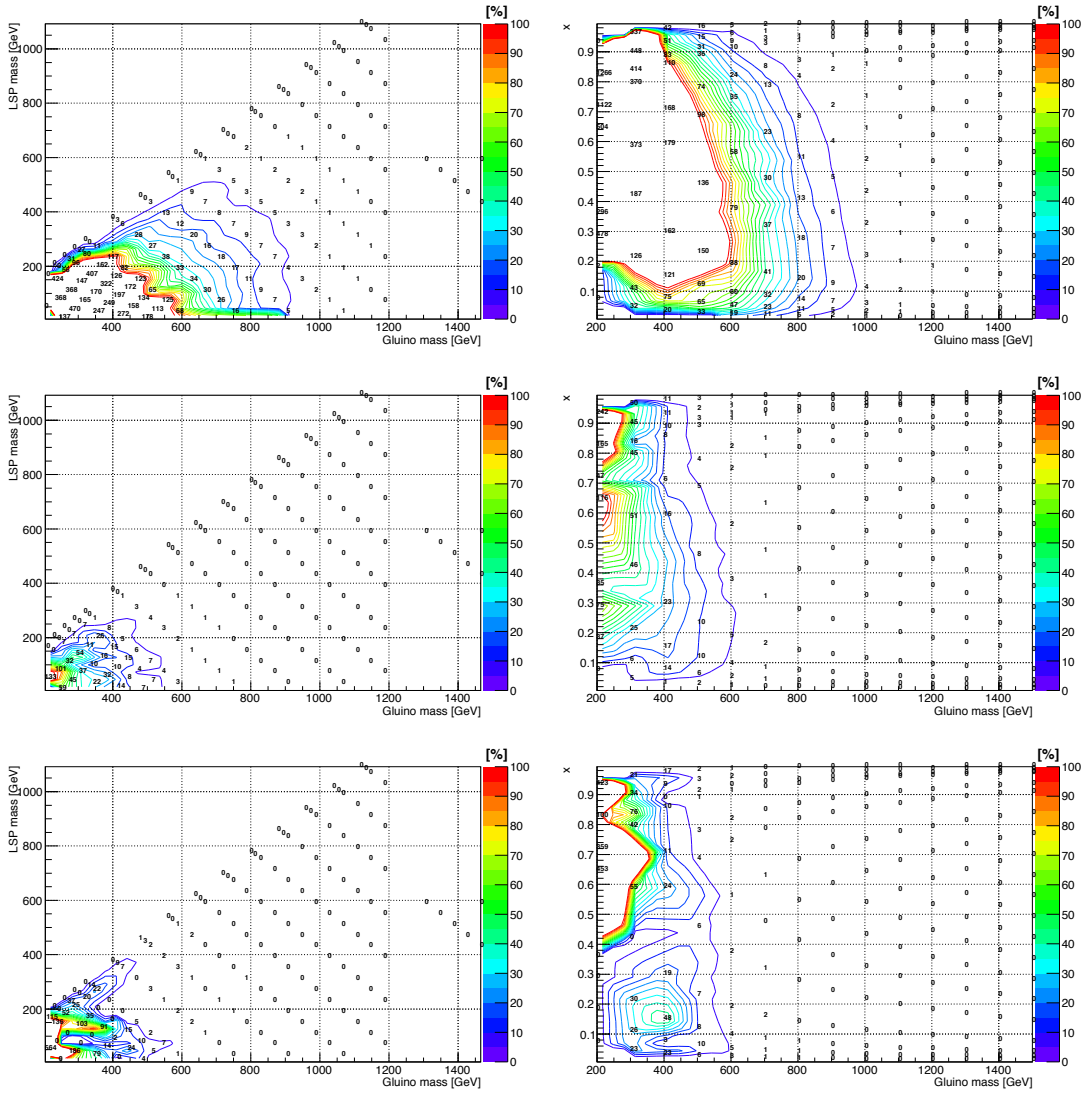

Figure 46: Signal contamination are shown for several signal models. Plots on the left column show $\tilde{g}$-$\tilde{g}$ production of Half-x grid and the right plots show $\tilde{g}$-$\tilde{g}$ production of Grid-x (see Table 11 for summary). The results for Tight, Loose and Soft Control Regions are placed from top to bottom. W+jets and $t\bar{t}$ Control Regions, also electron and muon channels are all combined. The z-axes show the contamination of signals in the Control Regions.

background estimation. One is the normalization as discussed in Section 6.2.1, which reduces the uncertainty on the number of jets by requiring the same jet selections between the Control and Signal Regions. This method is called as semi data-driven method since it reduces the dependence on Monte Carlo by using data. The extrapolation from a Control Region to Signal Region relies on Monte Carlo shape, which is not completely correct for extreme phase spaces. Therefore, we correct the shape using data after enhancing background components. We start from the primary background in our Signal Regions, i.e. $t\bar{t}$.

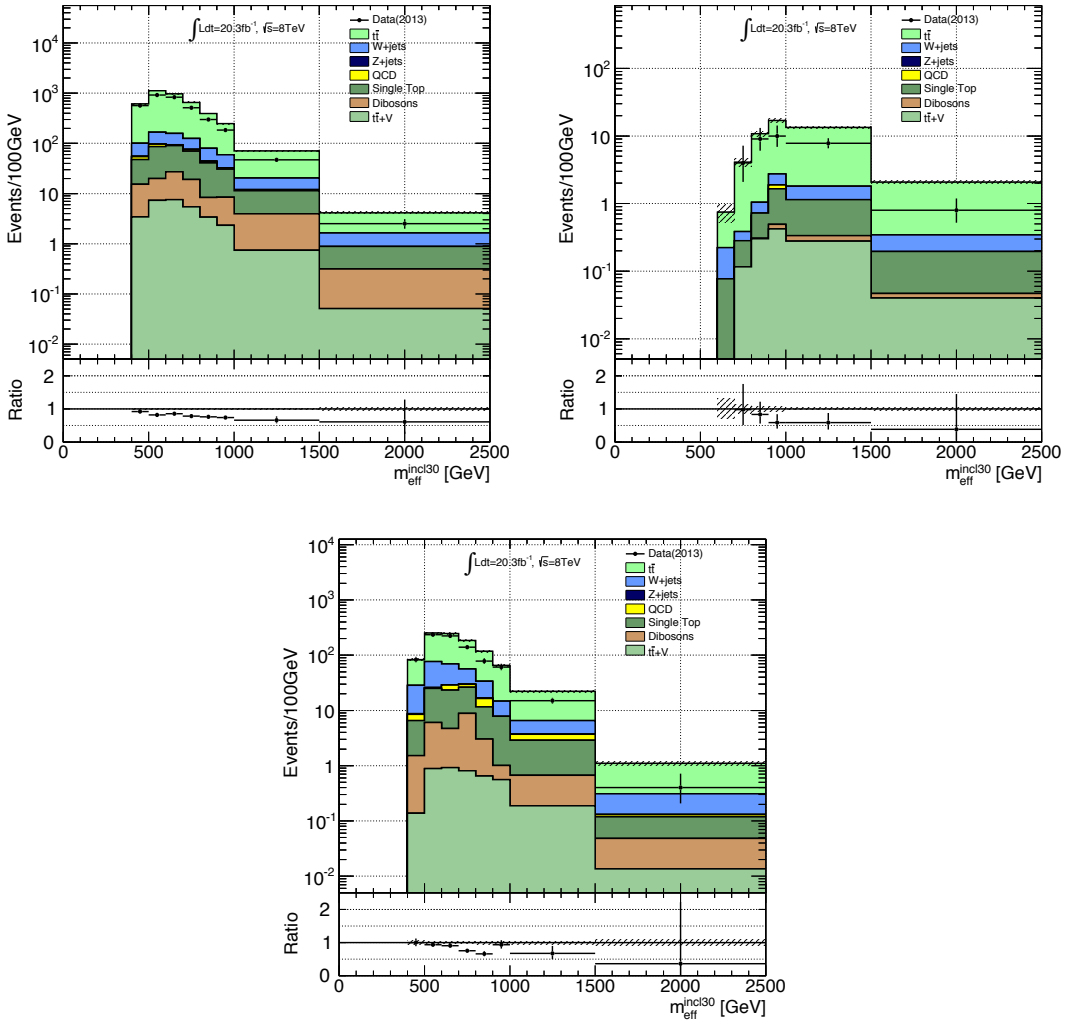

Figure 47: Data-MC comparison for m_{eff}. The right, left and bottom plots show Tight, Loose and Soft regions, respectively. In order to show the events in a wide phase space, upper limits for m_{T} and $E_{\mathrm{T}}^{\mathrm{miss}}$ are eliminated. To enhance $t\bar{t}$ events, at least one b-tagged jet with $p_{\mathrm{T}}^{\mathrm{jet}}$>40 GeV is required in the leading three jets.

Figures 47 show the m_{eff} distributions after applying Loose (left), Tight (right) and Soft (bottom) Control Region selections. In order to show a wide phase space, upper limits for m_{T} and $E_{\mathrm{T}}^{\mathrm{miss}}$ are eliminated. At least one b-tagged jet is required in the leading three jets with p_{T}>40 GeV to enhance $t\bar{t}$ events. Enhancements of number of events in simulated data for large m_{eff} are observed, which is also clearly

visible in the ratio plot in the bottom panels. The discrepancy is purely a background issue because the number of possible signal events is much smaller than the discrepancy observed here. Also note that $t\bar{t}$ is dominant over the other backgrounds, which ensures $t\bar{t}$ is responsible for the slopes. $E_{\mathrm{T}}^{\mathrm{miss}}$ and m_{T} are also examined, but they seem quite fine without any significant deviations. The extrapolation from the Control Regions to Signal or Validation Regions basically goes along $E_{\mathrm{T}}^{\mathrm{miss}}$ and m_{T}, therefore the final results are not affected much by the m_{eff} slope in principle. However, the kinematic selections introduce implicit biases on the population of events in m_{eff}, which indirectly spoils the extrapolation from Control to Signal Regions.

Several items are checked before applying corrections, so as to confirm that the slopes are not caused by instrumental problems but come from the generator:

- Pile-up jets contribute to m_{eff} and its uncertainty may impact the slope. This is checked by comparing m_{eff} with several pile-up suppression options for jets. No big difference is found.
- JES uncertainty (see Section 3.2.4) causes a shift on jet energies. But JES uncertainty is found to be too small to cover such a big discrepancy.
- Since at least one b-tagged jet is required in the plots, b-tagging efficiency and its uncertainty have an impact on the m_{eff} shape. To make sure that b-tagging is not the cause of the slope, b-tagging is removed and m_{T}>150 GeV is applied to ensure the dominance of $t\bar{t}$ events. The m_{eff} slope persists even with this selection criteria, which implies that b-tagging is nothing to do with the slope.

These items ensure that the problem is in the event generator, not in the instrumental side. Considering the fact that the significant slope is observed only in m_{eff}, not in $E_{\mathrm{T}}^{\mathrm{miss}}$ and m_{T}, the kinematics of $t\bar{t}$ system seems well reproduced in the generator, but rather additional jets may have a problem. Figure 48 gives a confirmation of this hypothesis. H_T^{ISR} defined below is plotted after requiring two b-tagged jets (b-jet1, b-jet2),

$$H_T^{\mathrm{ISR}} = \sum_{\mathrm{jets,p_T>40\ GeV}}^{i} p_T^i - (p_T^{b-\mathrm{jet1}} + p_T^{b-\mathrm{jet2}}). \tag{69}$$

For $t\bar{t}$ events, this variable gives the p_{T} sum of ISR, excluding the contribution from $t\bar{t}$ decay. In addition to two b-jets requirement, the following kinematic selections are applied to enrich leptonic decay samples of $t\bar{t}$ events: $E_{\mathrm{T}}^{\mathrm{miss}}$>40 GeV, two different flavor leptons and the invariant mass of the leptons should exceeds 100 GeV. The Monte Carlo clearly shows a slope-like discrepancy from data, which leads us to conclude that ISR are poorly reproduced by the generator.

$t\bar{t}$ events are generated at Next-to-Leading order Matrix-Element calculation for the core process and the additional jets (ISR) are emulated by Parton-Shower algorithm. As discussed in Section 4.2, Parton-Shower algorithm is based on the collinear approximation, therefore has a larger uncertainty. The size of the impact caused by this uncertainty is illustrated in Fig. 49. The following items are modified within the uncertainties provided from the ATLAS generator group [75, 42] to produce the systematic samples compared here.

- Parton-Shower algorithm stops ISR radiation when the incoming quark or gluon obtain a large virtuality and then passes the parton to Matrix-Element calculation. The maximum virtuality threshold is varied within the uncertainty.
- Λ_{QCD} for radiations from ISR parton is varied within its uncertainty.
- Renormalization scale (see Section 4.2) is varied.

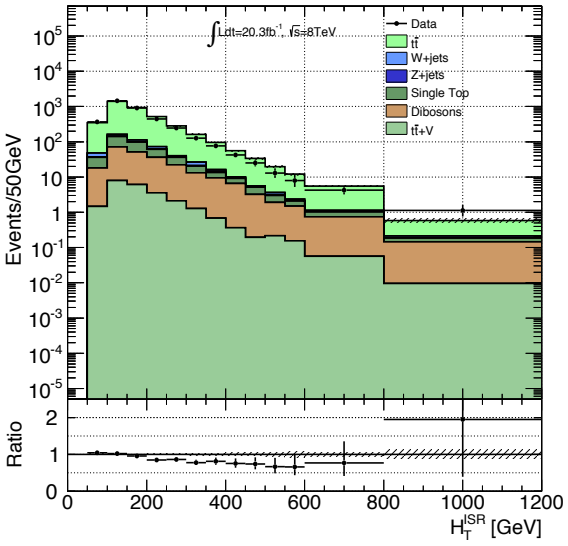

Figure 48: H_T^{ISR} after requiring two different flavor leptons, $E_{\mathrm{T}}^{\mathrm{miss}}$>40 GeV, di-lepton invariant mass m_{ll} > 100 GeV and two b-tagged jets.

A $O(10)$% level discrepancy is observed in H_T^{ISR}, which could explain the discrepancy observed in m_{eff}.

We define a simple 1-dimensional shape correction as a function of m_{eff}. We can ensure to remove the m_{eff} slope by this correction, however, for $E_{\mathrm{T}}^{\mathrm{miss}}$ and m_{T}, which are used in the extrapolation from the Control Regions to the Signal Regions, are not considered in the correction. Therefore, a systematic error should be included to cover a possible discrepancy introduced by the correction, which will be discussed later.

A first order polynomial function with an upper threshold is defined as follow,

$$f(m_{\mathrm{eff}}) = \begin{cases} p_0 + p_1 \cdot m_{\mathrm{eff}} & (m_{\mathrm{eff}} < E_{\mathrm{thres}}) \\ p_0 + p_1 \cdot E_{\mathrm{thres}} & (m_{\mathrm{eff}} \geq E_{\mathrm{thres}}), \end{cases} \tag{70}$$

where p_0 and p_1 are the parameters which will be determined in the fitting. E_{thres} is the threshold beyond which the fitting function is fixed as a constant. This is required because there are no enough events in large m_{eff} region thus the fitting does not make sense any more. We do not make a guess for such region, but use the final value we're sure. Based on available statistics, E_{thres} is defined for each region. Then, a fitting is performed on m_{eff} to determine the parameters. The same kinematics as the Control Region is required without m_{T} and $E_{\mathrm{T}}^{\mathrm{miss}}$ upper thresholds, but the events passing the Signal Region selections are all vetoed to be blinded to signal events.

Figure 50 shows the fitted results of m_{eff} for the Loose Region. Fitted distribution of $E_{\mathrm{T}}^{\mathrm{miss}}$ is also shown on the right. The black points show data and the gray line shows the other backgrounds except for $t\bar{t}$. The blue line shows the total backgrounds including the original $t\bar{t}$ without any correction and the red line shows the ones with the slope correction. The bottom panel shows the ratios with respect to the red line. For reference, a first order polynomial fit for the remaining slope in the corrected backgrounds is shown as a green line. The original slope is clearly eliminated by the correction in all m_{eff} range. The $E_{\mathrm{T}}^{\mathrm{miss}}$ plot does not show significant change on the slope, but shows a small improvement in the agreement between data and Monte Carlo. In the same way, the m_{eff} slope is corrected in the Tight and Soft regions.

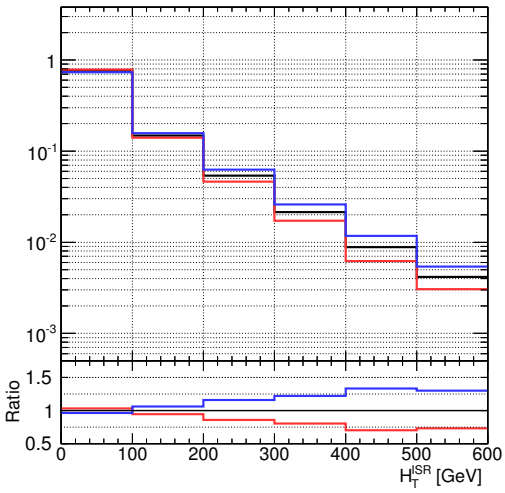

Figure 49: H_T^{ISR} distributions of two different parton shower tunes. The Red (blue) line represents the configuration for less (more) parton shower emission. H_T^{ISR} is defined in Eq. 69. No kinematic selection is applied. The variations are symmetrized.

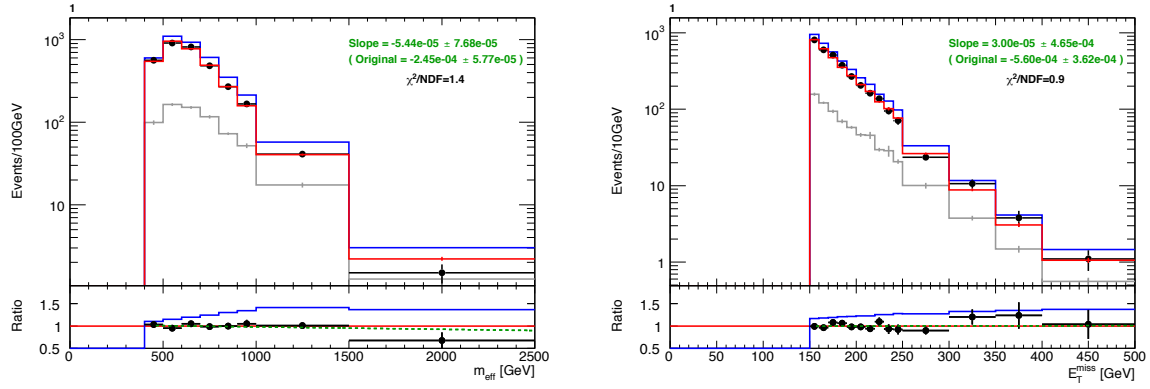

Figure 50: Fit results are shown for the Loose Region, m_{eff} is on the left and $E_{\mathrm{T}}^{\mathrm{miss}}$ is on the right. The black points show data, the gray line shows the other backgrounds except for $t\bar{t}$. The blue line shows the backgrounds with the original $t\bar{t}$ without any correction, and the red line shows the ones with the slope correction. The bottom panel shows the ratios with respect to the red lines, i.e. the corrected backgrounds. For reference, a first order polynomial fit for the remaining slope in the corrected backgrounds is shown as a green line.

Table 16 shows the fitted parameters obtained in Loose, Tight and Soft Regions. For Tight Region, a loosened kinematic selections are used to increase the statistics, keeping the same number of jets: the thresholds for $p_{\mathrm{T}}^{\mathrm{jet5}}$, m_{T} and $E_{\mathrm{T}}^{\mathrm{miss}}$ are lowered to 30 GeV, 60 GeV and 200 GeV, respectively. p_1 values are all around ~ -40 %/TeV, which implies that the slope correction does not depend on the jet topologies strongly in our target phase-spaces. The slight topology dependency is explained by a difference in ISR contributions due to different jet selections. p_0 is chosen so that the correction function $f(m_{\mathrm{eff}})$ gives 1 at $m_{\mathrm{eff}} = 500$ GeV.

Region	E_{thres} [TeV]	p_1 [%/TeV]
Tight	1.5	-24 ± 13
Loose	1.2	-42.6 ± 7.5
Soft	1.2	-56.4 ± 9.8

Table 16: Fit results for m_{eff} corrections for $t\bar{t}$. E_{thres} is the end-point of the slope correction and p_1 is the slope-correcting parameter.

As this m_{eff} correction is not an ideal way of correction but rather an ad-hoc solution, there exists a possibility of some variable being strained in a wrong way, which should be included as a systematic error. As shown later in Section 6.2.6, the kinematic distributions of $E_{\text{T}}^{\text{miss}}$ and m_{T} in the Validation Regions do not show such strains, or rather the correction seems to fix the small slopes found in the original distributions (This is also visible in $E_{\text{T}}^{\text{miss}}$ distribution in Fig. 50 on the right.). So, at least concerning the extrapolation from Control to Validation Regions, there is no need to introduce a punishment for the strain. However, a possibility of having a strain in the extrapolation to the Signal Regions cannot be excluded as data and Monte Carlo comparison in the Signal Region is not possible due to signal contamination.

To assign an uncertainty in the Signal Regions, first we evaluate the kinematic selection dependency of p_1 by varying E_{thres}, $E_{\text{T}}^{\text{miss}}$, m_{T}, N_{jet} and $p_{\text{T}}^{\text{jet}}$. The largest variation originates in N_{jet} selection and the other contributions are found to be small. The Control and Signal Regions basically share common jet selections, but the number of jets distributions may differ by the other kinematic biases. The difference is found to be well smaller than 2 jets in all regions, therefore we take the variations of p_1 values obtained in Tight and Loose regions and assign an uncertainty of 50%.

Table 17 summarizes the impacts of the correction on the transfer factor along $E_{\text{T}}^{\text{miss}}$ and m_{T}. They are estimated by calculating the ratio of the transfer factors with and without the correction. As the numerator and denominator have the same events in common, no statistical error is assigned. In average, the impact on m_{T} transfer factors seem much smaller than those of $E_{\text{T}}^{\text{miss}}$. The largest variation is 27% for the $E_{\text{T}}^{\text{miss}}$ transfer factor of Soft region, which is mainly because the m_{eff} selection of Soft Regions is wider than the other regions. As we assume a 50% error for slope correction, an uncertainty of 14% (= 27% × 50%) is assigned for the transfer factor. The uncertainties for the other corrections are also applied in the same way.

Region	Impact		
	m_{T}	$E_{\text{T}}^{\text{miss}}$	Total
Tight	+0.2%	-7.8%	-7.6%
Loose	+0.2%	-5.0%	-4.8%
Soft	-6.6%	-20.7%	-27.3%

Table 17: Impacts of slope corrections. The impact is defined as the size of change in the transfer factor from the Control to Validation Regions with and without the slope correction.

6.2.4 W+jets correction

W+jets events are generated at Leading-Order in Matrix-Element evaluation. Compared with Next-to-Leading-Order calculation, Leading-Order calculation has a large dependency on renormalization scale. A mis-modeling in α_S would lead to a wrong estimation of jet activity. Since W boson is kicked back against the sum of jets momentum, the momentum of W boson might also be wrongly predicted. As a result, the decay products of W boson, a lepton and a neutrino, also have wrong momentum. A problem arises here because the transfer factor from Control Regions to Signal Regions are mainly determined by the extrapolation on $E_{\mathrm{T}}^{\mathrm{miss}}$, the momentum of the neutrino.

Figures 51 show $E_{\mathrm{T}}^{\mathrm{miss}}$ (left) and m_{eff} (right) distributions in a W+jets enriched region, where 1 lepton, $E_{\mathrm{T}}^{\mathrm{miss}}$>100 GeV and $p_{\mathrm{T}}^{\mathrm{jet1}}$>80 GeV are required. If the event has a b-tagged jet, then the event is vetoed to reduce $t\bar{t}$ contribution. A clear discrepancy is observed in the ratio plots in both of the distributions. The slope is also observed with different kinematic selections. To cure the slope, we introduce a slope correction function for W+jets in a similar way as the $t\bar{t}$ correction.

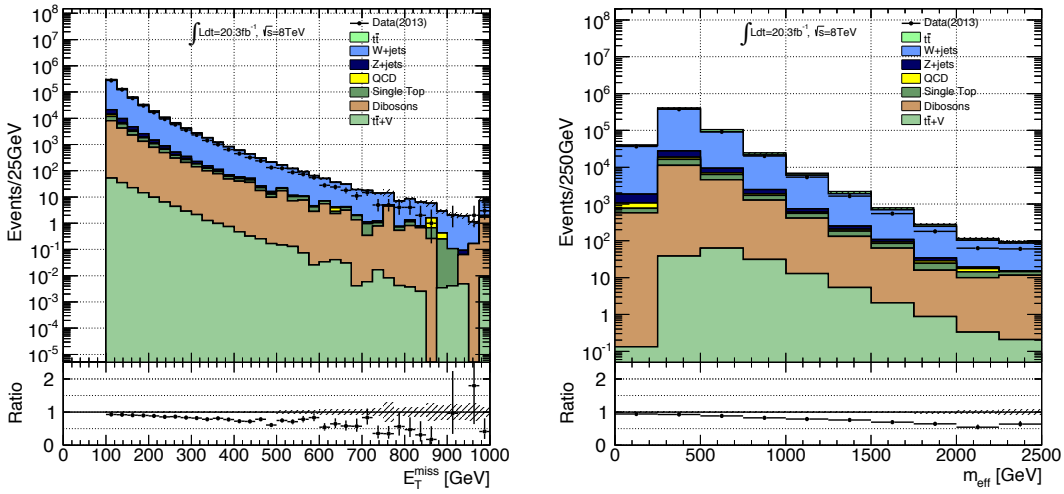

Figure 51: $E_{\mathrm{T}}^{\mathrm{miss}}$ (left) and m_{eff} (right) distributions after requiring 1 lepton, $E_{\mathrm{T}}^{\mathrm{miss}}$>100 GeV and $p_{\mathrm{T}}^{\mathrm{jet1}}$>80 GeV. The event with a b-tagged jet is vetoed to reduce $t\bar{t}$ contribution.

Before introducing a correction, one need to confirm that the slope is caused by a mis-modeling of the generator, not by instrumental problems nor mis-calibrations. $Z^0 \rightarrow ll$ events are selected and a quantity that is calculated purely from leptons is investigated so as to exclude JES uncertainty, which is the largest and dominant uncertainty in the ATLAS detector, Figure 52 (left) show p_T^{ll} distribution after requiring the following conditions:

- Two same-favor leptons.
- The leptons should have the opposite charges to each other.
- The di-lepton invariant mass m_{ll} should be matched to the Z boson mass : 66 GeV $< m_{ll} <$ 116 GeV.

This analysis is free from JES uncertainty as no jet condition is required. The uncertainty on lepton energy scale, lepton energy resolution and lepton efficiency are all at O(1)% level, thus negligible. Note that the same generator is used to produce Z+jets and W+jets, hence the insights obtained from Z+jets

is applicable to W+jets. A clear slope is observed in p_T^{ll} distribution, which means the transverse momentum of Z^0 boson is not fully reproduced by the generator. This conclusion encourages us to invent a correction function and apply it to W+jets events.

The following $H_T^{\rm ISR}$ is defined to see if ISR are well described for $Z^0 \to ll$,

$$H_T^{\rm ISR} = \sum_{\rm jets, p_T>30\ GeV}^{i} p_T^i. \tag{71}$$

The right plot of Fig. 52 shows $H_T^{\rm ISR}$ distribution, which clearly shows a discrepancy. Therefore ISR description seems to have a problem.

As we observed two large discrepancies in p_T^{ll} and $H_T^{\rm ISR}$, one can propose two correction functions: first one is a method based on the transverse momentum of the boson and the second is the one based on ISR activity. A detailed study shows that the latter choice seems better to correct all kinematic variables.

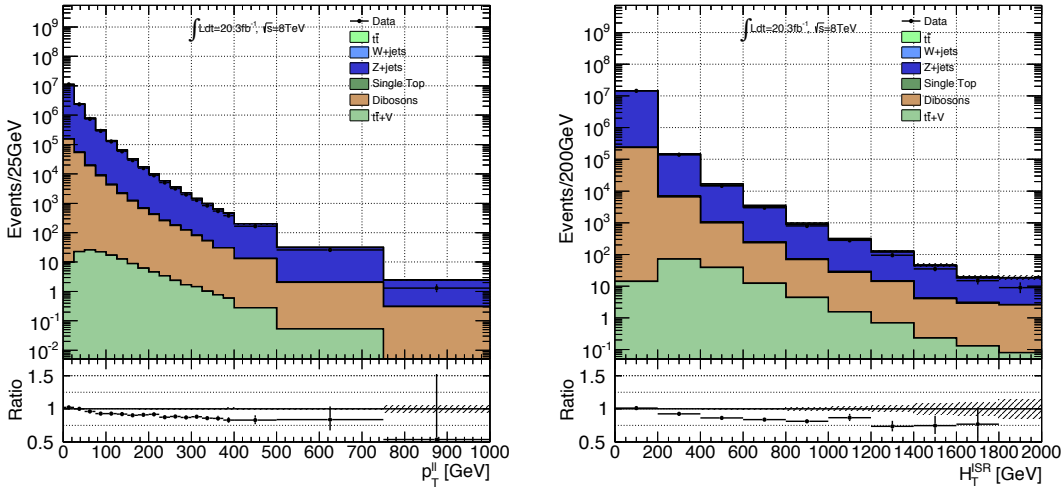

Figure 52: (Left) p_T^{ll} distribution after requiring two same-flavor leptons with opposite charges. An invariant mass selection of 66 GeV $< m_{ll} <$ 116 GeV is applied to obtain a good purity of Z+jets events. No jet is required, thus no JES uncertainty concerns. (Right) $H_T^{\rm ISR}$ is plotted with the same selection.

The following correction is introduced as a function of $m_{\rm eff}$,

$$f(m_{\rm eff}) = \begin{cases} p_0 + p_1 \cdot m_{\rm eff} & (m_{\rm eff} < E_{\rm thres}) \\ p_0 + p_1 \cdot E_{\rm thres} & (m_{\rm eff} \geq E_{\rm thres}), \end{cases} \tag{72}$$

where p_0 and p_1 are the parameters which will be determined in the fitting. $E_{\rm thres}$ is the threshold beyond which the fitting function is fixed to a constant. For Soft and Loose Regions, the same selections of jets are applied as the Control Regions, while for Tight Region the thresholds on the leading jet $p_{\rm T}$ and the fifth leading jet $p_{\rm T}$ are loosened to 80 GeV and 30 GeV to enhance the number of events. The soft lepton requirement ($p_{\rm T}^{\ell} < 25$ GeV) kills lots of W+jets events, thus the lepton selection is replaced to that of Hard Lepton analysis. As the lepton $p_{\rm T}$ has only a small contribution to $m_{\rm eff}$, this modification should not make a big bias in the results.

Table 18 shows the fitted parameters for the Tight, Loose and Soft Regions. The fitted p_1 values are all around ~ -35 %/TeV within the uncertainty, which suggests the slope correction does not depend on the jet topologies strongly in our target phase-spaces. The fitted result for the Loose region is shown on

the right plot of Fig. 53 and also $E_{\mathrm{T}}^{\mathrm{miss}}$ distribution after applying the same correction is shown on the right. The slope of m_{eff} is eliminated and also $E_{\mathrm{T}}^{\mathrm{miss}}$ becomes flat after the correction. This tendency is also true for Tight and Soft Regions. p_0 is chosen so that the correction function $f(m_{\mathrm{eff}})$ gives 1 at $m_{\mathrm{eff}} = 500$ GeV.

The uncertainty of the correction is assigned following the same way as $t\bar{t}$. As shown in Table 18, an uncertainty of ~40% is taken from the difference between p_1 values in Tight and Loose regions. Table 19 summarizes the impacts of correction on the transfer factor along $E_{\mathrm{T}}^{\mathrm{miss}}$ and m_{T}. As the numerator and denominator have the same events in common, no statistical error is assigned. In average, the impact on the m_{T} transfer factors seem much smaller than those of $E_{\mathrm{T}}^{\mathrm{miss}}$. The worst systematic error is 8% (= 20.2% × 40%) for the $E_{\mathrm{T}}^{\mathrm{miss}}$ transfer factor of the Tight Region and the others are much smaller. A similar correction on Z+jets shows that the m_{eff} correction fixes the discrepancy in p_T^{ll} almost completely, which means that, for W+jets, $E_{\mathrm{T}}^{\mathrm{miss}}$ is also fixed because it is determined by boson p_{T}.

The plots after applying the corrections on $t\bar{t}$ and W+jets are shown in Fig. 54. The combined selections of the Control and Validation Regions are used to choose the events (details will be discussed in Section 6.2.6). The magenta lines show the total backgrounds before applying $t\bar{t}$ and W+jets corrections. Since the similar m_{eff} regions are already selected, the impact of the slope correction does not look so significant, but we see the agreement is improved with the corrections.

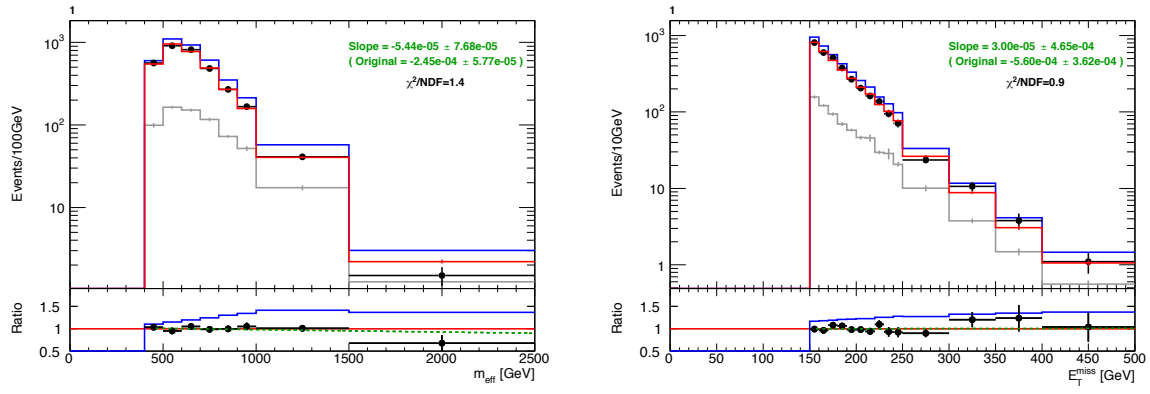

Figure 53: Fit results are shown for the Loose region, m_{eff} is on the left and $E_{\mathrm{T}}^{\mathrm{miss}}$ is on the right. Black points show the data, the gray line shows the other backgrounds except for W+jets. The blue line shows the backgrounds with the original W+jets without any correction, and the red line shows the ones with the slope correction on W+jets sample. The bottom panel shows the ratios with respect to the red lines. For reference, the green line shows a first order polynomial fit for the remaining slope in the corrected backgrounds.

Region	E_{thres} [TeV]	p_1 [%/TeV]
Tight	1.5	-48.4 ± 9.0
Loose	1.2	-34.7 ± 6.3
Soft	1.2	-30.7 ± 5.4

Table 18: Fit results for m_{eff} corrections for W+jets.

Region	Impact		
	m_{T}	$E_{\mathrm{T}}^{\mathrm{miss}}$	Total
Tight	-0.2%	-20.0%	-20.2%
Loose	-0.2%	-3.1%	-3.3%
Soft	-0.2%	-10.0%	-10.2%

Table 19: Impacts of the slope correction. The impact is defined as the amount of the changes in the transfer factor from the Control to Validation Regions with and without correction.

6.2.5 Fitting in the Control Regions

Tables 29-31 (in Appendix D) show the fitted results for Tight, Loose and Soft Control Regions. The errors include all the statistical and systematic errors. Note that the errors have correlations, thus the total size of errors differs from the ones obtained by a simple square-sum. As discussed in the first part of this section, normalization factors are expected to differ for each jet selections. Therefore three pairs of parameters are prepared for Tight, Loose and Soft regions, each for W+jets and $t\bar{t}$. In total, six normalization factors are determined in the fitting. Table 20 summarizes the fitted scale factors. The normalization factors are consistent with 1 within the uncertainties. The errors are mainly composed of statistical error and JES uncertainty with roughly the same contributions. JES uncertainty is absorbed by the normalization factors here, resulting in a great reduction in the Signal Regions. Third error source is b-tagging uncertainty, but the contribution is two (Loose, Soft) or five (Tight) times smaller than JES uncertainty.

Region	Scale Factor	
	$t\bar{t}$	W+jets
Tight	0.67±0.32	0.76±0.61
Loose	0.95±0.22	0.83±0.16
Soft	1.09±0.23	0.77±0.19

Table 20: Scale factors obtained in the fitting.

6.2.6 Data/MC comparison

Figures 54 show $E_{\mathrm{T}}^{\mathrm{miss}}$ (left) and m_{T} (right) distributions for Tight, Loose and Soft Regions. For $E_{\mathrm{T}}^{\mathrm{miss}}$ plots, the Control Region (CR) selections without the upper limit on $E_{\mathrm{T}}^{\mathrm{miss}}$ are applied to examine the entire $E_{\mathrm{T}}^{\mathrm{miss}}$ range. The region is equal to the sum of phase spaces spanned by CR and VR ($E_{\mathrm{T}}^{\mathrm{miss}}$). Similarly, for m_{T} plots, the Control Region selections without the upper limit on m_{T} are applied, which is equal to the phase space spanned by CR and VR (m_{T}). Here the error band includes JES uncertainty and statistical uncertainty of Monte Carlo. The background, which is dominated by $t\bar{t}$ and W+jets, describes the data points quite well within the uncertainties. No specific trend is observed in the plots, which confirms that $E_{\mathrm{T}}^{\mathrm{miss}}$ and m_{T} shapes are correctly reproduced, therefore the extrapolation from the Control Regions to the Validation Regions should also be correctly described.

Tables 32-37 (in Appendix E) give quantitative validations of the correctness, which show the number of observed and expected events in the Validation Regions. The observed numbers are all consistent with the background expectations within the errors, which contain statistical and systematic errors. Note that uncertainties mainly come from the normalization uncertainties in the Control Regions.

These results confirm that the extrapolation along $E_{\mathrm{T}}^{\mathrm{miss}}$ and m_{T} are correctly described. As the entire extrapolation from the Control to Signal Regions are composed of two steps of extrapolations along $E_{\mathrm{T}}^{\mathrm{miss}}$ and m_{T}, these validations make sure that our analysis should predict the background events well even in the Signal Regions.

6.3 Other backgrounds

In addition to $t\bar{t}$, W+jets and QCD multi-jets, the following components are included as the backgrounds:

- Dibosons (WW, WZ, ZZ productions with additional jets)
- Single top production
- $t\bar{t}$+V ($V = W, Z$)
- Z+jets

They are all estimated by using Monte Carlo with the nominal cross-sections, which are summarized in Table 10. They are not normalized in the Control Regions, thus the uncertainties on cross-section and acceptance into the Signal Regions directly affect the yield estimation. The uncertainties for these backgrounds are discussed in Section 7.2.

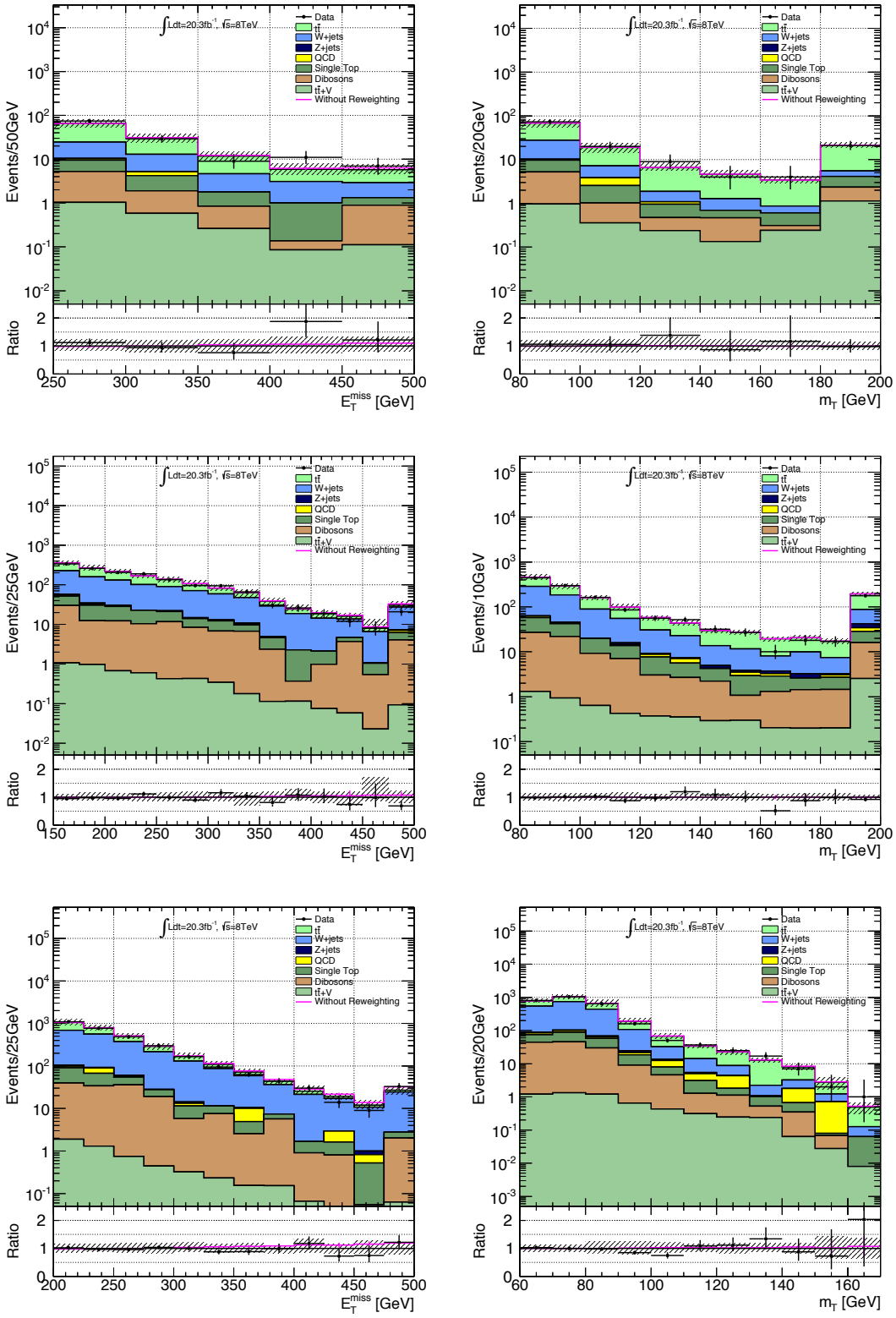

Figure 54: $E_{\mathrm{T}}^{\mathrm{miss}}$ (Left) and m_{T} (Right) distributions of Tight (Top), Loose (middle) and Soft (bottom) Regions. For $E_{\mathrm{T}}^{\mathrm{miss}}$ plots, the Control Region selections without the upper limit on $E_{\mathrm{T}}^{\mathrm{miss}}$ is required. Similarly, for m_{T} plot, the Control Regions without the upper limit on m_{T} is applied. The bottom panels show the ratio of data divided by the Monte Carlo. The normalization factors which are determined in the Control Regions are applied here. The error band includes JES uncertainty and statistical uncertainty of Monte Carlo. The magenta line shows the kinematic distributions without the corrections.

7 Uncertainties

7.1 Instrumental uncertainties

The ATLAS detector has been calibrated during two years' data-taking period, but there still remain inevitable uncertainties in the calibration, such as the uncertainty associating with Jet Energy Scale. These uncertainties and their impacts on the background estimation are discussed here. Note that the exact impact in the Signal Region is only determined after fitting as discussed in Section 8.1. So here we only show the rough size of impacts. The exact size of the uncertainties will be discussed after fitting. Instrumental uncertainties are evaluated for all backgrounds and signals.

7.1.1 Jet Energy Scale (JES) uncertainty

As documented in Section 3.2.4, jet calibration is made up of several steps, starting from a single pion calibration to *in-situ* calibrations. All the nuisance parameters introduced in the calibrations are summed up quadratically and taken into the analysis. Figures 55 show effects of JES uncertainty on m_{T} and the number of jets N_{jet}^{40} distributions using $t\bar{t}$ sample. Only minimal kinematic selections are applied in the plots: $p_{\mathrm{T}}^{\mathrm{jet1}}$>80 GeV, $p_{\mathrm{T}}^{\mathrm{jet3}}$>40 GeV, m_{T}>80 GeV, $E_{\mathrm{T}}^{\mathrm{miss}}$>150 GeV, and m_{eff}>500 GeV. The large shift in the entire scale comes form the cumulative impacts of the kinematic selections, which is absorbed after normalizing Monte Carlo in the Control Regions. The remaining shape difference is considered as the uncertainty on transfer factor, which is about 10%.

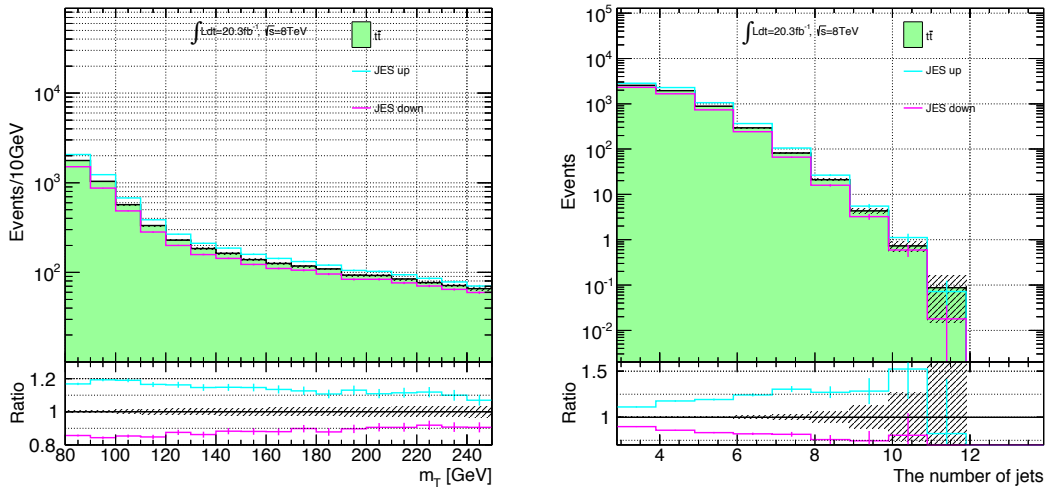

Figure 55: m_{T} (left) and the number of jets (right) comparisons with positive (cyan) and negative (magenta) JES uncertainties. Only $t\bar{t}$ sample is shown.

7.1.2 Jet Energy Resolution (JER) uncertainty

Uncertainty on jet energy resolution is also considered, which is propagated to $E_{\mathrm{T}}^{\mathrm{miss}}$, making an impact in the steep slope after the Jacobian peak in m_{T} as shown in Fig. 56. However, as we set Control Regions close to Signal Regions, overall difference is absorbed by the normalization factors, leaving only $O(1)$% uncertainty in the final results.

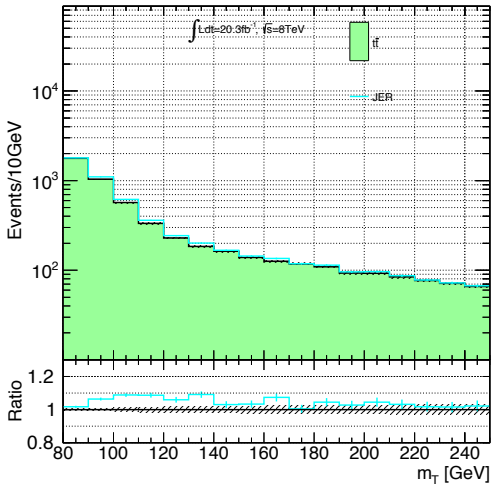

Figure 56: m_{T} comparison with JER uncertainty. Only $t\bar{t}$ sample is shown.

7.1.3 Lepton energy scale, resolution, and trigger/reconstruction efficiency uncertainties

The energy scale and resolution, and also the trigger/reconstruction efficiencies of leptons are calibrated mainly using $Z \rightarrow ll$ events. Errors on these calibrations are much smaller compared with JES uncertainty, in addition, normalization in the Control Region reduces the uncertainties quite a lot. Even before the normalization, the impacts are as small as 2% in the worst case, so neglected in the fitting.

7.1.4 $E_{\mathrm{T}}^{\mathrm{miss}}$ resolution uncertainties

The uncertainties of jets and leptons mentioned above are all propagated to $E_{\mathrm{T}}^{\mathrm{miss}}$. As shown in Eq. 51, the uncertainty on $E_T^{\mathrm{miss\,(Soft)}}$ is the last remaining term to be evaluated. Both the energy scale and resolution of the term are varied within the uncertainties, only to find that both of the uncertainties are well below 3%, thus not included in the fitting.

7.1.5 Pile-up uncertainties

The current pile-up simulation does not completely reproduce the number of primary vertex per a collision N_{PV}. Monte Carlo rather predicts 10% lower N_{PV} than that of data. We evaluate the impact of this discrepancy by shifting N_{PV} by ±10%. Since our analysis requires a large $E_{\mathrm{T}}^{\mathrm{miss}}$, the impact is only <2% level, thus not included in the fitting.

7.1.6 b-tagging efficiency uncertainty

b-tagging is used to separate W+jets and $t\bar{t}$, so the uncertainty directly affects the normalization scales in the Control Regions. b-tagging uncertainty is divided into three components by the flavor of jets: b-, c- and light-jets. The quadrature sum of the uncertainties is taken into the systematic error, which yields about 10% for $t\bar{t}$ in most of the kinematic selections. On the other hand, the uncertainty of mis-tagging is also studied for W+jets, giving a similar size of uncertainty.

7.2 Theoretical uncertainties

7.2.1 $t\bar{t}$

As discussed in Section 6.2.3, there observed a clear mis-modeling in Parton-Shower. We invented a correction function to fix the mis-modeling and obtained a good agreement. The uncertainty of this correction is 14% in the worst case for the Tight Signal Region.

On top of Parton-Shower uncertainty, the kinematics of $t\bar{t}$ system, which is mainly determined in Matrix-Element calculation, has extra uncertainties. We introduce the following uncertainties to cover a possible mis-modeling of $t\bar{t}$ system.

Renormalization and Factorization scales :

Generators have an inevitable uncertainty of the energy scale at which the strong coupling constant α_S is calculated, which is called renormalization scale. Another important energy scale is factorization scale, at which PDF is evaluated. The impact of the uncertainties of these scales are studied by comparing systematic samples with the nominal sample. Here, the systematic samples are the ones produced with the different parameter configurations. For these scale uncertainties, each of the scale is varied by factors of 0.5 or 2.0. In general, Next-to-Leading-Order generators are robust to these scale uncertainties, therefore, only a small impact is expected.

Figures 57 show the $E_{\mathrm{T}}^{\mathrm{miss}}$ and m_{T} distributions of the systematic samples. Due to a poor statistics of the systematic samples, no kinematic selection is applied. The largest slope is observed in the $E_{\mathrm{T}}^{\mathrm{miss}}$ distribution of renormalization systematic samples. A 5% of systematic error safely covers the uncertainty of the transfer factor for all regions. The slope in m_{T} is not so large, especially in terms of the transfer factor. No statistically significant variation is observed in m_{eff}.

PDF :

A study [6] shows that total PDF uncertainty is smaller than 3%, thus it is eliminated from the fit. The reason of the smallness is explained by the fact that $t\bar{t}$ is relatively light compared with the proton energies in the LHC, therefore the bulk regime of the parton momentum fraction x contributes to the production, where the uncertainty is small.

7.2.2 W+jets

As discussed in the last part of Section 6.2.4, the slope correction introduces an uncertainty. The largest uncertainty is observed in the Tight Region, giving 8% for the transfer factor. PDF uncertainty is evaluated using Eq. 73, whose contribution is found to be below 3%, thus neglected. Other generator uncertainties are also studied by systematic samples produced with Alpgen. First, renormalization and factorization scales Q are varied between 0.5 and 2.0. An empirical formula, $Q^2 = m_W^2 + \sum_j (m_j^2 + p_{T,j}^2)$ (j runs over all jets) is used to set Q in default, which is also varied to $Q^2 = m_W^2$ and $Q^2 = m_W^2 + p_{T,W}^2$ for further uncertainty estimation. But no significant impact in the transfer factor is found.

[6] PDF used in $t\bar{t}$ generation has 20 pairs of uncertainties coming from the experimental errors. The effect of these uncertainties on the transfer factor Ω is obtained by calculating the transfer factor for each of these variations ω (once up (+) and once down (-)) while keeping the other parameters fixed. This gives an asymmetric PDF uncertainty:

$$\begin{cases} \Omega_{\mathrm{up}} &= \sqrt{\sum_i [\max(\omega_{\mathrm{up}} - \omega_0, \omega_{\mathrm{down}} - \omega_0, 0)]^2} \\ \Omega_{\mathrm{down}} &= \sqrt{\sum_i [\max(\omega_0 - \omega_{\mathrm{up}}, \omega_0 - \omega_{\mathrm{down}}, 0)]^2} \end{cases} \tag{73}$$

where i is the index of PDF uncertainties.

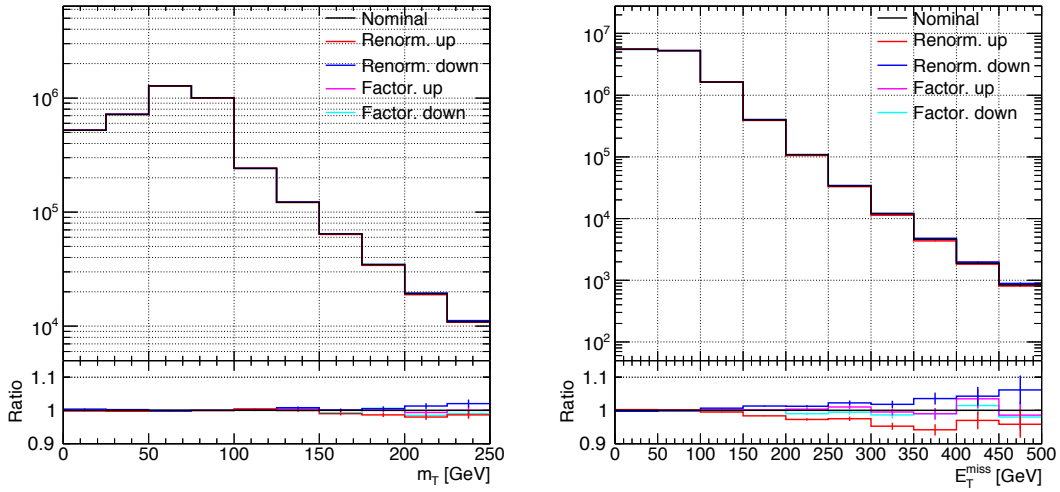

Figure 57: m_{T} (left) and $E_{\mathrm{T}}^{\mathrm{miss}}$ (right) distributions of renormalization and factorization scale systematic samples. No kinematic selections is applied.

7.2.3 Single Top

Background estimation of SingleTop is evaluated fully depending on Monte Carlo and its cross-section. Therefore, the theory uncertainties of SingleTop become important. Note that the SingleTop is one of the minor backgrounds, so a large uncertainty doesn't necessarily lead to loss of sensitivity. In fact, a comparison study with various fraction (from 20% up to 70%) of systematic errors doesn't give any significant difference in the fit results.

A generator comparison between `MC@NLO` and `Powheg` samples and the Parton-Shower variation using `Pythia` and `Jimmy` give ~10% errors at most.

W+t channel includes diagrams which share the same final states with $t\bar{t}$ [60, 61]. Such diagrams are already subtracted in event generation, however, as the subtraction method is not well-defined, there proposed two different subtraction algorithms: Diagram Subtraction (DS) and Diagram Removal (DR) [7]. As two algorithms give different SingleTop yields, we take the difference into the systematics, which amounts to 70%.

7.2.4 Z+jets

Though its large cross-section, Z+jets is one of the minor backgrounds once after requiring 1-lepton and tight $E_{\mathrm{T}}^{\mathrm{miss}}$ cuts. Z+jets is normalized by its theoretical cross-section, whose uncertainty is 12%. To be conservative, we use a 30% uncertainty in the fitting.

7.2.5 $t\bar{t}$+V

For $t\bar{t}$+V sample, two generator comparison and cross-section uncertainties are considered. A comparison between `Alpgen` and `MadGraph` shows that the difference is quite small (~5%) in all kinematic regions. A 30% of uncertainty is assigned considering the cross-section error, which is taken from the difference between LO and NLO calculations. Note that the uncertainty safely covers PDF and renormalization/factorization scale uncertainties.

[7] The nominal sample uses Diagram Removal method for the subtraction.

7.2.6 Dibosons

An uncertainty of 50% is applied, which comes from the cross-section uncertainty taken from the difference between LO and NLO cross-sections. A 50% uncertainty is sufficient to cover the other errors such as PDF and scale uncertainties.

7.2.7 QCD multi-jet

The uncertainty on QCD multi-jets estimation is dominated by the statistical error of data. As discussed in Section 6.1, QCD multi-jet background is evaluated by comparing the event numbers in fake-enriched and fake-suppressed regions. But even in the fake-enriched region, the event number is quite small after applying a large $E_{\mathrm{T}}^{\mathrm{miss}}$ selection. Uncertainties on ϵ_{fake} and ϵ_{real} are also included but have negligible impacts.

7.3 Signal uncertainties

The dominant uncertainty sources of signals are the cross-sections and acceptances in the Signal Regions, which are separately evaluated in the following. Also the instrumental uncertainties are included in the fitting, however, the contributions are much smaller than these theoretical uncertainties.

7.3.1 Cross-section uncertainty

There are several theoretical uncertainties that have an impact on the cross-section. The quadrature sum of uncertainties is shown in Fig. 28 for MSUGRA/CMSSM sample. Uncertainties of the Simplified Model are shown in Fig. 30 as the vertical error bars. They include the following uncertainties.

Scale uncertainty :
Renormalization and factorization scales are both set to the mass of the initial particles Q when calculating the cross-section (for squark-gluino production, the mean mass is taken, i.e. $Q = (m_{\tilde{g}} + m_{\tilde{\mathrm{q}}})/2$). This choice gives rise to an uncertainty and the difference between the ones with $\mu = 2Q$ and $\mu = Q/2$ are taken into account.

PDF uncertainty :
PDF uncertainty is estimated using the same method as described in Section 7.2.1.

α_S **uncertainty** :
Determination of PDF parameters has an overall uncertainty for the choice of α_S [76]. Two different cases are tested, and the variations on cross-sections is taken as uncertainty.

These uncertainties are separately evaluated using two PDF sets: `CTEQ6.6M` [77] and `MSTW2008NLO` [43, 44, 45], and the combination that gives the maximum variation are taken into account. Table 21 shows the size of these uncertainties for some representative points. PDF uncertainty gives a large error for high mass gluino productions, which is because a large parton momentum fraction x is required for gluons to produce massive gluinos. On the other hand, squark production has relatively small uncertainty from PDF because it can use valence quarks.

7.3.2 Acceptance uncertainty

Signal acceptance is defined as the fraction of events passing the signal region selection. Generator uncertainty also affects the signal acceptance. The following uncertainties are taken into account.

Signal		Uncertainty [%]		
Parameter [GeV]	Production	Scale	PDF	α_S
MSUGRA/CMSSM				
$(m_0, m_{1/2})$=(1000,650)	$\tilde{g}$-$\tilde{g}$	9	51	13
$(m_0, m_{1/2})$=(4000,450)	$\tilde{g}$-$\tilde{g}$	11	29	8
	$\tilde{q}$-$\tilde{q}$	19	41	7
Simplified Model				
$m_{\tilde{g}}$=1200	$\tilde{g}$-$\tilde{g}$	11	25	7
$m_{\tilde{g}}$=800	$\tilde{g}$-$\tilde{g}$	10	17	6
$m_{\tilde{q}}$=1200	$\tilde{q}$-$\tilde{q}$	11	18	6
$m_{\tilde{q}}$=800	$\tilde{q}$-$\tilde{q}$	11	12	4

Table 21: Decomposition of the signal uncertainty for some representative points. The relative size of the error is shown. Note that the gluino and squark masses are 1.5 (1.2) TeV and 1.6 (3.1) TeV for the MSUGRA/CMSSM points with $(m_0, m_{1/2})$=(1000,650) ($(m_0, m_{1/2})$=(4000,450)), respectively. $\tilde{q}$-$\tilde{q}$ uncertainties for the former point are not shown as it gives only negligible contribution.

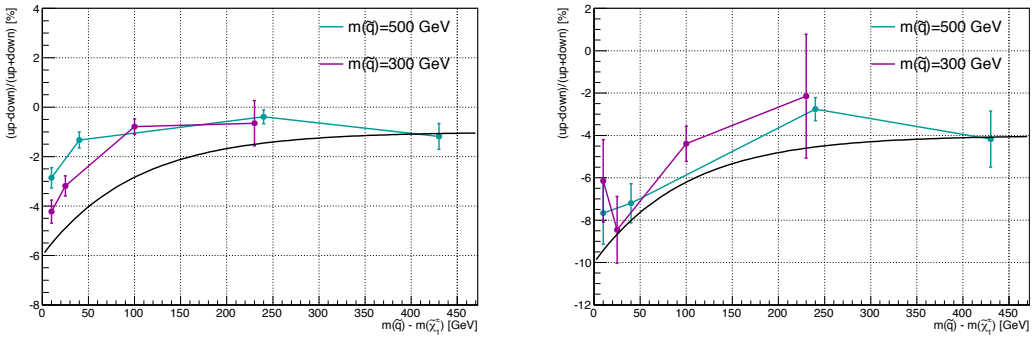

Figure 58: ISR uncertainty obtained for the Simplified model with $\tilde{q}$-$\tilde{q}$ production. The mass difference between $\tilde{q}$ and $\tilde{\chi}_1^{\pm}$ are taken as the x-axis. The y-axis shows the uncertainty defined in Eq. 74. The uncertainties given in Eq. 75 are shown in black lines. Two mass points with $m_{\tilde{q}}$=300 GeV (purple) and 500 GeV (blue) are shown. The kinematic selections are: (left) at least 1 lepton and $N_{\text{jet}}^{30} \geq 3$; (right) at least 1 lepton and $N_{\text{jet}}^{40} \geq 5$.

ISR uncertainty : Energy scale at which α_S is evaluated for ISR is varied from the nominal value to 0.5 or 2.0.

Scale uncertainty : This item is the same as the one mentioned in the previous section, but only the impact on acceptance is evaluated.

FSR uncertainty : Λ_{QCD} value used for FSR is varied by ±50% from its nominal.

Jet matching uncertainty : Jet matching scale at which the partons from Matrix-Element and Parton-Shower algorithms are separated is varied by a factor of 0.5 and 2.0.

PDF uncertainty : This uncertainty is the same as the one mentioned in the previous section, but only the impact on acceptance is evaluated.

Among these uncertainties, ISR uncertainty gives the largest impact on signal acceptance and the others are much smaller. Therefore we evaluate ISR uncertainty in the following and take it into the systematic uncertainty.

The primary impact of ISR uncertainty appears in the number of jets passing $p_{\mathrm{T}}^{\mathrm{jet}}$>40 GeV (Tight and Loose) or $p_{\mathrm{T}}^{\mathrm{jet}}$>30 GeV(Soft). In Simplified models, 2 jets ($\tilde{\mathrm{q}}$-$\tilde{\mathrm{q}}$ grid) and 4 jets ($\tilde{g}$-$\tilde{g}$ grid) are expected from decay chains, therefore, ISR uncertainty is more critical for $\tilde{\mathrm{q}}$-$\tilde{\mathrm{q}}$ grid. The size of ISR uncertainty is shown as a function of mass splitting between $\tilde{\mathrm{q}}$ and $\tilde{\chi}_1^{\pm}$ as it impacts jet p_{T} distribution. Two different samples (up/down) are generated with extreme ISR uncertainty configurations. The uncertainty is calculated as follow from the number of events in the signal region $N_{\mathrm{up/down}}$,

$$\text{uncertainty} = \frac{N_{\mathrm{up}} - N_{\mathrm{down}}}{N_{\mathrm{up}} + N_{\mathrm{down}}}, \tag{74}$$

Figure 58 show the uncertainties as a function the mass difference between $\tilde{\mathrm{q}}$ and $\tilde{\chi}_1^{\pm}$. At least 1 lepton is required. In addition, two jet selections are tested: $N_{\mathrm{jet}}^{30} \geq 3$ (left) and $N_{\mathrm{jet}}^{40} \geq 5$ (right). No other selection is required in the plots to obtain enough statistics. The uncertainty is larger for low mass splitting especially below 50 GeV, which is because the jet from $\tilde{\mathrm{q}}$ decay becomes as soft as the jet p_{T} threshold and ISR becomes more important. Two different squark mass points are plotted but they show similar tendencies. The following uncertainties are considered:

$$\text{ISR uncertainty [\%]} = \begin{cases} (4 + 6e^{-0.01\,x})\,\text{(Tight)} \\ (1 + 5e^{-0.01\,x})\,\text{(Loose, Soft)}, \end{cases} \tag{75}$$

where x is the mass difference between $\tilde{\mathrm{q}}$ ($\tilde{g}$) and $\tilde{\chi}_1^{\pm}$ in a unit of GeV. ISR uncertainty is quadratically added to the cross-section uncertainty in the fitting.

8 Results

As discussed in Section 6, dominant backgrounds, $t\bar{t}$ and W+jets, are normalized in the Control Regions to reduce generator uncertainties. In addition, $m_{\rm eff}$ slope correction is applied to correct the mis-modeling of ISR uncertainty. Two Validation Regions are prepared to justifies the extrapolations along $E_{\rm T}^{\rm miss}$ and $m_{\rm T}$, and both of them show good agreements. Since the background estimation in the Signal Region is composed of these two extrapolations, we expect that backgrounds in the Signal Region are also correctly estimated. These observations encourage us to un-blind the Signal Regions to search for an excess in data. If there is no signal-like excess, we calculate the mass limits using a binned likelihood method on $m_{\rm eff}$.

8.1 Un-blinding the Signal Regions

Table 22 (Tight SR), 23 (Loose SR) and 24 (Soft SR) show the observed event numbers in the Signal Regions with the expected number of background events. Lepton flavors are separated for Hard Lepton channels, while they are combined for Soft Lepton channel due to some technical reasons. In all the Signal Regions and channels, the number of observed events are consistent with the expected backgrounds within the errors. The errors cited as "bkg events" consider both statistical and systematic errors. All correlations among the errors are taken into account, therefore, the total size of the errors may become smaller than its components[8].

Table 38 (Tight SR), 39 (Loose SR) and 40 (Soft SR) (in Appendix G) give the raw size of errors assigned to systematic error sources. The largest systematic error comes from JES uncertainty, which is 10-15% for Loose and Soft Signal Regions. For Tight Signal Region, it becomes as large as 30% due to stringent kinematic selections. The scale factors of $t\bar{t}$ and W+jets are also dominant sources of the uncertainties, which is determined in the normalization in the Control Regions. JES uncertainty is strongly anti-correlated with normalization uncertainties of $t\bar{t}$ and W+jets, therefore the total systematic error is much smaller. In other words, JES uncertainty is absorbed by the scale factors by normalizing in the Control Regions.

Expected size of the fluctuation of observed events is denoted as $\sqrt{N_{\rm exp}}$. Since we set stringent cuts to maximize the sensitivity, the number of remaining events are quite small. For the Tight Signal Region, we expect only 11.8 events in total, therefore a large statistical error ($\pm$3.4) is assigned.

Figures 59 show $m_{\rm eff}$ plots in Tight (left), Loose (right) and Soft (bottom) Signal Regions. Several signals taken from around the exclusion limits are piled up on top of the background distributions. The same binning is used as the ones used in fitting. Both electron and muon channels are combined. Tight Signal Region is dominated by large statistical errors both for data and Monte Carlo. The data points are all consistent with the Monte Carlo expectations within the uncertainties.

The Loose Signal Region has smaller statistical errors, but the data points are still consistent with the Monte Carlo expectations. A slight downward tendency is actually seen in the ratio plot although it is inside the uncertainty band. An orthogonal region is defined by inverting $m_{\rm T}$ selection to 60 GeV $< m_{\rm T} <$ 120 GeV to check the origin of this tendency, however, $m_{\rm eff}$ distribution in the region seems quite flat without any specific structure. Therefore the downward slope is concluded to be a statistical fluctuation.

Overall distribution in the Soft Signal Region is consistent with the expectations. The leftmost bin has a slight excess in data though the statistical error is quite severe. This excess is checked further by loosening one of $E_{\rm T}^{\rm miss}$ or $m_{\rm T}$ selection to $E_{\rm T}^{\rm miss}$>200 GeV or $m_{\rm T}$>60 GeV and see the $m_{\rm eff}$ distributions

[8] For example, the uncertainty of b-tagging efficiency directly changes the fraction of the events classified to $t\bar{t}$ control region and W+jets Control Regions as they are separated by requiring at least one b-tagged jet. As a result, the yields of these two backgrounds are anti-correlated through b-tagging uncertainty. If we take the uncertainty of one component, it may look large. However, once they are summed up in Signal Region or Validation Regions, then the yield changes compensate each other, leading to a smaller uncertainty.

with finer bin width. The results show no significant structure therefore we conclude the excess is not caused by a specific problem but just a statistical fluctuation.

The $E_{\mathrm{T}}^{\mathrm{miss}}$ and m_{T} distributions of the events in these signal regions are shown in Appendix F.

channel	Tight SR (El)	Tight SR (Mu)
Observed events	8	4
bkg events	6.52 ± 1.17	5.31 ± 1.03
$t\bar{t}$ events	3.83 ± 1.23	3.44 ± 1.04
W+jets events	0.89 ± 0.57	0.67 ± 0.43
Z+jets events	0.00 ± 0.00	0.06 ± 0.04
Dibosons events	0.78 ± 0.43	$0.18^{+0.28}_{-0.18}$
Single Top events	0.48 ± 0.37	0.64 ± 0.46
$t\bar{t}+V$ events	0.37 ± 0.10	0.33 ± 0.09
QCD events	$0.16^{+0.21}_{-0.16}$	0.00 ± 0.02

Table 22: Background fit results for the Tight SR (El) and Tight SR (Mu) for an integrated luminosity of 20.3 fb^{-1}. The errors shown are the statistical plus systematic uncertainties.

channel	Loose SR (El)	Loose SR (Mu)
Observed events	179	132
bkg events	166.60 ± 20.35	161.12 ± 18.56
$t\bar{t}$ events	93.34 ± 19.77	86.31 ± 18.05
W+jets events	43.76 ± 5.93	43.15 ± 6.01
Z+jets events	0.85 ± 0.27	3.75 ± 1.17
Dibosons events	11.29 ± 5.87	12.13 ± 6.24
Single Top events	11.77 ± 8.32	9.41 ± 6.66
$t\bar{t}+V$ events	4.13 ± 0.36	3.38 ± 0.22
QCD events	$1.46^{+1.92}_{-1.46}$	2.99 ± 2.10

Table 23: Background fit results for the Loose SR (El) and Loose SR (Mu) for an integrated luminosity of 20.3 fb^{-1}. The errors shown are the statistical plus systematic uncertainties.

channel	Soft SR (El+Mu)
Observed events	40
bkg events	35.37 ± 4.57
$t\bar{t}$ events	16.65 ± 3.63
W+jets events	12.08 ± 1.21
Z+jets events	0.16 ± 0.15
Dibosons events	1.42 ± 0.73
Single Top events	2.93 ± 2.07
$t\bar{t}+V$ events	0.71 ± 0.06
QCD events	$1.43^{+1.55}_{-1.43}$

Table 24: Background fit results for the Soft SR (El+Mu) for an integrated luminosity of 20.3 fb^{-1}. The errors shown are the statistical plus systematic uncertainties.

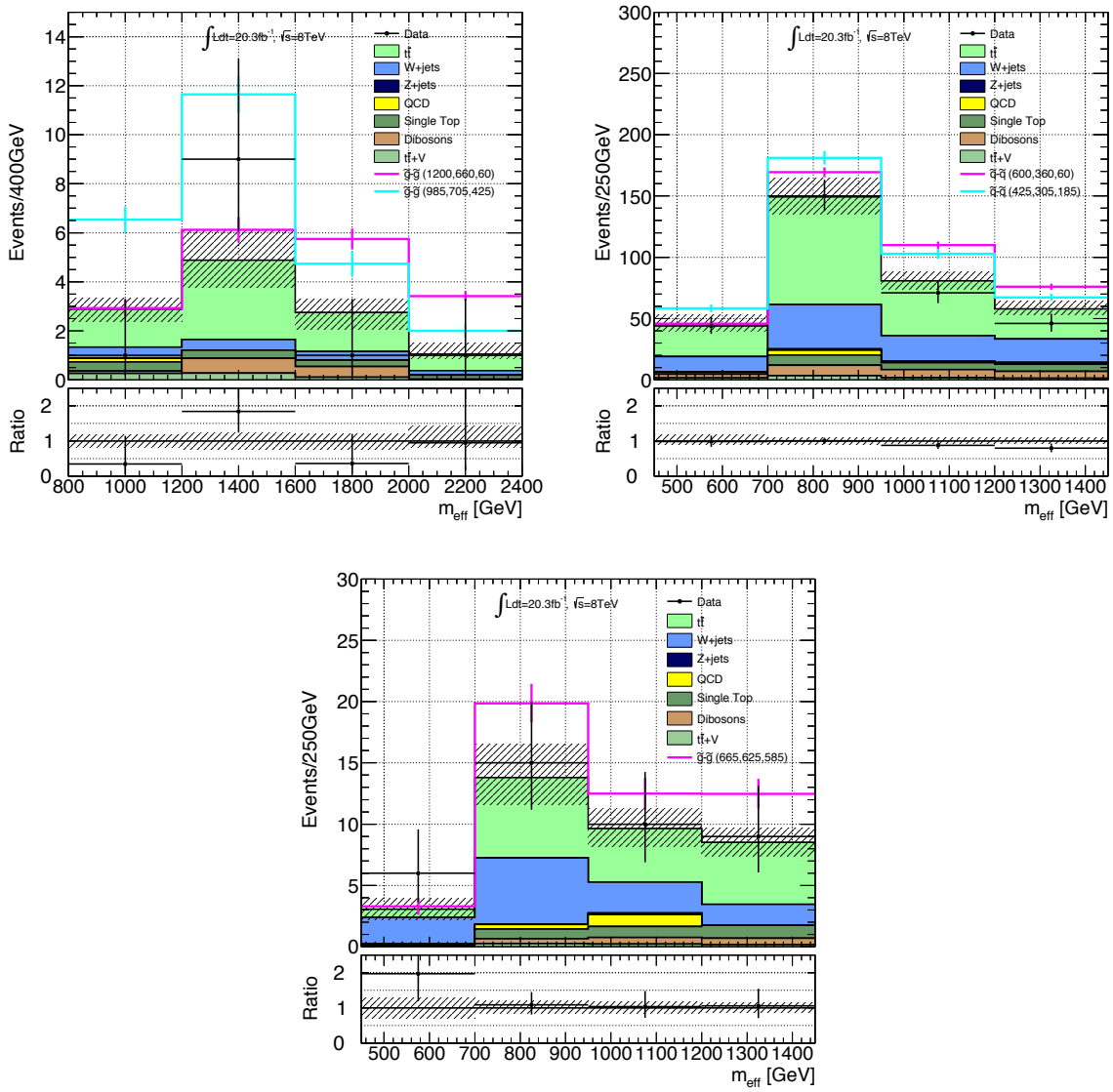

Figure 59: m_{eff} distributions in Tight (left), Loose (right) and Soft (bottom) Signal Regions. Signals taken from around the exclusion limits are piled up on top of the background distributions. For Tight SR, gluino pair productions with $(m_{\tilde{g}}, m_{\tilde{\chi}_1^\pm}, m_{\tilde{\chi}_1^0})$=(1200 GeV, 660 GeV, 60 GeV) (magenta) and $(m_{\tilde{g}}, m_{\tilde{\chi}_1^\pm}, m_{\tilde{\chi}_1^0})$=(985 GeV, 705 GeV, 425 GeV) (cyan) are shown. For Loose SR, squark pair productions with $(m_{\tilde{q}}, m_{\tilde{\chi}_1^\pm}, m_{\tilde{\chi}_1^0})$=(600 GeV, 360 GeV, 60 GeV) (magenta) and $(m_{\tilde{q}}, m_{\tilde{\chi}_1^\pm}, m_{\tilde{\chi}_1^0})$=(425 GeV, 305 GeV, 185 GeV) (cyan) are shown. For Soft SR, gluino pair production with $(m_{\tilde{g}}, m_{\tilde{\chi}_1^\pm}, m_{\tilde{\chi}_1^0})$=(665 GeV, 625 GeV, 585 GeV) is shown in magenta. The last bin includes the overflow events.

8.2 Limit calculation

As no signal-like excess is found in the Signal Regions, the results are interpreted as mass limits on two signal models. Limit calculation is based on Profile-Likelihood method (details are documented in Appendix. H). Likelihood function is composed of three parts,

$$\begin{aligned} L(\mu) &= L_{\text{Tight}}(\mu, \theta_{\text{Tight}}, \lambda^{W}_{\text{Tight}}, \lambda^{t\bar{t}}_{\text{Tight}}) \\ &\times L_{\text{Loose}}(\mu, \theta_{\text{Loose}}, \lambda^{W}_{\text{Loose}}, \lambda^{t\bar{t}}_{\text{Loose}}) \\ &\times L_{\text{Soft}}(\mu, \theta_{\text{Soft}}, \lambda^{W}_{\text{Soft}}, \lambda^{t\bar{t}}_{\text{Soft}}), \end{aligned} \tag{76}$$

where θ_X is a vector containing all the nuisance parameters in region X, λ^{W}_{X} and $\lambda^{t\bar{t}}_{X}$ are scale factors for W+jets and $t\bar{t}$. μ is a signal strength, which is defined as the ratio of a given (or fitted) signal yield over the nominal signal yield. All nuisance parameters and scale factors are defined separately for each region. Signal strength μ is the only common parameter over the regions. Figure 60 gives a schematic illustration of the structure. Since each likelihood function looks like a tower in the illustration, they are called as "Tight-tower", "Loose-tower" and "Soft-tower", respectively.

A detailed structure of one of the likelihood functions is given as

$$\begin{aligned} L_X(\mu, \theta_X, \lambda^{W}_{X}, \lambda^{t\bar{t}}_{X}) &= \prod^{i}_{\text{SRbins}} Pois(\mu s^{\text{SR,i}}_{X}(\theta) + \lambda^{W}_{X} w^{\text{SR,i}}_{X}(\theta) + \lambda^{t\bar{t}}_{X} t^{\text{SR,i}}_{X}(\theta); n^{\text{SR,i}}_{X}) \\ &\times Pois(\mu s^{\text{WR}}_{X}(\theta) + \lambda^{W}_{X} w^{\text{WR}}_{X}(\theta) + \lambda^{t\bar{t}}_{X} t^{\text{WR}}_{X}(\theta); n^{\text{WR}}_{X}) \\ &\times Pois(\mu s^{\text{TR}}_{X}(\theta) + \lambda^{W}_{X} w^{\text{TR}}_{X}(\theta) + \lambda^{t\bar{t}}_{X} t^{\text{TR}}_{X}(\theta); n^{\text{TR}}_{X}) \\ &\times L^{\text{constrain}}_{X}(\theta). \end{aligned} \tag{77}$$

The right-hand-side in the first line gives a Poisson probability for the observed number of events in a signal region of i-th bin, and the terms in the second and third line are the ones for W+jets and $t\bar{t}$ Control Regions. Here, $w^{Y}_{X}(\theta)$ and $t^{Y}_{X}(\theta)$ are the number of W+jets and $t\bar{t}$ backgrounds in Y-region of X-tower (as Signal Regions are divided into bins, bin index i is superscripted). Similarly, the number of observed events in Y-region of X-tower is represented as n^{Y}_{X}. The last term is a product of all constraining terms.

The constraining term consists of two parts: MC statistical error terms and systematic error terms. The former ones are responsible for statistical errors of Monte Carlo samples in each bin. The latter ones are to constrain the nuisance parameters of uncertainties such as JES, JER, etc. If a constrain is weak for a given systematic error and the corresponding nuisance parameter is able to move around freely, the error on signal strength μ also becomes larger. A larger error on signal strength μ means that a signal model is difficult to be classified to "with-signal" or "without-signal" hypotheses, thus the sensitivity becomes weaker.

Signal contamination in the Control Regions is correctly taken into account in this configuration. Therefore, even when a signal with a large cross-section would exist and contaminate to the Control Regions severely, we could still obtain a correct signal strength.

The Signal Regions are all divided into bins along m_{eff}. The Poisson probability in the bin that has the largest signal to background separation dominates the entire probability, which is equal to setting an optimized m_{eff} threshold for each signal model. As a result, the Signal Regions are sensitive for various signal models with different m_{eff} shapes.

Limits are then calculated using the likelihood function. A 95% confidence level (C.L.) is used throughout the analysis. Since the uncertainties on signal cross-sections and acceptances are not something to be fitted nor something to worsen the sensitivity, the uncertainties are excluded from fitting and the impact is explicitly shown in limit plots.

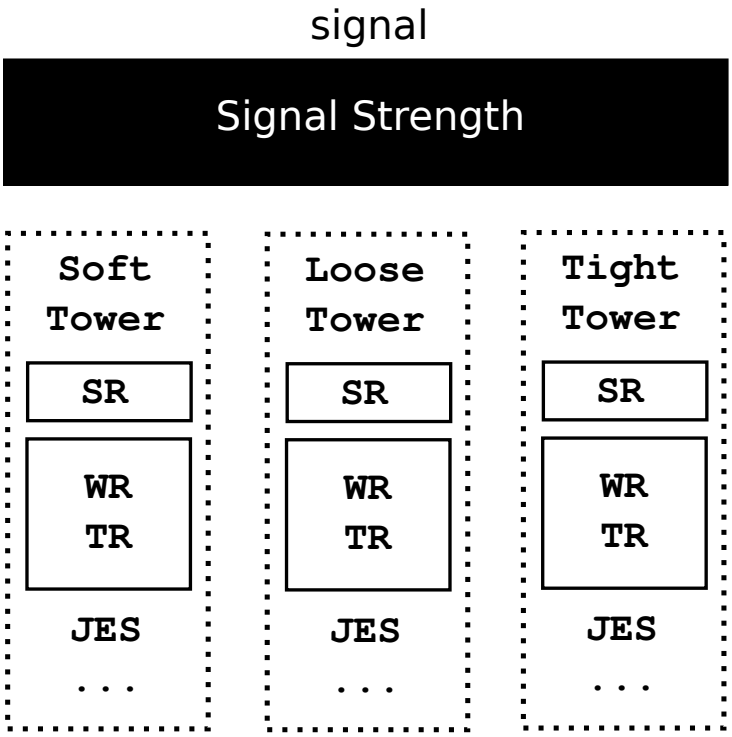

Figure 60: Illustration of fit setup. Signal strength is common among the towers, while each tower has its own systematics and normalization factors, separately.

8.3 Interpretation

8.3.1 MSUGRA/CMSSM

Figure 61 shows the observed (red) and expected (black) mass limits in the MSUGRA/CMSSM model with $\tan\beta = 30$, $A_0 = -2m_0$ and $\mu > 0$. Estimation error, including systematic and statistical uncertainties, is shown as the yellow band. Uncertainties related to signal cross-sections and acceptances are shown as the dotted red lines. Gluino and squark mass lines are also shown. The purple lines indicate the Higgs mass[9]. In all of the parameter space, sensitivity is driven by the Tight Signal Region because the MSUGRA/CMSSM model tends to have hard event kinematics.

The parameters used in the sample production are chosen so as to maximize the compatibility with the Higgs mass of 126 GeV [1]. Recent experimental results show that the branching fractions of the Higgs boson are consistent with the Standard Model Higgs boson [6], which is realized at maximum-mixing scenario in MSSM framework (see also Section 1.4.5). The scenario requires a large mixing between left- and right-handed stops, making one of the stops much lighter than the other squarks. As a result, stops are more likely to appear in decay chains, which increases the number of jets and also signal acceptances. A larger probability of lepton emission is expected from top decays, which also increases the events passing 1-lepton selection. Hence, a search requiring 1-lepton and multi-jet suits for the maximal-mixing configuration.

Since a squark mass becomes so heavy in high m_0 region, the region is dominated by $\tilde{g}$-$\tilde{g}$ production as shown in Fig. 33. A gluino then decays into two quarks and one chargino via three-body decay, $\tilde{g} \rightarrow qq\tilde{\chi}_1^{\pm}$ (here we take a case which has the dominant contribution to 1-lepton analysis), and the wino decays into a LSP, $\tilde{\chi}_1^{\pm} \rightarrow W^{\pm}\tilde{\chi}_1^0$. The supersymmetry particles appear in the decay chain are all gauginos [10]. As seen in Eq. 37, gaugino masses are (almost) independent of m_0, so the event topology does not change along the gluino mass contour, resulting in a constant signal acceptance. Production cross-section is also independent of m_0 because squarks are too heavy to be produced and only $\tilde{g}$-$\tilde{g}$ production occurs, therefore the analysis keeps the same sensitivity along the mass contour. A gluino mass up to 1200 GeV is excluded in high m_0 region in Fig. 61, which is expected to continue beyond the right edge of the plot.

A squark mass up to 1500 GeV is excluded except for $m_0 < 500$ GeV. The limit line does not simply follow the squark mass contour and loose sensitivity in the low m_0 and high $m_{1/2}$ region, which is explained by the following reasons: (1) As shown in Fig. 33, not only $\tilde{q}$-$\tilde{q}$ but also $\tilde{q}$-$\tilde{g}$ production occurs at around $m_0 \sim 1000$ GeV. Sensitivity is pushed up a lot by this contribution because a decay chain starting from $\tilde{g}$-$\tilde{q}$ has a large signal acceptance due to large number of jets. This production is suppressed in higher $m_{1/2}$ region, which leads to the sensitivity loss. (2) Since LSP mass is proportional to $m_{1/2}$, a heavy LSP is expected in the high $m_{1/2}$ region. In general, m_{eff} becomes soft for heavy LSPs since some fraction of energy is consumed to create heavy LSPs and smaller fraction of energy is left for visible objects. This also means that visible objects tends to be softer overall. As a result of these two contributions, small signal yields are expected in high $m_{1/2}$ and low m_0 region, therefore we loose the sensitivity.

[9] The Higgs mass contours run parallel to the squark mass contours as the Higgs mass is determined mainly by a stop mass.
[10] The Higgsino masses are about 1 TeV for this model, therefore they does not appear in the decay chains.

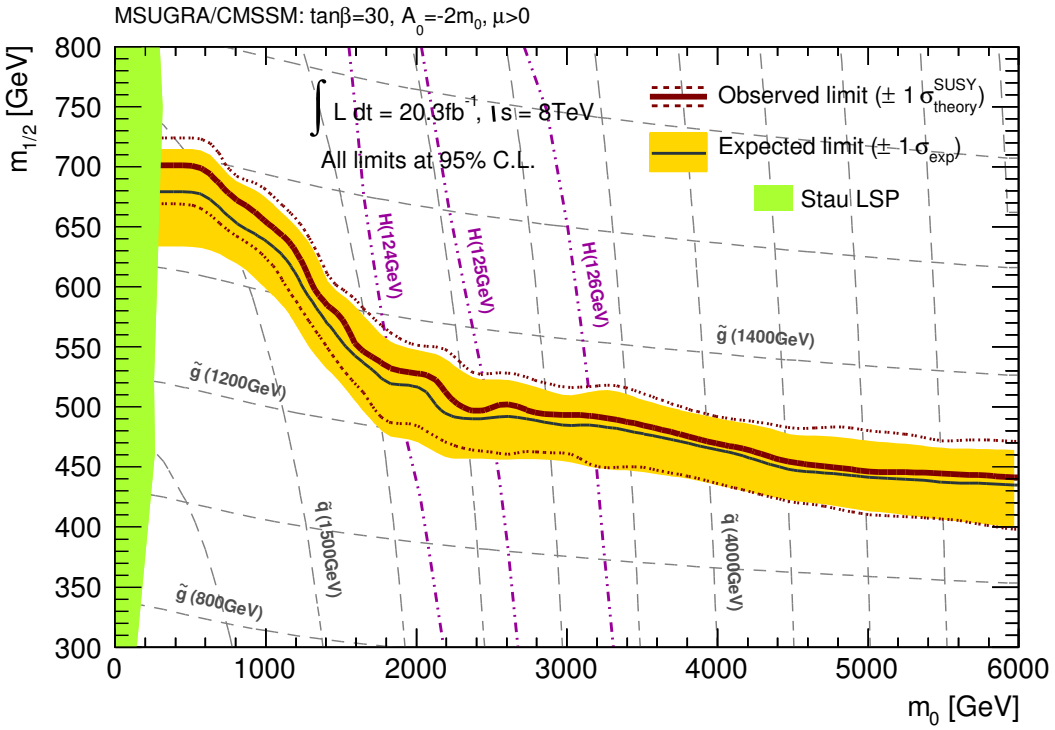

Figure 61: Observed and expected mass limits for the MSUGRA/CMSSM model with $\tan\beta = 30$, $A_0 = -2m_0$ and $\mu > 0$.

8.3.2 Simplified models

Figure 62 shows the observed (red) and expected (black) mass limits in the Simplified model assuming gluino pair productions and a LSP mass of 60 GeV. The x-axis shows gluino mass and the y-axis represents $x \equiv (m_{\tilde{\chi}_1^\pm} - m_{\tilde{\chi}_1^0})/(m_{\tilde{g}} - m_{\tilde{\chi}_1^0})$. Estimation error, including systematic and statistical uncertainties, is shown by the yellow band. The magenta, blue and green lines show separate limits of the Tight, Loose and Soft Signal Regions. Combined limit is basically driven by the Tight Signal Region, which is because a gluino pair production generally accompanies a large number of jets. The Loose Signal Region has a good sensitivity in high x regime, where gluino and chargino masses become degenerate. In most of x range ($0.3<x<0.8$), a gluino mass up to 1200 GeV is excluded. This is an improvement of 300 GeV from the previous limit [78] shown in the light blue area. For a severe condition of $x>0.1$, a gluino mass up to 1000 GeV is excluded.

Sensitivity loss in high x region for $m_{\tilde{g}}>1000$ GeV is caused by softer jet p_{T} spectra, thus the number of jet condition of the Tight Signal Region becomes hard to be satisfied. Instead, the Loose Signal Region gains sensitivity, though not enough to fully compensate the sensitivity loss of the Tight Signal Region.

On the other hand, in low x region around $m_{\tilde{g}} = 1000$ GeV, a chargino $\tilde{\chi}_1^\pm$ tends to have a large transverse momentum compared with the chargino mass, hence the decay products of the chargino, especially a lepton and a LSP, have a smaller opening angle. Resultant softer m_{T} leads to the sensitivity loss. This tendency is also seen in Fig. 39, where the signals with low-x (light magenta and light cyan) seem to have softer m_{T} distributions than those of high-x signals (dark magenta and dark cyan).

Figure 63 shows mass limits in the Simplified model assuming gluino pair productions with varying gluino and LSP masses. A chargino mass is set halfway between them. The x-axis shows gluino mass and the y-axis represents LSP mass. In the region where gluinos are much heavier than LSPs, the sensitivity is solely driven by the Tight Signal Region. When gluino and LSP degenerates and the mass splitting comes down to 100 GeV, the Tight Signal Regions looses the sensitivity due to an acceptance loss at the lepton selection. The Soft Signal Region covers the degenerate region until the mass difference becomes 30 GeV. Below the mass difference, we loose the sensitivity completely because the lepton emitted from decay often fall below our lowest lepton threshold, 6 GeV. Since no lepton is reconstructed in such a region, it should be covered by 0-lepton analysis [79].

A LSP mass up to 500 GeV is excluded in a wide range below $m_{\tilde{g}}$=1000 GeV. Assuming a chargino $\tilde{\chi}_1^\pm$ is produced at rest and W mass is negligible compared with LSP mass, the following equation gives a rough estimation of the LSP momentum:

$$p^{\mathrm{LSP}} \sim \frac{m_{\tilde{\chi}_1^\pm}}{2}\left[1 - \left(\frac{m_{\tilde{\chi}_1^0}}{m_{\tilde{\chi}_1^\pm}}\right)^2\right]. \tag{78}$$

$p_{\mathrm{T}}^{\mathrm{LSP}}$ is suppressed by the second term as LSP mass increases, which results in softer $E_{\mathrm{T}}^{\mathrm{miss}}$. Another impact of heavy LSP appears in m_{eff}, which becomes smaller for heavy LSPs because some fraction of the energy is consumed to create heavy LSPs. We perform a binned fit on m_{eff} to cope with such signals, however, low m_{eff} region is suffered from a large background thus we loose sensitivity. The sensitivity loss in $m_{\tilde{\chi}_1^0}>500$ GeV is mainly explained by these two reasons.

Figure 64 shows mass limits in the Simplified model assuming squark pair productions and a fixed LSP mass of 60 GeV. The y-axis represents $x \equiv (m_{\tilde{\chi}_1^\pm} - m_{\tilde{\chi}_1^0})/(m_{\tilde{q}} - m_{\tilde{\chi}_1^0})$. Both the Tight and Loose Signal Regions equally contributes to the combined limit. The observed limit reaches to 750 GeV, which is lower than the gluino limit because: (1) the cross-section of squark pair production is about 10 times lower than that of gluino around $m_{\tilde{\mathrm{q}}}$=$m_{\tilde{g}}$=750 GeV (see Fig. 30). (2) the acceptance of squark pair production is lower because the decay chain starting from squark has a smaller number of jets.

For $x > 0.2$, $m_{\tilde{q}} < 700$ GeV is excluded. The sensitivity loss in low-x region is explained in a similar way as gluino pair-production case.

Finally, Fig. 63 shows mass limits in the Simplified model assuming squark pair productions with varying gluino and LSP masses. A chargino mass is set halfway between them. Both the Tight and the Loose Signal Regions equally contribute to the combined limit. The Soft Signal Region recovers the sensitivity in the degenerate region around $m_{\tilde{q}}$=300 GeV. The combined limit exclude a LSP mass up to 200 GeV for $m_{\tilde{q}}$<750 GeV.

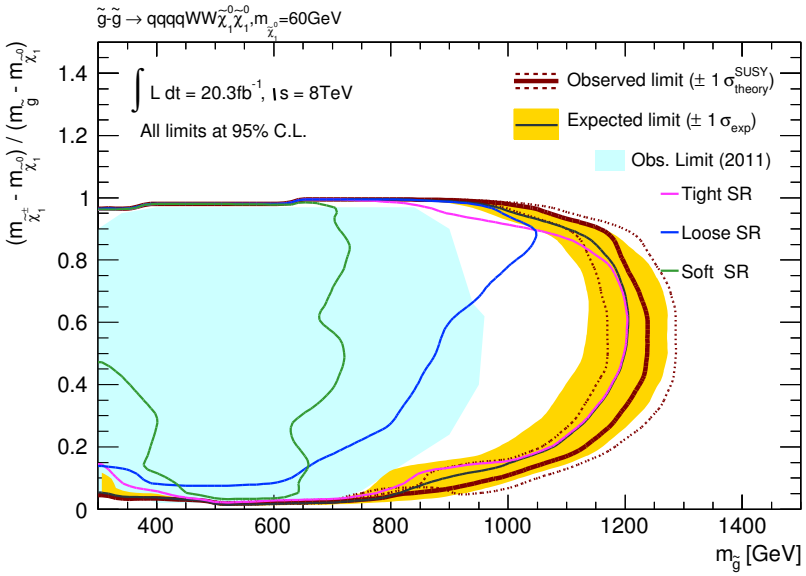

Figure 62: Observed and expected mass limits on $m_{\tilde{g}}$ and $x = (m_{\tilde{\chi}_1^\pm} - m_{\tilde{\chi}_1^0})/(m_{\tilde{g}} - m_{\tilde{\chi}_1^0})$ for the Simplified Model with $\tilde{g}$-$\tilde{g}$ production. $m_{\tilde{\chi}_1^0}$ is fixed at 60 GeV. The black line and the yellow band show the expected limit and its uncertainty ($\pm 1\sigma$). The solid red line shows the observed limit obtained by combining all the Signal Regions. The dotted red lines specify the impact of signal cross-section and acceptance uncertainties. The magenta, blue and green lines show separate limits of the Tight, Loose and Soft Signal Regions. The light blue area shows the previous limit [78] for reference.

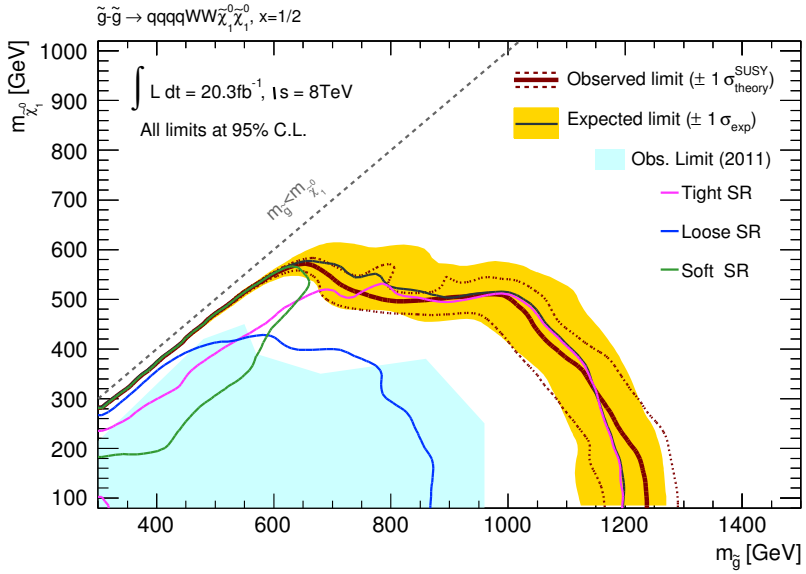

Figure 63: Observed and expected mass limits on $m_{\tilde{g}}$ and $m_{\tilde{\chi}_1^0}$for the Simplified Model with $\tilde{g}$-$\tilde{g}$ production. $x = (m_{\tilde{\chi}_1^\pm} - m_{\tilde{\chi}_1^0})/(m_{\tilde{g}} - m_{\tilde{\chi}_1^0})$ is fixed at 1/2. The black line and the yellow band show the expected limit and its uncertainty ($\pm 1\sigma$). The solid red line shows the observed limit obtained by combining all the Signal Regions. The dotted red lines specify the impact of signal cross-section and acceptance uncertainties. The magenta, blue and green lines show separate limits of the Tight, Loose and Soft Signal Regions. The light blue area shows the previous limit [78] for reference.

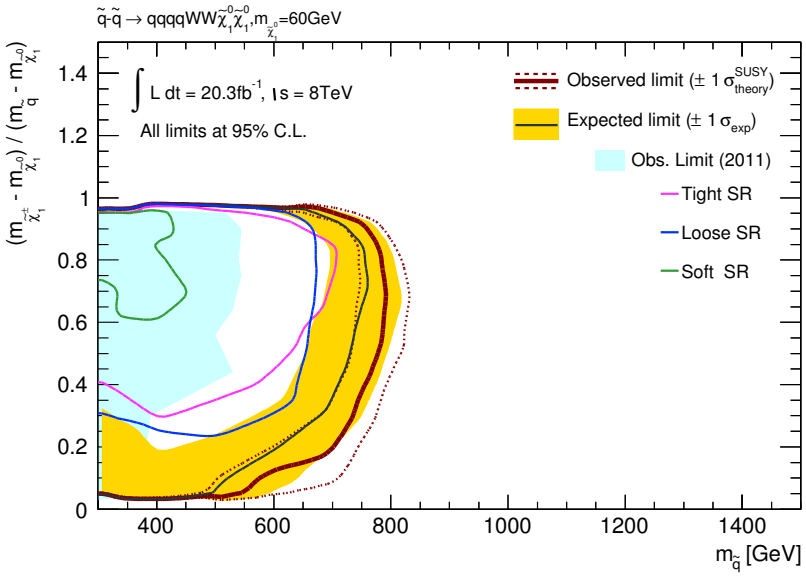

Figure 64: Observed and expected mass limits on $m_{\tilde{q}}$ and $x = (m_{\tilde{\chi}_1^\pm} - m_{\tilde{\chi}_1^0})/(m_{\tilde{q}} - m_{\tilde{\chi}_1^0})$ for the Simplified Model with $\tilde{q}$-$\tilde{q}$ production. $m_{\tilde{\chi}_1^0}$ is fixed at 60 GeV. The black line and the yellow band show the expected limit and its uncertainty ($\pm 1\sigma$). The solid red line shows the observed limit obtained by combining all the Signal Regions. The dotted red lines specify the impact of signal cross-section and acceptance uncertainties. The magenta, blue and green lines show separate limits of the Tight, Loose and Soft Signal Regions. The light blue area shows the previous limit [78] for reference.

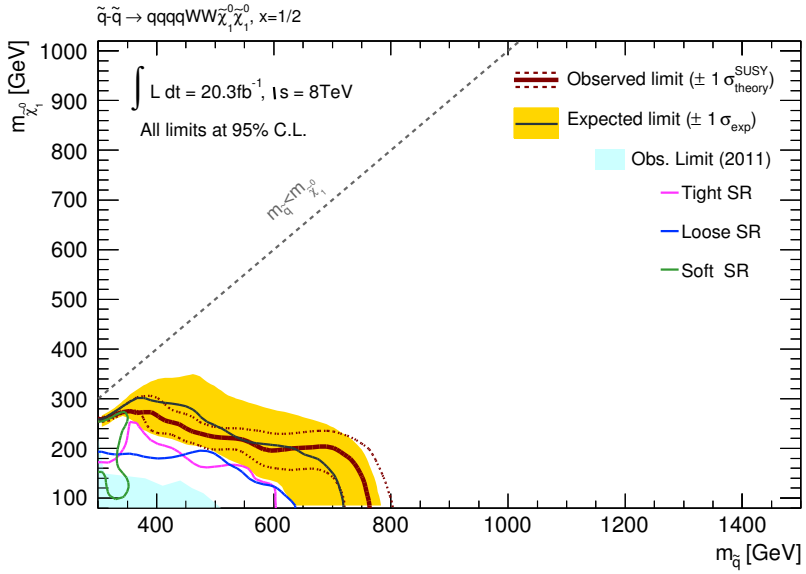

Figure 65: Observed and expected mass limits on $m_{\tilde{q}}$ and $m_{\tilde{\chi}_1^0}$for the Simplified Model with $\tilde{q}$-$\tilde{q}$ production. $x = (m_{\tilde{\chi}_1^\pm} - m_{\tilde{\chi}_1^0})/(m_{\tilde{q}} - m_{\tilde{\chi}_1^0})$ is fixed at 1/2. The black line and the yellow band show the expected limit and its uncertainty ($\pm 1\sigma$). The solid red line shows the observed limit obtained by combining all the Signal Regions. The dotted red lines specify the impact of signal cross-section and acceptance uncertainties. The magenta, blue and green lines show separate limits of the Tight, Loose and Soft Signal Regions. The light blue area shows the previous limit [78] for reference.

8.4 Discussion

We have looked through four types of simplified models in the previous section. Particularly interesting signals are $\tilde{g}$-$\tilde{g}$ productions because gluino mass is expected to lie at $O(1)$ TeV as discussed in Section 1.4.5. Therefore, we concentrate on the Simplified models starting from $\tilde{g}$-$\tilde{g}$ productions and set a model independent limit on gluino pair production cross-section in the following.

MSUGRA/CMSSM models have complicated decay chains, taking all the possible decays via electroweak gausinos into consideration, which increases a probability of having a lepton and many jets in the final states. Also, one of stops becomes 20-30% lighter than the other squarks in the maximal-mixing scenario thus more jets are expected in the final state. In contrast, Simplified models assume the simplest decay chains without taking in such effects, hence the limits obtained in Simplified models are in general conservative compared with the other physical scenarios. For example, the gluino mass limit obtained in MSUGRA/CMSSM model is better than the ones obtained in the Simplified model assuming gluino pair productions.

The maximum mass limit obtained in Simplified models is $m_{\tilde{g}}$>1200 GeV, but for more generality, we take $m_{\tilde{g}}$>1000 GeV as our gluino mass limit. The gluino mass of 1000 GeV seems mostly excluded in Figs. 62 and 63, however, there also exists some regions which are not yet excluded. We repeat the interpretations discussed in the previous section in the light of $m_{\tilde{g}}$=1000 GeV to summarize the applicable scope of our gluino mass limit.

First, the lepton acceptance has an impact on the sensitivity. As far as an on-shell W boson is emitted in a chargino decay, the lepton p_{T} does not strongly depend on the particle masses as shown in Fig. 36. When chargino and LSP are degenerate and only off-shell W is allowed, the lepton p_{T} becomes softer thus most of the lepton cannot pass the Hard Lepton p_{T} threshold of 25 GeV. The Soft Lepton selection is quite powerful to recover the lepton acceptance as shown in Fig. 36. This is also seen in the diagonal region in Fig. 63, where the Tight Signal Region looses sensitivity once the mass splitting between chargino and LSP gets below the mass of W boson. The Soft Signal Region keeps a good sensitivity even below the limit, until the mass difference becomes smaller than 15 GeV. In case of more degenerate signals, which do not emit any detectable leptons, 0-lepton analysis takes the place of Soft Lepton analysis.

Other regions are almost solely covered by the Tight Signal Region. The stringent $E_{\mathrm{T}}^{\mathrm{miss}}$ threshold of the Tight Signal Region ($E_{\mathrm{T}}^{\mathrm{miss}}$>350 GeV) is the next possibility of sensitivity loss. The sensitivity drop for $m_{\tilde{\chi}_1^0}$>500 GeV in Fig. 63 is mainly caused by this feature. In most of models, gluino mass is much heavier than electroweak gauginos therefore x is expected to be small. Since $E_{\mathrm{T}}^{\mathrm{miss}}$ is roughly proportional to the mass difference between chargino and LSP, the signal models assuming a chargino mass halfway between gluino and LSP gives a harder $E_{\mathrm{T}}^{\mathrm{miss}}$ distribution than usual models. So the Half-x Simplified model gives optimistic cases. But even in such cases, LSP mass heavier than 500 GeV is not excluded in our analysis, which puts an important exception on our limit. In addition, m_{eff} becomes small for a heavy LSP mass scenario because some fraction of the total energy is consumed to create heavy LSPs, leaving a small fraction of energy for visible particles, therefore we loose sensitivity further.

The low x regime in Fig. 62 is not excluded, which is explained by the soft m_{T} tendency due to the small opening angle between LSP and lepton (this tendency is clearly seen in Fig. 39). At $m_{\tilde{g}}$=1000 GeV, the sensitivity is lost around $x = 0.1$, where $m_{\tilde{\chi}_1^{\pm}}$ is 154 GeV and $m_{\tilde{\chi}_1^0}$ is 60 GeV. Only an energy of 94 GeV is available to produce and boost a W boson, thus the W boson is emitted almost the same direction as its parent chargino. The mass splitting between the gluino and chargino, on the other hand, is 846 GeV, therefore the chargino has a large momentum compared with the W boson, resulting in a small opening angle between the lepton and LSP. Such a case is also an exception of our limit.

Then, we set a model-independent cross-section limit for $\tilde{g}$-$\tilde{g}$ productions. This limit can be interpreted in any models as far as they contain $\tilde{g}$-$\tilde{g}$ productions. Simplified Models assume 100% branching fraction for $\tilde{g} \rightarrow qqW^{(*)}\tilde{\chi}_1^0$. In general SUSY models, the decay branch is suppressed due to several competitive decays, thus the cross-section limit is presented including the branching fraction $\mathrm{Br}\,(\tilde{g} \rightarrow qqW^{(*)}\tilde{\chi}_1^0)$. Requiring that both of the gluinos decay via charginos, the mass limit $m_{\tilde{g}}$>1000 GeV is interpreted as the cross-section upper limit of

$$\sigma\,(\tilde{g}\text{-}\tilde{g}) \times \mathrm{Br}\,(\tilde{g} \rightarrow qqW^{(*)}\tilde{\chi}_1^0)^2 < 20\,\mathrm{fb}.$$

This limit is a good approximation independent of the gluino decay pattern except for the following extreme cases:

- The mass difference between the chargino and LSP is smaller than 15 GeV.
- The mass of LSP is larger than 500 GeV for $m_{\tilde{g}}$=1000 GeV.
- The mass difference between chargino and LSP is small compared with the mass difference between gluino and chargino. For $m_{\tilde{g}}$=1000 GeV and $m_{\tilde{\chi}_1^0}$=60 GeV, a chargino lighter than $m_{\tilde{\chi}_1^\pm}$=150 GeV cannot be excluded.

9 Conclusion

Supersymmetry is one of the most attracting theories beyond the Standard Model. In the context of R-parity conserving supersymmetry model, the supersymmetric particles are produced in pairs and the lightest supersymmetric particle (LSP) is stable. Large gluino and squark production cross-sections are expected at the proton-proton collisions. Once gluinos and squarks are produced, they decay through a cascade of multiple stages to the final states with the LSP. The LSP is only weakly interacting and escapes detection, resulting in large missing transverse momentum $E_{\mathrm{T}}^{\mathrm{miss}}$. The decay also accompanies many hadronic jets and several leptons, which often give a distinct signature from the Standard Model processes.

A general search for supersymmetry in final states with jets, missing transverse momentum and one isolated electron or muon, using 20.3 fb^{-1} of proton-proton collision data at $\sqrt{s} = 8$ TeV recorded by the ATLAS detector at the LHC in 2012 is presented in this thesis.

One of the notorious backgrounds in proton-proton colliders is QCD multi-jet, which has an overwhelming cross-section, can be suppressed by requiring an isolated lepton (electron or muon). Therefore, leptonic analysis is an ideal way to search for new physics with small cross-sections at the LHC. Based on a topology selection of one lepton, large $E_{\mathrm{T}}^{\mathrm{miss}}$ and multiple jets, three signal regions are introduced to cover a wide range of signals in terms of different production processes and degenerate particle spectra. They are optimized based on the characteristic kinematic shapes of signals and further tuned using a full scan over all combinations of thresholds.

Tight Signal Region is optimized to be sensitive to the signals starting from gluino pair productions with a sufficiently large mass splitting between chargino and LSP. Loose Signal Region is designed to cover light squark pair productions, where small number of jets are expected. And finally, Soft Signal Region is defined to be sensitive to the degenerate region where the mass splitting between chargino and LSP is smaller than the mass of W boson.

The QCD multi-jet background is estimated in a data-driven way using Matrix-Method. The other backgrounds are estimated based on Monte Carlo simulations. Dominant background components, $t\bar{t}$ and W+jets, are normalized in Control Regions, which are designed to select the events having similar topologies to the events in Signal Region to cancel generator uncertainties. Mis-modelings in ISR emulation are further corrected based on data. As a result, our background estimation gives sufficiently good agreements to data, which is confirmed in dedicated Validation Regions and makes the analysis more reliable.

No excess over the Standard Model expectation is found in the Signal Regions, therefore the results are interpreted as mass limits in two models. In the MSUGRA/CMSSM model with $\tan\beta = 30, A_0 = -2\,m_0$ and $\mu > 0$, a gluino mass up to 1200 GeV is excluded at 95% C.L. for all range of universal scalar mass m_0 and universal gaugino mass $m_{1/2}$, and a squark mass is excluded up to 1500 GeV with an exception of $m_0 < 500$ GeV. In the Simplified models with the chargino mass halfway between the masses of the gluino/squark and LSP, gluinos (squarks) are excluded for masses below approximately 1200 (750) GeV for low values of the LSP mass. For the LSP mass of 500 GeV, gluino masses are excluded up to 1000 GeV. In the Simplified model with a fixed LSP mass and varying chargino and gluino/squark masses, gluino (squark) below approximately 1200 (750) GeV are excluded for a wide range of chargino masses.

The mass limit of $m_{\tilde{g}}$>1000 GeV is interpreted as an upper limit on the cross-section times branching fraction on the gluino pair-production cross-section $\sigma(\tilde{g}\text{-}\tilde{g})$ and branching fraction $\mathrm{Br}(\tilde{g} \to qqW^{(*)}\tilde{\chi}_1^0)$, which is

$$\sigma(\tilde{g}\text{-}\tilde{g}) \times \mathrm{Br}(\tilde{g} \to qqW^{(*)}\tilde{\chi}_1^0)^2 < 20\,\mathrm{fb}.$$

This limit is a good approximation independent of the gluino decay pattern except for the following

extreme cases:

- The mass difference between the chargino and LSP is smaller than 15 GeV.
- The mass of LSP is larger than 500 GeV for $m_{\tilde{g}}$=1000 GeV.
- The mass difference between chargino and LSP is small compared with the mass difference between gluino and chargino. For $m_{\tilde{g}}$=1000 GeV and $m_{\tilde{\chi}_1^0}$=60 GeV, a chargino lighter than $m_{\tilde{\chi}_1^\pm}$=150 GeV cannot be excluded.

Acknowledgements

I am really grateful to my supervisor, Prof. Shoji Asai, for helpful suggestions both for my analysis and for my private life. His positive attitude towards new physics always encourages me.

I would like to thank Prof. Naoko Kanaya. The discussion with her is always useful to unveil the structure of problems and gives me clues to the solutions.

I appreciate Dr. Shimpei Yamamoto and Prof. Junichi Tanaka for useful suggestions and for maintaining the computing resources in CERN.

I would appreciate Dr. Yosuke Kataoka and Dr. Takashi Yamanaka for their deep understanding of the ATLAS detector and Athena framework. They always give me clear suggestions when I encounter problems.

I am also thankful to all the professors, staffs, and students of analysis group in ICEPP, the University of Tokyo for fruitful discussions and supports during my stay at CERN. I would like to thank Prof. Tatsuo Kawamoto, Prof. Tomio Kobayashi, Prof. Koji Terashi, Dr. Tatsuya Masubuchi, Dr. Koji Nakamura, Dr. Taiki Yamamura, Dr. Yuji Enari, Dr. Keita Hanawa, Ginga Akimoto, Dr. Yuya Azuma, Dr. Hiroshi Yamaguchi, Shingo Kazama, Keisuke Yoshihara, Youhei Yamaguchi, Youichi Ninomiya, Masahiro Morinaga, Maya Okawa, and Yuki Kawanishi.

I would like to appreciate the members of analysis group at CERN: Dr. Aleksej Koutsman, Prof. Max Baak, Prof. Marie-Helene Genest, Dr. Zachary Louis Marshall, Ms. Jeanette Miriam Lorentz, Dr. Evgeny Khramov, Dr. Pedro Salvador Urrejola Pereira, Ms. Marija Vranjes Milosavljevic, Mr. Adrian Chitan, Ms. Kuwertz Emma Sian and Ms. Tudorache Valentina.

I am thankful to all members of the ATLAS collaboration and the LHC experts. Without their efforts, my work would not be completed.

I appreciate Prof. Claudio Santoni for useful discussion for the tile calorimeter calibration.

Finally, I would like to thank my family for supporting my life.

References

[1] ATLAS Collaboration Collaboration, *Combined measurements of the mass and signal strength of the Higgs-like boson with the ATLAS detector using up to 25 fb^{-1} of proton-proton collision data*, Tech. Rep. ATLAS-CONF-2013-014, CERN, Geneva, 2013.

[2] E. Komatsu et al., *Seven-year Wilkinson Microwave Anisotropy Probe (WMAP) Observations: Cosmological Interpretation*, The Astrophysical Journal Supplement Series **192** (2011) no. 2, 18.

[3] U. Amaldi, W. de Boer, and H. Fürstenau, *Comparison of grand unified theories with electroweak and strong coupling constants measured at LEP*, Physics Letters B **260** (1991) no. 3-4, 447–455.

[4] S. P. Martin, *A Supersymmetry primer*, `arXiv:hep-ph/9709356 [hep-ph]`.

[5] L. Hall, D. Pinner, and J. Ruderman, *A natural SUSY Higgs near 125 GeV*, Journal of High Energy Physics **2012** (2012) no. 4, 1–25.

[6] ATLAS Collaboration, *Combined coupling measurements of the Higgs-like boson with the ATLAS detector using up to 25 fb^{-1} of proton-proton collision data*, Tech. Rep. ATLAS-CONF-2013-034, CERN, Geneva, Mar, 2013.

[7] L. Randall and M. Reece, *Single-scale natural SUSY*, Journal of High Energy Physics **2013** (2013) no. 8, 1–31.

[8] M. Papucci, J. Ruderman, and A. Weiler, *Natural SUSY endures*, Journal of High Energy Physics **2012** (2012) no. 9, 1–45.

[9] L. Evans and P. Bryant, *LHC Machine*, Journal of Instrumentation **3** (2008) no. 08, S08001.

[10] CMS Collaboration, *CMS technical proposal*, tech. rep., CERN, CERN-LHCC-894-38, 1994.

[11] LHCb Collaboration, *LHCb technical proposal*, tech. rep., CERN, CERN-LHCC-98-004, 1994.

[12] ALICE Collaboration, *ALICE: Technical proposal for a Large Ion collider Experiment at the CERN LHC*, tech. rep., CERN, CERN-LHCC-95-71, 1997.

[13] ATLAS Collaboration, *ATLAS detector and physics performance : Technical Design Report, 1*, ATLAS-TDR-014, CERN-LHCC-99-014, 1999.

[14] ATLAS Collaboration, *ATLAS detector and physics performance : Technical Design Report, 2*, ATLAS-TDR-015, CERN-LHCC-99-015, 1999.

[15] ATLAS Collaboration, T. A. collaboration, *ATLAS Experiment at the CERN Large Hadron Collider*, JINST **3** (2008) S08003.

[16] G. Andres et al., *LHC Bunch Current Normalisation for the April-May 2010 Luminosity Calibration Measurements*, CERN-ATS-Note-2011-004, 2011.

[17] W. L. et al., *Calorimeter Clustering Algorithms: Description and Performance*, ATL-LARG-PUB-2008-002, 2008.

[18] M. Cacciari and G. P. Salam, *Dspelling the N^3 myth for the k_t jet-finder*, Phys. Lett. B **641** (2006) 57–61.

[19] M. Cacciari, G. P. Salam, and G. Soyez, *The anti-kt jet clustering algorithm*, Journal of High Energy Physics **2008** (2008) no. 04, 063.

[20] G. C. Blazey, J. R. Dittmann, S. D. Ellis, V. D. Elvira, K. Frame, S. Grinstein, R. Hirosky, R. Piegaia, H. Schellman, R. Snihur, V. Sorin, and D. Zeppenfeld, *Run II Jet Physics: Proceedings of the Run II QCD and Weak Boson Physics Workshop*, ArXiv High Energy Physics - Experiment e-prints (2000) , hep-ex/0005012.

[21] ATLAS Collaboration, G. Aad et al., *Jet energy measurement with the ATLAS detector in proton-proton collisions at* $\sqrt{s} = 7$ TeV, Eur.Phys.J. **C73** (2013) 2304, arXiv:1112.6426 [hep-ex].

[22] M. Cacciari and G. P. Salam, *Pileup subtraction using jet areas*, Physics Letters B **659** (2008) no. 1 - 2, 119 – 126.

[23] ATLAS Collaboration Collaboration, *Pile-up corrections for jets from proton-proton collisions at* $\sqrt{s} = 7$ TeV *in ATLAS in 2011*, Tech. Rep. ATLAS-CONF-2012-064, CERN, Geneva, Jul, 2012.

[24] ATLAS Collaboration, *Commissioning of the ATLAS high-performance b-tagging algorithms in the 7* TeV *collision data*, ATLAS-CONF-2011-102, 2011.

[25] G. Piacquadio and C. Weiser, *A new inclusive secondary vertex algorithm for b-jet tagging in ATLAS*, IEEE Transactions on Nuclear Science **57** (2010) no. 2, 760.

[26] ATLAS Collaboration, *Expected electron performance in the ATLAS experiment*, ATL-PHYS-PUB-2011-006, 2011.

[27] ATLAS Collaboration, *Electron performance measurements with the ATLAS detector using the 2010 LHC proton-proton collision data*, The European Physical Journal C **72** (2012) no. 3, 1–46.

[28] ATLAS Collaboration, G. Aad et al., *Expected Performance of the ATLAS Experiment - Detector, Trigger and Physics*, arXiv:0901.0512 [hep-ex].

[29] S. Hassani, L. Chevalier, E. Lancon, J. Laporte, R. Nicolaidou, et al., *A muon identification and combined reconstruction procedure for the ATLAS detector at the LHC using the (MUONBOY, STACO, MuTag) reconstruction packages*, Nucl.Instrum.Meth. **A572** (2007) 77–79.

[30] *Preliminary results on the muon reconstruction efficiency, momentum resolution, and momentum scale in ATLAS 2012 pp collision data*, Tech. Rep. ATLAS-CONF-2013-088, CERN, Geneva, Aug, 2013.

[31] ATLAS Collaboration, *Performance of Missing Transverse Momentum Reconstruction in ATLAS with 2011 Proton-Proton Collisions at* $\sqrt{s} = 7$ TeV, ATLAS-CONF-2012-101, 2012.

[32] ATLAS Collaboration, *Improved luminosity determination in pp collisions at* $\sqrt{s} = 7$ TeV *using the ATLAS detector at the LHC*, The European Physical Journal C **73** (2013) no. 8, 1–39.

[33] GEANT4 Collaboration, S. Agostinelli et al., *GEANT4: A Simulation toolkit*, Nucl.Instrum.Meth. **A506** (2003) 250–303.

[34] A. Buckley et al., *General-purpose event generators for LHC physics*, Physics Reports **504** (2011) no. 5, 145 – 233.

[35] J. Alwall et al., *Comparative study of various algorithms for the merging of parton showers and matrix elements in hadronic collisions*, The European Physical Journal C **53** (2008) no. 3, 473–500.

[36] F. Krauss, *Matrix Elements and Parton Showers in Hadronic Interactions*, Journal of High Energy Physics **2002** (2002) no. 08, 015.

[37] S. Catani, F. Krauss, B. R. Webber, and R. Kuhn, *QCD Matrix Elements + Parton Showers*, Journal of High Energy Physics **2001** (2001) no. 11, 063.

[38] V. Gribov and L. Lipatov, *Deep inelastic ep scattering in perturbation theory*, Sov.J.Nucl.Phys. **15** (1972) 438–450.

[39] G. Altarelli and G. Parisi, *Asymptotic Freedom in Parton Language*, Nucl.Phys. **B126** (1977) 298.

[40] Y. L. Dokshitzer, *Calculation of the Structure Functions for Deep Inelastic Scattering and e+ e- Annihilation by Perturbation Theory in Quantum Chromodynamics.*, Sov.Phys.JETP **46** (1977) 641–653.

[41] T. Sjostrand, S. Mrenna, and P. Skands, *A brief introduction to PYTHIA 8.1*, Computer Physics Communications **178** (2008) no. 11, 852 – 867.

[42] ATLAS Collaboration, *Further ATLAS tunes of Pythia6 and Pythia8*, ATL-PHYS-PUB-2011-014, 2011.

[43] A. Martin, W. Stirling, R. Thorne, and G. Watt, *Parton distributions for the LHC*, The European Physical Journal C **63** (2009) no. 2, 189–285.

[44] A. Martin, W. Stirling, R. Thorne, and G. Watt, *Uncertainties on α_S in global PDF analyses and implications forpredicted hadronic cross secions*, The European Physical Journal C **64** (2009) no. 4, 653–680.

[45] A. Martin, W. Stirling, R. Thorne, and G. Watt, *Heavy-quark mass dependence in global PDF analyses and 3- and 4-flavour parton distributions*, The European Physical Journal C **70** (2010) no. 1-2, 51–72.

[46] T. Gleisberg, S. Hoeche, F. Krauss, M. Schonherr, S. Schumann, et al., *Event generation with SHERPA 1.1*, JHEP **0902** (2009) 007, `arXiv:0811.4622 [hep-ph]`.

[47] H.-L. Lai, M. Guzzi, J. Huston, Z. Li, P. M. Nadolsky, J. Pumplin, and C.-P. Yuan, *New parton distributions for collider physics*, Phys. Rev. D **82** (2010) 074024.

[48] S. Catani and M. Grazzini, *Next-to-Next-to-Leading-Order Subtraction Formalism in Hadron Collisions and its Application to Higgs-Boson Production at the Large Hadron Collider*, Phys. Rev. Lett. **98** (2007) 222002.

[49] S. Catani, L. Cieri, G. Ferrera, D. de Florian, and M. Grazzini, *Vector Boson Production at Hadron Colliders: A Fully Exclusive QCD Calculation at Next-to-Next-to-Leading Order*, Phys. Rev. Lett. **103** (2009) 082001.

[50] S. Frixione, P. Nason, and G. Ridolfi, *A Positive-weight next-to-leading-order Monte Carlo for heavy flavour hadroproduction*, JHEP **0709** (2007) 126, `arXiv:0707.3088 [hep-ph]`.

[51] D. Stump, J. Huston, J. Pumplin, W.-K. Tung, H.-L. Lai, S. Kuhlmann, and J. F. Owens, *Inclusive jet production, parton distributions, and the search for new physics*, Journal of High Energy Physics **2003** (2003) no. 10, 046.

[52] S. M. T. Sjostrand and P. Skands, *PYTHIA 6.4 physics and manual*, JHEP **05** (2006) 026, arXiv:hep-ph/0603175.

[53] P. Z. Skands, *Tuning Monte Carlo generators: The Perugia tunes*, Phys. Rev. D **82** (2010) 074018.

[54] M. Aliev, H. Lacker, U. Langenfeld, S. Moch, P. Uwer, and M. Wiedermann, *HATHOR — HAdronic Top and Heavy quarks crOss section calculatoR*, Computer Physics Communications **182** (2011) no. 4, 1034 – 1046.

[55] M. Botje, J. Butterworth, A. Cooper-Sarkar, A. de Roeck, J. Feltesse, et al., *The PDF4LHC Working Group Interim Recommendations*, arXiv:1101.0538 [hep-ph].

[56] B. P. Kersevan and E. Richter-Was, *The Monte Carlo event generator AcerMC versions 2.0 to 3.8 with interfaces to PYTHIA 6.4, HERWIG 6.5 and ARIADNE 4.1*, Computer Physics Communications **184** (2013) no. 3, 919 – 985.

[57] N. Kidonakis, *Next-to-next-to-leading-order collinear and soft gluon corrections for t-channel single top quark production*, Phys. Rev. D **83** (2011) 091503.

[58] N. Kidonakis, *Next-to-next-to-leading logarithm resummation for s-channel single top quark production*, Phys. Rev. D **81** (2010) 054028.

[59] N. Kidonakis, *Two-loop soft anomalous dimensions for single top quark associated production with a W^- or H^-*, Phys. Rev. D **82** (2010) 054018.

[60] S. Frixione, E. Laenen, P. Motylinski, B. Webber, and C. D. White, *Single-top hadroproduction in association with a W boson*, arXiv:0805.3067 [hep-ex].

[61] E. Re, *Single-top Wt-channel production matched with parton showers using the POWHEG method*, arXiv:1009.2450 [hep-ex].

[62] J. Campbell and R. K. Ellis, *Radiative corrections to $Zb\bar{b}$ production*, Phys. Rev. D **62** (2000) 114012.

[63] J. Alwall et al., *MadGraph/MadEvent v4: The New Web Generation*, JHEP **09** (2007) 028, arXiv:0706.2334 [hep-ph].

[64] J. M. Campbell and R. K. Ellis, *$t\bar{t}W^{\pm}$ production and decay at NLO*, JHEP **1207** (2012) 052, arXiv:1204.5678 [hep-ph].

[65] M. Garzelli, A. Kardos, C. Papadopoulos, and Z. Trcsnyi, *$t\bar{t}W^{\pm}$ + $t\bar{t}Z$ hadroproduction at NLO accuracy in QCD with Parton Shower and Hadronization effects*, Journal of High Energy Physics **2012** (2012) no. 11, 1–21.

[66] D. Alves et al., *Simplified models for LHC new physics searches*, Journal of Physics G: Nuclear and Particle Physics **39** (2012) no. 10, 105005.

[67] ATLAS Collaboration, *Observation of a new particle in the search for the Standard Model Higgs boson with the ATLAS detector at the LHC*, Physics Letters B **716** (2012) no. 1, 1 – 29.

[68] W. Beenakker, S. Brensing, M. Krämer, A. Kulesza, E. Laenen, L. Motyka, and I. Niessen, *Squark and gluino hadroproduction*, Int. J. Mod. Phys. **A26** (2011) 2637–2664.

[69] W. Beenakker, R. Hopker, M. Spira, and P. Zerwas, *Squark and gluino production at hadron colliders*, Nucl. Phys. **B492** (1997) 51.

[70] A. Djouadi, M. Muhlleitner, and M. Spira, *Decays of supersymmetric particles: The Program SUSY-HIT (SUspect-SdecaY-Hdecay-InTerface)*, Acta Phys. Polon. **B38** (2007) 635–644, arXiv:hep-ph/0609292.

[71] B. C. Allanach, *SOFTSUSY: a program for calculating supersymmetric spectra*, Comput. Phys. Commun. **143** (2002) 305–331, arXiv:hep-ph/0104145.

[72] M. Muhlleitner, A. Djouadi, and Y. Mambrini, *SDECAY: A Fortran code for the decays of the supersymmetric particles in the MSSM*, Comput. Phys. Commun. **168** (2005) 46–70, arXiv:hep-ph/0311167.

[73] M. B. et al., *Herwig++ Physics and Manual*, Eur. Phys. J. **C58** (2008) 639.

[74] DELPHI Collaboration, *Searches for supersymmetric particles in e+ e- collisions up to 208 GeV and interpretation of the results within the MSSM*, The European Physical Journal C - Particles and Fields **31** (2003) no. 4, 421–479.

[75] ATLAS Collaboration, *ATLAS tunes of Pythia6 and Pythia8 for MC11*, ATL-PHYS-PUB-2011-009, 2011.

[76] H.-L. Lai, J. Huston, Z. Li, P. Nadolsky, J. Pumplin, et al., *Uncertainty induced by QCD coupling in the CTEQ global analysis of parton distributions*, Phys.Rev. **D82** (2010) 054021, arXiv:1004.4624 [hep-ph].

[77] P. M. Nadolsky, H.-L. Lai, Q.-H. Cao, J. Huston, J. Pumplin, et al., *Implications of CTEQ global analysis for collider observables*, Phys.Rev. **D78** (2008) 013004, arXiv:0802.0007 [hep-ph].

[78] ATLAS Collaboration, *Further search for supersymmetry at* $\sqrt{s}$=7 TeV *in final states with jets, missing transverse momentum, and isolated leptons with the ATLAS detector*, Phys. Rev. D **86** (2012) 092002.

[79] *Search for squarks and gluinos with the ATLAS detector in final states with jets and missing transverse momentum and 20.3* fb^{-1} *of* $\sqrt{s}$ = 8 *TeV proton-proton collision data*, Tech. Rep. ATLAS-CONF-2013-047, CERN, Geneva, May, 2013.

[80] ATLAS Collaboration, *Electron performance measurements with the ATLAS detector using the 2010 LHC proton-proton collision data*, The European Physical Journal C **72** (2012) no. 3, 1–46.

[81] G. Cowan, K. Cranmer, E. Gross, and O. Vitells, *Asymptotic formulae for likelihood-based tests of new physics*, The European Physical Journal C **71** (2011) no. 2, 1–19.

[82] ATLAS Collaboration, *ATLAS muon spectrometer: Technical Design Report*. Technical Design Report ATLAS. CERN, Geneva, 1997. distribution.

[83] ATLAS Collaboration, *ATLAS magnet system: Technical Design Report, 1*. Technical Design Report ATLAS. CERN, Geneva, 1997.

[84] J. Allison et al., *Geant4 developments and applications*, Nuclear Science, IEEE Transactions on **53** (2006) no. 1, 270–278.

[85] E. Lund, L. Bugge, I. Gavrilenko, and A. Strandlie, *Track parameter propagation through the application of a new adaptive Runge-Kutta-Nystroem method in the ATLAS experiment*, JINST **4** (2009) P04001.

[86] ATLAS Collaboration, *Testbeam studies of production modules of the ATLAS Tile Calorimeter*, Nuclear Instruments and Methods in Physics Research Section A: Accelerators, Spectrometers, Detectors and Associated Equipment **606** (2009) no. 3, 362 – 394.

A Higgs mechanism

A.1 Electroweak theory

Considering a W boson decay such as $W^+ \to l_L^+ + \nu_L$, or its transposition $l_L^- + W^+ \to \nu_L$, in which the left-handed down-type lepton is converted to the left-handed neutrino (up-type), one presumes the correspondence between W boson and the raising operator of $SU(2)_L$. Here using the Pauli spin matrix (τ_i, $i = 0, 1, 2$), raising (lowering) operator ($\tau_{+(-)}$) is defined as $\tau_\pm = \frac{1}{2}(\tau_1 \pm i\tau_2)$. The interaction of 0-th Pauli matrix might be then presumed to be the counterpart of Z^0 boson, however, the past experiments show that Z^0 boson interacts not only left-handed but also right-handed fermions. Therefore, the counterpart of 0-th Pauli matrix, W^0, must be mixed with another interaction. A U(1) interaction is introduced for this purpose (subscript Y is assigned), which is blind to $SU(2)_L$ charge but proportional to weak hypercharge Y. We define weak hypercharge Y for each particle so that electromagnetic charge Q (in a unit of e) and the eigenvalue of the weak charge T^0 satisfy the following relation:

$$Q = T^0 + \frac{Y}{2}. \tag{79}$$

The interaction Lagrangian, then, consists of three vector fields W_μ^i coupled with strength g to weak isospin current J_μ^i, together with a single vector field B_μ coupled to weak hypercharge current j_μ^Y, with strength conventionally taken to be $g'/2$. The Lagrangian is constructed as

$$\mathcal{L}_{\text{int}} = -ig(J^i)^\mu W_\mu^i - i\frac{g'}{2}(j^Y)^\mu B_\mu. \tag{80}$$

Since no physical correspondence is observed for W_μ^0 and B_μ, they must mix in such a way that to give Z^0 boson and a photon A^0.

$$\begin{cases} A_\mu^0 &= B_\mu \cos\theta_W + W_\mu^0 \sin\theta_W \\ Z_\mu^0 &= -B_\mu \sin\theta_W + W_\mu^0 \cos\theta_W \end{cases} \tag{81}$$

where θ_W is called Weinberg angle.

Considering Eq. 79-81, the following relation holds,

$$\mathcal{L}_{\text{int}} = -ie j_\mu^{\text{EM}} A^\mu - i\frac{g}{\cos\theta_W} J_\mu^{\text{NC}} Z^\mu, \tag{82}$$

where,

$$\begin{aligned} j_\mu^{\text{EM}} &= J_\mu^0 + \tfrac{1}{2} j_\mu^Y \\ J_\mu^{\text{NC}} &= J_\mu^0 - \sin^2\theta_W j_\mu^{\text{EM}} \end{aligned} \tag{83}$$

Electromagnetic and weak forces are united in this picture, therefore, this theory is called electroweak theory.

A.2 Gauge theory

Gauge theory derives the interactions between fermions and gauge bosons from symmetries. In the previous section, we've already seen that electroweak theory consists of $SU(2)_L$ and $U(1)_Y$ symmetries. In this section, we discuss the concept in more detail.

We start from considering the following transformation

$$\Psi(x) \to e^{i\alpha(x)}\Psi(x), \tag{84}$$

where $\Psi(x)$ is a Dirac field and $\alpha(x)$ is a phase parameter depending on space and time in a completely arbitrary way. The following Lagrangian is required to be invariant under the transformation,

$$\mathcal{L} = i\bar{\Psi}\gamma^\mu\partial_\mu\Psi - m\bar{\Psi}\Psi. \tag{85}$$

This is not attainable when α is a function of space-time, because the partial derivative gives rise to an extra term as

$$\partial_\mu \Psi \to e^{i\alpha(x)} \partial_\mu \Psi + i e^{i\alpha(x)} \Psi \partial_\mu \alpha(x). \tag{86}$$

To remove the last term, we introduce a modified derivative, D_μ or "covariant derivative", so that the term is invariant under the transformation

$$D_\mu \Psi \to e^{i\alpha(x)} D_\mu \Psi. \tag{87}$$

We must introduce a vector field A_μ with transformation properties such that the unwanted term is canceled. This can be accomplished by the construction,

$$D_\mu = \partial_\mu - ieA_\mu, \tag{88}$$

where A_μ transforms as,

$$A_\mu \to A_\mu + \frac{1}{e}\partial_\mu \alpha(x). \tag{89}$$

By replacing ∂_μ by D_μ, the Lagrangian obtains the invariance to the arbitrary phase transformation. The Lagrangian is then

$$\begin{aligned} \mathcal{L} &= i\bar{\Psi}\gamma^\mu D_\mu \Psi - m\bar{\Psi}\Psi & (90)\\ &= \bar{\Psi}(i\gamma^\mu \partial_\mu - m)\Psi + e\bar{\Psi}\gamma^\mu \Psi A_\mu. & (91) \end{aligned}$$

The first term in the last line is the kinematic term of the Dirac particle and the second term represents the interaction of a photon A_μ and the Dirac particle with an electric charge of $-e$.

The same procedure is applicable to weak isospin symmetry $\mathrm{SU}(2)_L$, which gives the weak interaction Lagrangian. However, it is known that a trivial mass term breaks the gauge invariance. This is easily understood for $\mathrm{U}(1)_Y$ symmetry case as follow,

$$-\frac{1}{2}m^2 A^\mu A_\mu \to -\frac{1}{2}m^2 (A^\mu + \frac{1}{e}\partial_\mu \alpha)(A_\mu + \frac{1}{e}\partial^\mu \alpha) \neq -\frac{1}{2}m^2 A^\mu A_\mu. \tag{92}$$

This fact casts a shadow on the gauge theory of weak force because weak bosons are known as massive particles, therefore a special mechanism should be introduced to bear mass without adding a trivial mass term.

A.3 Higgs mechanism

The Higgs mechanism introduces an $\mathrm{SU}(2)_L$ doublet of complex scalar fields:

$$\phi = \frac{1}{\sqrt{2}} \begin{pmatrix} \phi_1 + i\phi_2 \\ \phi_3 + i\phi_4 \end{pmatrix}, \tag{93}$$

and considers the Lagrangian

$$\mathcal{L} = (\partial_\mu \phi)^\dagger (\partial^\mu \phi) - \mu^2 \phi^\dagger \phi - \lambda (\phi^\dagger \phi)^2, \tag{94}$$

where $\mu^2 < 0$ and $\lambda > 0$. The first term represents the kinematic energy followed by a negative mass term and a four-point interaction term. The latter two terms are interpreted as a potential of ϕ field and denoted as $V(\phi)$.

To keep the Lagrangian invariant under $\mathrm{SU}(2)_L$ transformation,

$$\phi \to \phi' = e^{i\alpha_a \tau_a/2}\phi, \tag{95}$$

the partial derivative ∂_μ is replaced by the covariant derivative,

$$D_\mu = \partial_\mu + ig\frac{\tau_a}{2}W_\mu^a. \tag{96}$$

Here we introduced three gauge fields of $SU(2)_L$, $W_\mu^a(x)$, with $a = 0, 1, 2$. For an infinitesimal gauge transformation of $\boldsymbol{\alpha}$ (here the three components are represented in the form of vector), the gauge fields, $\mathbf{W}_\mu$, transform as,

$$\mathbf{W}_\mu \to \mathbf{W}_\mu - \frac{1}{g}\partial_\mu\boldsymbol{\alpha} - \boldsymbol{\alpha}\times\mathbf{W}_\mu. \tag{97}$$

The potential $V(\phi)$ is not stable at $\phi = 0$ because of the negative mass term. The minimal of the potential is realized when the following relation is satisfied:

$$\phi^\dagger\phi = \frac{1}{2}\left(\phi_1^2 + \phi_2^2 + \phi_3^2 + \phi_4^2\right) = -\frac{\mu^2}{2\lambda}. \tag{98}$$

$\phi^\dagger\phi$ is invariant under $SU(2)_L$ transformation, therefore we can choose

$$\phi_1 = \phi_2 = \phi_4 = 0, \;\; \phi_3^2 = -\frac{\mu^2}{\lambda} \equiv v^2, \tag{99}$$

without loosing generality. v is called vacuum expectation value and often abbreviated as VEV.

We now expand $\phi(x)$ about this particular vacuum:

$$\phi_0 \equiv \frac{1}{\sqrt{2}}\begin{pmatrix} 0 \\ v \end{pmatrix}. \tag{100}$$

A small variation around ϕ_0 along the real axis gives a new particle field, Higgs particle $H(x)$,

$$\phi(x) = \frac{1}{\sqrt{2}}\begin{pmatrix} 0 \\ v + H(x) \end{pmatrix}. \tag{101}$$

This choice seems arbitrary, however, due to the gauge symmetry, we can always choose the direction along the real axis. By expanding the potential $V(\phi)$ around ϕ_0, we get the term proportional to H^2, which gives a positive Higgs mass of

$$m_H = \sqrt{2v^2\lambda}. \tag{102}$$

The goal of the Higgs mechanism is to make electroweak bosons massive without introducing a trivial mass term. Now one specific vacuum point ϕ_0 is chosen as a stable state (Spontaneous Symmetry Breaking: SSB), and the quadrature of electroweak boson fields appears though the covariant derivative (Eq. 96). The mass term, including all the electroweak gauge symmetries, is then represented as follow:

$$\left|\left(-ig\frac{\tau_a}{2}W_\mu^a - i\frac{g'}{2}B_\mu\right)\phi_0\right|^2 = \left(\frac{1}{2}vg\right)^2 W_\mu^+W^{-\mu} + \frac{1}{8}\left(W_\mu^0, B_\mu\right)\begin{pmatrix} g^2 & -gg' \\ -gg' & g'^2 \end{pmatrix}\begin{pmatrix} W^{0\mu} \\ B_\mu \end{pmatrix} \tag{103}$$

The boson masses are, then,

$$m(W^\pm) = \frac{1}{2}vg, \tag{104}$$

$$m(Z^0) = \frac{1}{2}v\sqrt{g^2 + g'^2}, \tag{105}$$

$$m(A^0) = 0. \tag{106}$$

Massless bosons have only two degrees of freedom, while massive bosons have three. The additional degree is provided from the three components in the original scalar doublet, ϕ_1, ϕ_2, ϕ_4. The remaining one degree of freedom is observed as the physical Higgs particle, $H(x)$.

In the framework of the Higgs mechanism, fermion mass is also obtained though the vacuum expectation value. For an electron case, the mass Lagrangian is

$$\begin{aligned} \mathcal{L}_{\text{electron mass}} &= -y_e \left(\bar{L} \phi_0 e_R + \bar{e}_R \phi_0^\dagger L \right) && (107) \\ &= -\frac{y_e v}{\sqrt{2}} \bar{e} e, && (108) \end{aligned}$$

where L is the weak isospin doublet for left-handed leptons of the first generation, $L = \begin{pmatrix} \nu_L \\ e_L \end{pmatrix}$, e_R is the right-handed electron and y_e is a constant called Yukawa coupling. The Yukawa coupling y_e is determined by the following mass relation,

$$m_e = \frac{y_e v}{\sqrt{2}}. \tag{109}$$

The Higgs mechanism doesn't predict fermion mass, however, several implications, such as the proportional coupling strength to the fermion mass, can be inferred.

B Details of Signal Region optimization

B.1 Setup

As discussed in the text, an ideal way of optimization is to test all the possible combinations of selections and find the best set. Therefore we perform a sensitivity scan over all combinations of thresholds listed in Table 25. In total 12960 (Hard Lepton) and 10800 (Soft Lepton) trial signal regions C are defined uniformly in the phase space spanned by the kinematic variables. The numbers of events of signal and background are then converted into Score Ψ_C^Q, which is defined as

$$\Psi_C^Q = \frac{1}{N(Q)} \sum_i^Q \text{median}[Z_0|S'_{i,C} + B'_C], \tag{110}$$

where Q is the collection of signals in which the selection C is optimized and $N(Q)$ is the number of the signals. Typical tendencies over the signal collections can be obtained by taking the average of the scores.

$$\text{median}[Z_0|S_C + B_C] \sim \sqrt{2((S_C + B_C)\ln(1 + S_C/B_C) - S_C)}, \tag{111}$$

where S_C (B_C) is the number of signal (background) events after applying cut C. median$[Z_0|S_C + B_C]$ gives an approximate sensitivity based on Profile-likelihood method (detail is given in Section H). To take uncertainties $\Delta S_C, \Delta B_C$ into account, the following event numbers are used in Eq. 110

$$S_C \rightarrow S'_C = S_C - \Delta S_C, \tag{112}$$

$$B_C \rightarrow B'_C = B_C + \Delta B_C. \tag{113}$$

This configuration gives the most conservative sensitivity. The size of the uncertainties are set to 30% for both signal and background. Since signal regions are dominated by statistical errors, the optimization is not affected if we use 50% for the uncertainty.

One practical difficulty occurs when one of the background samples lefts no event after a harsh cut, which gives unphysical optimization results. To avoid this problem, the minimum number of events is set for the major background samples: W+jets and $t\bar{t}$. Since $t\bar{t}$ events are generated plenty enough, the minimum number is set to 0, while that of W+jets is set to 2.5 events.

Before scanning the cuts, the following conditions are applied as pre-selections:

Hard Lepton pre-selection :

- Exactly 1 signal lepton,
- No crack electron.

Soft Lepton pre-selection :

- Exactly 1 soft signal lepton,
- No crack electron,
- $\min_{\text{jet}} \Delta R(\text{lep}, \text{jet}) > 1.0$.

Table 26 shows the signal models and parameter spaces used to define Q for each signal region. The parameter spaces are chosen so that the signals with representative topologies are selected. Note that Hard Lepton SR (Tight, Loose) and Soft SR are defined orthogonally by the different lepton p_{T} selections, while Tight and Loose SRs may have an overlap. The overlap is resolved by requiring an upper limit on the number of jets in Loose Signal Region in the final limit calculation, but it is not considered in the optimization procedure.

Variable	Trial thresholds	
	Hard Lepton	Soft Lepton
#jets	$N_{\text{jet}}^{40} \geq$[3, 4, 5, 6]	$N_{\text{jet}}^{30} \geq$[3, 4, 5, 6]
$p_{\text{T}}^{\text{jet1}}$	[80, 120, 160, 200, 240]	[30, 60, 90, 120, 150]
$p_{\text{T}}^{\text{jet2}}$	[40, 70, 100, 130, 160, 190]	[30, 60, 90, 120, 150]
m_{T}	[100, 150, 200]	[100, 120, 150]
$E_{\text{T}}^{\text{miss}}$	[200, 250, 300, 350, 400, 450]	[200, 250, 300, 350, 400, 450]
m_{eff}	[400, 800, 1200, 1600, 2000, 2400]	[400, 800, 1200, 1600, 2000, 2400]

Table 25: List of the kinematic variables and their trial thresholds.

Signal Region	Signal Model	Parameter space
Tight	Simplified Model	$m_{\tilde{\chi}_1^0}$=60 GeV
	$\tilde{g}$-$\tilde{g}$ production	$m_{\tilde{g}}$=1000-1300 GeV
Loose	Simplified Model	$m_{\tilde{\chi}_1^0}$=60 GeV
	$\tilde{\text{q}}$-$\tilde{\text{q}}$ production	$m_{\tilde{\text{q}}}$=450-600 GeV
		x <0.3
Soft	Simplified Model	$m_{\tilde{\chi}_1^0}$>60 GeV
	$\tilde{g}$-$\tilde{g}$ production	$m_{\tilde{g}}$=500-800 GeV
		($m_{\tilde{g}}$-$m_{\tilde{\chi}_1^0}$)<200 GeV

Table 26: Combination of Signal model and the parameter space which defines Q for each signal region. $x \equiv (m_{\tilde{\chi}_1^\pm} - m_{\tilde{\chi}_1^0})/(m_{\tilde{g}/\tilde{q}} - m_{\tilde{\chi}_1^0})$.

B.2 Results

The top panels of Fig. 66-68 show the Score Φ_C distributions for Tight, Loose and Soft SRs, respectively. The scores are classified to low (blue), middle (purple) high (orange) groups. The thresholds of these groups are chosen so that clear tendencies are seen with meaningful statistics. Our goal is to withdraw the characteristics of the selections classified to high score group. To visualize the characteristics, distributions of the thresholds are shown in the bottom panels of Fig. 66-68. They are all normalized so that the largest bin is always 1, and the colors correspond to the ones in the score distributions in the top panel.

We take N_{jet}^{40} histogram of Fig. 66 as an example. The orange broken line shows a histogram of the thresholds classified as high-scored group. The histogram peaks at $N_{jets}^{40} = 5$, which means the high scored selections tend to favor the number of jets larger than five. This is an expected result as we found in Section 5.1.4. With a close look at the histograms, we get the following insights:

Tight SR :

- The number of jets $N^{\text{jet}} \geq 5$ is favored. The leading jet favors $p_{\text{T}}^{\text{jet1}} > 120$ GeV, while histogram of the next leading jet is constantly decreasing, which means the lower p_{T} threshold is favored for the next leading jet.
- Tight m_{T} selection is clearly favored. Although it cannot be read from the plot, $m_{\text{T}} > 150$ GeV is favored in the high-scored group.
- Large m_{eff} is favored due to heavy initial particles.
- High score group has a peak around 350 GeV. We then take $E_{\text{T}}^{\text{miss}} > 350$ GeV for the Tight SR.

Loose SR :

- Small number of jets is favored. Thus the number of jets $N^{\text{jet}} \geq 3$ is chosen for the Loose SR.
- $m_{\text{T}} > 120$ GeV is favored.
- $E_{\text{T}}^{\text{miss}} > 250$GeV is clearly favored.

Soft SR :

- High-scored group tend to favor lower values for the number of jets, the transverse momentum of the next leading jets, m_{T} and m_{eff}.
- $p_{\text{T}}^{\text{jet1}}$ favors a moderate threshold. Here we use 100 GeV for the threshold.
- $E_{\text{T}}^{\text{miss}}$ plot peaks at around 300-400 GeV. We then require $E_{\text{T}}^{\text{miss}} > 300$ GeV.

Note that these observations are consistent with our findings in Section 5.1.4. The optimized results are summarized in Table 12.

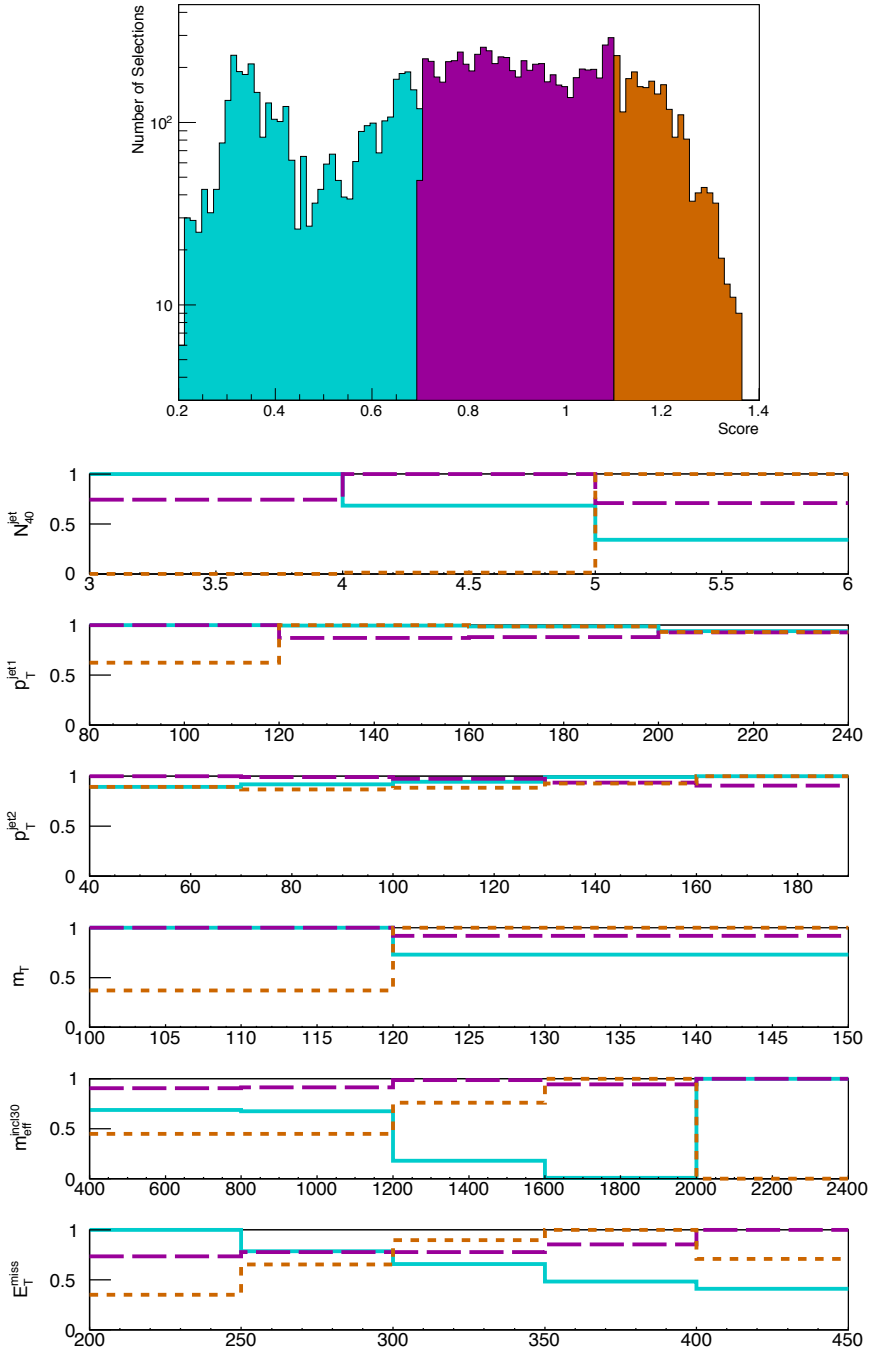

Figure 66: Plots used in the optimization of Tight SR are shown. (Top) Score distribution obtained in the full threshold scan, separated by three colors, blue is for the low score, purple for the middle score, and orange for the high score. (Bottom) The distributions of the thresholds are shown. x-axes show the minimum thresholds applied to the kinematic variables. The colors on top panel correspond to the histograms in the bottom panel.

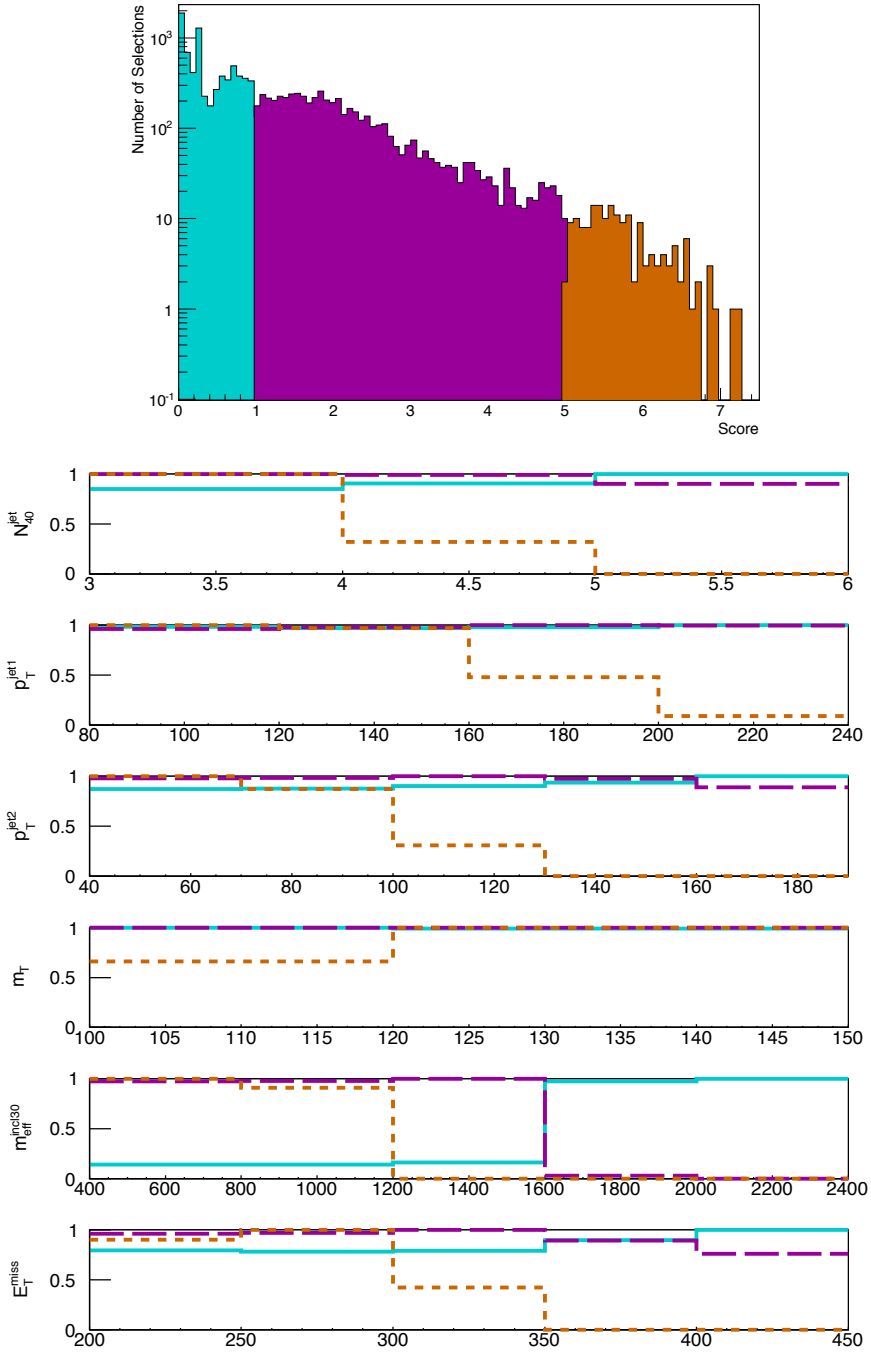

Figure 67: Plots used in the optimization of Loose SR are shown. (Top) Score distribution obtained in the full threshold scan, separated by three colors, blue is for the low score, purple for the middle score, and orange for the high score. (Bottom) The distributions of the thresholds are shown. x-axes show the minimum thresholds applied to the kinematic variables. The colors on top panel correspond to the histograms in the bottom panel.

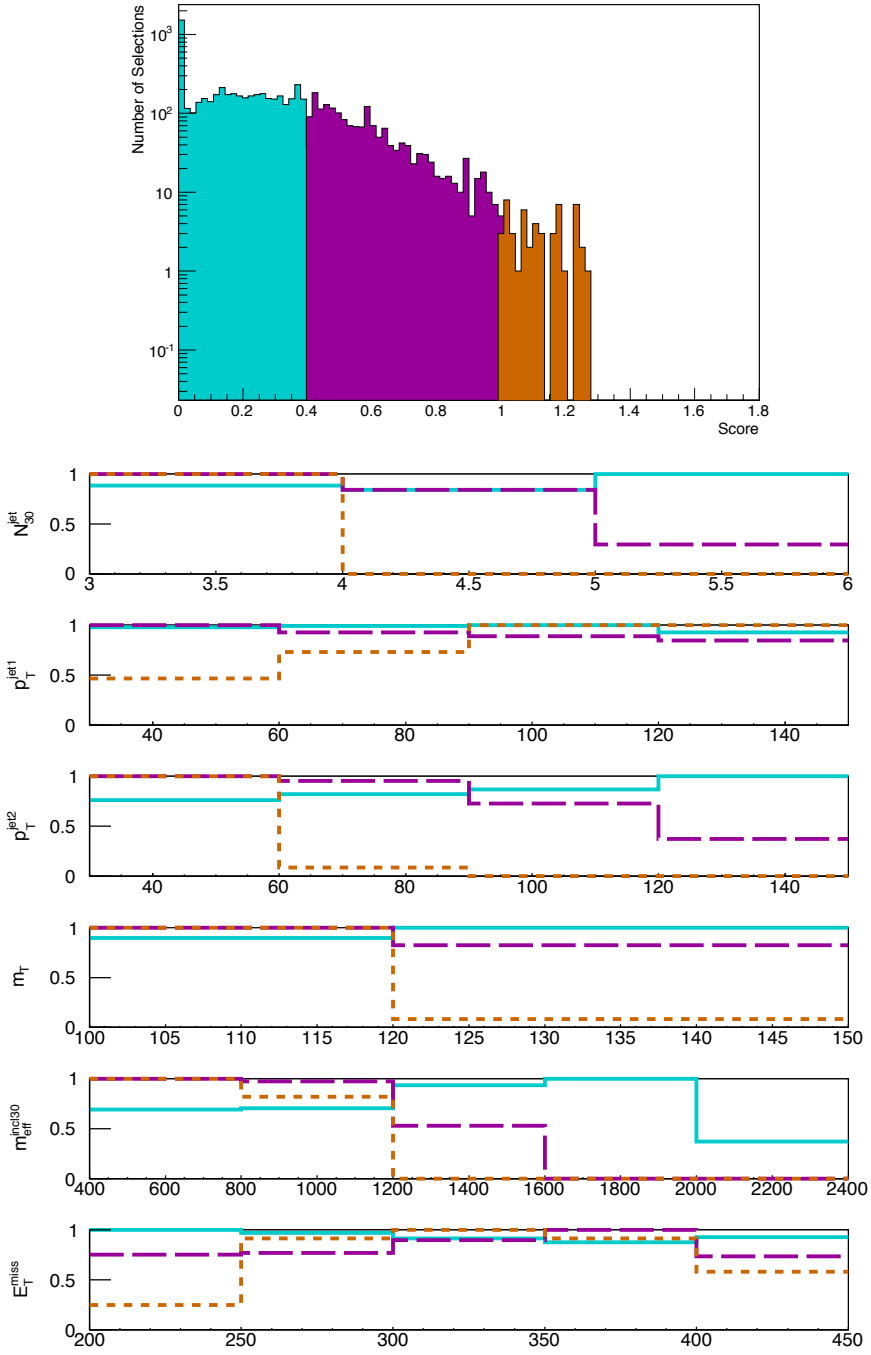

Figure 68: Plots used in the optimization of Soft SR are shown. (Top) Score distribution obtained in the full threshold scan, separated by three colors, blue is for the low score, purple for the middle score, and orange for the high score. (Bottom) The distributions of the thresholds are shown. x-axes show the minimum thresholds applied to the kinematic variables. The colors on top panel correspond to the histograms in the bottom panel.

C Matrix-Method

Matrix-Method estimates the shape and yield of QCD multi-jets from the difference between fake-enriched and fake-suppressed distributions. Fake-enriched region is defined by loosening the lepton isolation to "Loose" conditions. Fake-suppressed region is defined by selecting "Signal" leptons. For simplicity, we call these two leptons as Loose and Tight leptons. The difference between Loose and Tight lepton definitions are summarized in Table 27 (electron) and 28 (muon). Their exact definitions are documented in Tables 4, 5 (electron), 6, 7 (muon). We also abbreviate QCD multi-jet events as fake events.

items	Hard Lepton	Soft Lepton
Identification criteria	`Medium++`→`Tight++`	-
Track isolation	`ptcone20`/$p_{\mathrm{T}} < 0.10$	`ptcone30`/$p_{\mathrm{T}} < 0.16$
Transverse IP	$d_0^{\mathrm{PV}} \leq 1$ mm	$\lvert d_0^{\mathrm{PV}}/\sigma(d_0^{\mathrm{PV}})\rvert \leq 5$
Longitudinal IP	$\lvert z_0^{\mathrm{PV}}\rvert \leq 2$ mm	$\lvert z_0^{\mathrm{PV}} \times \sin(\theta)\rvert \leq 0.4$ mm

Table 27: Isolation conditions which defines Tight electron from Loose one.

items	Hard Lepton	Soft Lepton
Track isolation	`ptcone20` < 1.8 GeV	`ptcone30`< 1.2 GeV
Transverse IP	-	$\lvert d_0^{\mathrm{PV}}/\sigma(d_0^{\mathrm{PV}})\rvert \leq 3$
Longitudinal IP	-	$\lvert z_0^{\mathrm{PV}} \times \sin(\theta)\rvert \leq 0.4$ mm

Table 28: Isolation conditions which defines Tight muon from Loose one.

The events with 1 Loose lepton are selected to define the population, and the number of events whose lepton passes also Tight lepton selection is denoted as N_{pass}, while the number of the failing events is N_{fail}. Two efficiencies are defined for both real and fake leptons, based on the fraction of events passing Tight lepton selection out of Loose lepton events,

$$\epsilon_{\mathrm{real}} = \frac{N_{\mathrm{real}}^{\mathrm{Tight}}}{N_{\mathrm{real}}^{\mathrm{Loose}}}, \quad \epsilon_{\mathrm{fake}} = \frac{N_{\mathrm{fake}}^{\mathrm{Tight}}}{N_{\mathrm{fake}}^{\mathrm{Loose}}}. \tag{114}$$

Then we consider the following relations,

$$\begin{cases} N_{\mathrm{pass}} = & \epsilon_{\mathrm{fake}} \cdot N_{\mathrm{fake}} + & \epsilon_{\mathrm{real}} \cdot N_{\mathrm{real}} \\ N_{\mathrm{fail}} = & (1-\epsilon_{\mathrm{fake}}) \cdot N_{\mathrm{fake}} + & (1-\epsilon_{\mathrm{real}}) \cdot N_{\mathrm{real}} \end{cases}, \tag{115}$$

where N_{real} and N_{fake} are the number of real and fake lepton events. The number of fake events passing Tight lepton selection $N_{\mathrm{fake}}^{\mathrm{Tight}}$ is obtained by solving Eq. 115,

$$N_{\mathrm{fake}}^{\mathrm{Tight}} = \epsilon_{\mathrm{fake}} \cdot \frac{\epsilon_{\mathrm{real}} \cdot N_{\mathrm{fail}} - (1-\epsilon_{\mathrm{real}}) \cdot N_{\mathrm{pass}}}{\epsilon_{\mathrm{real}} - \epsilon_{\mathrm{fake}}}. \tag{116}$$

$N_{\mathrm{fake}}^{\mathrm{Tight}}$ gives the evaluation of QCD multi-jets that passes our Signal lepton selections.

C.1 Lepton misidentification rate

ϵ_{fake} is evaluated in a dedicated Control Region (Multi-jets control region) using data. The multi-jet Control Region is defined as follow:

- $E_{\mathrm{T}}^{\mathrm{miss}}$<30 GeV and m_{T}<40 GeV.
- Exactly one Loose lepton. The lepton is also required to be separated from the overlap removal jets (defined in Table 2) by $\Delta R > 0.4$.
- At least one jet with p_{T}>60 GeV.

The last item is applied so as to select the events with a topology close to our target kinematic selections. However, ϵ_{fake} is found to be robust against the jet p_{T} and the number of jets.

Then ϵ_{fake} is calculated by dividing the number of fake events surviving Tight lepton selection by the total number of fake events passing Loose lepton selection. Real leptons from W+jets and Z+jets are removed by using Monte Carlo, taking 20% of cross-section uncertainty into systematic errors. The following three regions are introduced to measure ϵ_{fake} under b-tagged, b-vetoed and b-inclusive conditions.

Heavy Flavor enriched region At least one b-tagged jet is required.

Light Flavor enriched region No b-tagged jet is allowed.

Inclusive region Do no apply any requirements on b-tagged jets.

ϵ_{fake} measured in Heavy Flavor (Light Flavor) enriched region is used in $t\bar{t}$ (W+jets) Control Regions. ϵ_{fake} obtained in Inclusive region is used in the Validation and Signal Regions, where no b-jet selection is required.

Figures 70 show ϵ_{fake} for Hard (left) and Soft (right) electron selections in Inclusive region. Similarly, Fig. 71 show ϵ_{fake} for muons. Hard Lepton results are on the left column and soft lepton ones are on the right. For better visualization, the graphs with different η selections are superimposed with shifts within the p_{T} ranges. The gray vertical lines show the p_{T} bins. The error bars include the systematic errors from 20% uncertainty of W/Z+jets subtractions and the statistical uncertainties. Note that only p_{T}<25 (>25) GeV is used in Soft (Hard) lepton plots. ϵ_{fake} measured in Heavy and Light flavor enriched regions show similar values, with the difference of 5% at most.

C.2 Lepton identification efficiency

Isolation efficiencies for real leptons ϵ_{real} are estimated by using tag-and-probe method [80] on $Z^0 \to ll$ events. Control sample is selected by requiring the following conditions:

- At least one electron (muon) which has p_{T}>10 (6) GeV and fires a lepton trigger.
- Exactly two opposite sign and same flavor leptons which satisfy Loose lepton criteria (defined in Table 4, 5, 6, 7).
- Two leptons are well-separated from the overlap removal jets with $\Delta R > 0.4$.
- The invariant mass of the two leptons must satisfy 80 GeV < m_{ll} < 100 GeV.

The m_{ll} and opposite sign selections ensure that the leptons are real leptons coming from $Z^0 \to ll$. Then one of the leptons is tested if it passes Tight lepton selection. Isolation efficiency ϵ_{real} is calculated by dividing the number of events passing Tight lepton selection by the total event numbers. Since the numerator and denominator are not statistically independent, the following formula is used to calculate correct statistical errors,

$$\Delta\epsilon_{\mathrm{real}}^{\mathrm{stat}} = \sqrt{\frac{\epsilon_{\mathrm{real}}(1-\epsilon_{\mathrm{real}})}{N_{\mathrm{real}}^{\mathrm{Loose}}}}. \tag{117}$$

The difference in the values measured in data and Monte Carlo is taken as systematic errors. Figure 72 and 73 show ϵ_{real} for electron and muon, respectively. No b-jet selections is applied. The error bars include both systematic and statistical errors.

C.3 Validation

To validate the methodology of Matrix-Method and the parameters obtained above, QCD multi-jet estimation is compared with data.Figure 69 shows the m_{T} distributions after requiring 1 electron and at least 1 jet with p_{T}>80 GeV. The yield and shape of QCD multi-jet component are correctly estimated within the uncertainty band shown as the shaded area.

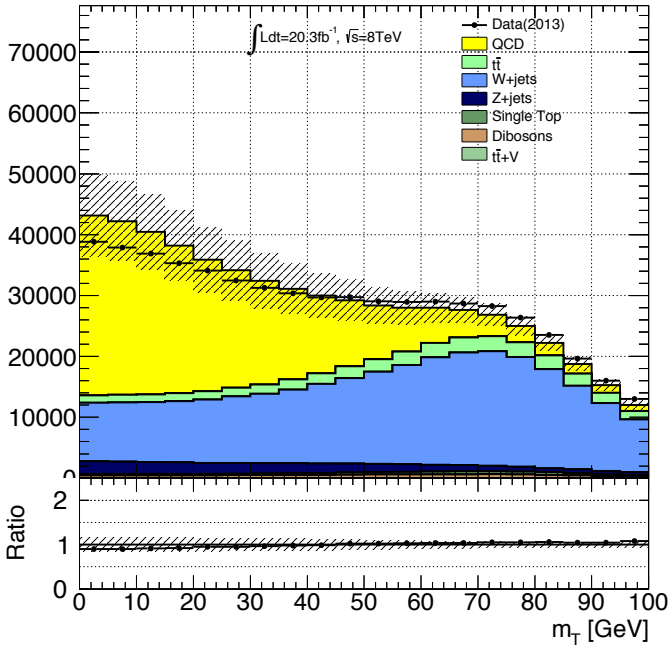

Figure 69: m_{T} distribution for the electron channel after requiring 1 electron and at least 1 jet with p_{T}>80 GeV.

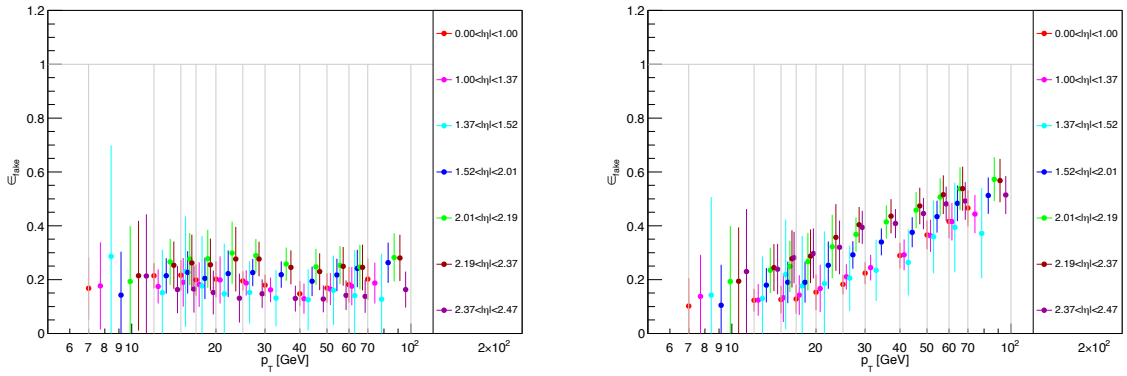

Figure 70: ϵ_{fake} of the electrons are plotted as a function of p_{T}^{ℓ} for various η ranges. No b-jet requirement is applied. Hard (Soft) Lepton result is shown on the left (right). For better visualization, the graphs with different η selections are superimposed with shifts within the p_{T} ranges.

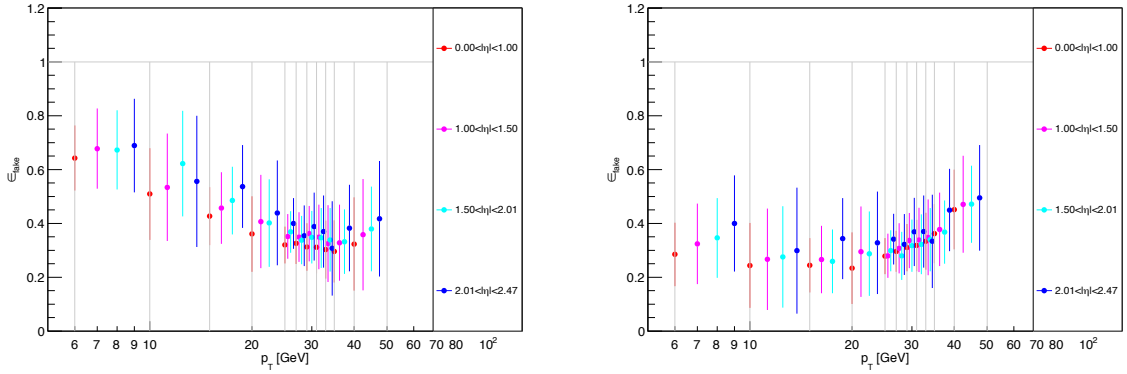

Figure 71: ϵ_{fake} of the muons are plotted as a function of p_{T}^{ℓ} for various η ranges. Hard (Soft) Lepton result is shown on the left (right). For better visualization, the graphs with different η selections are superimposed with shifts within the p_{T} ranges.

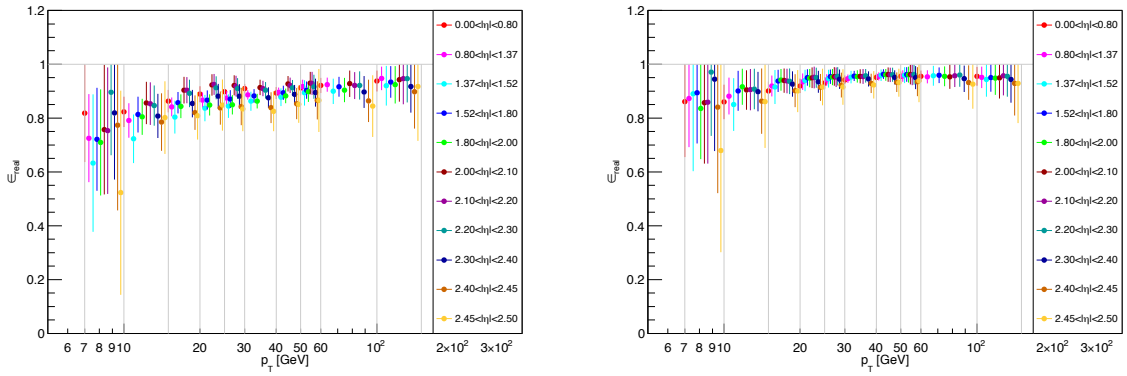

Figure 72: ϵ_{real} of electrons are plotted as a function of p_{T}^{ℓ} for various η ranges. Hard (Soft) Lepton result is shown on the left (right). For better visualization, the graphs are superimposed with shifts within the p_{T} ranges.

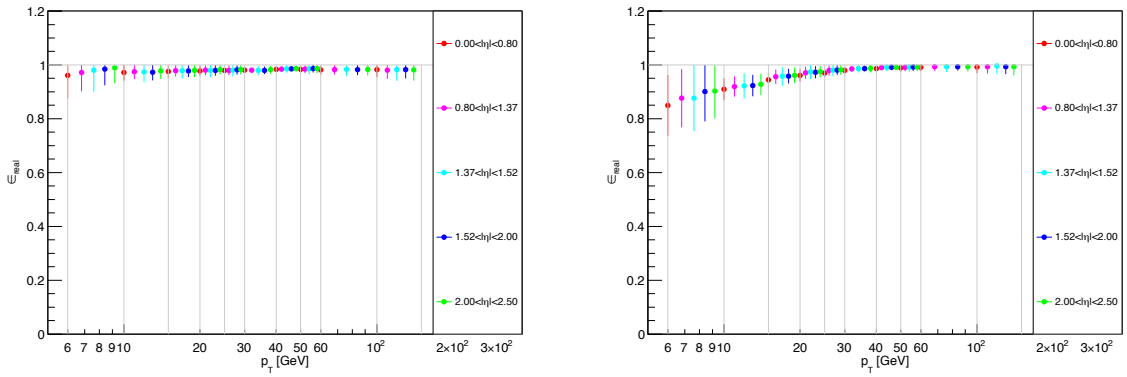

Figure 73: ϵ_{real} of muons are plotted as a function of p_{T}^{ℓ} for various η ranges. Hard (Soft) Lepton result is shown on the left (right). For better visualization, the graphs are superimposed with shifts within the p_{T} ranges.

D Fit results for the Control Regions

Tables 29-31 show the fit results for the Loose, Tight and Soft Validation Regions. No signal is assumed in the fitting. For detail, see the descriptions in Section 6.2.5.

channel	Tight WR (El)	Tight WR (Mu)	Tight TR (El)	Tight TR (Mu)
Observed events	27	36	18	22
bkg events	30.48 ± 4.51	32.32 ± 4.21	21.42 ± 3.61	18.24 ± 2.81
$t\bar{t}$ events	15.53 ± 4.96	13.70 ± 4.52	17.31 ± 4.45	14.44 ± 3.70
W+jets events	10.87 ± 6.73	10.47 ± 6.36	1.21 ± 0.76	1.16 ± 0.79
Z+jets events	$0.01^{+0.02}_{-0.01}$	$0.12^{+0.12}_{-0.12}$	0.00 ± 0.00	0.00 ± 0.00
Dibosons events	1.78 ± 0.95	4.53 ± 3.14	$0.15^{+0.64}_{-0.15}$	0.00 ± 0.00
Single Top events	1.61 ± 1.21	1.60 ± 1.34	2.17 ± 1.60	2.16 ± 1.82
$t\bar{t}$+V events	0.47 ± 0.11	0.32 ± 0.10	0.49 ± 0.18	0.43 ± 0.09
QCD events	$0.20^{+0.27}_{-0.20}$	1.58 ± 1.34	$0.10^{+0.16}_{-0.10}$	$0.05^{+0.23}_{-0.05}$

Table 29: Background fit results for the Tight WR (El), Tight WR (Mu), Tight TR (El) and Tight TR (Mu) for an integrated luminosity of 20.3 fb^{-1}. The errors shown are the statistical plus systematic uncertainties.

channel	Loose WR (El)	Loose WR (Mu)	Loose TR (El)	Loose TR (Mu)
Observed events	363	303	183	144
bkg events	354.83 ± 13.82	310.67 ± 13.18	177.00 ± 10.33	150.61 ± 8.31
$t\bar{t}$ events	84.40 ± 23.39	69.97 ± 20.10	126.56 ± 21.08	103.03 ± 17.07
W+jets events	221.41 ± 28.36	203.98 ± 26.14	20.51 ± 3.87	17.02 ± 3.11
Z+jets events	0.54 ± 0.19	4.41 ± 1.55	0.03 ± 0.01	0.79 ± 0.35
Dibosons events	31.21 ± 14.41	17.17 ± 8.01	6.36 ± 3.03	8.18 ± 4.06
Single Top events	16.40 ± 11.16	10.90 ± 7.46	22.45 ± 15.12	18.99 ± 12.69
$t\bar{t}$+V events	0.72 ± 0.11	0.61 ± 0.08	1.07 ± 0.10	0.90 ± 0.07
QCD events	$0.15^{+1.86}_{-0.15}$	$3.63^{+3.78}_{-3.63}$	$0.02^{+0.78}_{-0.02}$	$1.70^{+1.88}_{-1.70}$

Table 30: Background fit results for the Loose WR (El), Loose WR (Mu), Loose TR (El) and Loose TR (Mu) for an integrated luminosity of 20.3 fb^{-1}. The errors shown are the statistical plus systematic uncertainties.

channel	Soft WR (El+Mu)	Soft TR (El+Mu)
Observed events	2328	730
bkg events	2327.92 ± 50.26	729.99 ± 27.82
$t\bar{t}$ events	389.78 ± 82.87	530.96 ± 60.65
W+jets events	1724.14 ± 128.66	107.21 ± 15.06
Z+jets events	14.95 ± 5.65	1.58 ± 0.49
Dibosons events	119.32 ± 61.58	15.09 ± 7.55
Single Top events	58.23 ± 40.93	62.13 ± 43.26
$t\bar{t}$+V events	1.88 ± 0.27	2.64 ± 0.31
QCD events	$19.62^{+38.35}_{-19.62}$	$10.38^{+15.16}_{-10.38}$

Table 31: Background fit results for the Soft WR (El+Mu) and Soft TR (El+Mu) for an integrated luminosity of 20.3 fb^{-1}. The errors shown are the statistical plus systematic uncertainties.

E Fit results for the Validation Regions

Tables 32-37 show the expect and observed event numbers in the Loose, Tight and Soft Validation Regions. Each region has two Validation Regions. One is to check the extrapolation along m_{T}, called VR (m_{T}), while the other one is to check the extrapolation along $E_{\mathrm{T}}^{\mathrm{miss}}$, called VR ($E_{\mathrm{T}}^{\mathrm{miss}}$). The extrapolations on $t\bar{t}$ and W+jets background are separately checked by requiring or vetoing a b-tagged jet, denoted as TR or WR. For detail, see the descriptions in Section 6.2.6.

	Tight			
channel	VR (m_{T}; WR, El)	VR (m_{T}; WR, Mu)	VR (m_{T}; TR, El)	VR (m_{T}; TR, Mu)
Observed events	7	5	6	10
bkg events	7.93 ± 1.89	6.91 ± 1.70	6.73 ± 1.68	6.58 ± 1.48
$t\bar{t}$ events	5.22 ± 1.86	4.49 ± 1.60	5.52 ± 1.74	5.52 ± 1.49
W+jets events	0.65 ± 0.43	1.16 ± 0.81	0.14 ± 0.12	0.16 ± 0.16
Z+jets events	$0.01^{+0.27}_{-0.01}$	$0.02^{+0.08}_{-0.02}$	0.01 ± 0.00	0.00 ± 0.00
Dibosons events	0.87 ± 0.47	0.56 ± 0.40	0.00 ± 0.00	0.08 ± 0.07
Single Top events	0.80 ± 0.59	0.42 ± 0.39	0.62 ± 0.47	0.39 ± 0.29
$t\bar{t}$+V events	0.37 ± 0.09	0.25 ± 0.08	0.43 ± 0.08	0.42 ± 0.08
QCD events	$0.00^{+0.05}_{-0.00}$	0.00 ± 0.03	0.00 ± 0.02	0.00 ± 0.06

Table 32: Background fit results for the Tight VR (m_{T}; WR, El), Tight VR (m_{T}; WR, Mu), Tight VR (m_{T}; TR, El) and Tight VR (m_{T}; TR, Mu) for an integrated luminosity of 20.3 fb^{-1}. The errors shown are the statistical plus systematic uncertainties.

	Tight			
channel	VR ($E_{\mathrm{T}}^{\mathrm{miss}}$; WR, El)	VR ($E_{\mathrm{T}}^{\mathrm{miss}}$; WR, Mu)	VR ($E_{\mathrm{T}}^{\mathrm{miss}}$; TR, El)	VR ($E_{\mathrm{T}}^{\mathrm{miss}}$; TR, Mu)
Observed events	13	9	2	3
bkg events	9.52 ± 1.89	7.37 ± 1.76	4.95 ± 1.33	3.84 ± 0.87
$t\bar{t}$ events	4.25 ± 1.42	2.87 ± 1.10	3.64 ± 1.00	2.61 ± 0.72
W+jets events	3.52 ± 2.14	3.07 ± 1.89	0.29 ± 0.25	0.43 ± 0.29
Z+jets events	0.10 ± 0.03	$0.07^{+0.35}_{-0.07}$	0.00 ± 0.00	0.00 ± 0.00
Dibosons events	0.74 ± 0.40	0.71 ± 0.49	0.10 ± 0.06	$0.00^{+0.00}_{-0.00}$
Single Top events	0.76 ± 0.63	$0.57^{+0.78}_{-0.57}$	$0.74^{+0.85}_{-0.74}$	0.66 ± 0.59
$t\bar{t}$+V events	0.15 ± 0.08	0.08 ± 0.03	0.16 ± 0.07	0.13 ± 0.06
QCD events	0.00 ± 0.03	0.00 ± 0.03	$0.02^{+0.03}_{-0.02}$	0.00 ± 0.03

Table 33: Background fit results for the Tight VR ($E_{\mathrm{T}}^{\mathrm{miss}}$; WR, El), Tight VR ($E_{\mathrm{T}}^{\mathrm{miss}}$; WR, Mu), Tight VR ($E_{\mathrm{T}}^{\mathrm{miss}}$; TR, El) and Tight VR ($E_{\mathrm{T}}^{\mathrm{miss}}$; TR, Mu) for an integrated luminosity of 20.3 fb^{-1}. The errors shown are the statistical plus systematic uncertainties.

	Loose			
channel	VR (m_{T}; WR, El)	VR (m_{T}; WR, Mu)	VR (m_{T}; TR, El)	VR (m_{T}; TR, Mu)
Observed events	114	89	95	92
bkg events	110.99 ± 13.72	114.16 ± 13.57	96.61 ± 14.99	82.01 ± 12.85
$t\bar{t}$ events	39.35 ± 12.27	36.84 ± 11.47	74.51 ± 13.47	62.54 ± 11.54
W+jets events	50.49 ± 7.34	50.07 ± 7.79	6.36 ± 1.33	4.98 ± 0.89
Z+jets events	2.94 ± 0.92	6.88 ± 2.10	0.57 ± 0.20	0.95 ± 0.31
Dibosons events	10.96 ± 5.54	9.38 ± 4.87	2.61 ± 1.32	1.82 ± 0.95
Single Top events	4.64 ± 3.40	4.48 ± 3.26	10.05 ± 7.10	8.76 ± 6.18
$t\bar{t}$+V events	0.80 ± 0.14	0.72 ± 0.10	1.62 ± 0.15	1.26 ± 0.10
QCD events	$1.77^{+2.16}_{-1.77}$	5.78 ± 4.07	$0.90^{+1.34}_{-0.90}$	$1.70^{+2.22}_{-1.70}$

Table 34: Background fit results for the Loose VR (m_{T}; WR, El), Loose VR (m_{T}; WR, Mu), Loose VR (m_{T}; TR, El) and Loose VR (m_{T}; TR, Mu) for an integrated luminosity of 20.3 fb^{-1}. The errors shown are the statistical plus systematic uncertainties.

	Loose			
channel	VR ($E_{\mathrm{T}}^{\mathrm{miss}}$; WR, El)	VR ($E_{\mathrm{T}}^{\mathrm{miss}}$; WR, Mu)	VR ($E_{\mathrm{T}}^{\mathrm{miss}}$; TR, El)	VR ($E_{\mathrm{T}}^{\mathrm{miss}}$; TR, Mu)
Observed events	179	187	73	70
bkg events	199.82 ± 19.70	182.66 ± 20.03	76.45 ± 11.75	61.03 ± 9.73
$t\bar{t}$ events	32.32 ± 9.15	25.97 ± 7.30	49.56 ± 9.19	37.50 ± 6.83
W+jets events	140.15 ± 18.66	126.31 ± 17.20	10.96 ± 2.02	10.33 ± 1.92
Z+jets events	0.25 ± 0.08	2.59 ± 0.81	0.00 ± 0.00	0.19 ± 0.07
Dibosons events	18.69 ± 10.01	18.34 ± 10.32	5.84 ± 3.06	2.83 ± 1.48
Single Top events	7.33 ± 5.34	6.96 ± 5.11	9.08 ± 6.54	9.21 ± 6.60
$t\bar{t}$+V events	0.41 ± 0.07	0.28 ± 0.03	0.65 ± 0.07	0.51 ± 0.05
QCD events	$0.66^{+1.51}_{-0.66}$	$2.22^{+3.11}_{-2.22}$	$0.36^{+0.67}_{-0.36}$	$0.47^{+0.87}_{-0.47}$

Table 35: Background fit results for the Loose VR ($E_{\mathrm{T}}^{\mathrm{miss}}$; WR, El), Loose VR ($E_{\mathrm{T}}^{\mathrm{miss}}$; WR, Mu), Loose VR ($E_{\mathrm{T}}^{\mathrm{miss}}$; TR, El) and Loose VR ($E_{\mathrm{T}}^{\mathrm{miss}}$; TR, Mu) for an integrated luminosity of 20.3 fb^{-1}. The errors shown are the statistical plus systematic uncertainties.

	Soft	
channel	VR (m_{T}; WR, El+Mu)	VR (m_{T}; TR, El+Mu)
Observed events	79	71
bkg events	90.47 ± 9.49	68.36 ± 8.10
$t\bar{t}$ events	38.14 ± 8.68	52.30 ± 7.00
W+jets events	35.31 ± 2.46	4.04 ± 0.53
Z+jets events	1.65 ± 0.51	0.04 ± 0.02
Dibosons events	4.21 ± 2.31	2.65 ± 1.36
Single Top events	3.14 ± 2.35	4.13 ± 2.97
$t\bar{t}+V$ events	0.53 ± 0.06	0.85 ± 0.10
QCD events	7.49 ± 2.90	4.34 ± 2.69

Table 36: Background fit results for the Soft VR (m_{T}; WR, El+Mu) and Soft VR (m_{T}; TR, El+Mu) for an integrated luminosity of 20.3 fb^{-1}. The errors shown are the statistical plus systematic uncertainties.

	Soft	
channel	VR ($E_{\mathrm{T}}^{\mathrm{miss}}$; WR, El+Mu)	VR ($E_{\mathrm{T}}^{\mathrm{miss}}$; TR, El+Mu)
Observed events	381	75
bkg events	390.54 ± 26.95	89.61 ± 11.94
$t\bar{t}$ events	40.16 ± 10.15	50.85 ± 8.46
W+jets events	317.02 ± 28.35	19.73 ± 3.11
Z+jets events	2.76 ± 0.97	0.12 ± 0.05
Dibosons events	19.61 ± 10.71	5.88 ± 3.15
Single Top events	6.64 ± 4.86	9.73 ± 6.94
$t\bar{t}+V$ events	0.41 ± 0.07	0.66 ± 0.09
QCD events	$3.93^{+7.78}_{-3.93}$	$2.63^{+3.52}_{-2.63}$

Table 37: Background fit results for the Soft VR ($E_{\mathrm{T}}^{\mathrm{miss}}$; WR, El+Mu) and Soft VR ($E_{\mathrm{T}}^{\mathrm{miss}}$; TR, El+Mu) for an integrated luminosity of 20.3 fb^{-1}. The errors shown are the statistical plus systematic uncertainties.

F $E_{\mathrm{T}}^{\mathrm{miss}}$ and m_{T} for the events in the SRs

$E_{\mathrm{T}}^{\mathrm{miss}}$ and m_{T} distributions of the events left in the Signal Regions are shown in Fig. 74 and Fig. 75, respectively. The overflow events are included in the last bin. Several signals taken from around the exclusion limits are piled up on top of the background distributions.

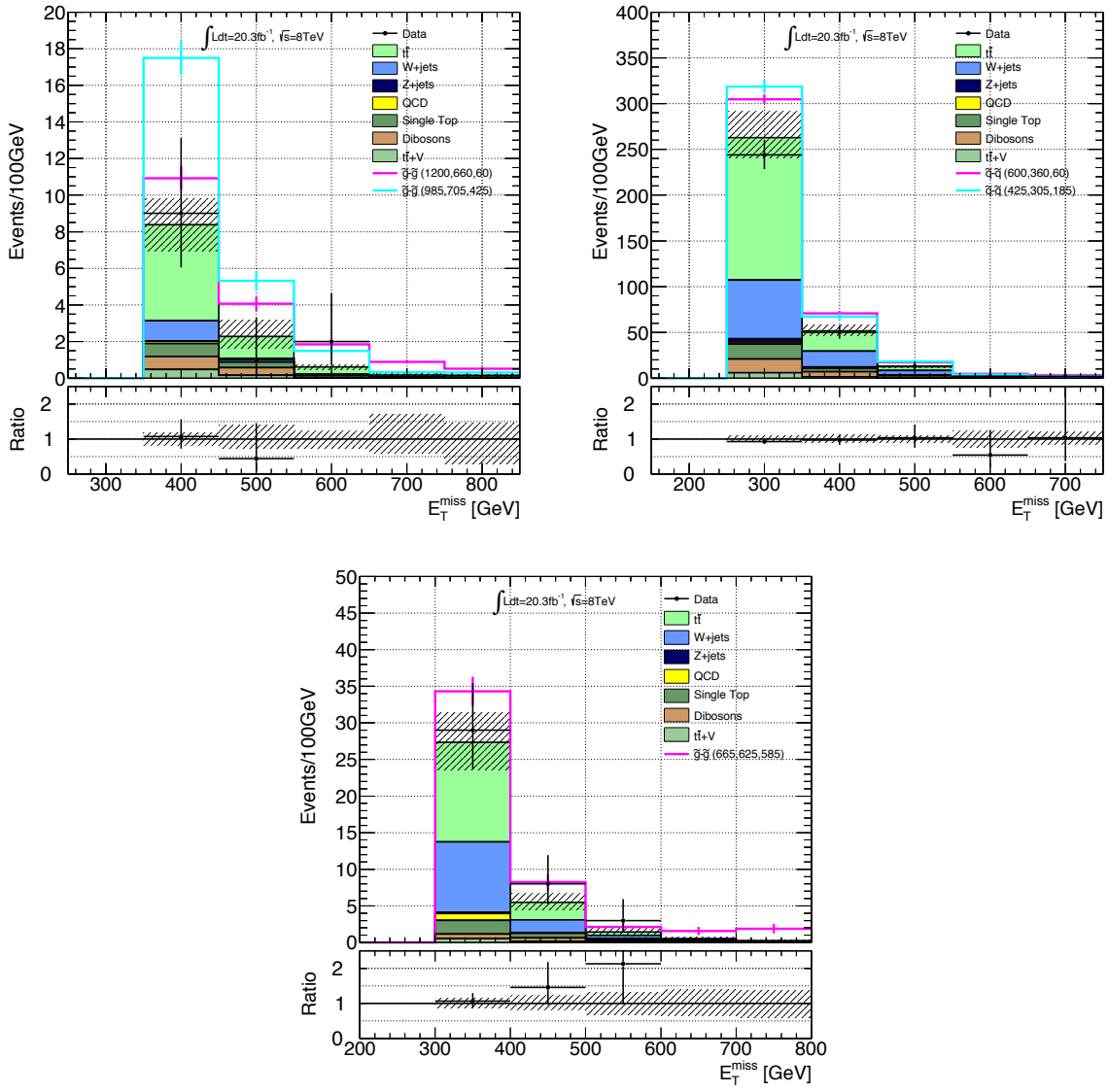

Figure 74: $E_{\mathrm{T}}^{\mathrm{miss}}$ distributions in Tight (left), Loose (right) and Soft (bottom) Signal Regions. Signals taken from around the exclusion limits are piled up on top of the background distributions. For Tight SR, gluino pair productions with $(m_{\tilde{g}},m_{\tilde{\chi}_1^\pm},m_{\tilde{\chi}_1^0})$=(1200 GeV, 660 GeV, 60 GeV) (magenta) and $(m_{\tilde{g}},m_{\tilde{\chi}_1^\pm},m_{\tilde{\chi}_1^0})$=(985 GeV, 705 GeV, 425 GeV) (cyan) are shown. For Loose SR, squark pair productions with $(m_{\tilde{\mathrm{q}}},m_{\tilde{\chi}_1^\pm},m_{\tilde{\chi}_1^0})$=(600 GeV, 360 GeV, 60 GeV) (magenta) and $(m_{\tilde{\mathrm{q}}},m_{\tilde{\chi}_1^\pm},m_{\tilde{\chi}_1^0})$=(425 GeV, 305 GeV, 185 GeV) (cyan) are shown. For Soft SR, gluino pair production with $(m_{\tilde{g}},m_{\tilde{\chi}_1^\pm},m_{\tilde{\chi}_1^0})$=(665 GeV, 625 GeV, 585 GeV) is shown in magenta. The last bin includes the overflow events.

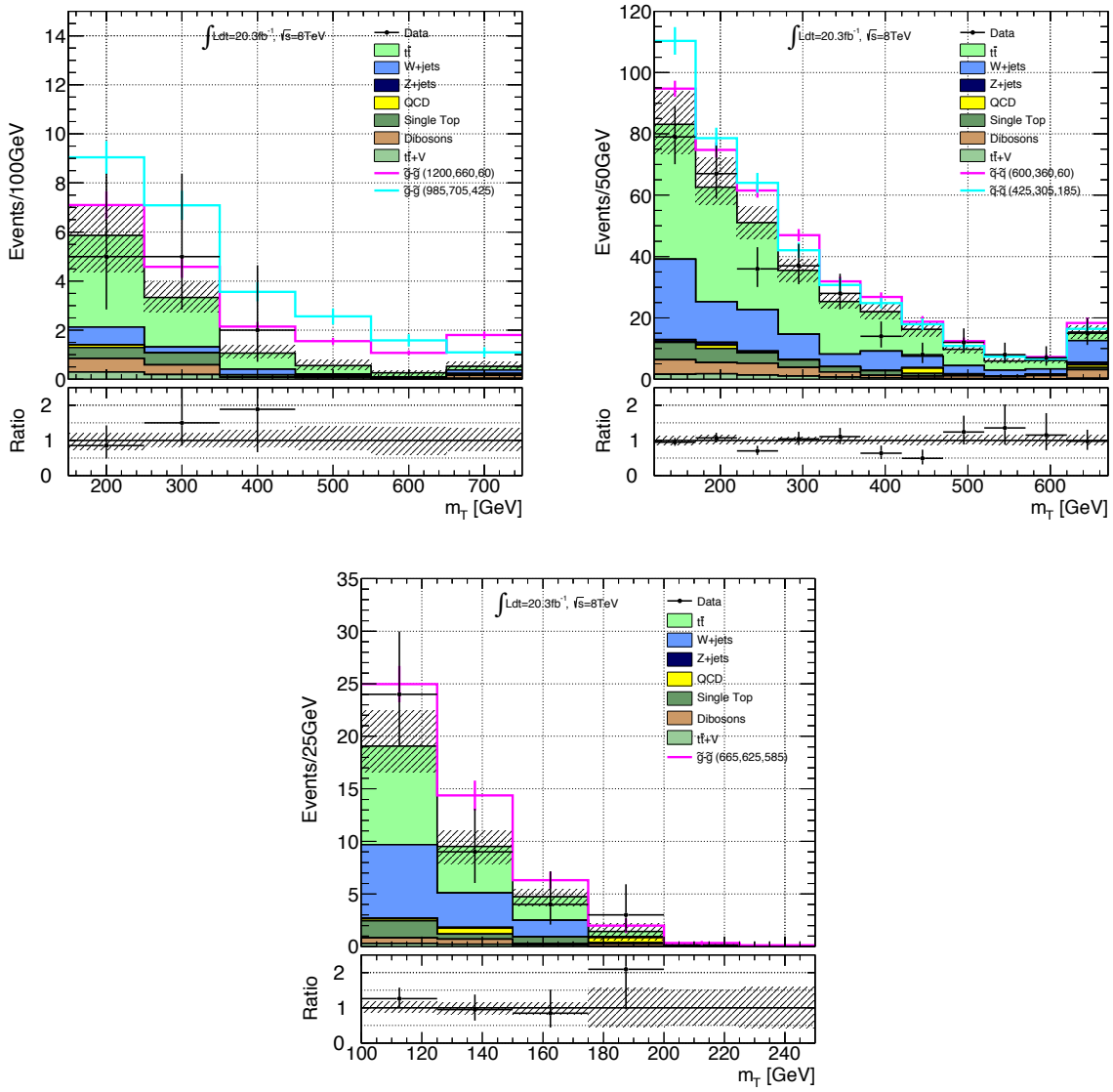

Figure 75: m_{T} distributions in Tight (left), Loose (right) and Soft (bottom) Signal Regions. Signals taken from around the exclusion limits are piled up on top of the background distributions. For Tight SR, gluino pair productions with $(m_{\tilde{g}},m_{\tilde{\chi}_1^{\pm}},m_{\tilde{\chi}_1^0})$=(1200 GeV, 660 GeV, 60 GeV) (magenta) and $(m_{\tilde{g}},m_{\tilde{\chi}_1^{\pm}},m_{\tilde{\chi}_1^0})$=(985 GeV, 705 GeV, 425 GeV) (cyan) are shown. For Loose SR, squark pair productions with $(m_{\tilde{\mathrm{q}}},m_{\tilde{\chi}_1^{\pm}},m_{\tilde{\chi}_1^0})$=(600 GeV, 360 GeV, 60 GeV) (magenta) and $(m_{\tilde{\mathrm{q}}},m_{\tilde{\chi}_1^{\pm}},m_{\tilde{\chi}_1^0})$=(425 GeV, 305 GeV, 185 GeV) (cyan) are shown. For Soft SR, gluino pair production with $(m_{\tilde{g}},m_{\tilde{\chi}_1^{\pm}},m_{\tilde{\chi}_1^0})$=(665 GeV, 625 GeV, 585 GeV) is shown in magenta. The last bin includes the overflow events.

G Fit results for the Signal Regions

Tables 38-40 show the decomposition of the errors. Negligible backgrounds are omitted from the tables. The percentages show the size of the uncertainty relative to the total expected background. Normalization errors for $t\bar{t}$ and W+jets are dominated by the statistical uncertainties determined in the Control Regions, which are strongly anti-correlated to the JES uncertainties, therefore the total uncertainties are evaluated to be much smaller than the simple square-sum of these components. Normalization errors for the other minor backgrounds are uncertainties assigned to their cross-sections and the acceptances as discussed in Section 7.2. Theory uncertainties are discussed in Section 7.2. For more details and interpretations, see the text in Section 8.1.

channel	Tight SR (El)	Tight SR (Mu)
Total background expectation	6.52	5.31
Total statistical ($\sqrt{N_{\text{exp}}}$)	±2.55	±2.30
Total background systematic	±1.17 [17.99%]	±1.03 [19.40%]
Normalization ($t\bar{t}$)	±1.83 [28.0%]	±1.64 [31.0%]
Normalization (W+jets)	±0.71 [10.9%]	±0.53 [10.0%]
JES	±1.84 [28.3%]	±1.71 [32.2%]
JER	±0.13 [2.1%]	±0.02 [0.44%]
Theory ($t\bar{t}$)	±0.27 [4.2%]	±0.24 [4.6%]
Theory (W+jets)	±0.07 [1.1%]	±0.05 [1.0%]
Normalization (Z+jets)	±0.00 [0.00%]	±0.02 [0.31%]
Normalization (Dibosons)	±0.39 [6.0%]	±0.09 [1.7%]
Normalization (Single Top)	±0.34 [5.2%]	±0.45 [8.5%]
b-Tag	±0.15 [2.3%]	±0.03 [0.65%]
QCD (ele)	±0.21 [3.2%]	±0.00 [0.00%]
QCD (muo)	±0.00 [0.00%]	±0.02 [0.38%]

Table 38: Breakdown of the dominant systematic uncertainties on background estimates in the Tight Signal Regions. Note that the individual uncertainties can be correlated, and do not necessarily add up quadratically to the total background uncertainty. The percentages show the size of the uncertainty relative to the total expected background.

channel	Loose SR (El)	Loose SR (Mu)
Total background expectation	166.60	161.12
Total statistical ($\sqrt{N_{\text{exp}}}$)	±12.91	±12.69
Total background systematic	±20.35 [12.22%]	±18.56 [11.52%]
Normalization ($t\bar{t}$)	±21.88 [13.1%]	±20.23 [12.6%]
Normalization (W+jets)	±8.47 [5.1%]	±8.35 [5.2%]
JES	±15.88 [9.5%]	±14.72 [9.1%]
JER	±0.07 [0.04%]	±0.06 [0.04%]
Theory ($t\bar{t}$)	±6.03 [3.6%]	±5.58 [3.5%]
Theory (W+jets)	±0.58 [0.35%]	±0.57 [0.35%]
Normalization (Z+jets)	±0.26 [0.15%]	±1.12 [0.70%]
Normalization (Dibosons)	±5.65 [3.4%]	±6.07 [3.8%]
Normalization (Single Top)	±8.24 [4.9%]	±6.59 [4.1%]
b-Tag	±0.92 [0.55%]	±0.34 [0.21%]
QCD (ele)	±1.92 [1.2%]	±0.00 [0.00%]
QCD (muo)	±0.00 [0.00%]	±2.10 [1.3%]

Table 39: Breakdown of the dominant systematic uncertainties on background estimates in the Loose Signal Regions. Note that the individual uncertainties can be correlated, and do not necessarily add up quadratically to the total background uncertainty. The percentages show the size of the uncertainty relative to the total expected background.

channel	Soft SR (El+Mu)
Total background expectation	35.37
Total statistical ($\sqrt{N_{\text{exp}}}$)	±5.95
Total background systematic	±4.57 [12.91%]
Normalization ($t\bar{t}$)	±3.54 [10.0%]
Normalization (W+jets)	±2.95 [8.4%]
JES	±5.22 [14.7%]
JER	±0.00 [0.01%]
Theory ($t\bar{t}$)	±2.48 [7.0%]
Theory (W+jets)	±0.49 [1.4%]
Normalization (Z+jets)	±0.05 [0.14%]
Normalization (Dibosons)	±0.71 [2.0%]
Normalization (Single Top)	±2.05 [5.8%]
b-Tag	±0.12 [0.35%]
QCD (ele+muo)	±1.55 [4.4%]

Table 40: Breakdown of the dominant systematic uncertainties on background estimates in the Signal Regions. Note that the individual uncertainties can be correlated, and do not necessarily add up quadratically to the total background uncertainty. The percentages show the size of the uncertainty relative to the total expected background.

H Profile-likelihood and $\mathrm{CL_s}$

We use a complicated likelihood function in the limit calculation, containing a lot of parameters. Among them, Parameter Of Interest (POI) is namely the one we are interested in, and the others are called nuisance parameters. Profile-Likelihood method eliminates the nuisance parameters and defines a simple likelihood as a function of POI to be used in the limit calculation.

The analyses in proton-proton collider in general suffer from large backgrounds, which leads to a big statistical fluctuation in the observed number of events. As a result, there frequently happen the cases in which an under-fluctuation mistakenly excludes a given signal model. To avoid this, a quantity called $\mathrm{CL_s}$ is used to set the limit, which includes a punishment term for such problems and gives a conservative limit.

H.1 Likelihood

We begins with a simple experiment, in which only one background and one signal compose all observed events. They are provided as histograms with multiple bins for the signal region and a 1-binned histogram for the control region where the background is normalized. Then likelihood function L is defined as

$$L(\mu, \theta) = \prod_{j=1}^{N} Pois(\mu s_j(\theta) + b_j(\theta); n_j) \cdot Pois(u(\theta); m) \cdot L_{constrain}(\theta), \tag{118}$$

where θ is the vector of all nuisance parameters, $j = 1..N$ is the index of bins in the signal region histogram, $s_j(\theta)$ and $b_j(\theta)$ are the expected number of signal and background in the signal region, n_j is the number of observed events in j-th bin in the signal region, and $u(\theta)$ and m are the expected and observed number of events in the control region. POI of this likelihood function is μ, called Signal Strength, which is defined as the fraction of a given signal yield with respect to the nominal one. The scale factor for the background is not explicitly shown but included in θ. $Pois(\lambda; n)$ is Poisson probability function with n observed and λ expected events. The explicit form of $Pois(\lambda, n)$ is the following.

$$Pois(\lambda; n) = \frac{\lambda^n}{n!} e^{-\lambda}. \tag{119}$$

$L_{constrain}(\theta)$ is a term to constrain θ. In practice, Gaussian function is mostly used. For example, assuming θ_i are constrained around c_i with the errors of σ_i, then $L_{constrain}(\theta)$ is written as,

$$L_{constrain}(\theta) = \prod_{i=1}^{K} \frac{1}{\sqrt{2\pi}\sigma_i} exp\left(-\frac{(\theta_i - c_i)^2}{2\sigma_i^2}\right), \tag{120}$$

where K is the number of nuisance parameters included in θ

H.2 Profile-likelihood

Profile likelihood ratio is then defined as

$$\lambda(\mu) = \frac{L(\mu, \theta_{max}(\mu))}{L(\mu_{max}, \theta_{max})}, \tag{121}$$

where $\theta_{max}(\mu)$ is a set of nuisance parameters which maximizes the likelihood function L for a given μ. μ_{max} and θ_{max} in the denominator are the values which maximize the likelihood function L. In other words, the denominator is the maximum-likelihood. It is also convenient to use a statistic

$$t_\mu = -2 \ln \lambda(\mu) \tag{122}$$

Figure 76: Illustration of the relation between p_μ and $f(t_\mu|\mu)$. This plot is cited from Ref. [81].

as an estimator. Note that $\lambda(\mu)$ runs from 0 to 1, thus t_μ can take all real value.

Then, we can think of a Probability Density Function (PDF) of t_μ for a given μ. Let's put it as $f(t_\mu|\mu)$. For example, the probability of disagreement p_μ for a given μ can be shown as below using $f(t_\mu|\mu)$,

$$p_\mu = \int_{t_{\mu,\mathrm{obs}}}^{\infty} f(t_\mu|\mu) dt_\mu, \tag{123}$$

where $t_{\mu,\mathrm{obs}}$ is the value of the statistic t_μ calculated from the observed data. Figure 76 illustrates the relation of these variables.

H.2.1 Constraints and approximations

An important constraint on the signal strength μ is the prohibition of unphysical negative value. So, if one finds the data such that $\mu_{max} < 0$, then the best physical agreement occurs at $\mu_{max} = 0$. We define $\tilde{\lambda}(\mu)$ as follow:

$$\tilde{\lambda}(\mu) = \begin{cases} \frac{L(\mu,\theta_{max}(\mu))}{L(\mu_{max},\theta_{max})} & (\mu_{max} \geq 0) \\ \frac{L(\mu,\theta_{max}(\mu))}{L(0,\theta_{max}(0))} & (\mu_{max} < 0) \end{cases}, \tag{124}$$

where $\theta_{max}(0)$ is a set of nuisance parameters which maximize the likelihood function L under a constraint of $\mu = 0$. Then, t_μ is also modified as,

$$\tilde{t_\mu} = -2 \ln \tilde{\lambda}(\mu). \tag{125}$$

We then think of an approximation of the complicated function, which is used in the optimization procedure in Appendix B. First, we introduce a function which converts p-values into an equivalent significance, Z, defined such that a Gaussian distributed variable found Z standard deviations above its mean has an upper-tail probability equal to p. That is,

$$Z = \Phi^{-1}(1 - p), \tag{126}$$

where Φ^{-1} is the quantile (inverse of the cumulative distribution) of the standard Gaussian. The significance of finding no signal under the assumption of the nominal signal strength, med$[Z_0|1]$, is approximated as,

$$\mathrm{med}[Z_0|1] = \sqrt{q_0} \sim \sqrt{2((s+b)\ln(1+s/b) - s)}. \tag{127}$$

Expanding the logarithm, one finds,

$$\mathrm{med}[Z_0|1] \sim \frac{s}{\sqrt{b}}. \tag{128}$$

This is a well-known formula widely used for the cases where $s + b$ is large enough.

H.3 $\mathrm{CL_s}$ method

The p-value for the upper limit is defined as the upper-tail probability for the observed events under the assumption of a signal existence. As this p-value assumes both signal and backgrounds, it is denoted as p_{s+b}. On the other hand, the p-value assuming only background is denoted as p_b. If the observed events is completely consistent with the expected background events, p_b becomes 1.

We define $\mathrm{CL_{s+b}}$ as follow,

$$\mathrm{CL_{s+b}} = 1 - p_{s+b}. \tag{129}$$

A given signal model is excluded at 95% Confidence Level (CL) if $\mathrm{CL_{s+b}} < 0.95$ for this model.

Figure 77: Illustration of the problem of $\mathrm{CL_s}$ method. $f(q|s+b)$ and $f(q|b)$ show the probability density functions for signal+background and background-only hypotheses. q_{obs} is q calculated from observed number of events. p_{s+b} and p_s are the p-values for signal+background and background-only hypotheses. This plot is cited from Ref. [81].

The problem of $\mathrm{CL_{s+b}}$ method is illustrated in Fig. 77. $f(q|s+b)$ and $f(q|b)$ show the probability density functions for signal+background and background-only hypotheses. q_{obs} is q calculated from observed number of events. p_{s+b} and p_s are the p-values for signal+background and background-only hypotheses. In the illustration, the number of background events b is so large compared with the number of signal events s that the probability density function of signal+background hypothesis $f(q|s+b)$ does not differ much from the one of the background-only hypothesis, rather almost overlapping each other. In such a case, $\mathrm{CL_{s+b}}$ often (once in twenty times at the limit of $b \gg s$) excludes a given signal model mistakenly due to an under-fluctuation of observed events.

Naturally, a model with small number of signal events with respect to the number of backgrounds, should loose the sensitivity. $\mathrm{CL_s}$is defined with a penalty term, considering this requirement, as

$$\mathrm{CL_s} = \frac{\mathrm{CL_{s+b}}}{\mathrm{CL_b}}. \tag{130}$$

If the two distributions $f(q|b)$ and $f(q|s+b)$ are widely separated, then $\mathrm{CL_b} = 1 - p_b$ is only slightly less than 1, and thus exclusion based on $\mathrm{CL_s}$ is similar to that obtained from $\mathrm{CL_s}$. If, however, one has little sensitivity to the signal model, i.e. the two distributions are close together, $1 - p_b$ becomes small, thus the p-value of $s + b$ is penalized. In this way, one is prevented from excluding signal models mistakenly in cases of low sensitivity. As can be read from the equation, $\mathrm{CL_s}$ always gives more conservative exclusion sensitivity than $\mathrm{CL_{s+b}}$ does.

I Tile Calorimeter calibration using scrapping muon

I.1 Introduction

In March 2010, the ATLAS detector was exposed to muons produced by a 450 GeV proton beam partially hitting (scrapping) one of the LHC collimators placed at a distance of about 180 m from the center of the detector. The data are used to validate the inter-calibration of the hadronic calorimeter (TileCal). Inter-calibration, or uniformity, of Tile calorimeter is important because it tells us if all components are working as expected. The uniformity is compared with Monte Carlo simulation, therefore is is also a good validation that the geometry and response are well described in the Monte Carlo.

I.1.1 Tile calorimeter

TileCal is a sampling plastic-scintillator/steel detector. It is divided into four cylindrical sections, referred to as long barrels (LBA and LBC) and extended barrels (EBA and EBC). Each cylinder is composed of 64 azimuthal segments, referred to as modules. The modules are segmented in z-axis and in radial-depth by routing optical fibers to different Photo Multiplier Tubes (PMT) forming cells. The resulting typical cell dimensions are approximately $\Delta\eta \times \Delta\phi = 0.1 \times 0.1$ (0.2×0.1 in the last radial layer). The layout of the LBA and EBA cells is shown in Fig. 78.

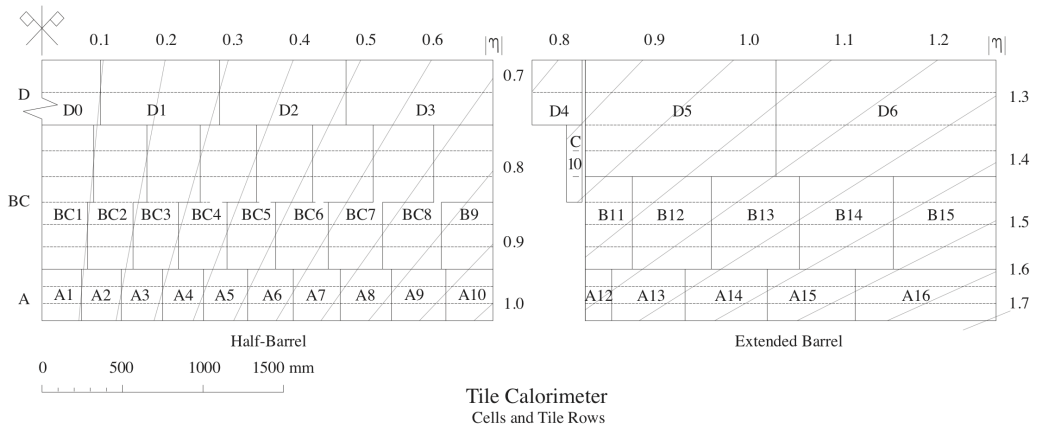

Figure 78: Long Barrel (LBA) (left) and Extended Barrel (EBA) (right) sections of the calorimeter. Horizontal lines deliminate the 11 rows of scintillating tiles. Full horizontal lines define the radial layers. Full vertical lines show the cell boundaries formed by grouping optical fibers from the scintillating tiles for read-out by separate photo-multipliers. Also shown are lines of pseudo-rapidity η. The maximum longitudinal distance between the sections is 72 cm. The LBA and EBA sections cover the regions of $0 \leq \eta \leq 1.0$ and $0.8 \leq \eta \leq 1.7$ respectively. The LBC and EBC sections cover symmetrically the negative pseudo-rapidity region.

I.1.2 Muon spectrometer system

Muon Spectrometer (MS) is immersed in a magnetic field provided by three toroids, one in the barrel ($|\eta| \leq 1.1$) and one for each end-cap ($1.1 < |\eta| \leq 2.7$), with an integral field strength of 2-8 T·m. For most of the acceptance, Monitored Drift Tube (MDT) chambers are deployed [82]. In the end-cap of the inner region, Cathode Strip Chambers (CSC) [82] are used because of their capability to cope with high background rates. MDT chambers are composed of two Multi Layers (ML) made of three or four layers of tubes. The spatial resolution attainable with a single tube is about 80 μm. Information from MDT was

used in this analysis to determine the momentum of the muons from scraping beam in C-side (z<0) after crossing TileCal.

I.1.3 Trigger system

The direction of the muons forms a small angle with respect to the beam axis (see Fig. 79 and Section I.2), therefore, the downstream wheels of TGC [82] were used as trigger. Due to the large distance between the End-Caps, only the TGC placed downstream were in time with the beam. They also allowed a measurement of the coordinate of the muons in the radial direction parallel to MDT wires. The toroid magnetic field [83] was turned on during the run.

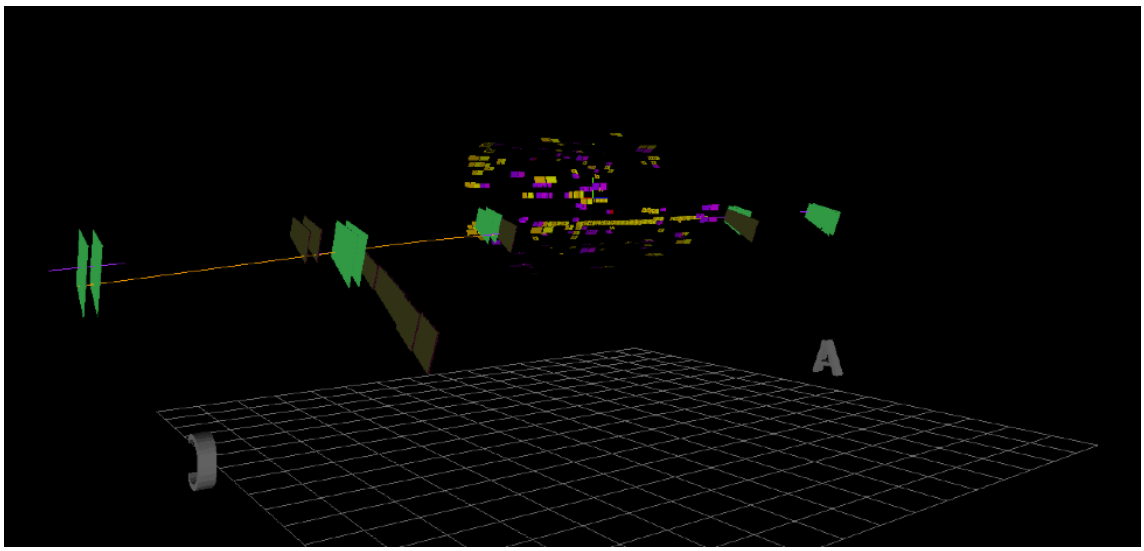

Figure 79: Display of one measured muon event. The muon arrives from the A-side (z>0), which is shown as the horizontal yellow line. The green panels are muon spectrometers with hits recorded, and the yellow and magenta cells show the calorimeter activities.

I.1.4 Scraping beam

The muons from the scraping proton beam were produced by moving the jaws of TCTH (horizontal tertiary collimators) towards the beam in 100 μm steps. Data were taken when an ATLAS trigger rate ranged between 100-500 Hz.

I.2 Data analysis

The analysis is based on about 410 k recorded events. The tracks are reconstructed using the information of Muon Spectrometer. In C-side, the measurement of three coordinates of each data point allows determination of the track momentum, polar and azimuth angles. In A-side, TGCs were out of time, thus only raw track information could be obtained.

I.2.1 Muon track selection criteria

The following selection criteria are applied:

1. Exactly one reconstructed track in C-side of MS detector.

2. The reconstruction quality of the tracks is enhanced by requiring a number of MDT hits larger than 20.

The distribution of the reconstructed momentum is shown in Fig. 80.

3. A event is retained when the momentum p reconstructed using MS chambers of C-side is larger than p_{min}=4 GeV.

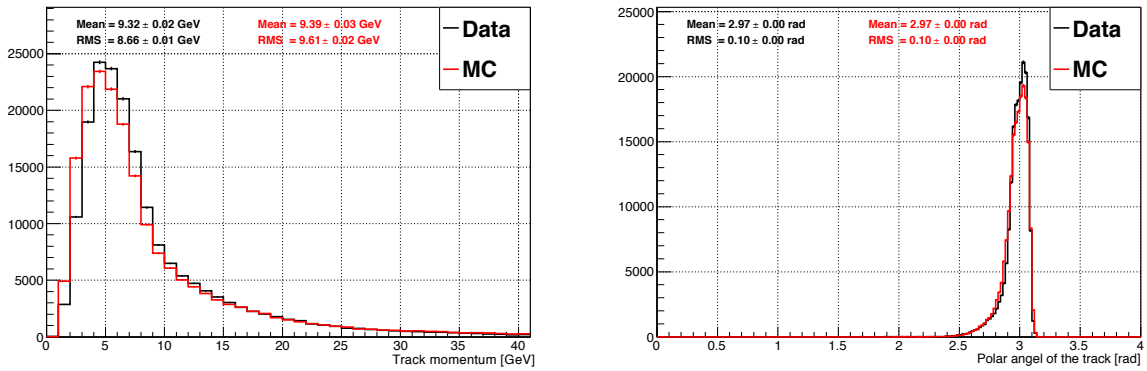

Figure 80: Distributions of the reconstructed track momentum (left) and its polar angle (right) at z=-6150 mm (C-side). The black (red) histogram is obtained using experimental (simulated) events selected applying the cut 1 and cut 2 discussed in the text. The same colors indicate the Mean and the RMS of the two distributions respectively.

I.2.2 Monte Carlo simulation

Monte Carlo (MC) that simulates the interaction of muons from scraping beam within the ATLAS detector is based on GEANT4 [33, 84] and Athena that provide the physics models, the geometry description and the tracking tools. The track momentum, x and y positions measured in C-side is extrapolated back to the A-side using the method described in Ref. [85]. Numerical propagation of the track parameters and covariance matrix that takes into account the materials and magnetic field is employed here. The extrapolated kinematic quantities in A-side are used to generate simulation events. Consequently, these simulated muons are propagated to C-side, reconstructed there, and extrapolated back to A-side, where their spectra are compared to the original ones. Differences between the experimental and simulated spectra are taken into account in the determination of systematic uncertainties. The digitization step of calorimeter simulation, which emulates the behavior of electronics, allows applying the same energy reconstruction procedure to experimental and simulated events.

I.2.3 Calorimeter response and further selection criteria

The estimator of the muon response for each TileCal cell is defined using the ratio of the energy dE deposited by the track in crossed cells. The track extrapolation, discussed in Section I.2.2, provides crossing points of the muon track in each layer. Additional linear interpolations are performed using detailed cell geometry to define the entry and exit points in the crossed cells. The track path length dl is then evaluated as the distance between these points for every cell crossed by the muon.

Identified tracks can be accompanied by other tracks that are not reconstructed because they do not reach the MS at C-side. They can affect the measurement of the energy deposit in a cell. To reduce such effects, an isolation criterion is applied:

4. The number of adjacent cells (the definition is illustrated in Fig. 81) with an energy larger than 60 MeV, N_{ne}, to the one crossed by the reconstructed track is required to be smaller or equal to $N_{ne,low}$=2.

To improve the quality of measurements, additional cuts are applied:

5. Only cell signals produced by tracks with dl >100 mm are retained.

6. To reduce extrapolation errors due to multiple scattering and to remove residual noise contribution, a cut $dE > dE_{cut}$=60 MeV is applied to the measured cell energy dE.

7. The cells with more than 10% of tracks producing a signal that is compatible with pedestal (dE <60 MeV), are not considered in the analysis.

8. Malfunctioning cells are identified when the absolute difference of the mean values of dE/dl between data and MC exceeds 5 times of the uncertainty. These cells are removed from both data and MC.

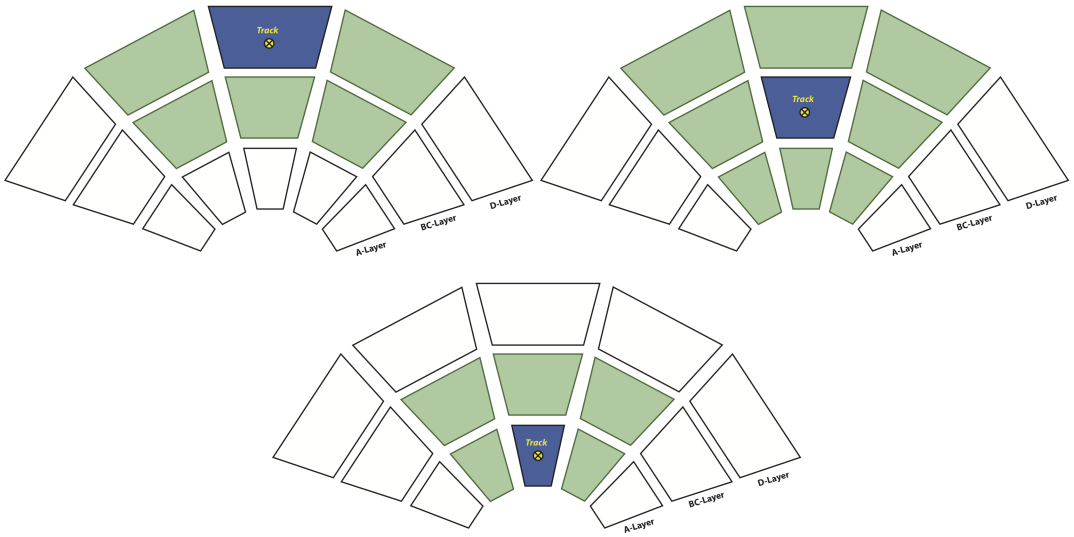

Figure 81: Illustration of how adjacent cells are defined. The figures show the cells viewed from the beam axis. The blue cell is the one crossed by the reconstructed track. The 5 (8) green cells in A, D (BC(B)) layers are considered as adjacent cells.

Truncated mean, $\langle dE/dl \rangle_t$, is used to define the response to muons for the layers with pseudo-rapidity η_c. The mean is computed by truncating a fraction (F=1%) of entries in the upper side of the dE/dl distributions. It is preferred to a normal mean because it is less affected by rare energy-loss processes, such as bremsstrahlung or energetic γ-rays, which can cause large fluctuations on the full mean. The results show some non-linearity and other residual non-uniformities such as differences in momentum and path spectra along η and layers. To compensate for these effects, the ratio of truncated means between experimental and simulated data

$$R = \frac{\langle dE/dl \rangle_t}{\langle dE/dl \rangle_t^{MC}}. \tag{131}$$

is defined.

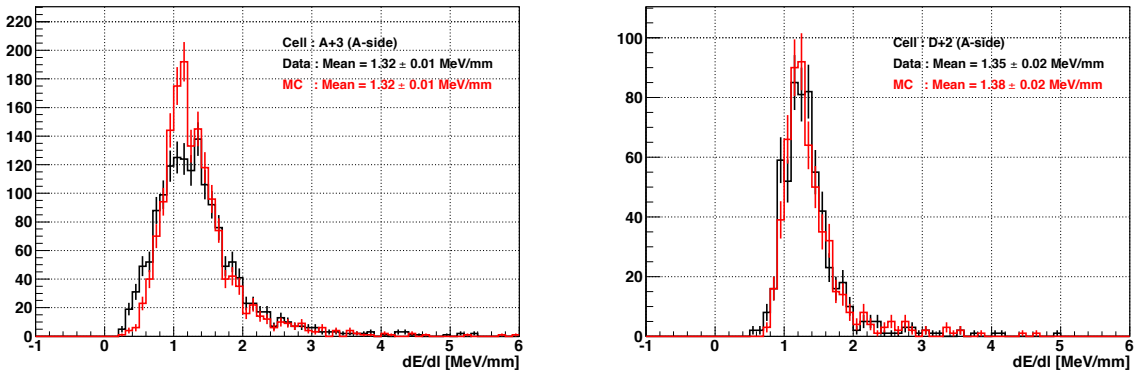

Figure 82: Distribution of dE/dl for the cells LB-A3 (left) and LB-D2 (right) (See Fig. 78) obtained from experimental (black) and simulated data (red).

I.3 Results

The experimental results: a) uniformity of the response of the cells and b) layer inter-calibration, are discussed in this section.

I.3.1 Uniformity of calorimeter cell response

Here, the determinations of the ratios Eq. (131) of a given pseudo-rapidity η_c and layer are discussed. To make the ratios statistically meaningful, the following condition is introduced:

9. Only cells with more than 50 entries in data and MC are considered.

Figure. 83 shows the results as a function of η_c for the cells belonging to the different radial layers. The response of the cells of a given radial layer is found to be uniform inside the errors. The horizontal lines in Fig. 83 correspond to the determination means.

I.3.2 Inter-calibration of radial layers

The systematic uncertainties on the inter-calibration of the radial layers are discussed in this section.

To take correlations into account, the ratios of μ_ϕ for each pair of layers

$$I_{l,l'} = \frac{\mu_\phi(l)}{\mu_\phi(l')} \tag{132}$$

is defined. In Eq. 132 l and l' indicate the layers LB-A, LB-BC, LB-D, EB-A, EB-B and EB-D.

Systematic effects on determination of $I_{l,l'}$ are evaluated considering the following sources:

1. The minimum momentum of tracks (cut 3) in Section I.2.1. In the systematic error study p_{min}=0 GeV and p_{min}=8 GeV are used.

2. The maximum number of adjacent cells, N_{ne}, with $dE > dE_{ne}$=60 MeV (cut 4) in Section I.2.3. Two cases, $N_{ne,low}$=0 and $N_{ne,low}$=4, are considered.

3. The cut value of dE_{cut} (cut 6) in Section I.2.3. Two values of dE_{cut}=30 MeV and 90 MeV are used.

4. The fraction F used in truncated mean (see Section I.2.3). The fractions F equal to 0% and 2% instead of F=1% are used to obtain the systematic errors.

		EB			LB		
		A	B	D	A	BC	D
EB	A	-	$0.990^{+0.013}_{-0.014}$	$0.995^{+0.017}_{-0.013}$	$1.003^{+0.013}_{-0.015}$	$1.012^{+0.011}_{-0.011}$	$1.000^{+0.019}_{-0.019}$
	B	$1.010^{+0.013}_{-0.013}$	-	$1.005^{+0.011}_{-0.013}$	$1.012^{+0.011}_{-0.010}$	$1.021^{+0.008}_{-0.010}$	$1.009^{+0.016}_{-0.016}$
	D	$1.005^{+0.013}_{-0.013}$	$0.995^{+0.010}_{-0.013}$	-	$1.008^{+0.012}_{-0.017}$	$1.017^{+0.010}_{-0.010}$	$1.005^{+0.017}_{-0.018}$
LB	A	$0.997^{+0.013}_{-0.015}$	$0.988^{+0.012}_{-0.010}$	$0.993^{+0.015}_{-0.016}$	-	$1.009^{+0.010}_{-0.011}$	$0.997^{+0.018}_{-0.017}$
	BC	$0.988^{+0.014}_{-0.010}$	$0.979^{+0.011}_{-0.009}$	$0.984^{+0.015}_{-0.010}$	$0.991^{+0.013}_{-0.010}$	-	$0.988^{+0.017}_{-0.016}$
	D	$1.000^{+0.028}_{-0.019}$	$0.991^{+0.023}_{-0.016}$	$0.995^{+0.025}_{-0.018}$	$1.003^{+0.025}_{-0.017}$	$1.012^{+0.020}_{-0.017}$	-

Table 41: Results of the layer responses $I_{l,l'}$. Total errors, including statistical and systematic effects, are reported.

5. The effect of the cell removing (cuts 7, 8 discussed in Section I.2.3) is estimated by removing these criteria in the analysis. The estimated largest systematic effect is smaller than 0.5%.

Other considered systematic errors are:

6. As shown in Fig. 80, the differences between data and MC track momentum varies with layers. Differences up to ±20% are observed. The effects on the relative responses are uncorrelated and are estimated to be 0.4% by Bethe-Bloch formula.

7. The uncertainty on the radial correction measured in beam test using 90° muons [86] were also considered. The effects of this systematic source are uncorrelated and are estimated to be 0.3% corresponding to the statistical errors of the measurements at beam tests.

The determinations of $I_{l,l'}$ are reported in Table 41. The total errors include statistical and systematic errors (sources 1 to 7). They are obtained by adding positive and negative deviations separately in quadrature. In the case where the differences between the obtained values of $I_{l,l'}$ and the one corresponding to the nominal value of the parameter have the same sign, the larger variation in absolute value is retained in the determination of the total systematic error.

I.3.3 Conclusion

Muon events produced by scraping 450 GeV protons in one collimator of the LHC machine have been used to test the calibration of hadronic barrel calorimeter, TileCal, of the ATLAS detector. The analysis is based on the comparison between experimental and simulated data. For each layer, the response of the different cells is quite flat without any structure. The responses of all the layer pairs are found to be consistent within 1-2 % uncertainties including systematics. They are consistent with the scale value of the jet energy measurement set at beam tests using electrons [86].

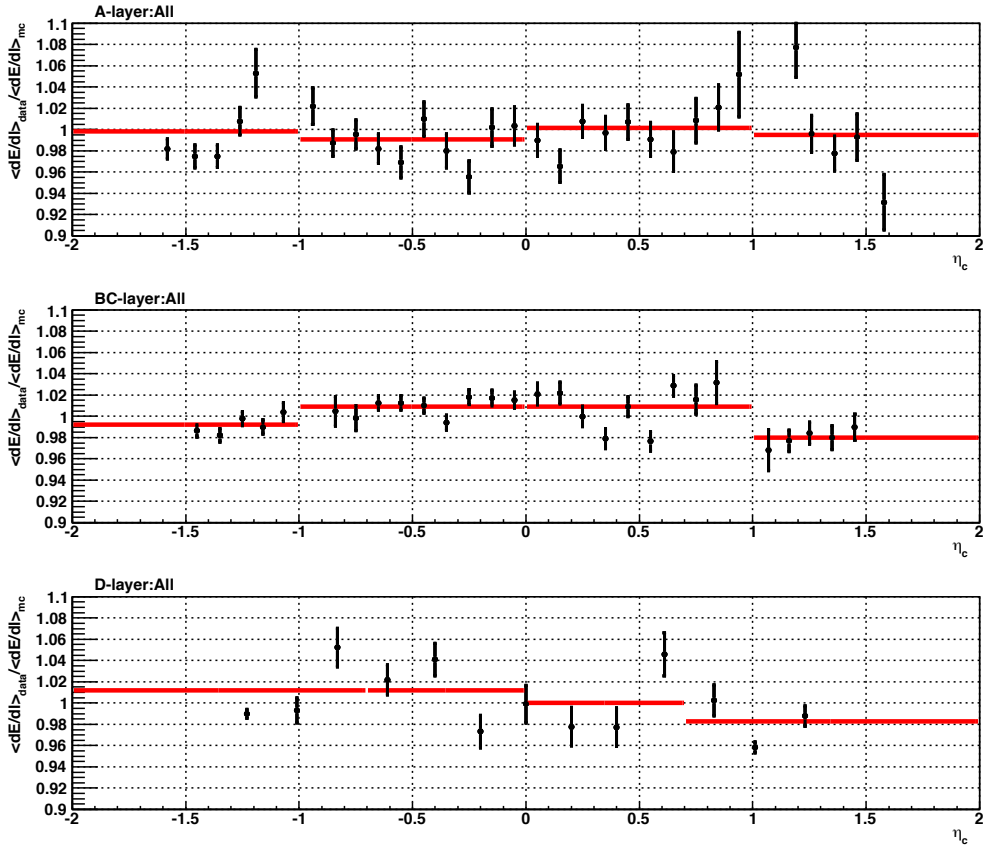

Figure 83: Ratios of the truncated means of the experimental and simulated distributions of the energy deposited in the cells by muons from the scraping beam per unit of path length as a function of the cell's pseudo-rapidity η_c. Results and statistical errors obtained for the cell belonging to layers A (top), BC and B (middle) and D (bottom) are reported. The horizontal lines correspond to the means of the EBA, LBA, LBC and EBC measurements.